BERICHTE AUS DEM

ZENTRUM FÜR MEERES- UND KLIMAFORSCHUNG

Reihe A: Meteorologie

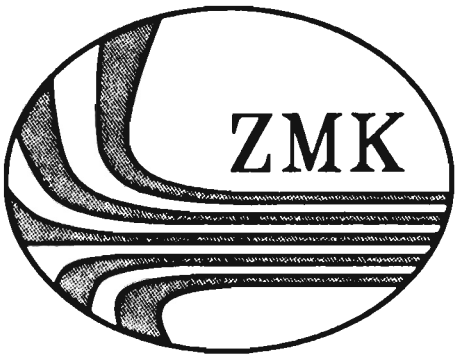

Nr. 33

Field Experiment FRAMZY 1999

CYCLONES OVER THE FRAM STRAIT AND THEIR IMPACT ON SEA ICE

Field Report with Examples of Measurements

Edited by
Burghard Brümmer

Zentrum für Meeres- und Klimaforschung der Universität Hamburg
Meteorologisches Institut
2000

Berichte aus dem Zentrum für Meeres- und Klimaforschung
Reihe A: Meteorologie

Nr. 33

Field Experiment FRAMZY 1999

CYCLONES OVER THE FRAM STRAIT AND THEIR IMPACT ON SEA ICE

Field Report with Examples of Measurements

Edited by
Burghard Brümmer

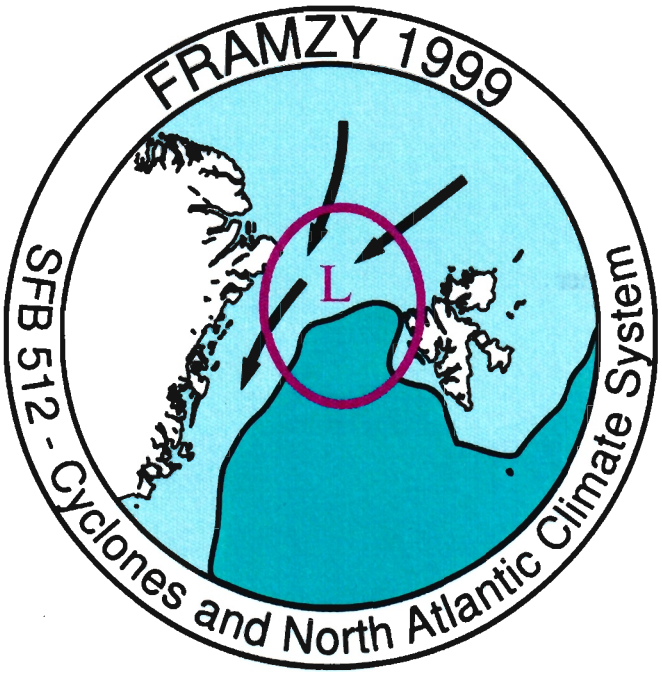

Meteorologisches Institut
Hamburg 2000

Editor Address:
Prof. Dr. Burghard Brümmer
Meteorological Institute
University of Hamburg
Bundesstrasse 55
20146 Hamburg
Tel.: 0049-40-42838 5083
Fax: 0049-40-42838 5452
E-mail: bruemmer@dkrz.de

Content

Summary

In April 1999 the Fram Strait Cyclone Experiment, FRAMZY 1999, was performed in the Fram Strait and Greenland Sea region. Using aircraft, ice buoys, ship, and satellite measurements a data set was compiled to investigate the properties of Fram Strait cyclones, their cyclogenetic conditions on the large- and meso-scale, and their local effects on sea ice drift and sea ice distribution and, thus, on the freshwater flow through the Fram Strait. Furthermore, the data will be used for validation of cyclone simulations with coupled mesoscale models of the atmosphere-ice-ocean system. In this report the field phase of the FRAMZY 1999 experiment is presented together with some model results.

1. Introduction

(Burghard Brümmer, Meteorological Institute, University of Hamburg)

1.1 Motivation

The ice drift in the Arctic Ocean is dominated by two transport regimes: the Transpolar Drift Stream extending from the Siberian coast to the Fram Strait and the Beaufort Gyre located in the American-Canadian sector of the Arctic Ocean (Fig. 1.1). Per annum, about 10-20% of the Arctic sea ice is transported through the Fram Strait into the Atlantic Ocean. Concerning freshwater inflow into the Atlantic, the importance of the ice export via the Fram Strait is only surpassed by that of the Amazon river. The Arctic freshwater export has impacts on the oceanic density stratification and hence on the conditions for deep oceanic convection in the Greenland Sea. Deep convection in this region is a main driving mechanism for the global oceanic circulation (conveyor belt).

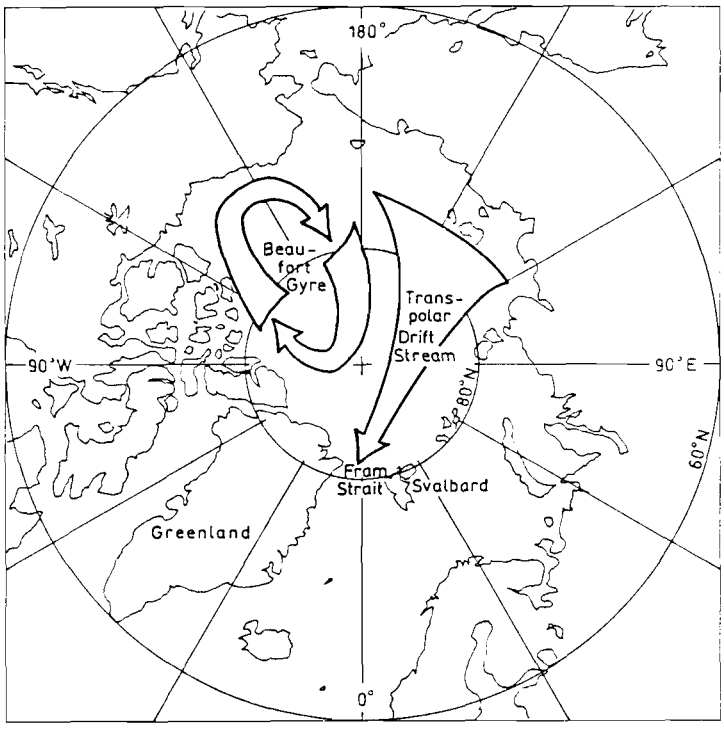

Figure 1.1: *Schematic view of the two dominant ice transport systems inside the Arctic Ocean: The Transpolar Drift Stream and the Beaufort Gyre.*

The ice export via the Fram Strait exhibits pronounced temporal variations. Model-based estimates of the ice export through the Fram Strait for the period 1955 to 1975 (Häkkinen, 1993) and for the period 1986 to 1992 (Harder et al., 1998) result in 2150 km^3/a (minimum 1150, maximum 3600) and 2700 km^3/a (minimum 1900, maximum 3700), respectively (Fig. 1.2). Based on measurements of the vertical ice thickness performed by anchored upward looking sonars, Vinje et al. (1998) estimated an ice export of 2850 km^3/a (minimum 2050, maximum 4700) for the period 1990 to 1996. The strong peak in ice export which occurred 1968 is considered to be responsible for the great salinity anomaly observed in the North Atlantic during the period from 1968 to 1982 (Dickson et al., 1988).

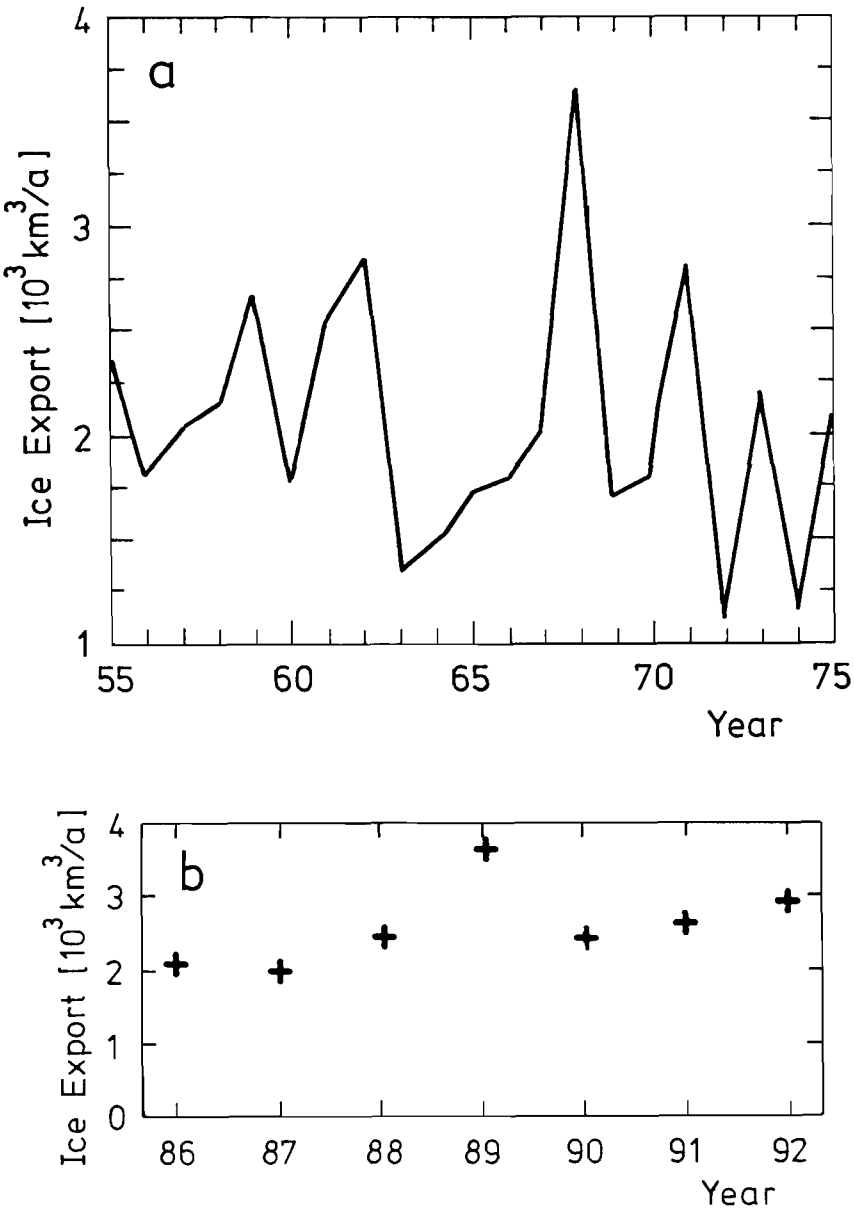

Figure 1.2: *Annual ice drift through the Fram Strait, based on model calculations performed by (a) Häkkinen (1993) for the time interval 1955-1975 and (b) Harder et al. (1998) for the time interval 1986-1992.*

The calculations performed by Harder et al. (1998) indicate that the ice export shows an annual variation whose average amplitude amounts to about 2050 km^3/a. The maximum occurs in March and the minimum in August. Long-term time series valid for the individual months (not shown) reveal variations whose magnitudes are of the order of the long-term averages.

The variability in ice export through the Fram Strait depends on regional conditions as well as on conditions over the entire Arctic Ocean. On one hand, the ice export is influenced by the general atmospheric circulation over the Arctic. For instance, Proshutinsky and Johnson (1997) analysed two wind-driven circulation regimes in the Arctic Ocean: a clockwise transpolar ice drift occurring under predominantly anticyclonic conditions and a counter-clockwise transpolar ice drift developing under predominantly cyclonic conditions (Fig. 1.3).

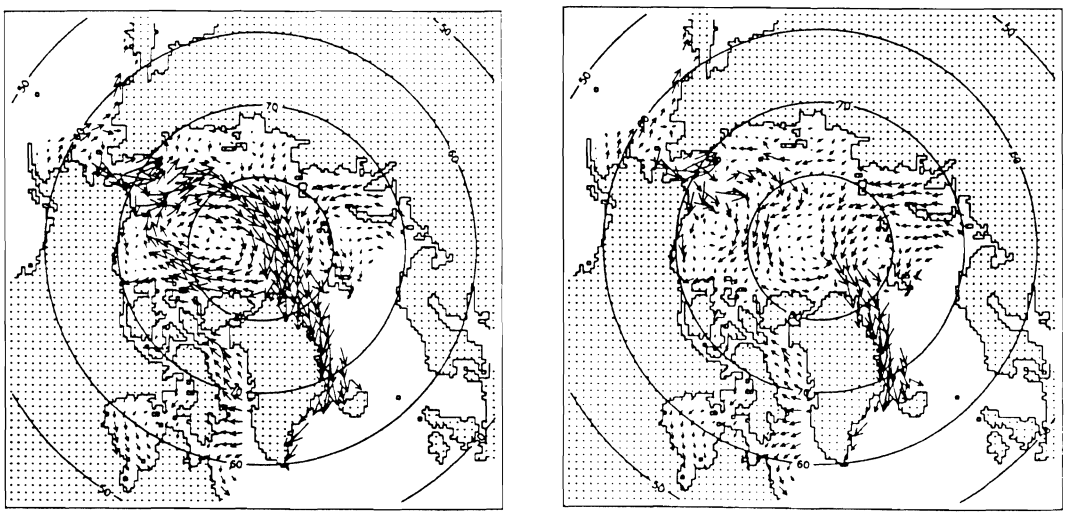

Figure 1.3: *The two dominant wind-driven circulation systems in the Arctic Ocean analysed by Prohutinsky et al. (1997): mean ice drift under predominantly anticyclonic conditions during the periods 1946-52, 1958-63, 1972-79, 1984-88 (left) and under predominantly cyclonic conditions during the periods 1953-57, 1964-71, 1980-83, 1989-93 (right).*

On the other hand, the ice drift is affected by regional conditions. Here, cyclones are of primary importance because the inhomogeneous and time-dependent wind field of a moving cyclone causes ice pressing or dilatation and tends to reduce the inherent ice stress. The ice pack is loosened and can break up. As a result, the outflow of the loosened ice through the "bottle neck" of the Fram Strait is facilitated and increases.

The ice drift is not only affected by the direct dynamical effect of cyclones, but also by an indirect thermodynamical effect associated with clouds. Ahead of the cyclone, advection of moist and warm air over the ice is associated with cloud formation. If clouds are present, the radiation budget and thus the heat budget changes considerably near the ice surface. In this case, the ice temperature increases in comparison with the ice temperature under cloudless conditions. It is a well known phenomenon that clouds tend to persist for many days in the stably stratified Arctic atmosphere.

1.2 Preceding observations

Systematic research on the ice drift through the Fram Strait and its dependence on cyclones has not been performed before. However, there are some former more or less incidental field observations which give indication of the effect.

During the field experiment ARKTIS 1993, a meososcale cyclone was observed over the Fram Strait on 13 March 1993. Based on surface and radiosonde measurements and data from ice buoys positioned around the research ice breaker Polarstern, the characteristics of the cyclone and its effect on the ice drift were analysed by Brümmer and Hoeber (1999). The cyclone developed in the baroclinic zone over the ice edge of the Fram Strait and moved northward over the ice (Fig. 1.4) at a speed of about 5 m/s. The cyclone was relatively small and shallow: its radius was confined to about 150 km and its vertical extension was essentially restricted to the lowest two km of the atmosphere. About 100 km north of the ice edge, the Polarstern observed a near-surface temperature difference of 25 K between the air in the warm sector and the surrounding cold air. The associated pressure difference amounted to about 15 hPa between the centre and the surroundings, while the low-level wind speed reached up to 20 m/s. The northeast-southwest oriented ice drift trajectory exhibits a complete loop caused by the passing cyclone (Fig. 1.5) and the wind factor, i.e. the ratio of ice drift speed to wind speed, increased substantially from 5 % before to 9 % after the cyclone's passage. Dramatically increasing values of ice deformation and large variations in the ice strain-rate tensor occurred during the cyclone's passage.

A further in-situ observation of a mesoscale cyclone over the Fram Strait could be achieved during the CEAREX experiment on April 1989 (Rasmussen et al., 1997). The atmospheric properties of this cyclone (also small and flat) resemble that observed during the ARKTIS 1993 experiment. However, the cyclone's effect on the ice was not observed during CEAREX.

A third in-situ observation of a cyclone over the Fram Strait took place in March 1998 during the ACSYS experiment (Brümmer and Thiemann, 1999). In this case it was demonstrated that aircraft measurements carried out inside a mesoscale cyclone are technically and logistically feasible and can provide the necessary atmospheric information about the cyclone's properties and its horizontal and vertical structure. Furthermore, this case showed that different models analysed the cyclone differently.

The surface pressure analysis (Fig. 1.6a), produced by the global model (GM) of the Deutscher Wetterdienst (DWD) and valid for 16 March 1998, 12 UTC, shows a trough which extends from the main low pressure system over the Greenland Sea to the Fram Strait. The main low pressure system and the northward extending trough is also seen on the 12 hour wind prediction chart (Fig. 1.6b) produced by the regional model HIRLAM of the Norwegian Meteorological Institute (DNMI) and also valid for 16 March 1998, 12 UTC. But, in contrast to GM/DWD the uppermost grid-point wind arrows of HIRLAM reveal a weak westerly wind and thus indicate the presence of an additional low pressure centre.

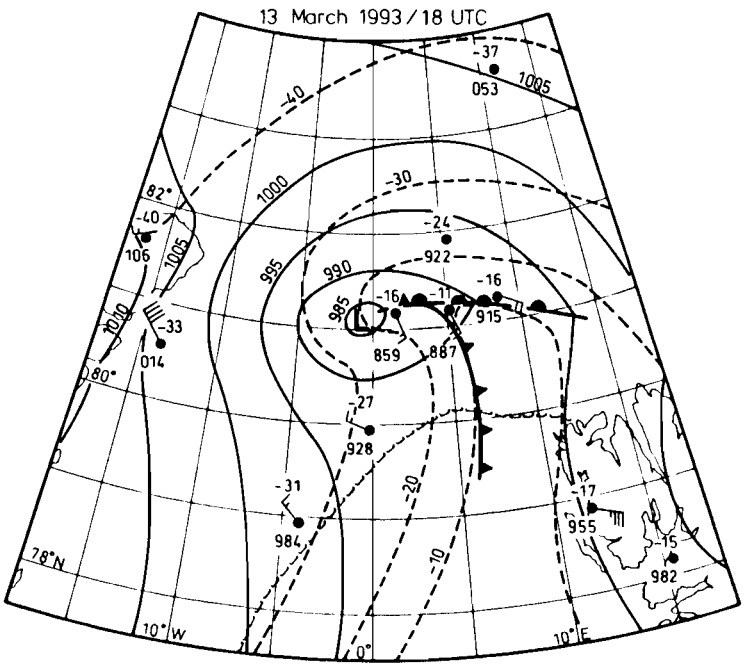

Figure 1.4: *Surface weather map showing isobars (full lines), isotherms (broken lines) and wind information in the vicinity of the mesoscale low on 13 March 1993 at 18 UTC. The low which has formed over the ice edge is moving northward at a speed of 5 m/s over the ice. The research ice breaker Polarstern is located at 81.2°N, 1.5°E while the ice buoys are located at (81.9°N, 5.5°E), (81.2°N, 1.5°E), (81.2°N, 8.0°E), (79.8°N, 0°E), (78.8°N, 4°W).*

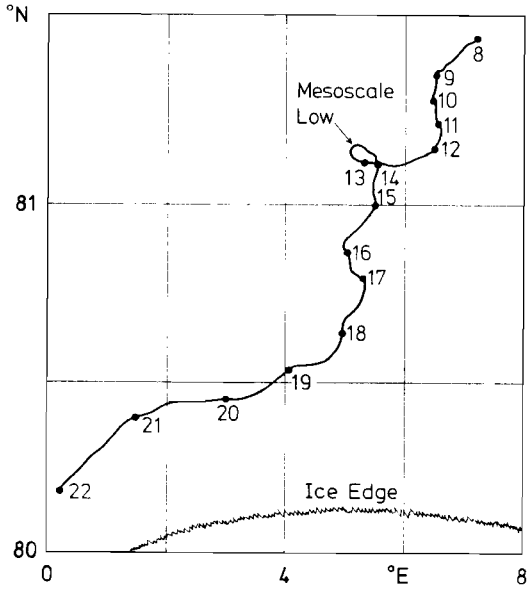

Figure 1.5: *Polarstern's drift in the pack ice from 8 to 22 March 1993. Numbers mark the daily positions at noon. The passing low caused a loop in the trajectory.*

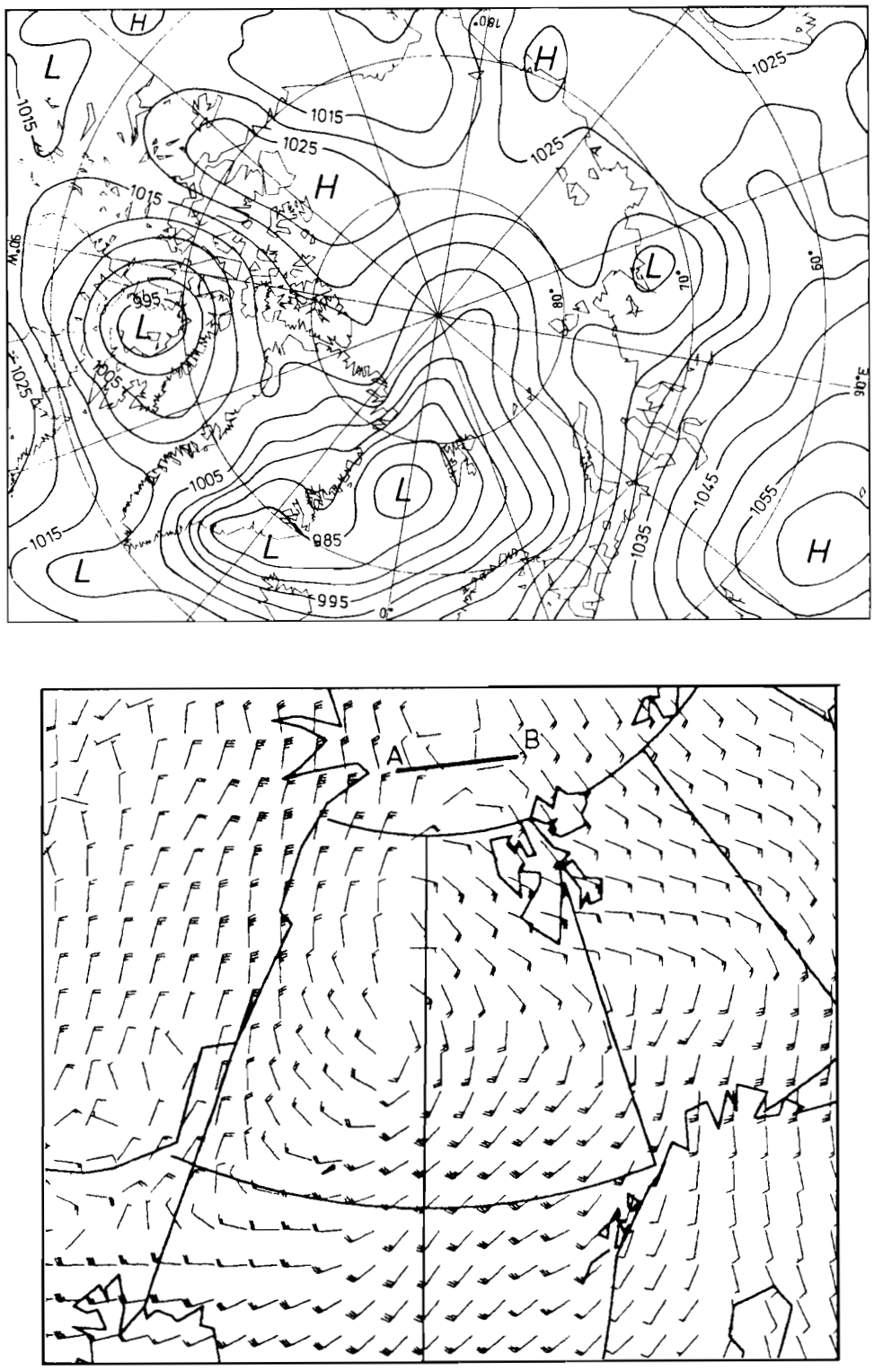

Figure 1.6: *(a) Surface pressure analysis of the global model (GM) of the Deutscher Wetterdienst (DWD), valid for 16 March 1998, 12 UTC. (b) 12 hour wind prediction of the regional model HIRLAM of the Norwegian Weather Service and also valid for 16 March 1998, 12 UTC. Line A-B marks the flight path of research aircraft Falcon.*

In the present case, a verification was possible because measurements had been carried out by the research aircraft Falcon along the line A-B in Fig. 1.6b during the time interval from 10 to 12 UTC. The aircraft measurements confirm the 12 h prognosis of the regional model HIRLAM (westerly winds) and thus the presence of an additional low pressure centre north of the experimental area. At point A, a northwest storm and a temperature of -26° C were encountered, whereas 80 km further to the east the wind blew weakly from southwest and the temperature was 17 K higher. As in case of the cyclone observed during ARKTIS 1993, the large temperature contrast showed up only inside a 500 m deep layer.

The frequency of cyclone occurrence over the Fram Strait has been investigated by Brümmer et al. (2000) on the basis of 6-hourly analyses of the European Centre for Medium Range Weather Forecasting (ECMWF) for the winter months (November to March) of the winters 1986/87 to 1993/94. Until 1991, the horizontal grid resolution was 1.125°, while it has been refined to 0.5° thereafter. The number of cyclones in the Fram Strait area, 75° N - 81° N and 20° W - 15° E, varies from 0 to 13 per month (Fig. 1.7). The long-term average amounts to 6.25 cyclones per month and about 50 % of the analysed cyclones have developed over the Fram Strait. It is unknown, whether the increase of the cyclone frequency observed during the last 3 years of the investigation period is due to natural causes or is an artificial result of the refined grid resolution.

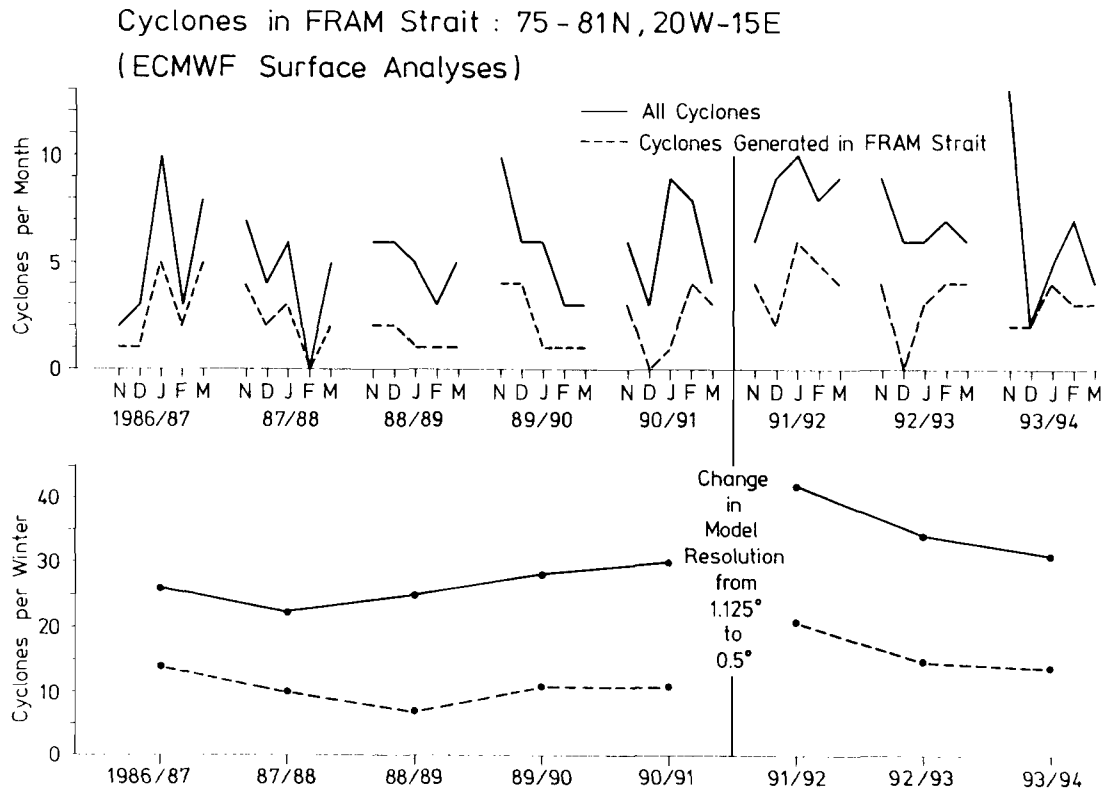

Figure 1.7: *Monthly frequency of cyclone occurrence over the Fram Strait (75°N - 81°N and 20°W - 15°E) from November to March during the winters 1986/87 to 1993/94. The investigation is based on 6 hourly analyses of the ECMWF. The two curves show the frequency of cyclones developed over the Fram Strait and the frequency of all cyclones, respectively (after Brümmer et al., 2000).*

1.3 Objectives

The availability of meteorological data in the Fram Strait is very limited. Apart from special research campaigns (see e.g. Section 1.2) and occasionally passing ice buoys of the International Arctic Buoy Programme, atmospheric routine measurements are absent. Only at the Fram Strait's margins at Spitsbergen and at the coast of Greenland there are a few stations taking routine observations. Since Fram Strait cyclones are presumably often mesoscale events, it is rather unlikely that all cyclones occuring over the Fram Strait are analysed by the models of the various weather services. Even in case of cyclones showing up in the models it is unlikely that the cyclone properties which determine the effect on the ice drift are represented correctly.

A correct prediction of the ice drift through the Fram Strait by coupled atmosphere-ice and atmosphere-ice-ocean models requires a correct prediction of the atmospheric conditions. Here, cyclones are most important. Hence, a correct prediction is especially required for the causes of cyclogenesis (baroclinicity, lee waves) and the atmospheric properties of the cyclones (horizontal structure of wind, pressure and temperature fields; the cyclone's vertical extension revealed by the temperature and pressure fields; surface fluxes of momentum and heat; characteristics of clouds).

In order to improve the data base appropriate for an investigation of Fram Strait cyclones the field campaign FRAMZY 1999 was carried out in the Fram Strait and Greenland Sea area in April 1999 (Fig. 1.8).

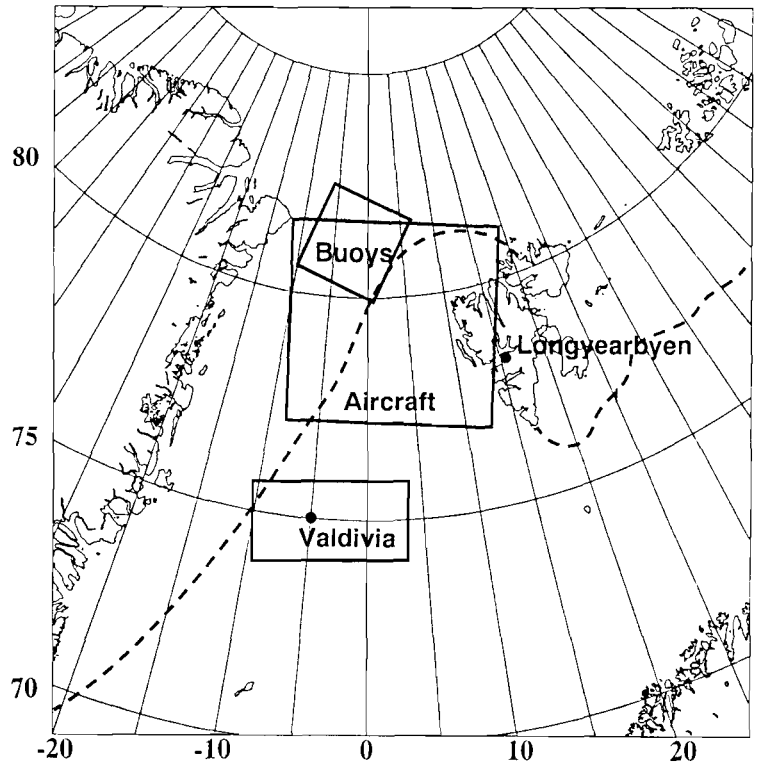

Figure 1.8: *FRAMZY experimental area: the area of aircraft operations, the initial position of the ice-buoy array and the operation area of research vessel Valdivia are indicated. Dashed line shows the approximate position of the ice edge in April 1999.*

Employing the research aircraft Falcon out of Longyearbyen (Spitsbergen), an array of 15 ice buoys in the Fram Strait, the research vessel Valdivia in the Greenland Sea, and information available from island and coastal stations, large-scale and mesoscale weather analyses and satellite remote sensing, a data set was compiled suited to address the following scientific objectives:

a. the cyclogenesis and its dependence on large-scale baroclinicity, on lee waves behind Greenland or Spitsbergen, and on the air flow relative to the ice edge;

b. the atmospheric properties of the cyclones: horizontal scale, vertical extent, surface fluxes of momentum (as atmospheric forcing of the ice drift) and heat at the ice and water surface, and characteristics of the cloud field (base, top, liquid-water content, microphysics);

c. the local effect of the cyclones on the ice drift and on ice distribution and, thus, on fresh water flow through the Fram Strait;

d. verification of cyclone simulations with mesoscale coupled atmosphere-ice models REMO and METRAS (see Section 7) initialized and forced by routine analyses of large-scale weather prediction models and tailored in space and time to the data of the campaign;

e. verification of cyclone simulations with a coupled atmosphere-ice-ocean model (running in "climate mode") initialized and forced by routine analyses of large-scale weather prediction models and tailored in space and time to the data of the campaign;

f. test of the plausibility of long-term time series of cyclone frequency and of the ice drift in the Fram Strait, derived from routine data of the weather services and satellite operators with the objective to provide information on the climate role of the cyclones;

g. use of the data as "ground-truth" for improving satellite remote sensing methodologies for the observation of atmospheric and sea ice parameters.

The items a. to c. focus on the improvement of the knowledge about the interaction between cyclones and ice drift, whereas the items d. to g. focus on the verification and improvement of coupled models and space-borne remote sensing by using the in-situ measured data. The two groups of objectives are interconnected in such a way that, for instance, the models will also be applied for sensitivity studies which can be used - in addition to the in-situ measurements - to improve the understanding of processes.

1.4 Participating institutions and acknowledgement

The following institutions participated in or contributed to the field experiment FRAMZY 1999:

Meteorologisches Institut der Universität Hamburg (co-ordinator)
Institut für Meereskunde der Universität Hamburg
Max-Planck-Institut für Meteorologie, Hamburg
Deutsches Zentrum für Luft- und Raumfahrt (DLR) at Oberpfaffenhofen

GKSS Forschungszentrum Geesthacht, Geesthacht
Deutscher Wetterdienst, Zentralamt Offenbach
Det Norske Meteorologiske Institutt (DNMI), Longyearbyen and Oslo
Tromsø Satellite Station, Tromsø
Norsk Polar Institutt, Longyearbyen
Spitsbergen Travel (SPITRA), Longyearbyen
Lufttransport AS, Longyearbyen and Tromsø

We thank all participants from these institutions for their efforts and support to make FRAMZY 1999 a successful field campaign.

Furthermore, thanks are due to the Deutsche Forschungsgemeinschaft, Bonn, which funded most of the FRAMZY 1999 field activities within the framework of the Sonderforschungsbereich 512 "Tiefdruckgebiete und Klimasystem des Nordatlantiks" established at the University of Hamburg.

1.5 References

Brümmer, B. and S. Thiemann, 1999: Field campaign ACSYS 1998: aircraft measurements in Arctic on-ice air flows. Berichte Zentr. f. Meeres- u. Klimaforsch. Reihe A, Nr. 32, 35 pp.

Brümmer, B., and H. Hoeber, 1999: A mesoscale cyclone over the Fram Strait and its effects on the sea ice. J. Geophys. Res. 104, 19.085-19.098.

Brümmer, B., S. Thiemann, and A. Kirchgäßner, 2000: A cyclone statistics for the Arctic based on European Centre re-analysis data. Submitted to Met. Atm. Phys.

Dickson, R., J. Meincke, S.-A. Malmberg, A. Lee, 1988: The "Great Salinity Anomaly" in the northern Atlantic 1968-1982. Progr. Oceanogr. 20, 103-151.

Häkkinen, S., 1993: An Arctic source of the Great Salinity Anomaly: A simulation of the Arctic ice-ocean system for 1955-1975. J. Geophys. Res. 98 (C9), 16397-16410.

Harder, M., P. Lemke, and M. Hilmer, 1998: Simulation of sea ice transport through Fram Strait: Natural variability and sensitivity to forcing. J. Geophys. Res. 103 (C3), 5595-5606.

Proshutinsky, A., and M. Johnson, 1997: Two circulation regimes of the wind-driven Arctic ocean. J. Geophys. Res. 102 (C6), 12493-12514.

Rasmussen, E., P. Guest, and K. Davidson, 1997: Synoptic and mesoscale features over the ice-covered portion of the Fram Strait in Spring. J. Geophys. Res. 102 (D12), 13975-13986.

Vinje, T., N. Nordlund, and A. Kvambekk, 1998: Monitoring ice thickness in Fram Strait. J. Geophys. Res. 103 (C5), 10437-10449.

2. The synoptic conditions during FRAMZY '99

(Burghard Brümmer and Björn Affeld, Meteorological Institute, University of Hamburg)

This section briefly describes the synoptic conditions in the Fram Strait region and over the Arctic Ocean during the period 1 to 30 April 1999. The description is based on the daily 12 UTC weather maps for the surface and the 500 hPa level as analysed by the Deutscher Wetterdienst (DWD) in Offenbach and as published in the „Europäischer Wetterbericht". The maps are presented day by day in Appendix A showing only the Arctic section. Furthermore, six-hourly analyses of the European Centre of Medium-Range Weather Forecast (ECMWF) are used.

2.1 Course of weather events

The synoptic conditions in the experimental region during April 1999 can be subdivided into four phases: (a) Phase I from 1 to 7 April with predominantly cyclonic conditions, (b) Phase II from 8 to 15 April with predominantly anticyclonic conditions, (c) 16 to 26 April with again predominantly cyclonic conditions, and (d) Phase IV from 27 to 30 April with again anticyclonic conditions.

a. Phase I (1 - 7 April):
This phase begins with a comprehensive low-pressure system centered over the Arctic Ocean. Until 4 April the center shifts from the North Pole region to the eastern Barents Sea along a trajectory located to the east of Spitsbergen. On 2 and 3 April the Fram Strait is in a cold and strong northwesterly flow on the rear side of the low. In this situation, on 3 April, with winds up to 20 m/s, the ice buoys were deployed with parachutes from an aircraft (see Section 4). On 5 April a new cyclone approaches the Fram Strait from southwest, but does not reach this area. It moves eastward into the Barents Sea passing on its way the south tip of Spitsbergen. A rapid weather change with strong snowfall and storm over Spitsbergen on 6 April prevented the research aircraft Falcon (and all other air traffic) to land at Longyearbyen (see Section 3). The Falcon which was already in the air towards Longyearbyen had to return to Kiruna in Sweden from where it had departed and arrived only one day later in Longyearbyen. These extremely bad weather conditions over Spitsbergen occurred when the cyclone at the surface merged with a cold air low at 500 hPa.

b. Phase II (8 - 15 April):
During this phase a high pressure zone developes and strengthens over the central Arctic. It reaches its highest pressure with values of more than 1040 hPa on 10 April. A ridge of high pressure extends to the eastern part of Greenland. This situation continues until 13 April. Later, the high pressure zone still remains in the area, but weakens and divides into several centers. Cyclone activity during this phase takes place far to the south of the Fram Strait region over the Norwegian Sea and southern Barents Sea and later even over southern Scandinavia. During the entire phase northeasterly winds occurred over the Fram Strait. Wind speed was largest during the days from 9 to 11 April and decreased slowly until 15 April. Continuous strong northeasterly winds caused at least parts of the buoy array to drift rather rapidly southwestwards (see Section 4). Since the high pressure conditions lasted for such a long period and the aircraft Falcon was only available until 21 April, it was decided to perform also aircraft missions in this situation.

Thus, on 10, 12, and 14 April three aircraft missions under three different wind speed conditions were flown (see Section 3). All three missions had two aims: (a) to measure the atmospheric forcing over the ice buoy array in order to obtain data sets for testing the mesoscale coupled atmosphere-ice models REMO and METRAS (see Section 7) and (b) to measure the baroclinic conditions around the ice edge under ice-parallel wind direction, a situation for which observations are particularly seldom. The long persistence of high surface pressure conditions was steered and supported at 500 hPa by a high pressure cell over the central Arctic and later by a ridge extending from Greenland into the central Arctic.

c. Phase III (16 - 26 April):
While high pressure conditions continue to occur over the central Arctic until 18 April, a cyclone over the southern Norwegian Sea moves slowly northward. It reaches the southern Greenland Sea on 17 April, the middle Greenland Sea on 18 April, and crosses the Fram Strait on 19 April. During this time its central pressure is continuously rising from $\leq$ 995 hPa to $\leq$ 1010 hPa. Strong pressure gradients occurred on the north and northwest side of the cyclone. At RV Valdivia's position at 73.6°N, 6.5°W, winds at ship's level reached nearly 20 m/s on 17 April (see Section 5), so that radiosonde launches from the ship's deck were forbidden for persons' safety reasons. On 18 and 19 April two Falcon flight missions took place in the cyclone. On 18 April measurements were performed over the buoy array at the northwest edge of the cyclone during strong low-level winds. In addition a cross-section through the cyclone was flown. On 19 April, when the cyclone crossed the ice edge, two cross-sections through the cyclone were flown over the ice. The cyclone trajectory follows roughly the predominantly southerly air flow at 500 hPa.

On 19 April, another cyclone is present at the Norwegian coast. But it moves along a slightly more northeasterly trajectory through the Barents Sea and passes Spitsbergen to the east. It joins on 20 April with the above-mentioned Fram Strait cyclone and a low northwest of Greenland. Supported by an upper level trough this leads to a strong cyclogenesis north/northeast of Novaja Semlja. This cyclone extends to high levels and persists for several days more or less in the same region and influences also the Fram Strait area at least until 23 April. Thereafter, until 26 April, weak pressure gradients are present over the Fram Strait and Greenland Sea. In this situation weak and small cyclones are generated over the southern and middle parts of the Greenland Sea. However, they do not reach the Fram Strait, but instead move eastward with the 500 hPa flow and stay with their centers south of Spitsbergen.

d. Phase IV (27 - 30 April):
In this phase pressure rises over the Alaskian and Canadian Sector of the Arctic Ocean. A ridge extends towards the East-Greenland coast and influences the Fram Strait region with northerly to easterly winds.

2.2 The Fram Strait cyclone of 17-20 April 1999

Although the Fram Strait was influenced for many days by cyclonic conditions, only one cyclone center passed through it (on 18/19 April). The cyclone was not generated locally by the baroclinic conditions in the Greenland Sea, but existed already many days in advance. It was „born" on 14 April near Brittany (France). Its trajectory and its corresponding central pressure are shown in Figure 2.1. Both Figures are based on the 6-hourly analyses of the ECMWF.

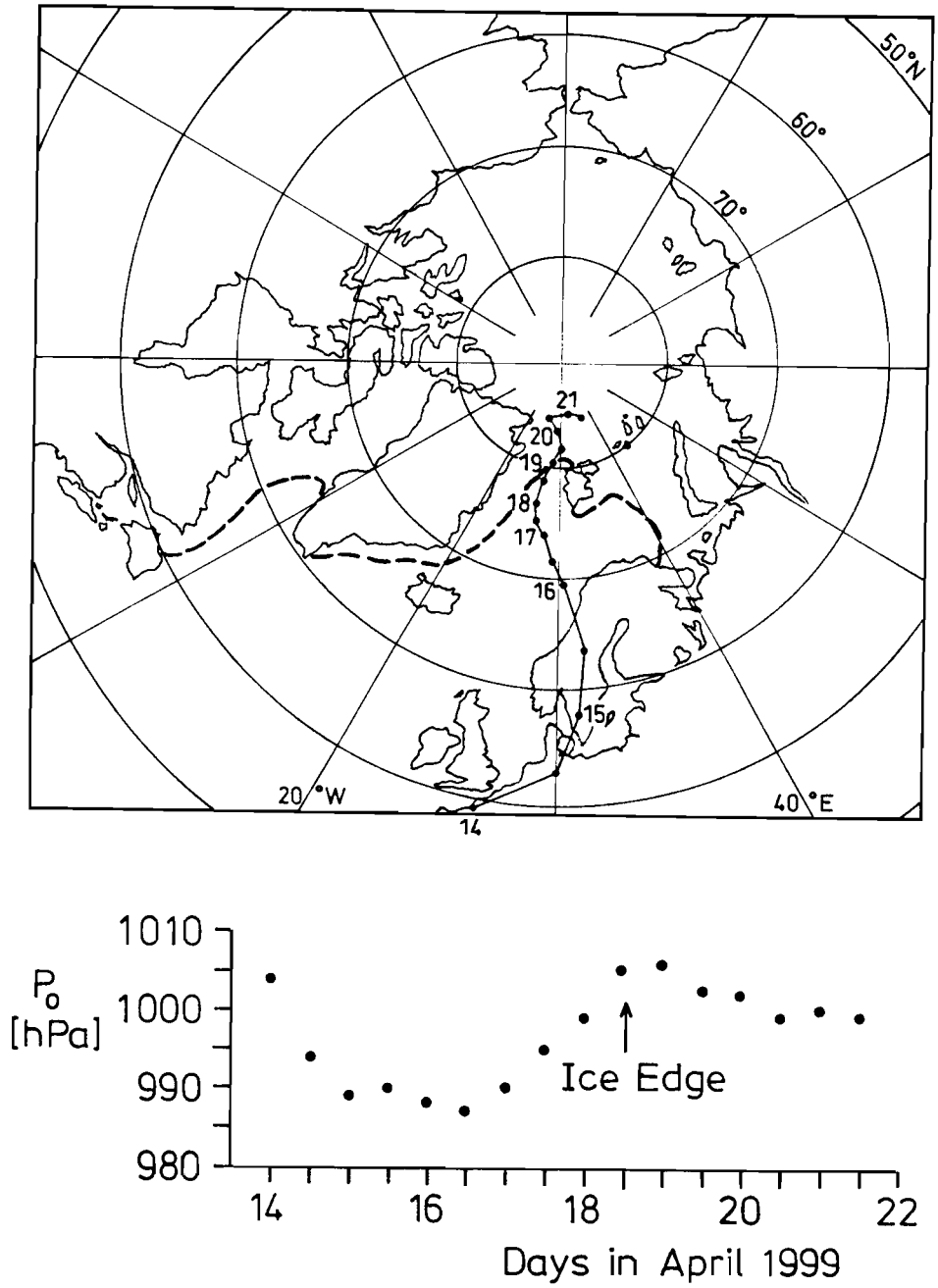

Figure 2.1: *Trajectory (a) and central surface pressure p_0 (b) of the Fram Strait cyclone at 12-hourly intervals as analysed by ECMWF. Numbers mark the 12 UTC position on the respective day in April 1999.*

The passage of the cyclone through the Fram Strait between 17 and 20 April is shown in Figures 2.2a-f as analysed by ECMWF. In addition the positions of the Argos ice buoys (see Section 4), the position of research vessel Valdivia (see Section 5), and the positions of the aircraft flight missions (see Section 3) on 18 and 19 April are diplayed in Figures 2.2. The cyclone passes east of Valdivia and of the buoy array over the open water of the West-Spitsbergen Current northwards and weakens during that time.

The ice edge in the ECMWF analyses is located too far south and east (up to 100 km) in the Fram Strait. For example, on 19 April 12 UTC the true ice edge was observed by aircraft at the northeastern corner of the flight pattern. This incorrectness in the location of the ice edge complicates direct comparisons between observations and model analyses or even makes them meaningless.

One cyclone per three weeks in the Fram Strait, as observed in April 1999, belongs to the lowest frequencies of monthly cyclones in the Fram Strait. A statistical study of Brümmer et al. (2000) for the years 1986/87 to 1993/94 gives a range of 0 to 13 cyclones. Complete absence of cyclones occurred in only one out of 40 months (see Fig. 1.7).

Cyclones in the Fram Strait often develope in a trough situation at the edge of the comprehensive Icelandic low-pressure system. In April 1999 the Islandic low was relatively weak. This is reflected both in the mean sea level pressure distribution for the main FRAMZY period 3-24 April 1999 which is displayed in Figure 2.3 and in a low value of the North Atlantic Oscillation Index, NAOI, which is displayed for the last 50 years (1950 to 1999) in Figure 2.4. During April 1999 the cyclonic activity was instead relatively frequent over the Barents Sea and Kara Sea. Often the cyclones were stronger there than over the Islandic region.

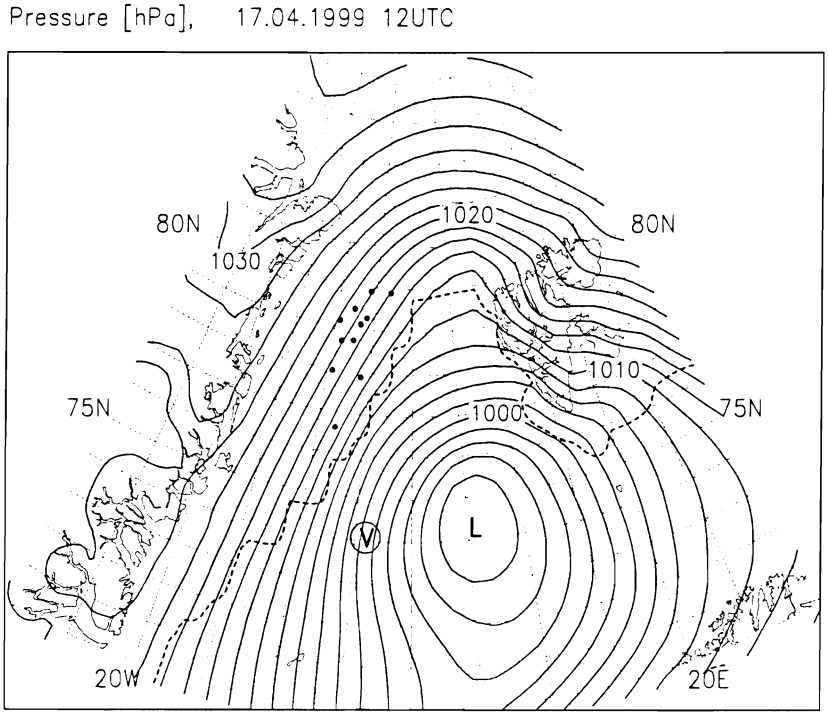

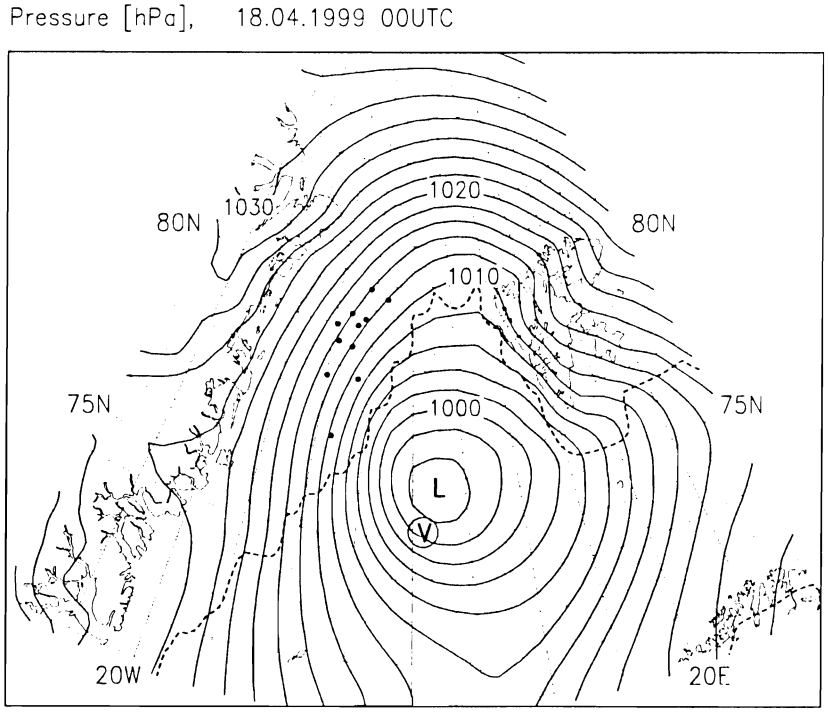

Figure 2.2 (a)-(f): *12-hourly sea-level pressure maps between 17 April 12 UTC and 20 April 00 UTC as analysed by ECMWF (T 213; 0.5° resolution). L marks cyclone centre, V position of research vessel Valdivia. Dots mark position of ice buoys and full lines mark flight patterns of research aircraft Falcon. The dashed line represents the ice edge (-1.8°C isoline of surface temperature) as used in the ECMWF analyses.*

Pressure [hPa], 18.04.1999 12UTC

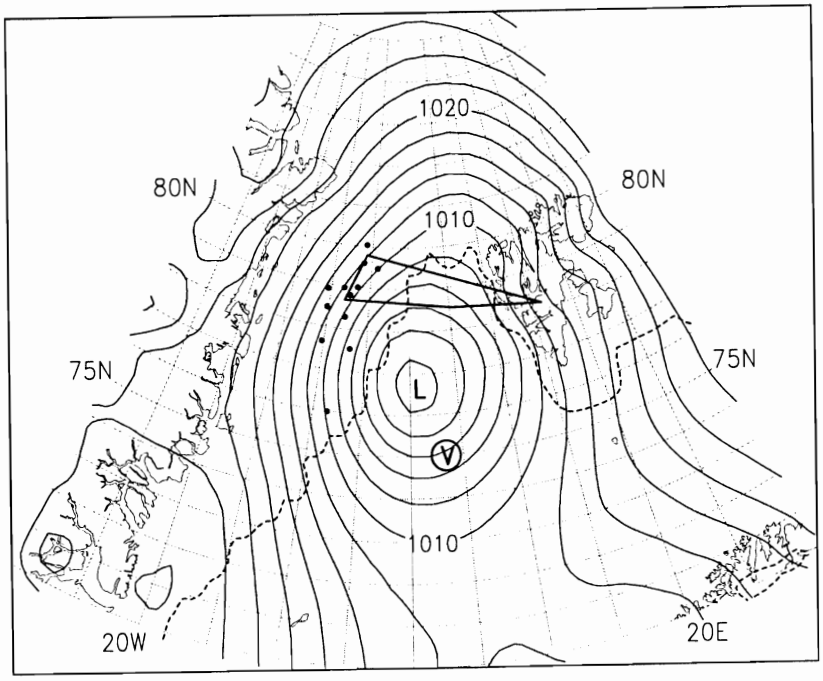

Pressure [hPa], 19.04.1999 00UTC

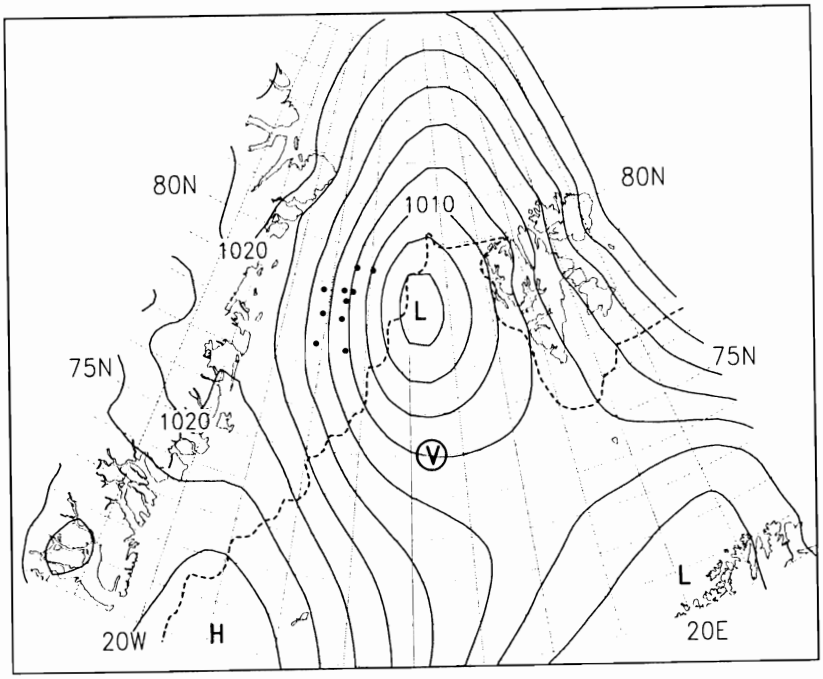

Pressure [hPa], 19.04.1999 12UTC

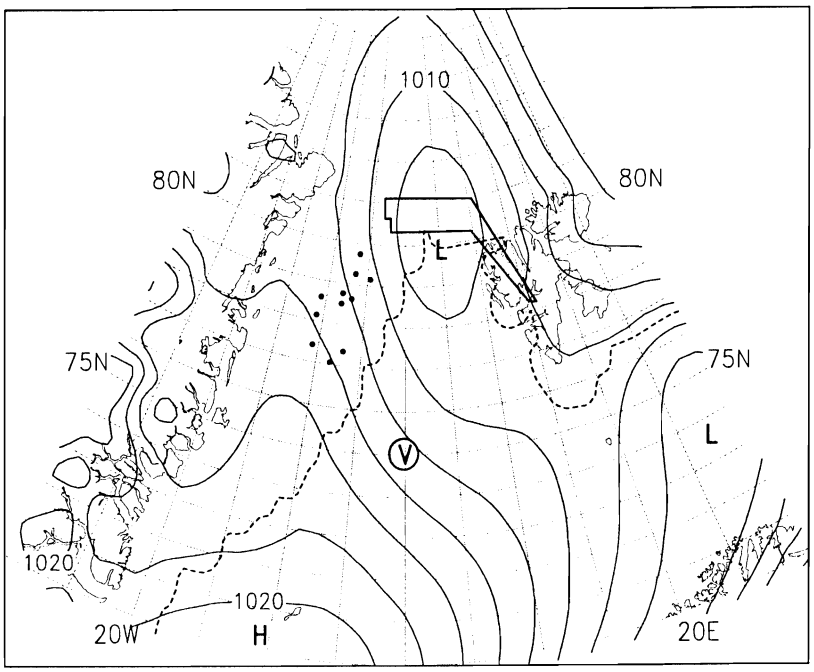

Pressure [hPa], 20.04.1999 00UTC

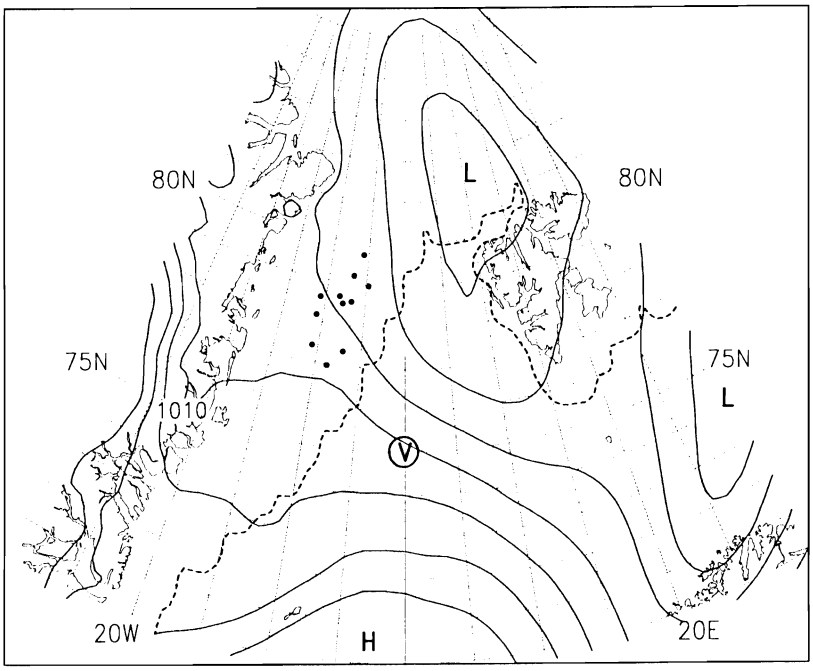

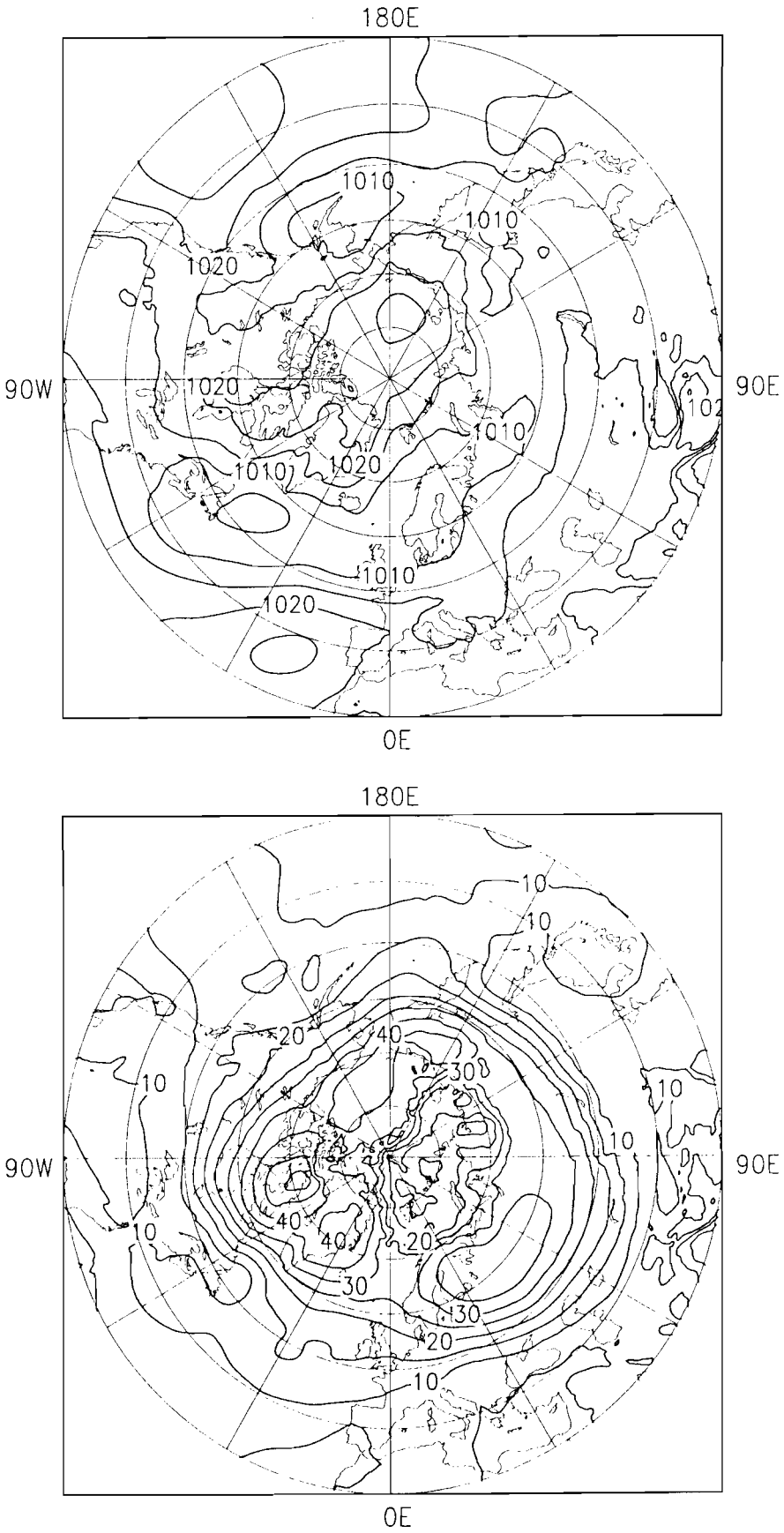

Figure 2.3: *Mean sea level pressure distribution (above) and variance (below) for the FRAMZY period from 3-24 April 1999 based on 6-hourly ECMWF analyses.*

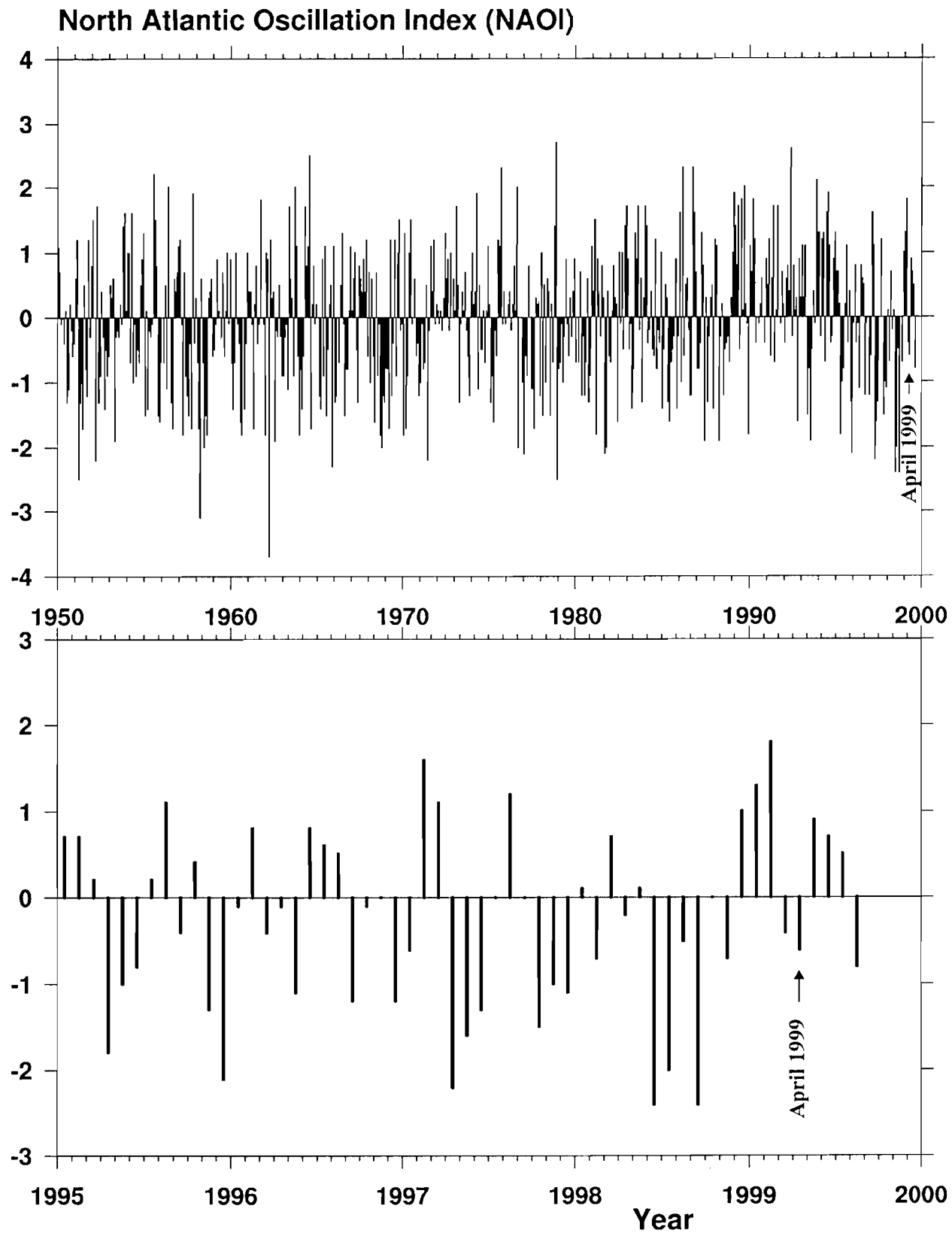

Figure 2.4: *Time series of monthly North-Atlantic Oscillation Index, NAOI, for the periods January 1950 to August 1999 and January 1995 to August 1999 (enlarged).*

3. Research aircraft Falcon

(Gerd Müller and Burghard Brümmer, Meteorological Institute, University of Hamburg)

3.1 General remarks

The research aircraft Falcon-20 of the DLR (Deutsches Zentrum für Luft- und Raumfahrt, Oberpfaffenhofen) was the most important platform among those which sampled atmospheric information during the field campaign FRAMZY'99. During the period from 7 to 20 April 1999, the Falcon was stationed at the airfield Longyearbyen (78° 15'N and 15° 30'E) on the island of Spitsbergen. On five days, 10, 12, 14, 18, and 19 April 1999, the Falcon flew missions above the array of Argos ice buoys installed in the Fram Strait in an area of about 200 km x 200 km centered around 81.2°N and 5°W. During these missions, the horizontal (150 km x 150 km) and the vertical (15 m - 3000 m) distribution of the atmospheric mean and turbulent state as well as the atmospheric forcing of the buoy and ice drift could be measured in detail successfully. In addition to atmospheric parameters, also ice information, such as ice coverage and ice-surface temperature, had been detected.

The first three missions took place under a northeastern, nearly ice-parallel air flow, while the last two ones were flown under cyclonic conditions. The last mission took place right through the center of the cyclone. During all flight missions the baroclinicity at the ice edge was measured in order to assess its potential for cyclone generation.

The flight patterns consisted of along-wind and cross-wind oriented horizontal legs and of vertical soundings. Two so-called "stacks" composed of several horizontal cross-wind flight legs located one upon the other at different altitudes have been flown during the first, second and fourth mission. In case of the first three missions, the lowest legs were between 10 m to 20 m, whereas in case of the last two missions the lowest legs were between 60 m to 70 m above ice and between 15 m and 30 m above open water. Due to safety reasons, the aircraft was not allowed to fly below 60 m above ice during the last two missions, since the visibility was relatively bad and the turbulence was relatively strong above ice inside the cyclone. An overview of all Falcon flight patterns during FRAMZY'99 is given in Figure 3.1.

Planning meetings in the operation center (office rooms of the Norsk Polarinstitutt) at the air field took place twice per day, one in the morning to decide on the activities of the day and the other one in the afternoon to plan tentatively the activities of the next day. Aircraft missions were planned and guided by NOAA satellite images and numerical weather predictions of the Deutscher Wetterdienst (DWD) and Det Norske Meteorologiske Institutt (DNMI). Satellite information included infrared and visible quick-look images from Dundee and AVHRR images (two times per day) from Tromsø. Meteorological flight briefings for pilots and scientists were hold by the staff of the local airfield weather station. The engaged support by Mr. Arne Tolas is particularly mentioned.

Weather conditions at the airfield, either during planned take-off or forecasted for time of arrival, were sometimes adverse when falling or blowing snow and runway cross winds caused conditions beyond international flight rules or aircraft specifications. In a few cases, this prevented planned flight missions. However, this was not a serious cut since the weather conditions in April 1999 were most times favourable.

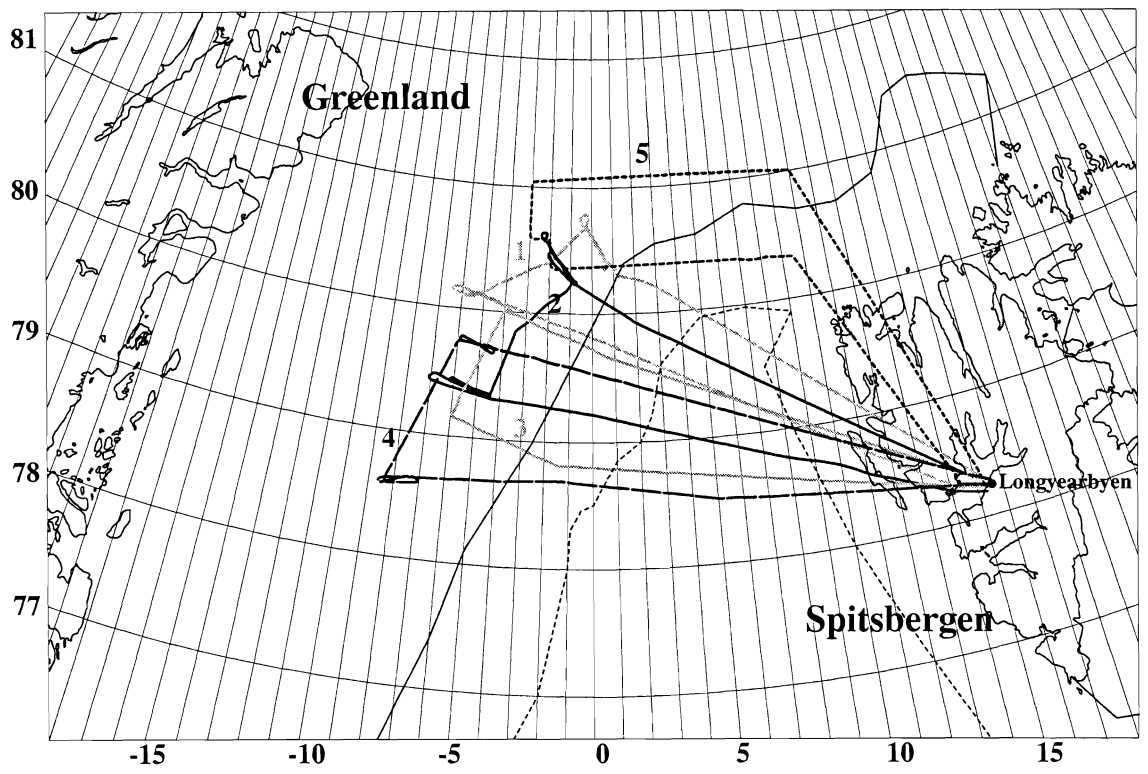

Figure 3.1: *Positions of all flight patterns of Falcon-20 during FRAMZY'99 ((1) 10, (2) 12, (3) 14, (4) 18, (5) 19 April 1999) and ice coverage from DNMI ice chart (solid curve: 90%), (dashed curve 10%) on 6 April 1999.*

The participants in the FRAMZY'99 aircraft program are listed below:
Meteorologisches Institut der Universität Hamburg: B. Brümmer, G. Müller.
Max-Planck-Institut für Meteorologie, Hamburg: F. Papke.
GKSS-Forschungszentrum, Geesthacht: N. Buschmann, U. Maixner, A. Reuter.
Deutsches Zentrum für Luft- und Raumfahrt, Oberpfaffenhofen: P. Gieb, S. Grillenbeck, W. Meier, R. Welser, D. Zander.

3.2 Aircraft and Instrumentation

The Falcon-20 is a twin engine jet aircraft with a wingspan of about 16 m and a length of about 17 m (Figure 3.2). The typical flight speed during low-level operations in the boundary layer is about 100 m/s and about 250 m/s during high-level transit flights. The maximum operation height is 41000 feet. The Falcon-20 is equipped with new engines (since 1997) allowing an operational endurance at low levels of about 5 hours.

The Falcon was equipped with two temperature sensors, three humidity sensors, sensors for static and dynamic pressure, and a gust probe system to measure the three-dimensional wind vector in connection with an inertial reference system. Furthermore, it was equipped with a GPS navigation system, a radio altimeter, a surface temperature infrared radiometer, upward and downward facing pyranometers and pyrgeometers to measure short- and longwave radiation

Figure 3.2: *The Falcon-20 of the DLR.*

fluxes from above and below. A forward facing video camera was fixed at the cockpit window and recorded the experimental conditions during the entire flight mission.

For the measurement of cloud microphysical properties, the Falcon was equipped with 3 different PMS (Particle Measuring Systems) probes covering a size range of 2 - 6400 mm and with a Nevzorov LWC/TWC (liquid water content / total water content) probe. GKSS Research Center (Geesthacht, Germany) hold responsible for the calibration and operation of this equipment. Details concerning cloud-microphysics-data acquisition are given in section 3.4.6.

Specifications of accuracies and sampling frequencies of all sensors are listed in Table 3.1. Apart from the relative wind measured at a 1.8 m long carbon fibre boom in the undisturbed flow ahead of the aircraft and apart from cloud particles measured by probes which were installed in separate tubes below the aircraft, all parameters were measured at the fuselage of the plane. A detailed description of the Falcon standard instrumentation is given by Fimpel (1987).

The signals of the meteorological and aircraft-related sensors were recorded on cassettes. Parallel to this, data were processed on-line during the flight, so that the aircraft scientist had immediate information about a selected number of parameters (including the three-dimensional wind vector). These on-line informations were displayed on screen and printed on paper. Details of the on-board data acquisition system are reported by Wilcke and Gehricke (1988).

Table 3.1: Instrumentation of the Falcon-20

Parameter	Accuracy	Resolution	Sampling frequency (Hz)	Sampling dist. (m)	Sensor type, hardware, manufacturer
Wind					
u,v	± 1.0 m/s	± 0.02 m/s	100	1	5-Hole probe (Rose-mount 858J) and Honey-well IRS 1761
w	± 0.5 m/s	± 0.02 m/s	100	1	
Temperature					
T	± 0.5 K	± 0.006 K	100	1	Pt-100 (Rosem.102 BM/BV)
T	± 0.5 K	± 0.006 K	10	10	Pt-500 (Rosem.102 AU2AG)
Humidity					
ϱ_v	± 0.5 g/m^3	± 0.002 g/m^3	100	1	Lyman-α-Humidometer (El. Res. Corp. BLR)
RH	± 2 %	± 0.007 %	10	10	Vaisala Humicap HMP 11
T_D	± 1.0 K	± 0.006 K	10	10	Dewpoint sensor (General Eastern 1011B)
Pressure					
p	± 1 hPa	± 0.07 hPa	100	1	Pitot-tube (Rosem.)
Altitude					
z	± 5 m	±0.5 m	10	10	Radioaltimeter
Position					
Lat., long.	(~ 400 m/h)	± 0.0003"	10	10	Honeywell IRS 1761
Lat., long.	± 10 m	± 1 m	10	10	GPS
Surface temp.					
T_S	± 1.0 K	± 0.01 K	10	10	Infrared radiation thermometer KT-19
Radiation					
K↓, K↑	± 4 W/m^2	± 0.1 W/m^2	10	10	Pyranometer (Epply PSP)
L↓, L↑	± 10 W/m^2	± 0.2 W/m^2	10	10	Pyrgeometer (Epply PIR)
Cloud particles					
1D-Probe	± 0.2 %	± 1	50	2	PMS FSSP-100 (2-47μm)
2D-Probe	± 0.2 % of total	± 1	50	2	PMS OAP-2D2-C (25-800 μm)
Precipitation Particles					
2D-Probe	± 0.2 % of total	± 1	50	2	PMS OAP-2D2-P (200-6400 μm)
Cloud LWC/IWC					
Hot wire probe	± 5 % of total		50	2	Nevzerov LWC/IWC probe

A quicklook processing of all vertical soundings and horizontal flight legs was made immediately after the flight at the operation center at Longyearbyen in order to obtain a general view of the entire flight and to look at other parameters not displayed by the on-line system. The final

complete processing of all data channels with the highest time resolution (100 Hz) was performed after the experiment at Hamburg.

References

Fimpel, H.P. (1987): The DLR meteorological research aircraft FALCON-E: Instrumentation and examples of measured data. Reprint: Proceedings of the sixth symposium on meteorological observations and instrumentations. Am. Met. Soc., 12-16 January 1987, New Orleans, LA.

Wilcke, G., and A. Gehricke (1988): On-board data acquisition system of the FALCON-E aircraft, a new approach. International telemetering conference, Las Vegas, 17-20 October, 1988.

3.3 Flight missions

During the field experiment FRAMZY'99, five missions were flown with the Falcon-20. All missions took place west/northwest of Spitsbergen in the Fram Strait (Figure 3.1). The first three ones took place under a northeastern, nearly ice-parallel air flow while the last two ones were flown under cyclonic conditions. The last mission took place right through the center of the cyclone. A brief summary of the aircraft missions is listed in Table 3.2.

Table 3.2: Summary of the flight missions during the FRAMZY'99 experiment: date, start, and landing time, flight-number, total number of vertical profiles (P) and horizontal flight legs (H) and a brief description of the mission.

Date	Time (UT)	Flight-No. Pattern	Objectives and Comments
10041999	13:02:34 -15:49:20	3195 8P 10H	(1) Atmospheric boundary layer structure, (2) atmospheric forcing of the ice drift in the buoy area and (3) baroclinicity at the ice edge under N/NE ice-edge parallel air flow conditions. Cloudfree conditions, but blowing snow or haze of ice crystals inside the boundary layer in the experimental area.
12041999	10:04:11 -13:08:12	3196 11P 12H	(1) Atmospheric boundary layer structure, (2) atmospheric forcing of the ice drift in the buoy area and (3) baroclinicity at the ice edge under N/NE ice-edge parallel air flow conditions. Cloudfree conditions, but blowing snow or haze of ice crystals inside the boundary layer in the experimental area. (Similar mission and conditions as in case of Flight-No. 3195.)
14041999	12:09:02 -14:09:12	3197 11P 6H	(1) Atmospheric boundary layer structure, (2) atmospheric forcing of the ice drift in the buoy area, (3) baroclinicity at the ice edge and (4) convergence near the ice edge inside a weak northerly flow. Cloudfree conditions above ice, but a pronounced cloud band parallel to the ice edge.
18041999	10:04:45 -12:47:20	3198 12P 10H	(1) Atmospheric boundary layer structure and (2) atmospheric forcing of the ice drift in the buoy area and (3) baroclinicity at the ice edge inside a northward moving Fram Strait cyclone.
19041999	09:51:05 -12:11:41	3199 8P 5h	(1) Atmospheric boundary layer structure and (2) atmospheric forcing of the ice drift somewhat north of the buoy area inside a Fram Strait cyclone with a W-E traverse through the center of the cyclone.

Details of the five missions as altitudes (for horizontal flight legs) and height intervals (for vertical soundings), locations, times, and headings for the horizontal flight legs (called runs) are summarized in flight reports as follows. Visual observations made by the aircraft scientist (cloud situation, sea-ice situation, etc.) needed for the interpretation of the data are also listed.

Flight reports

Flight reports of research aircraft Falcon missions during FRAMZY'99. (P indicates vertical profile, H horizontal run, CB cloud base and CT cloud top. Capital letters (A, B, C...) indicate corner points in flight patterns.

FRAMZY'99 No. 1, **Date:** 10.04.99, **FALCON-flight No.:** 3195, **T/O:** 13:02:34 UT, **T/D:** 15:49:20 UT

Mission: (1) Atmospheric boundary layer structure above ice and open water, (2) atmospheric forcing of the ice drift in the buoy area and (3) baroclinicity at the ice edge under N/NE ice-edge parallel air flow conditions.

Synoptic situation: Low (980 hPa) SE of Spitsbergen above the Barents Sea and high pressure above the pole and Greenland cause an N/NE flow in the experimental area.

Coordinates of flight patterns: **A**: 80° 25' N 0° 30' E, **B**: 80° 40' N 0° 15' W, **C**: 80° 03' N 3° 55' W, **D**: 80° 10' N 5° 15' W

Time (UT)	Patterns and Heights	Hdg.	Remarks (Weather etc.)
0,54344907407	Start at Longyearbyen		
13:02:04-13:33:09	Transit		
13:33:09-13:39:06	P1 3023-102 m to A		4/8 - 6/8 Cu partially in streets above water. Ice border 80° 15' N 2° 30' E. Above ice 2/8 - 3/8 Cu/St with CT 1200', CB 700'.
13:40:30-13:42:18	H1 26-92 m to A	320°	Cloudless. Ice 98% - 100%.
13:42:18-13:48:15	H2 15-22 m A-B	330°	Cloudless. Ice 100%. Some hummocks are very large.
13:48:15-13:50:24	P2a 17-1561 m at B		Cloudless. Ice 100%. Turbulence below 600'.
13:50:24-13:53:03	P2b 1561-72 m at B		
13:53:03-13:57:45	H3 85m B-A	145°	More turbulence than during H2. Very hazy southward.
14:01:23-14:06:49	H4 165 m A-B	335°	Turbulence decreases from 14:03:23 to 14:04:04. Ice 96% with cracks.
14:08:16-14:14:19	H5 13-42 m B-D 1st half	230°	Cloudless, but at 14:11:30 snow crystals. Very hazy. 14:12:10 open water pond. 14:13:23 very large hummock.
14:14:19-14:16:43	P3 15-1508 m B-D		Sea foam from open ponds. Turbulence and hazy layer end at 1200'. 80° 21' N 2° 42' E relatively large crack.
14:16:43-14:19:20	P4 1508-23 m B-D		14:17:18 above large crack at 80° 18' N 3° 15' E. Hazy below 3000'.
14:19:20-14:24:16	H6 15-47 m B-D 2nd half	250°	100% smooth white ice. Strong turbulence. Blowing snow.
14:24:16-14:27:07	P5a 45-1530 m at D		Blowing snow/ice crystals up to 1000'. Ice almost 100% with small cracks. Upper boundary of inversion at 1400'. Hazy below 3000'.
14:27:07-14:30:23	P5b 1530-242 m at D		
14:30:23-14:37:30	H7 230-245 m D-C	100°	Initially weak turbulence. Turbulence ends after 14:33:20 with short interruptions (intermittent turbulence). Very hazy. Ice 100%
14:39:29-14:45:08	H8 123-130 m C-D	295°	Inside layer of haze clouds. Haze clouds (2/8) are organized in lenticularis bands parallel to the wind direction (observed during sinking H7 - H8).
14:48:12-14:52:50	H9 9-25 m D-C	100°	Strong turbulence. Very hazy. Better visibility SE-ward. Large ridges at 14:49:20. Blowing snow.
14:52:50-15:06:14	H10 7-54 m C-open water	100°	Very hazy. Increasing visibility after 14:55:40. Below 1/8 - 3/8 St from 14:58:40 on. Above ice, but large open water ponds at 15:01:00, 15:02:15 - 15:02:19, 15:02:35 - 15:02:48. Compact ice changes to small ice floes towards ice edge. Ice border 79° 50.3' N 0° 26' W. Clouds above open water.
15:06:14-15:14:07	P6 32-7599 m open water-LYB		Clouds with CB 1000', CT 3100' - 3500'. Second, very thin cloud layer with CT 5500'. Snow falls out of the clouds.
15:14:07-15:49:20	Transit		
0,65905092593	Landing at Longyearbyen		

Commentary: In the experimental area, the N/NE flow was oriented almost parallel to the ice border. The near-surface wind velocity ranged from 10 m/s to 15 m/s. Above open water, the boundary layer depth was about 1.5 km. Above the ice, the boundary layer depth ranged from 200 m to 400 m and the temperature inversion at the top of the boundary layer was between 2°C to 3°C. The horizontal flight legs flown near the top of the boundary layer indicate that Kelvin-Helmholtz waves were present. Blowing snow showed up at the snow-covered sea ice. No clouds showed up above ice in the experimental area, but the boundary layer was filled with haze of ice crystals. It was not clear whether these ice crystals originated from blowing snow elevated to higher levels or from condensation/sublimation inside the boundary layer.

Ice conditions showed large variations: Snow-covered old ice, leads covered with thin new ice without snow, leads with open water.
The flight pattern includes two stacks composed of three horizontal cross-wind flight legs at different heights: stack I: H2, H3, H4 and stack II: H7, H8, H9.

FRAMZY'99 No. 2,	**Date:** 12.04.99, **FALCON-flight No.:** 3196, **T/O:** 10:04:11 UT, **T/D:** 13:08:12 UT
Mission:	(1) Atmospheric boundary layer structure above ice and open water, (2) atmospheric forcing of the ice drift in the buoy area and (3) baroclinicity at the ice edge under NE ice-edge parallel air flow conditions.
Synoptic situation:	NE flow in the experimental area between a high pressure area above the pole region and Greenland (1035 hPa) and a low S of Barents Sea and Kara Sea.
Coordinates of flight patterns:	**A**: 79° 50' N 2° 30' E, **B**: 80° 15' N 1° 00' W, **C**: 80° 30' N 2° 00' W, **D**: 79° 52' N 3° 30' W, **E**: 79° 20' N 4° 30' W, **F**: 79° 30' N 6° 30' W, **G**: 79° 15' N 0° 00' E

Time (UT)	Patterns and Heights	Hdg.	Remarks (Weather etc.)
0,41957175926	Start at Longyearbyen		
10:04:11-10:28:06	Transit		
10:28:06-10:38:24	P1 7660-152 m to A		Through 4/8-6/8 Cu, CT: 4600' (max.), 4200' (most), CB: 2000' - 2400', snow shower.
10:38:24-10:48:20	H1 19-152 m A-B	300°	From water to ice. Ice border at 79° 59' N 01° 23' E. 10:39:50-10:41:15 band of convection with heavy snowfall (8/8). After 10:42:30 cloud depths and heights decrease (2/8 - 5/8 Cu streets/frazzles).
10:48:20-10:50:49	P2 26-1541 m A-B at B		Cloudless. Turbulence ends above 500' to 800'. Ice: A lot of ponds and cracks, partially with open water and partially freshly frozen.
10:50:49-10:53:26	P3 1541-37 m at B		- " -
10:53:26-10:57:38	H2 12-37 m B-C	330°	A lot of freshly frozen ice. 10:55:26 extremely high ridges.
10:57:38-11:00:43	P4a 19-2120 m at C		Cloudless. Inversion height 130 m. ΔT = 3 K.
11:00:43-11:03:19	P4b 2120-176 m at C		
11:04:15-11:1:01	H3 140-174 m C-B	150°	Cloudless. Weak turbulence.
11:13:03-11:17:42	H4 72-86 m B-C	330°	Cloudless. Moderate turbulence. Ice almost 100%.
11:19:09-11:23:08	H5 220-230 m C-B	125°	Cloudless. Inside inversion. No turbulence.
11 24 49-11:31:16	H6 16-21 m B-D	225°	Almost parallel to isobars. Hazy. Blowing snow. FF 20-25 kts, DD 40°. Locally thick haze/fog (clouds or raised crystals of blowing show?).
11:31:16-11:33:32	P5 28-1516 m B-D at D		Turbulence below 800'. Thin layer of haze. Inversion: 150 m - 170 m, ΔT = 4 K. Broken ice with cracks and ponds mostly covered by new ice.
11:33:32-11:35:53	P6 1516-16 m D-E at D		Cloudless. Turbulence below 500'/600'. Inversion: 150 m - 170 m, ΔT = 4 K. Broken ice with cracks and ponds mostly covered by new ice.
11:35:53-11:42:32	H7 15-20 m D-E	200°	Parallel to the wind or stripes of blowing snow, respectively. Blowing snow is swirled up by hummocks.
11:43:30-11:47:50	H8 13-21 m E-F	290°	Cloudless. Ice 100% and very rough. Strong turbulence. Very hazy. Inside blowing snow. Horizon not discernible.
11:47:50-11:50:59	P7a 16-2170 m E-F at F		Cloudless, but hazy up to 3000'/3500'.
11:53:42-12:01:23	H9 241-269 m F-E	100°	Cloudless. Inside inversion. Inside hazy layer. High clouds visible in SE direction.
12:02:27-12:07:46	H10 141-178 m E-F	290°	First near, later inside turbulent layer.
12:08:53-12:13:16	H11 71-83 m F-E	105°	Ice 100%. Inside hazy layer.
12:13:49-12:16:07	P8 15-1511 m E-G at E		Cloudless, but clouds in E/SE direction. Turbulence below 800'.
12:16:07-12:18:30	P9 1511-14 m E-G at E		Two cloud layers visible ahead of the aircraft: About 1/8 at about 800', Cu/St with CB at 4000' and CT at 5000'.
12:18:30-12:30:50	H12 14-130 m E-G	90°	50' above ice, 300' above open water. Strong turbulence at 50' above ice. 12:22:00 compact cloud wall ahead. 12:23:00 inside clouds/fog reaching down to the surface. 12:23:45 increasing visibility. Ice border at 79° 15' N 1° 37' W. Strong convergence with cloud wall at ice border. Wind above ice: 8° m/s. Wind above water: 14 m/s 40°. 5/8 - 7/8 Cu/St with snow showers above open water. 12:27:50 - 12:30:00 inside snow shower.
12:30:50-12:34:14	P10 131-3110 m G-LYB at G		Clouds: 8/8, CB not discernible due to snowfall. CT 4800' (max. 5400'). Profile traverses area with highest clouds if compared with the surrounding.
12:34:14-13:08:12	Transit		
0,54736111111	Landing at Longyearbyen		

Commentary: In the experimental area, the NE flow was oriented almost parallel to the ice border. Above open water, the well-mixed boundary layer revealed a depth of about 1 km at A and 1.5 km at G, a weak inversion of about 1 to 2 K, and an air-sea temperature difference of -6 K to -8 K. Clouds extended from the top of the boundary layer almost down to the surface. The wind velocity was about 12 m/s to 14 m/s and wind direction was from 50° to 60°. Above the ice, the boundary layer depth ranged from 200 m to 300 m, and the temperature inversion at the top of the

boundary layer was about 3 K to 4 K, while the air-ice temperature difference indicated slightly stable stratification (1 K). FF ranged from 12 m/s to 13 m/s and DD from 10° to 30°. As in case of the first mission, no clouds showed up above ice in the experimental area, but the boundary layer was again filled with haze of ice crystals. A line of strong convergence/convection oriented parallel to the ice border was located somewhat seaward of the ice border. The flight pattern includes two stacks composed of four horizontal cross-wind flight legs at different heights. Two staples have been flown. Staple I: H2, H3, H4, H5, staple II: H8, H9, H10, H11.

FRAMZY'99 No. 3, **Date:** 14.04.99, **FALCON-flight No.:** 3197, **T/O:** 12:09:02 UT, **T/D:** 14:09:12 UT

Mission: (1) Atmospheric boundary layer structure above ice and open water, (2) atmospheric forcing of the ice drift in the buoy area, (3) baroclinicity at the ice edge and (4) convergence near the ice edge in a weak northerly flow.

Synoptic situation: High pressure area (1030 hPa) above the experimental area. Pressure gradients are very weak in the experimental area.

Coordinates of flight patterns: **A**: 79° 40' N 1° 00' E, **B**: 80° 00' N 4° 00' W, **C**: 79° 10' N 6° 00' W, **D**: 78° 50' N 1° 30' W

Time (UT)	Patterns and Heights	Hdg.	Remarks (Weather etc.)
0,50627314815	Start at Longyearbyen		
12:09:02-12:32:09	Transit		
12:32:09-12:41:49	P1 5600-30 m to A		Below 13000' in haze layer. Above 4/8 - 6/8 Sc/Cu organized in bands/streets. The bands/streets are formed by open/closed cells. NW-wards more closed cells. Through 6/8 Sc with CT 3000' - 3100', CB 2100'. No white crests on sea surface.
12:41:49-12:49:55	H1 10-30 m A-B 1st half	290°	8/8 St. Snow shower. Ice border 79° 45' N 0° 23' W. First open ice, then small ice floes with increasing diameter. 6/8 Sc until 12:47:50. Thick ice starts at 12:49:40.
12:49:55-12:52:02	P2 21-1520 m A-B mid		2/8 - 3/8 Sc with CB 2600', CT 3000'.
12:52:02-12:54:28	P3 1520-21 m A-B mid		Cloudless.
12:54:28-12:56:43	H2 13-23 m A-B 2nd half	290°	Ice 100%. Compact ice with numerous ridges. Sunny. No turbulence.
12:56:43-12:58:50	P4 15-1530 m at B		Thin cloud or fog bands (2/8) at about 50'. Orientation of the bands 225°.
12:58:50-13:01:14	P5 1530-29 m at B		Thin cloud or fog bands (2/8) at about 50'. Orientation of the bands 225°.
13:01:14-13:02:27	H3 15-37 m B-C	205°	Sea smoke above open water ponds.
13:02:27-13:06:33	P6 22-2987 m B-C mid		Clouds developed from open water sea smoke southwest (in wind direction) of the open water.
13:06:33-13:10:54	P7 2987-18 m B-C mid		Large Sc field, CB 3000' - 3200', CT 3600' left of aircraft.
13:10:54-13:13:26	H4 11-23 m B-C 2nd half	195°	100% ice alternating thick and thin. No turbulence.
13:13:26-13:15:37	P8 24-1510 m at C		Cloud field (8/8 Sc, CB 3000', CT 4000') southeast of aircraft.
13:15:37-13:17:51	P9 1510-37 m at C		CB 3100', CT 3700'.
13:17:51-13:22:06	H5 12-37 m C-D 1st half	107°	100% thick ice. 13:18:30 - 13:18:37 strong turbulence above open water pond. Cloud wall or fog towards east. Hazy. Moderate turbulence after 13:20:00.
13:22:06-13:24:22	P10 20-1501 m C-D mid		Turbulence around 2400'. Sc, CB 3200', CT 4800'.
13:24:22-13:26:54	P11 1501-10 m C-D mid		CT 4300', CB 2500' (diffuse). Compact ice changes to open ice. Snow shower above ice. Profile ends above ice shortly ahead of the ice edge.
13:26:54-13:31:29	H6 7-20 m C-D 2nd half	110°	Ice border 78° 55' N 2° 43' W. Snow shower visible above open water. 13:28:50 inside snow shower. 13:29:50 cloud cover ends. Good visibility.
13:31:29-13:36:59	P12 14-5605m D-LYB		Turbulence below clouds in the middle of the boundary layer. 3/8 - 4/8 Sc, CB 2800', CT 3600'.
13:36:59-14:09:12	Transit		
0,58972222222	Landing at Longyearbyen		

Commentary: In the experimental area, the synoptic-scale pressure gradient was weak resulting in very small wind speed. At the ice border, a marked convergence line with a cloud layer from 2500' to 4300' and northwesterly wind above ice, but northeasterly wind above open water was present.
Almost no turbulence has been found above ice as well as above open water. Above ice, a very thin inversion overlaid the ice. Very flat (CT 50') stripes of fog (like waves) were located near point B. The flight pattern consists of low-level runs and profiles. Staples have not been flown.

FRAMZY'99 No. 4, **Date:** 18.04.99, **FALCON-flight No.:** 3198, **T/O:** 10:04:45 UT, **T/D:** 12:47:20 UT

Mission: (1) Atmospheric boundary layer structure above ice and open water, (2) atmospheric forcing of the ice drift in the buoy area and (3) baroclinicity at the ice edge inside the NW sector of a northward moving Fram Strait cyclone.

Synoptic situation: Strong NE flow in the experimental area inside the NW sector of a northward moving Fram Strait cyclone (1000 hPa).

Coordinates of flight patterns **A**: 79° 35' N 0° 30' E, **B**: 79° 45' N 6° 00' W, **C**: 78° 35' N 8°30' W, **D**: 78° 40' N 3° 45' W

Time (UT)	Patterns and Heights	Hdg.	Remarks (Weather etc.)
0.41996527778	Start at Longyearbyen		
10:04:45-10:26:41	Transit		Permanently inside clouds.
10:26:41-10:36:03	P1 6670-194 to A		Profile starts in Cirrus layer. Sun shines through clouds until 8000'. Turbulence below 4700'. Sea surface (with white crest waves) becomes visible below 600'. Fog between surface and 600'.
10:36:03-10:44:33	H1 23-194 m A-B	290°	Ice border at 10:39:15 (79° 34.3' N 0° 42' W).
10:44:33-10:47:01	P2 23-1605 m A-B 1st half		Relatively small ice floes. Bad visibility. CB 1700'.
10:47:01-10:49:40	P3 1605-110 m A-B 1st half		At 3000' no downward visibility. Cloudfree layer from 2900' to 1900'. 8/8 St, CT 1900', CB reaching down to the surface. 10:48:59 large open water pond.
10:49:40-10:54:56	H2 90-110 m A-B 2nd half	289°	Permanently inside 8/8 St. Strong turbulence. Large open water pond. Blowing snow.
10:56:29-11:00:40	H3 173-182 m B-A at B	100°	Permanently inside 8/8 St. Strong turbulence.
11:02:18-11:06:23	H4 240-276 m A-B at B	285°	Permanently inside 8/8 St, but the surface is visible. Turbulence. Blowing snow. Sea smoke from open water ponds. Mostly above 100% ice.
11:06:31-11:08:28	P4 276-1500 m B-C at B		Permanently inside 8/8 St. Turbulence ends above 1500'.
11:08:28-11:12:06	P5 1500-61 m B-C at B		Permanently inside 8/8 St. Turbulence starts below 1300' - 1100'.
11:12:06-11:18:05	H5 61-90 m B-C mid	204°	Permanently inside fog. No contrasts. 100% ice. 11:14:40 - 11:15:20 above open water pond causing strong turbulence. Stripes of ice. Then again 100% ice, but turbulence continues.
11:18:05-11:21:35	P6 85-2442 m B-C 2nd half		Permanently inside 8/8 St. Turbulence ends above 1200'. Cloud layers not discernable.
11:21:35-11:25:50	P7 2442-118 m B-C at C		Turbulence starts below 900'.
11:25:50-11:29:59	H6 104-118 m C-D at C	70°	Permanently inside clouds, but surface is visible. 100% ice.
11:31:58-11:35:44	H7 238-249 m D-C at C	200°	Permanently inside clouds. Surface not visible. Reduced turbulence.
11 36 41-11:40:26	H8 349-360 m C-D at C	60°	No visibility. Turbulence is still active.
11:40:26-11:42:26	P8 355-1499 m C-D 1st half		Turbulence ends above 1500'. Sun becomes visible at 5000'.
11:42:26-11:45:04	P9 1499-67 m C-D 1st half		Sun remains visible down to 2500'. Turbulence below 1200'. Profile ends inside fog.
11:45:04-11:55:04	H9 53-67 m C-D to D	95°	Mostly 100% ice. Bad visibility, except above open water ponds. The belt of broken ice near ice border is broader and consists of smaller ice floes than during the adjacent missions. Ice border at 11:52:48 (78° 40' N 4° 27' W). Open water with sporadic drifting ice floes. Sea crests in stripes. 11:53:40 small field of drifting ice. Clouds reach down to the surface. Visibility about 1000 m - 1500 m.
11:55:04-12:00:50	P10 59-4820 m D-LYB		CB down to the surface. Turbulence ends above 1600'. Clouds end above 7000'.
12:11:13-12:20:22	P11 4810-34 m D-LYB		Transparent Cirrus, CT 13000', CB 10000'. Good visibility at 7000'. Thin cloud frazzles at about 6000'. 8/8 Sc, CB 4600' (max.) 4100' (most), CB 3400'. Second cloud layer with CT 2700' - 2200'. Snow shower reaching down to the surface.
12:20:22-12:21:59	H10 30-35 m D-LYB	95°	Run ends inside snow shower band.
12:21:59-12:27:32	P12 34-4825 m D-LYB		Profile traverses snow shower band. 8/8 St, CB down to the surface, CT 4500' (4800' max.) Impression from above: 8/8 Sc. Good visibility S- and SW-wards.
12:27:32-12:47:20	Transit		
0.53287037037	Landing at Longyearbyen		

Commentary: The experimental area was located inside the NW sector of a northward moving Fram Strait cyclone. Strong N - NE winds (FF 20 m/s to 25 m/s, DD 5° to 20°) have been observed above ice. As a result of the strong wind, the ice was considerably broken up. Thin St or fog was present in the entire experimental area. Due to bad visibility, the lowest flight levels were confined to 50 m to 100 m. Above ice, turbulence ends above about 450 m, while the strong temperature inversion starts already above 350 m. Below 350 m, a well mixed, neutrally stratified mixed layer was present. The wind profiles showed a pronounced inflection point.

P11, H10 and P12 took place above open water in the middle of the West-Spitsbergen current. These three flight sections were located E of the through axis inside the warm sector of the cyclone and inside moderate SE flow (FF 9 m/s, DD 145°).

The flight pattern includes two stacks composed of three horizontal cross-wind flight legs at different heights. Two staples have been flown. Staple I: H2, H3, H4, staple II: H6, H7, H8.

FRAMZY'99 No. 5, **Date:** 19.04.99, **FALCON-flight No.:** 3199, **T/O:** 09:51:05 UT, **T/D:** 12:11:41 UT

Mission: (1) Atmospheric boundary layer structure and (2) atmospheric forcing of the ice drift somewhat north of the ice-buoy area inside a Fram Strait cyclone with a W-E traverse through the center of the cyclone.

Synoptic situation: Small Fram Strait cyclone (1004 hPa) at about (80° 20' N 2° 40' E).

Coordinates of flight patterns: **A**: 81° 00' N 10° 00' E, **B**: 81° 05' N 3° 00' W, **C**: 80° 20' N 2°00' W, **D**: 80° 20' N 9° 30' E

Time (UT)	Patterns and Heights	Hdg.	Remarks (Weather etc.)
0,41047453704	Start at Longyearbyen		
09:51:05-10:08:19	Transit		
10:08:19-10:21:06	P1 7560-124 m to A		8/8 Sc between northern coast of Spitsbergen and ice border. Northwards As layer (CT 14000', CB 10500') above the Sc layer. Snow falls out of the As layer. 8/8 Ac/Sc, CT 8500', CB 7200'. Second cloud layer, CT 5000', CB down to the surface. Profile ends above water with open ice.
10:20:50-10:55:23	H1 52-105 m A-B	265°	Run starts above open water. Ice border 10:22:08, 81° 01' N 9° 21' E. Thereafter 100% ice. Completely inside 8/8 St. Casually open water ponds. Weak waves at open water. Relatively weak turbulence. Many new breakages with open water. Very hazy. 10:40:15 increasing visibility and cloud wall ahead. 10:45:05 snow shower above open water pond. 10:50:30 very good visibility. 10:52:30 - 10:53:00 open water with ice mush. 10:53:00 thin new ice and increasing turbulence. 10:53:55 decreasing visibility, but occasionally sunny spots.
10:55:56-11:00:09	P2 68-3010 m B-C at B		Turbulence up to 1000'. Several cloud layers.
11:00:09-11:04:50	P3 3010-56m B-C mid		CB 1300'.
11:05:19-11:08:29	H2 53-60 m B-C to C	170°	Run ends above open water pond.
11:09:41-11:13:08	H3 47-57 m C-D at C	87°	
11:13:22-11:15:40	P4 12-1525 m C-D 1st half		Turbulence ends above 800'. Thin St layer at 1000'. At 2600' above large St layer.
11:15:40-11:18:15	P5 1525-64m C-D 1st half		Good visibility above 8/8 St, CT 3400' (sharply marked), CB 300'. Profile ends at ice border (very disrupted) at 80° 22' N 1° 26' E.
11:18:15-11:25:10	H4 55-64 m C-D mid	90°	Above open water. 11:22:15 - 11:24:00 inside shower band. Shower band marks probably the axis of the cyclone at 80° 23' N 2° 43' E. Until 12:24:35 more showers in the environments. 12:24:35 good visibility.
11:25:29-11:29:44	P6 15-3072 m C-D mid		Good visibility. 6/8 Sc, CB 800' - 900', CT 1600'. Second cloud layer 4/8 Sc, CB 5500', CT 6000' (6600' max.). Cloudfree above 6600'.
11:29:44-11:35:04	P7 3072-15 m C-D 2nd half		8/8 Sc, CT (3200' max.) 2600', CB 500' - 600'.
11:35:04-11:38:50	H5 13-19 m at D	95°	From 10:36:00 on continuously inside snow shower until the end of run.
11:38:50-11:56:50	P8 19-7540 m C-D		CT 1600'. Various cloud layers above: 4600' - 4900', at 6000'. CT of highest clouds 7400'. Northwards even higher cloud layers.
11:56:50-12:11:41	Transit		
0,50811342593	Landing at Longyearbyen		

Commentary: The experimental area was located north of the center (1004 hPa) of a small Fram Strait cyclone. The southern W-E traverse (line C-D) led almost directly through the center of the cyclone. The very long E-W low level run (H1) was located north of the center of the low. The temperature transition between the warm and cold sector was not sharply marked, since the temperature changed continuously from -1 K to -14 K (from east to west) inside the boundary layer above ice, while the wind direction veered from SE to N during H1. FF was about 8 m/s inside the warm sector and about 12 m/s inside the cold sector. Above the ice, the well-mixed boundary layer reached up to about 300 m.

The cyclone center was crossed during H4 at 80° 23' N 1° 30' E. At this point, FF is almost zero and DD jumps sharply from SE to NE.

Due to bad visibility, the lowest flight levels were confined 50 m to 100 m. The flight pattern consists of vertical soundings and low-level runs, but no stacks have been flown.

3.4 Examples of measurements

3.4.1 Baroclinicity near ice edge, inflection point in wind profile and waves in the stably stratified atmosphere on 10 April 1999

The flight pattern of the Falcon-20 and the location of ice border on 10 April 1999 are shown in Figure 3.3, where the numbering of the flight legs corresponds with that in the previously shown flight reports. Horizontal runs H2, H3, H4 form stack I (stack: several horizontal cross-wind flight legs located one upon the other) and H7, H8, H9 form stack II. Except P1 (first half), P6, and the last part of H10, the measurements have been performed above ice.

Figure 3.4 shows low-level wind information encountered during horizontal low-level runs. The wind information is averaged over 10 seconds (corresponding to a flight distance of about 1 km) and plotted every 50 seconds (every 5 km, respectively). It is seen that the experimental area was situated inside a N/NE flow with wind velocities from about 10 m/s to 15 m/s.

Vertical soundings are shown in Figure 3.5. Profiles P1, P2, and P5 were located above ice. Here, above ice, the boundary-layer temperature decreases with increasing distance from the ice border from - 11°C (P1 which ends above ice) to -18°C (P5) and the depth of the boundary layer z_i decreases with increasing distance from the ice border from 350 m (P1) to 130 m (P5). There is a strong baroclinicity across the ice edge. The is obvious when comparing the above-ice temperature profiles with the above-water temperature profile (P6) which indicates a boundary-layer temperature of about -5°C. Above open water, a convective, well-mixed boundary layer heated from below is present and z_i reaches 1.5 km.
The mixing ratio inside the boundary layer shows a decrease from E (P6, open water) to W (P5, ice) similar to that in the temperature.
The above-ice profiles of wind velocity FF show a strong wind shear below z_i and maximum velocities near the capping inversion, while wind direction DD shows pronounced veering within the capping inversion and an inflection point in the upper part of the capping inversion.

The characteristics of the wind profiles above ice in connection with stable stratification are favourable conditions for the formation of dynamically driven roll-like convection patterns or internal waves as Kelvin Helmholtz waves. The presence of wave-like structures in the flow is clearly indicated by the time series of the uppermost horizontal run H7 in stack II (Figure 3.7). H7 was located at z = 240 m slightly above z_i inside strongly stable stratification (compare P5 which was located near the start point of H7). H7 shows pronounced undulations in air temperature, mixing ratio, vertical velocity, wind velocity and direction. The horizontal scale of these undulations is about 1.3 km. (The time scale in the abscissa can be converted to a length scale applying the mean Falcon flight speed of approximately 100 m/s.) Except sea smoke arising from open water ponds, no clouds showed up above ice. Hence, the waves were not reflected in cloud patterns.

Figure 3.6 shows H2, the lowest cross-wind run in stack I above ice. The surface temperature measured by the downward facing KT19 (grey curve) gives useful information about the ice coverage because open-water spots are clearly reflected in the time series of surface temperature. The ice coverage is also reflected in the albedo time series, but when interpreting the albedo time

series it has to be taken into account that the albedo is calculated from the measurements of downward and upward facing pyranometers looking into a spheric halfspace and that dark ice (not covered by snow) is connected with an albedo similar to that of open water.

Figure 3.8 shows the time series of the low-level runs H9 and H10 (H10 followed immediately after H9) starting at point D and ending near the ice edge above open water. The baroclinicity across the ice edge is clearly illustrated when regarding the time series of the static temperature. The static temperature (black curve) increases continuously between D and the open water, whereas the surface pressure decreases. The increase of static temperature is accompanied by an increase of mixing ratio. The increasingly broken structure of the ice towards the ice edge is reflected by peaks in the surface temperature. The ice edge which was crossed after 1010 s can be identified very well by the abrupt change in surface temperature.

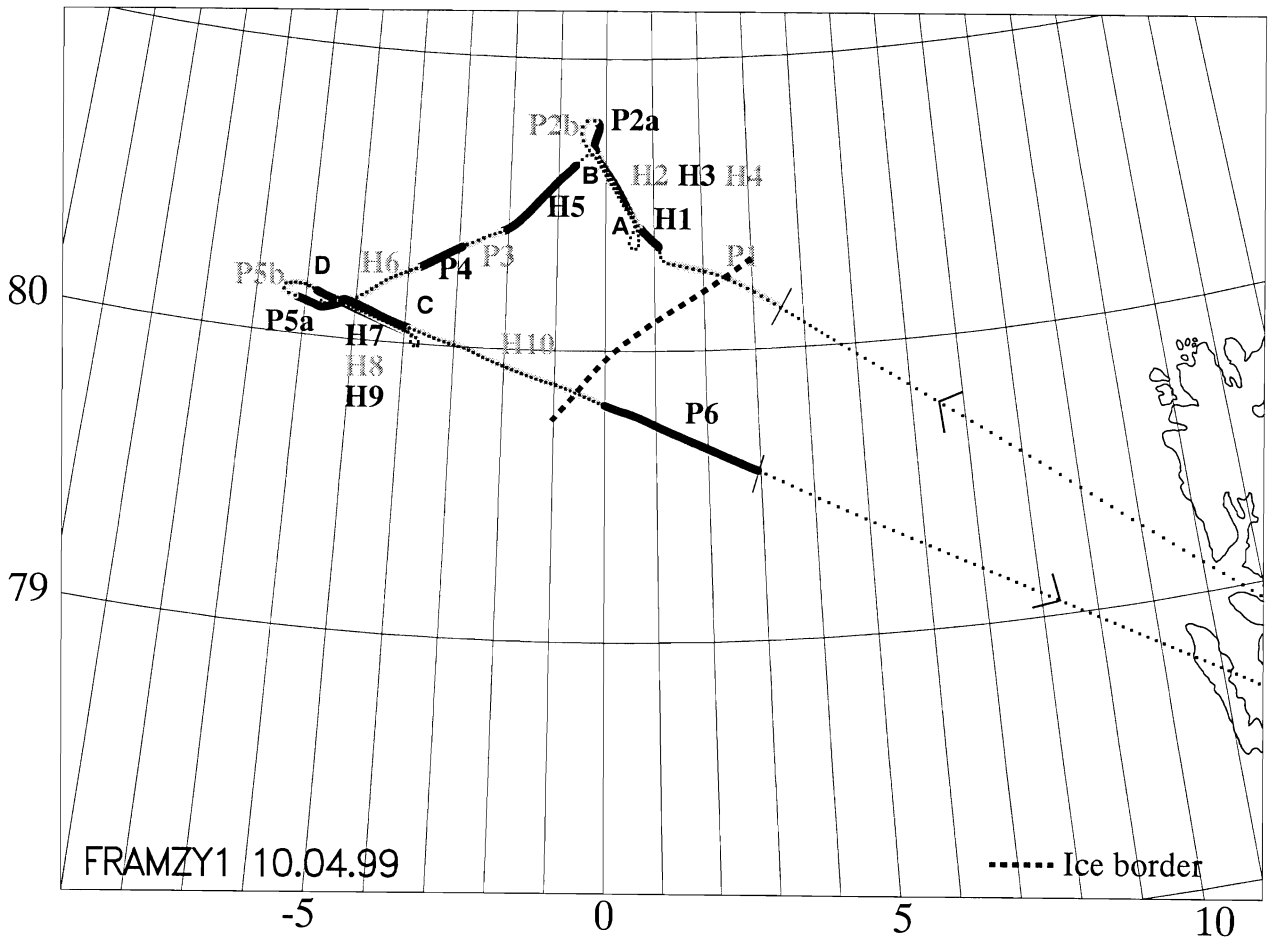

Figure 3.3: *Flight pattern of the Falcon-20 and location of ice border on 10 April 1999. The numbering of the flight legs (P: vertical soundings, H horizontal runs) correspond with that in the previously shown flight reports. A, B, C, D... indicate corner points of the flight pattern.*

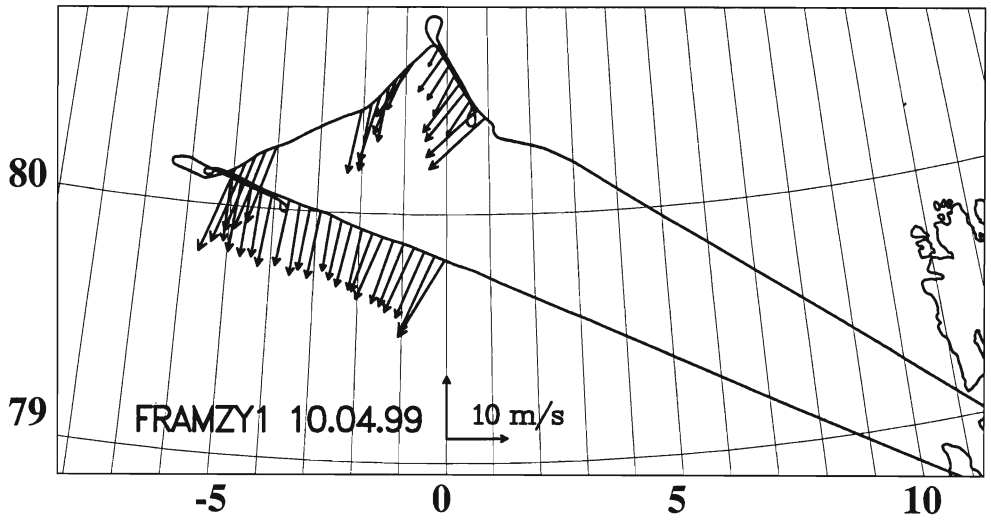

Figure 3.4: *Flight pattern and horizontal wind speed and direction (arrows) encountered during low-level horizontal runs by the Falcon-20 on 10 April 1999. The wind information is averaged over 10 seconds (corresponding to a flight distance of about 1 km) and plotted every 50 seconds (every 5 km, respectively).*

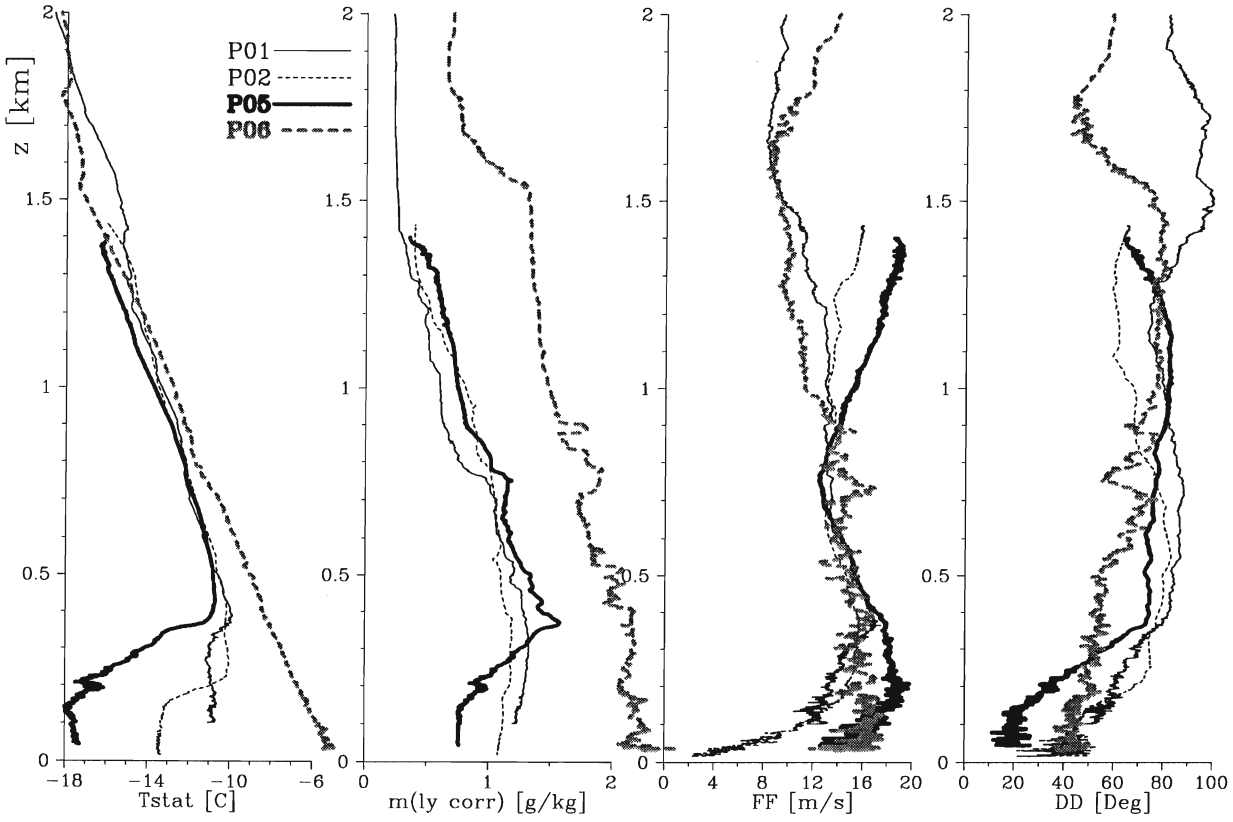

Figure 3.5: *Vertical profiles (plot rate 10 Hz, no averaging) of static temperature T_{stat}, water vapour mixing ratio m_{ly_corr} (Lyman-a-sensor, corrected by adding a height-independent offset given by the difference between the lowest 10 s averages of mly and water vapour mixing ratio measured by Vaisala Humicap), horizontal wind speed FF and horizontal wind direction DD encountered by the Falcon-20 at different locations on 10 April 1999.*

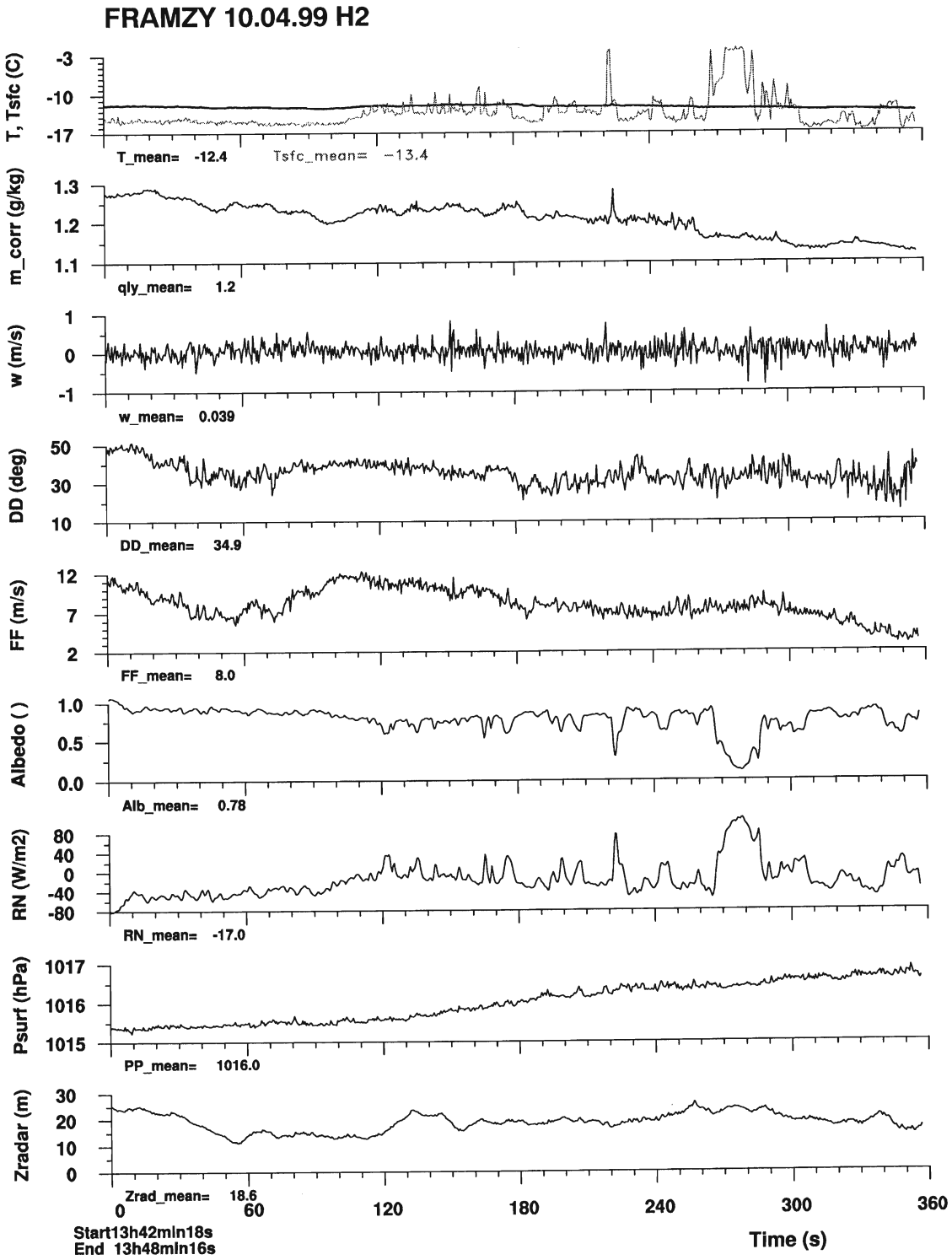

Figure 3.6: *Surface temperature T_{sfc} (grey), static temperature T (black), water vapour mixing ratio m_{ly_corr} (Lyman-a-sensor, corrected by a constant offset given by the difference between averages of m_{ly} and of water vapour mixing ratio measured by Vaisala Humicap), vertical velocity w, wind direction DD, wind speed FF, albedo, net radiation flux R, surface pressure P_{surf}, and height z_{radar} (measured by radar) encountered by the Falcon-20 during horizontal flight leg H2 on 10 April 1999 (plot rate 2 Hz, averaged over 0.5 s). The time scale in the abscissa can be converted to a length scale applying the mean Falcon flight speed of approximately 100 m/s.*

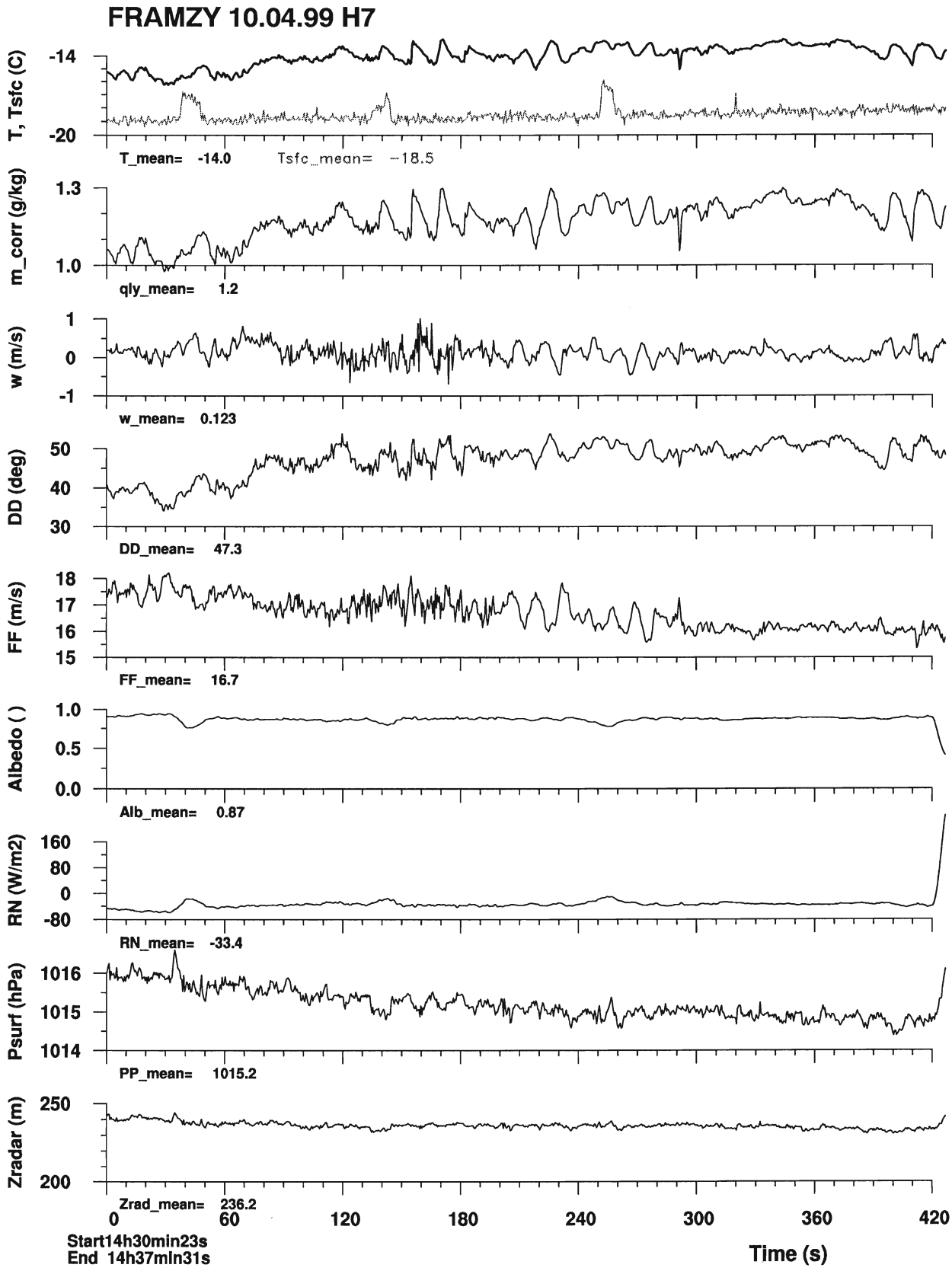

Figure 3.7: *As Figure 3.6, but for horizontal flight leg H7 on 10 April 1999.*

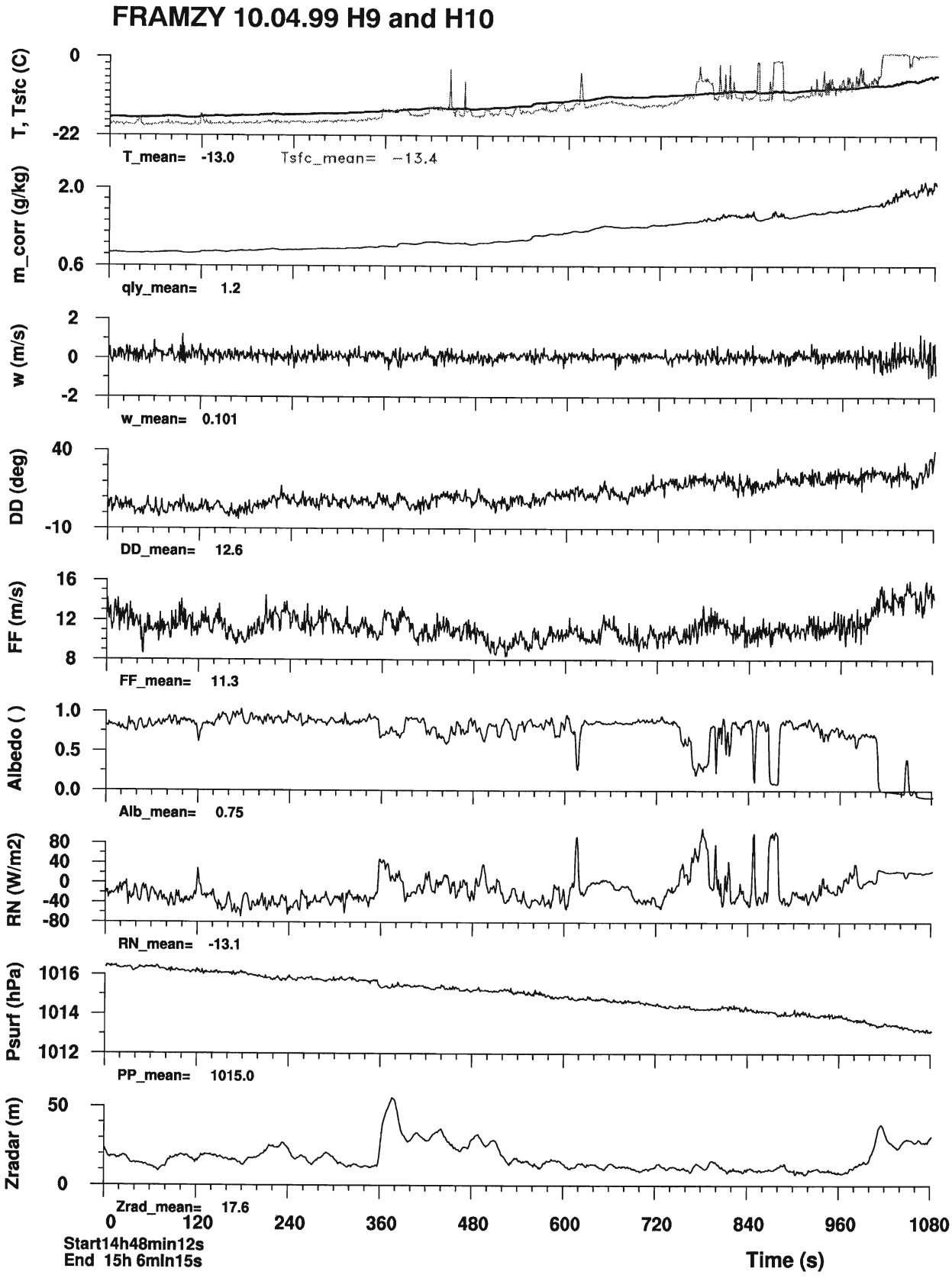

Figure 3.8: *As Figure 3.6, but for horizontal flight legs H9 and H10 on 10 April 1999.*

3.4.2 Baroclinicity and convergence near ice edge on 12 April 1999

Figure 3.9 shows the flight pattern and the location of ice border on 12 April 1999. Again two stacks have been flown. H2, H3, H4, H5 form stack I and H8, H9, H10, H11 form stack II. Except P1 and P10 and parts of H1 and H12 (low-level runs crossing the ice edge), the flight pattern was located above ice.

From the low-level wind information encountered during horizontal low-level runs and shown in Figure 3.10 it is seen that the experimental area was situated inside a NE flow almost parallel to the ice border with FF ranging between about 10 m/s and 15 m/s. At the southern cross-wind track of the flight pattern an area of convergence located near the ice edge is discernable.

Profiles P7 and P9 in Figure 3.11 were located above ice where no clouds were present. Here, the boundary-layer temperature decreases with increasing distance from the ice border from -12.5°C (P 9) to -15°C (P10). The stratification inside the boundary layer is more stable than on 10 April and z_i increases with increasing distance from the ice border from 100 m (P9) to 180 m (P10). Above ice, the boundary layer is drier than the overlaying air and the wind profiles show similar characteristics than on 10 April: maximum velocities near the capping inversion, a veering in DD and an inflection point in DD within the capping inversion. The turbulent structure of the boundary layer is indicated by increased scatter in FF and DD below z_i. Indicating the baroclinicity across the ice edge, P10 (above open water) reveals a boundary-layer temperature of only -6°C. Here, the air-ocean temperature difference is about -6 K and the well-mixed boundary layer heated from below reaches a height of 1.5 km below a weak inversion of 1 K to 2 K. Clouds extend from the top of the boundary layer almost down to the open water.

Figure 3.12 shows the cross-wind run H11 in stack II above ice and the cross-wind run H12 which crosses the ice border. This example shows the baroclinicty across the ice edge and it is well suited to compare the different conditions above ice and open water which is reached after about 925 s. When comparing DD and FF on the one hand with T_{sfc} and albedo on the other hand between 905 s and 925 s, it is seen that the line of convergence is not located exactly above the ice edge. It is located above ice about 2 km ahead of the shore line. The location of the line of convergence may be influenced by the general flow which is almost, but not exactly parallel to the ice border. It is noteworthy, that a convective cloud wall was located near the ice edge above open water.

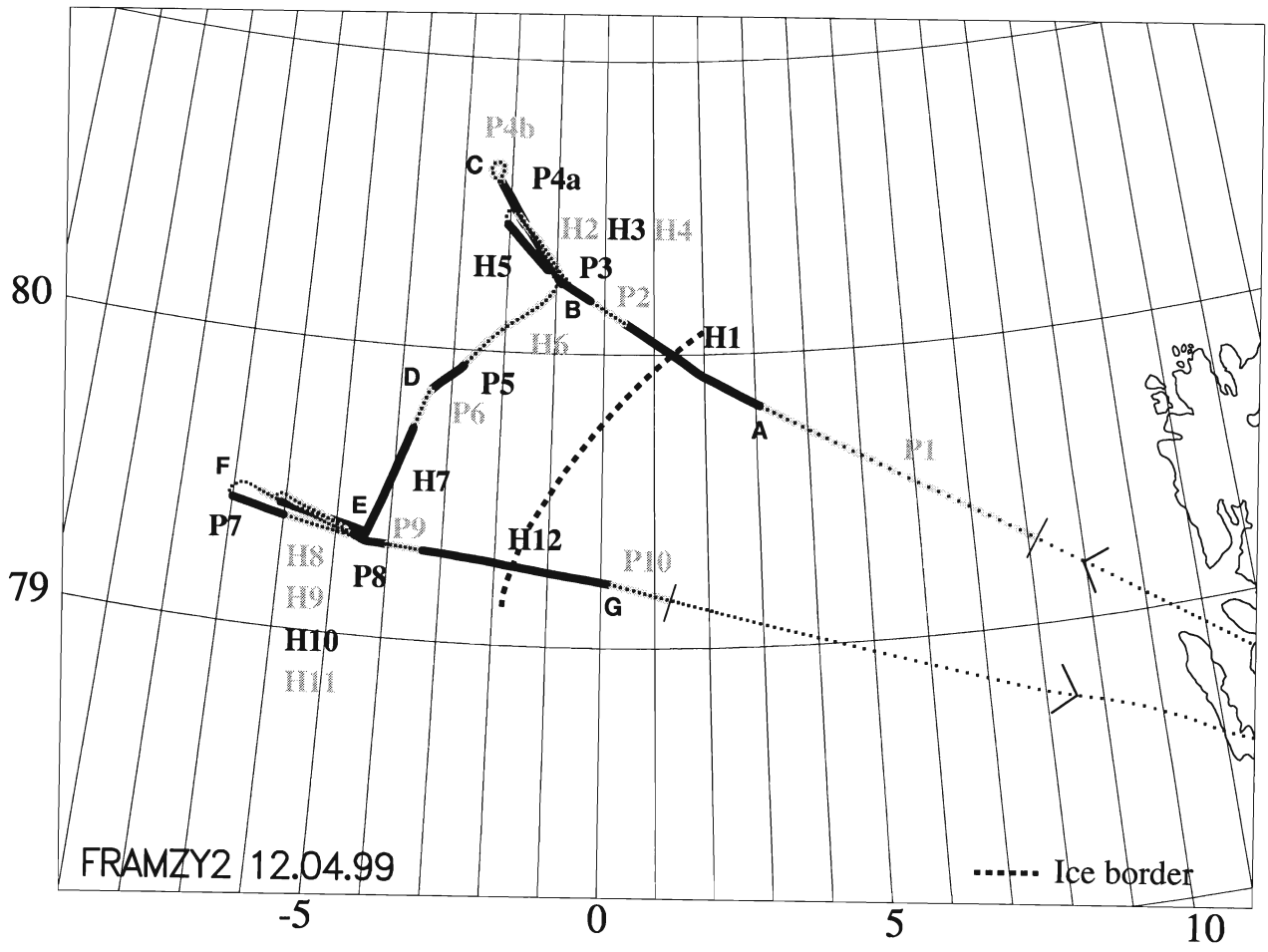

Figure 3.9: *As Figure 3.3, but for 12 April 1999.*

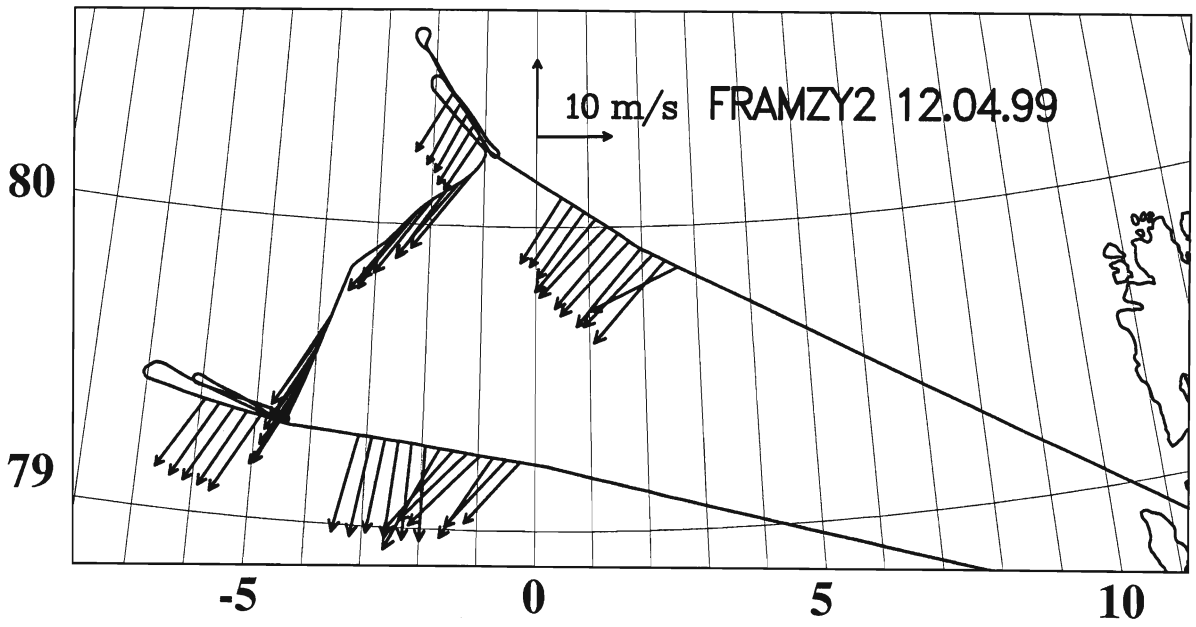

Figure 3.10: *As Figure 3.4, but for 12 April 1999.*

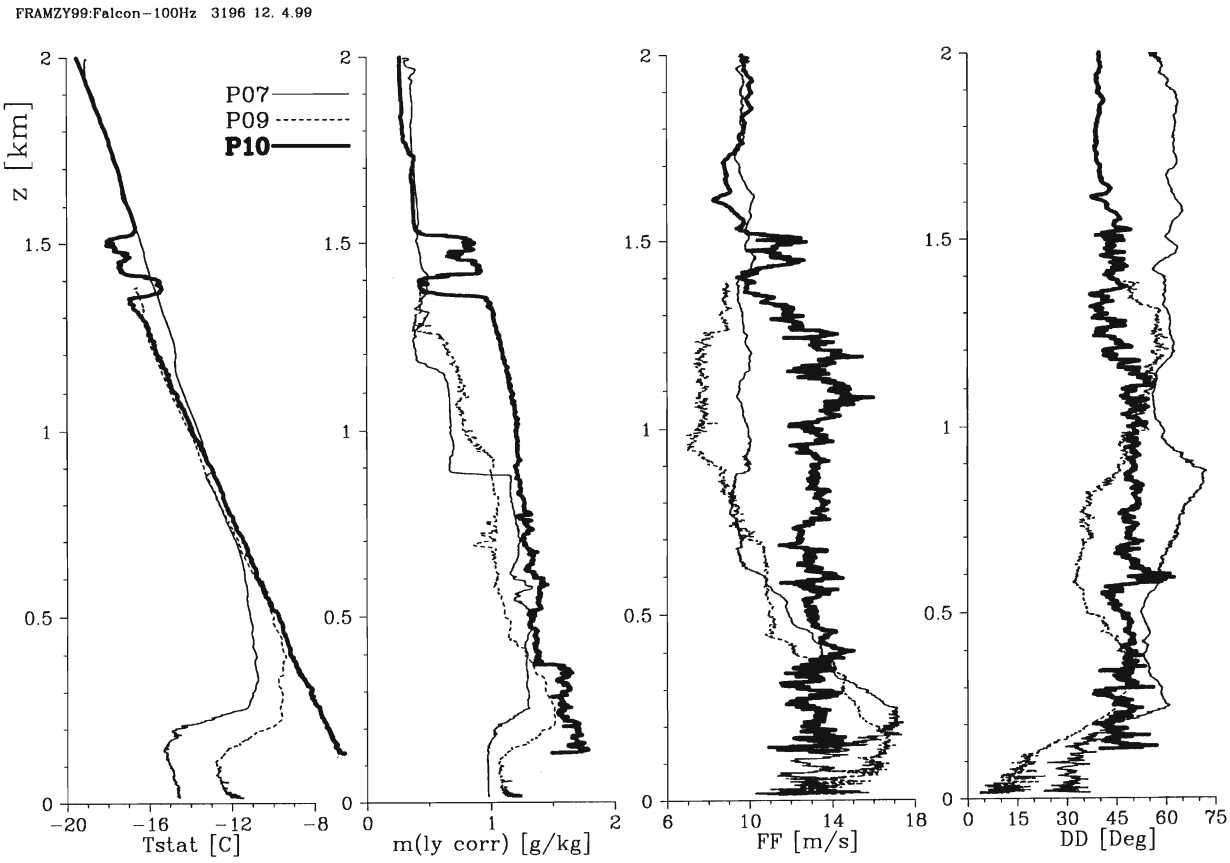

Figure 3.11: *As Figure 3.5, but for 12 April 1999.*

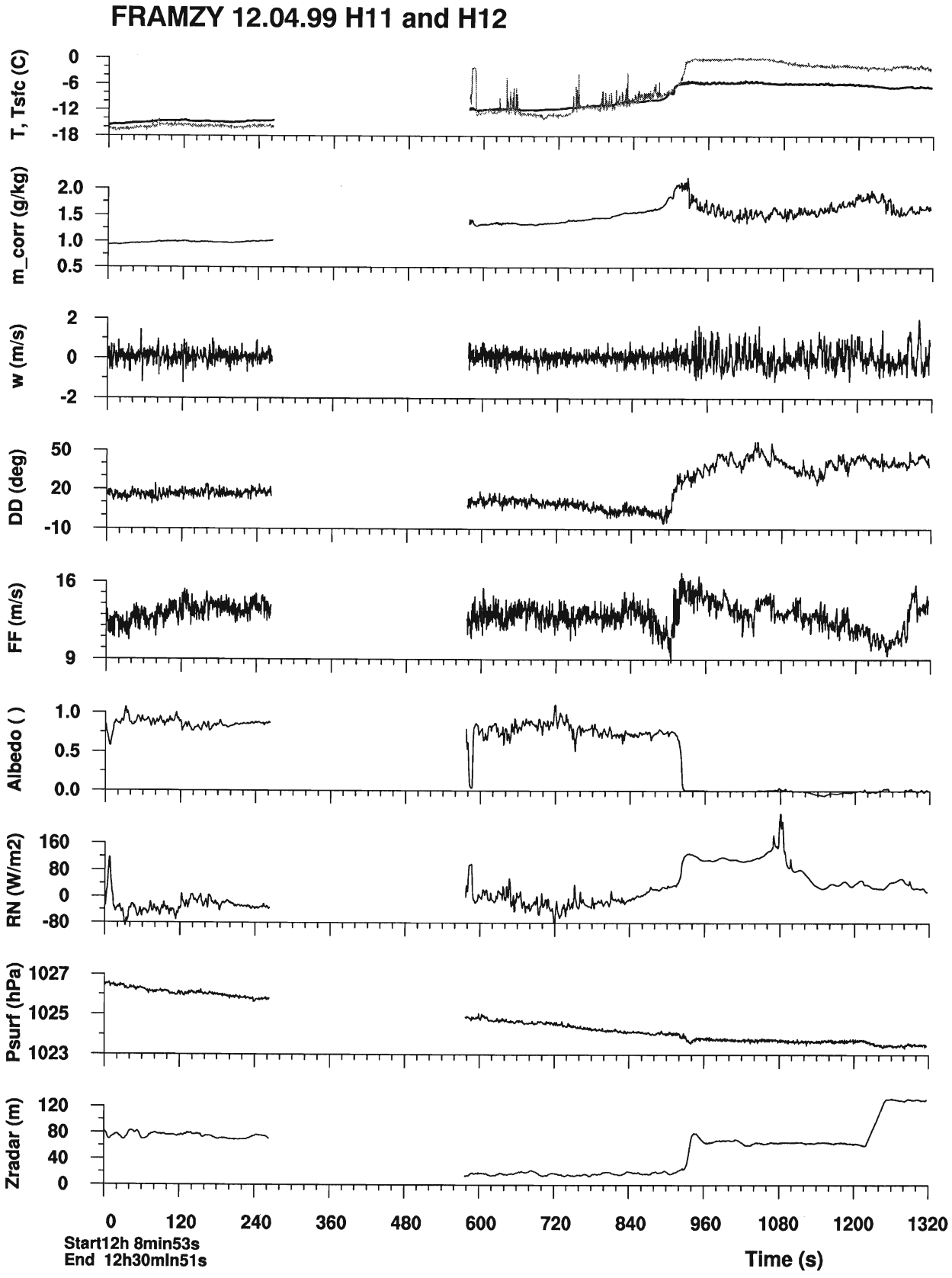

Figure 3.12: *As Figure 3.6, but for horizontal flight legs H11 and H12 on 12 April 1999.*

3.4.3 Baroclinicity and convergence line near ice edge on 14 April 1999

On 14 April 1999, the flight pattern (Figure 3.13) resembles those of the previous missions and includes low-level runs and profile soundings, but no stacks have been flown on this day.

The low-level wind information encountered during horizontal low-level runs (Figure 3.14) shows that the experimental area was located inside a very weak N flow. At the northern and southern tracks of the flight pattern, a line of convergence located near the ice edge with NW wind against NE wind had been crossed.

Profile P1 in Figure 3.15 was located above open water, P2 above ice in the vicinity of the ice border, and P4 above ice at the NW corner point B of the flight pattern. The decrease of static temperature from E to W (about 6 K) seen in these profiles again indicates the presence of baroclinicity across the ice edge.
Above open water, the depth of the convective boundary layer reaches about 900 m. Above ice, not far away from the ice border, z_i ranges around 190 m (P2). At the NW corner point B (P4) where low-level wind is almost negligible, a very thin inversion overlays the ice. Here, very flat stripes of fog with cloud tops not higher than 15 m have been observed.

Figure 3.16 shows the cross-wind run H1 which started above open water and crosses the ice border after 285 s. It is striking that the ice temperature (T_{sfc}) is warmer than -10°C during the first time above ice between 280 s and 440 s (corresponding with a distance of 16 km) where open water ponds are present, whereas T_{sfc} decreases down to -18°C from 440 s on. This may indicate that thick old ice was located below the last part of the run while thinner and newer ice was located below the first 16 km behind the ice border.
When comparing DD and FF on the one hand with T_{sfc} and albedo on the other hand between 185 s and 285 s, it is seen that the line of convergence is not located above the ice edge. It is located above open water about 10 km ahead of the shore line. In case of the preceding mission (12 April 1999), the line of convergence was located above ice about 2 km behind the shore line. As already mentioned, the location of the convergence line is influenced by the general flow on that day. The impact of the general flow is almost negligible on 14 April 1999.

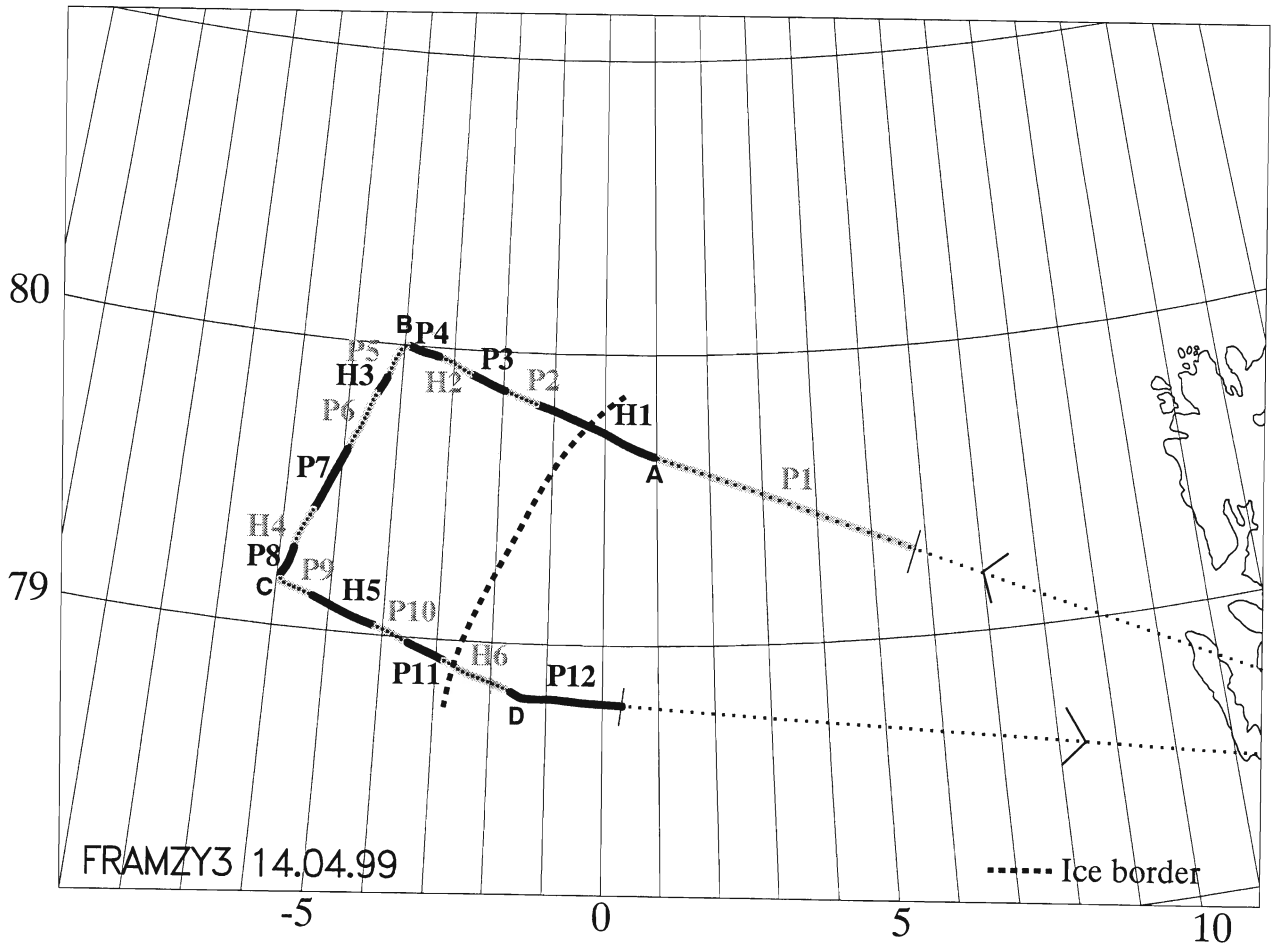

Figure 3.13: *As Figure 3.3, but for 14 April 1999.*

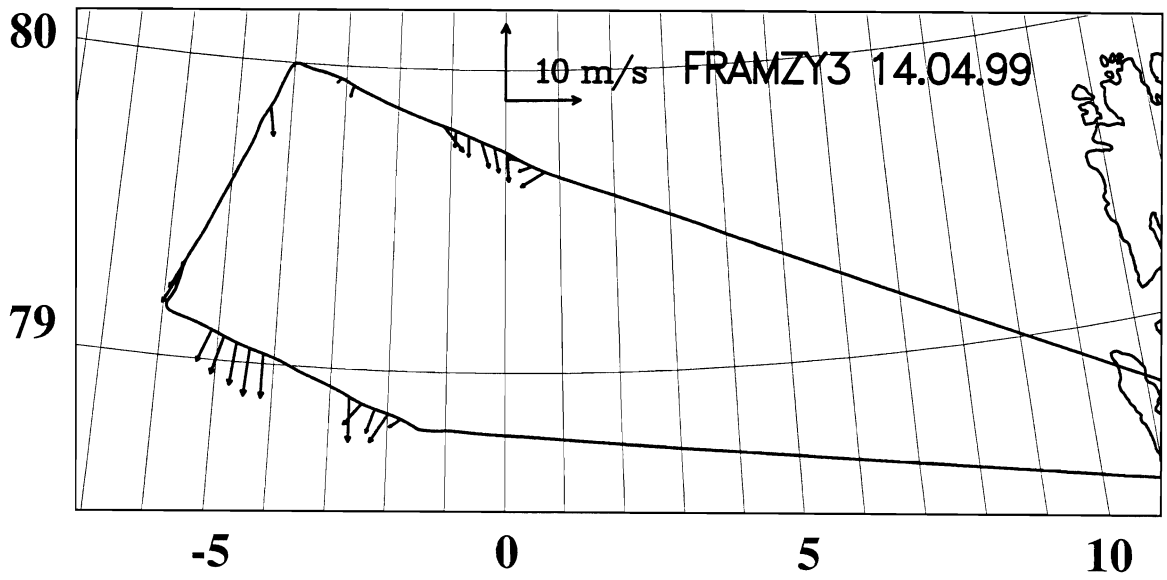

Figure 3.14: *As Figure 3.4, but for 14 April 1999.*

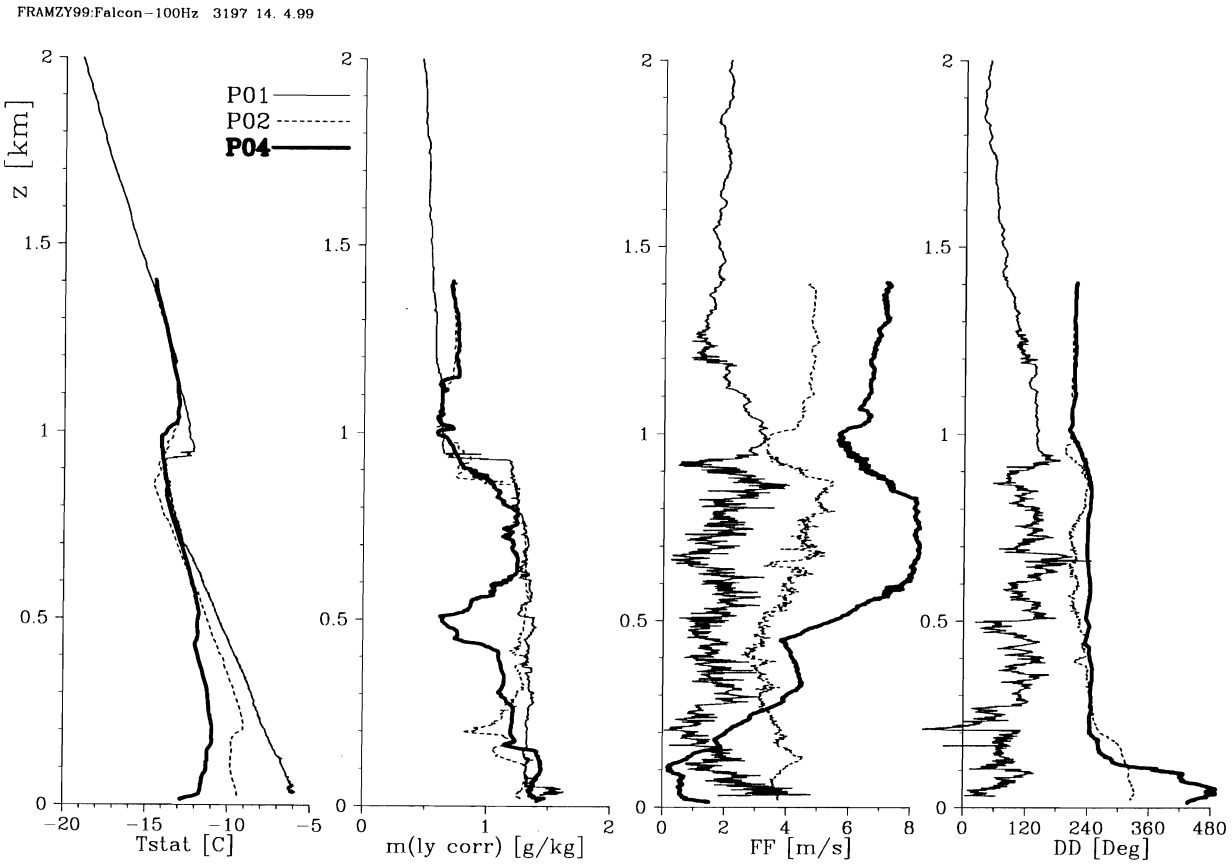

Figure 3.15: *As Figure 3.5, but for 14 April 1999.*

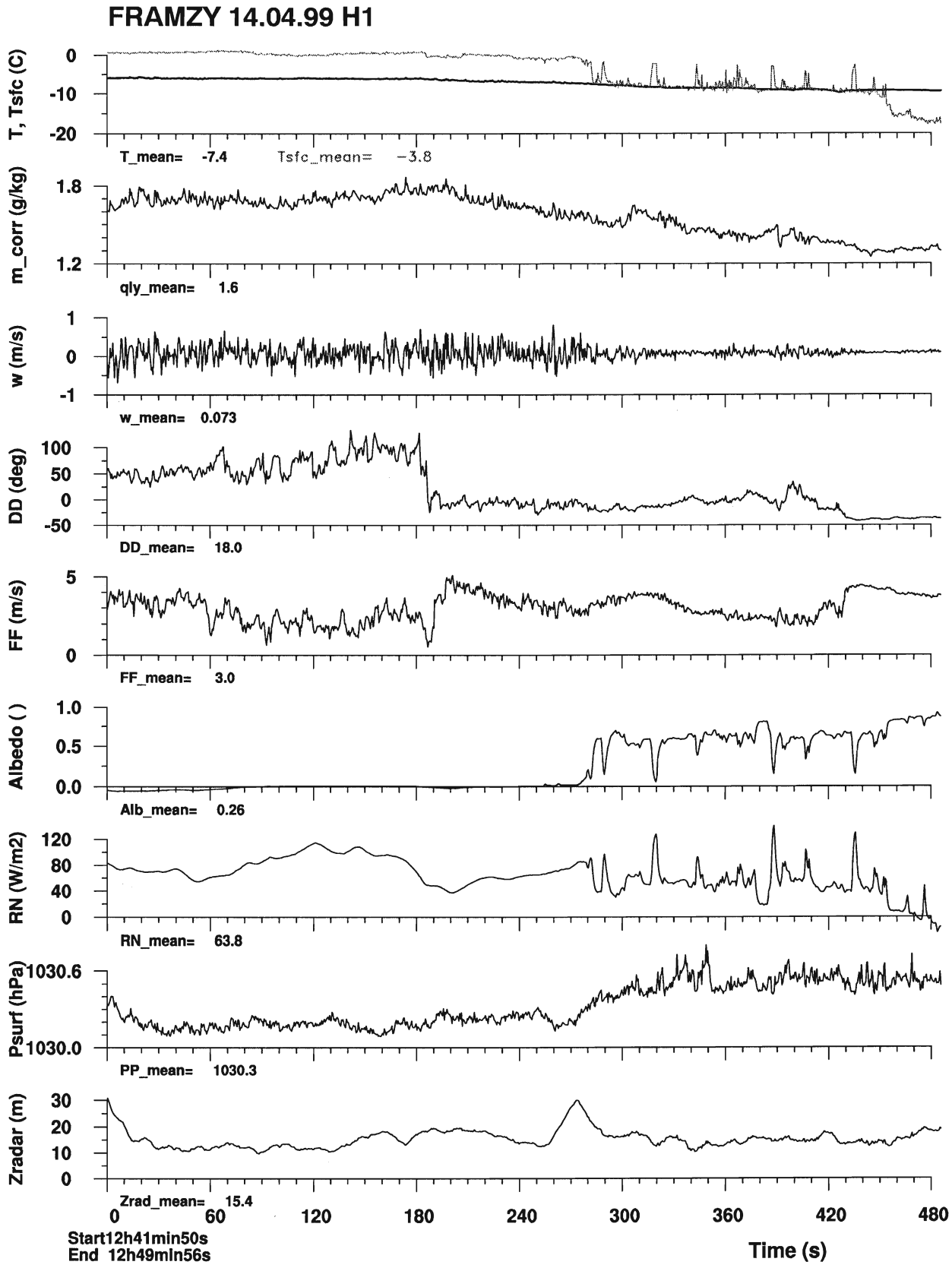

Figure 3.16: *As Figure 3.6, but for horizontal flight leg H1 on 14 April 1999.*

3.4.4 In the northwestern sector of a Fram Strait cyclone on 18 April 1999

Figure 3.17 shows the ice edge and flight pattern on 18 April 1999. On that day, the experimental area was predominantly located above ice inside the NW sector of a small, northward moving cyclone in the Fram Strait. H1 and H9 were located partially above ice and partially above open water while P1, P10, P11, P12, and H10 were located above open water. The above-water pattern P11 - H10 - P12 has been carried out in order to catch the NE sector of the cyclone. Two cross-wind stacks have been flown on this day: stack I comprises H2, H3, H4 and stack II H6, H7, H8.

Figure 3.18 (wind pattern from low-level runs) shows strong N - NE winds (FF 20 m/s to 25 m/s, DD 5° to 20°) in the experimental area. SE wind encountered during H10 between the ice border and the coast of Spitsbergen indicates that H10 is located east of the low axis.

P6 and P9 in the profile plot (Figure 3.19) represent above-ice conditions where P9 is closer to the ice edge than P6. Above ice, a well mixed boundary layer (see profiles of T_{stat} and of mixing ratio) of depth 300 m to 350 m and with T_{stat} ranging from -13°C to -16°C is present. Inside the level of the sharply marked capping inversion, the mixing ratio increases with height. The well mixed state of the boundary layer can be attributed to be the result of mechanically generated turbulence caused by the interaction between strong wind and the rough ice surface. The scatter in FF below z_i (which indicates the strength of turbulence) is larger than during the previous missions. The above-ice profiles of wind velocity FF show a strong wind shear below z_i with maximum velocities near the capping inversion, a veering in DD and an inflection point in DD within the capping inversion. (Qualitatively similar FF profiles have been found on 10 and 12 April.) One impact of the strong wind is the fact that the ice has been observed to be considerably broken up if compared with the preceding missions.
P10, encountered above open water, indicates a boundary-layer temperature of -5.5°C (baroclincity across the ice edge). The boundary-layer air captured during P10 has not been for a long time above open water because the wind blows almost from N while the ice edge reveals an alignment from SW to NE. Hence, although heating from below is active, the depth of the boundary layer (400 m) is still in the range of that above ice.
Representing conditions E of the through axis, P12 indicates a well mixed boundary layer of depth 1350 m and a relatively weak (FF 5 m/s to 10 m/s) flow from SE (DD 140°).

Figure 3.20 shows the along-wind low-level run H5 located above ice between B and C. Due to bad visibility, the lowest flight levels were confined to 50 m - 100 m. Between 140 s and 200 s, H6 crossed a broad lead of open water whose width is in the range of 6 km. Indicating increased flux of sensible and latent heat, the time series of vertical velocity, mixing ratio, and static temperature (the latter one not well discernable due to the low-resolving range of the temperature axis) show increased fluctuations above the lead.
It is striking that the boundary-layer temperature T is almost identical with the surface temperature of closed ice (T_{sfc}). This again indicates the efficiency of turbulent mixing occurring inside the boundary layer.

Figure 3.21 shows the horizontal flight legs H6, H9, H10 representing an W-E cross-section through the cyclone. H6 starts at point C. H9 crosses the ice border after 3/4 of run time. The time

series of H9 indicates the baroclinicity across the ice edge. That H10 is located somewhat E of the cyclone axis is indicated by DD (150° at H10 against 10° at H6 and H9) and by the trend in the surface pressure.

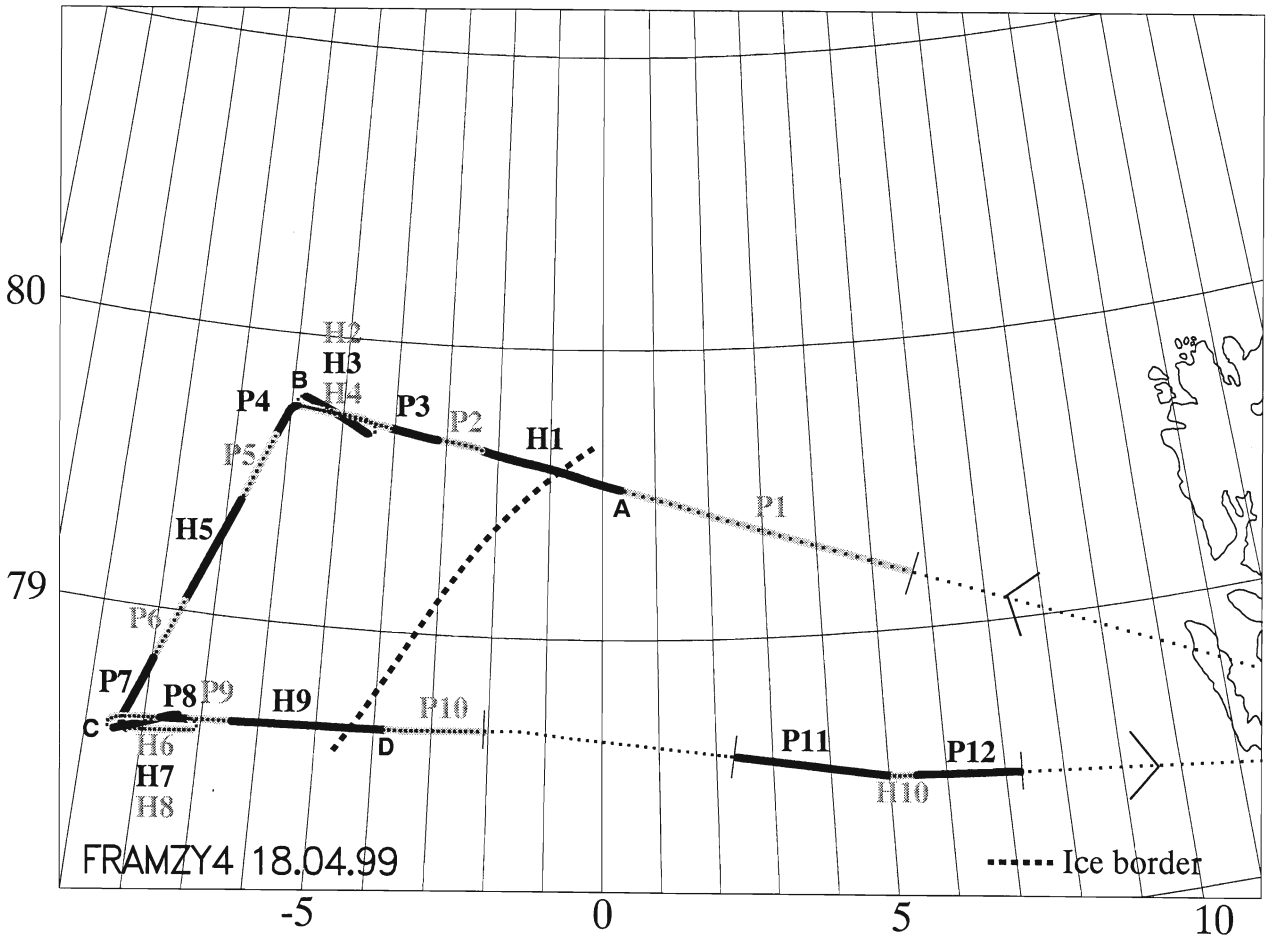

Figure 3.17: *As Figure 3.3, but for 18 April 1999.*

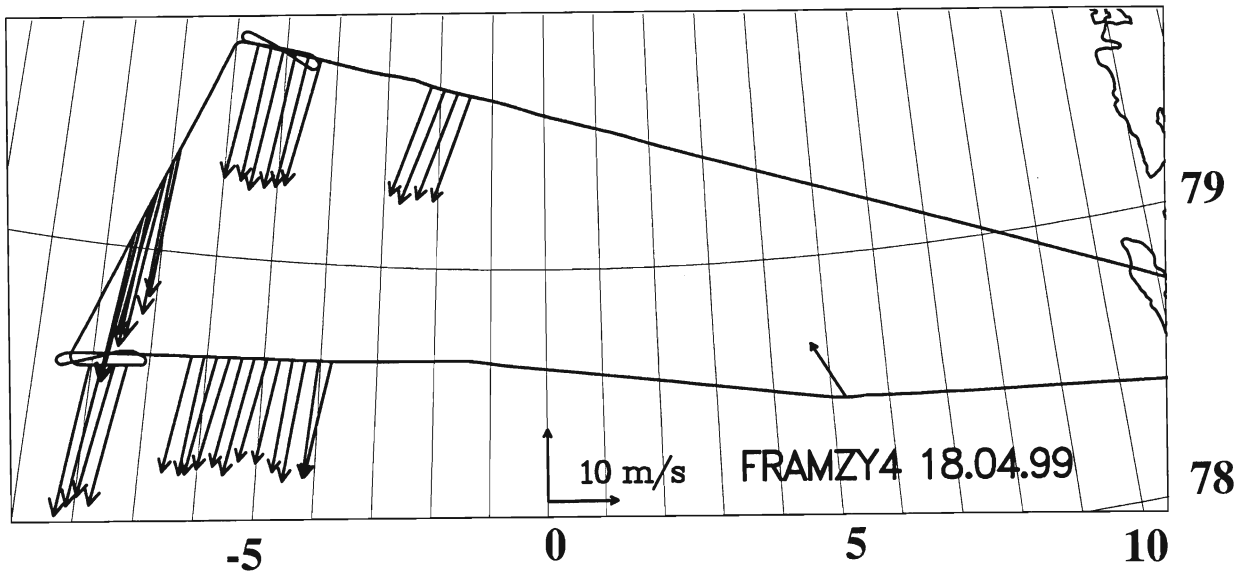

Figure 3.18: *As Figure 3.4, but for 18 April 1999.*

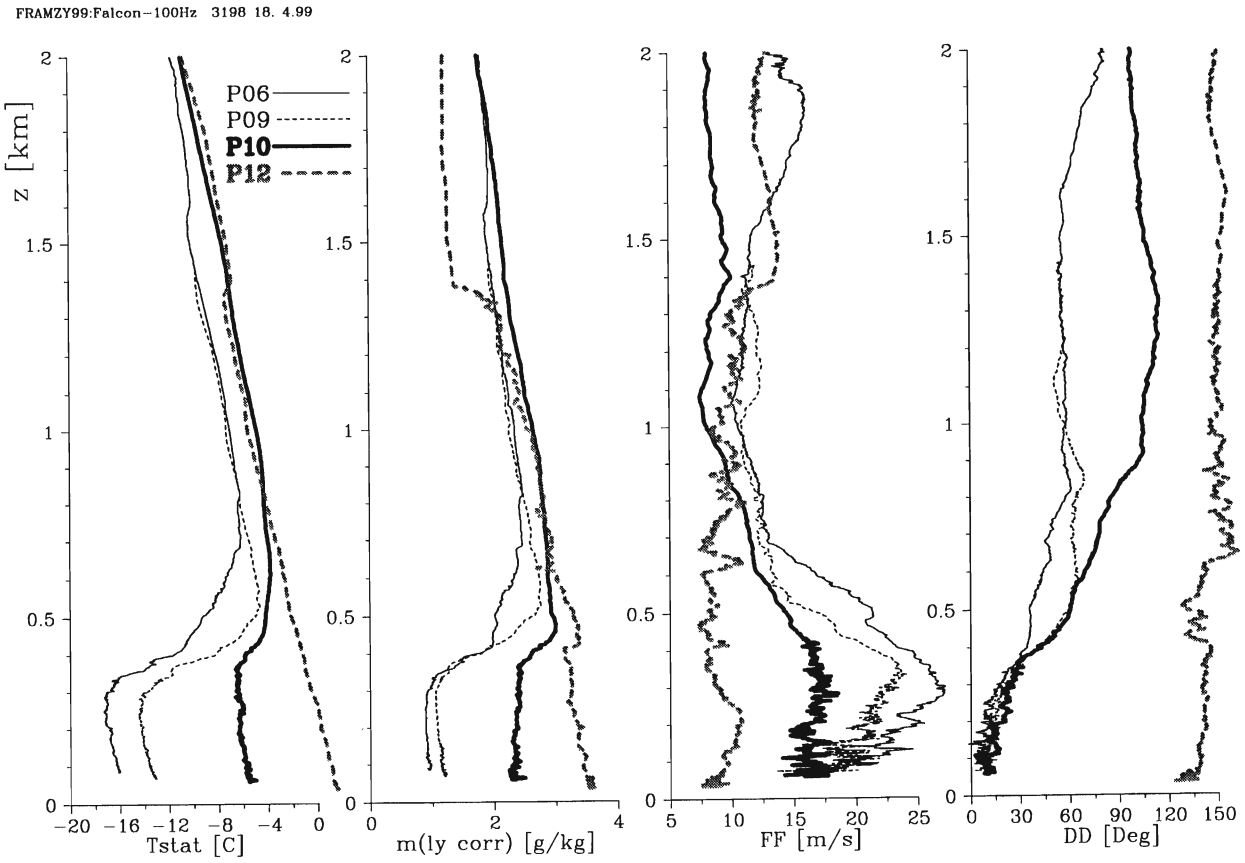

Figure 3.19: *As Figure 3.5, but for 18 April 1999.*

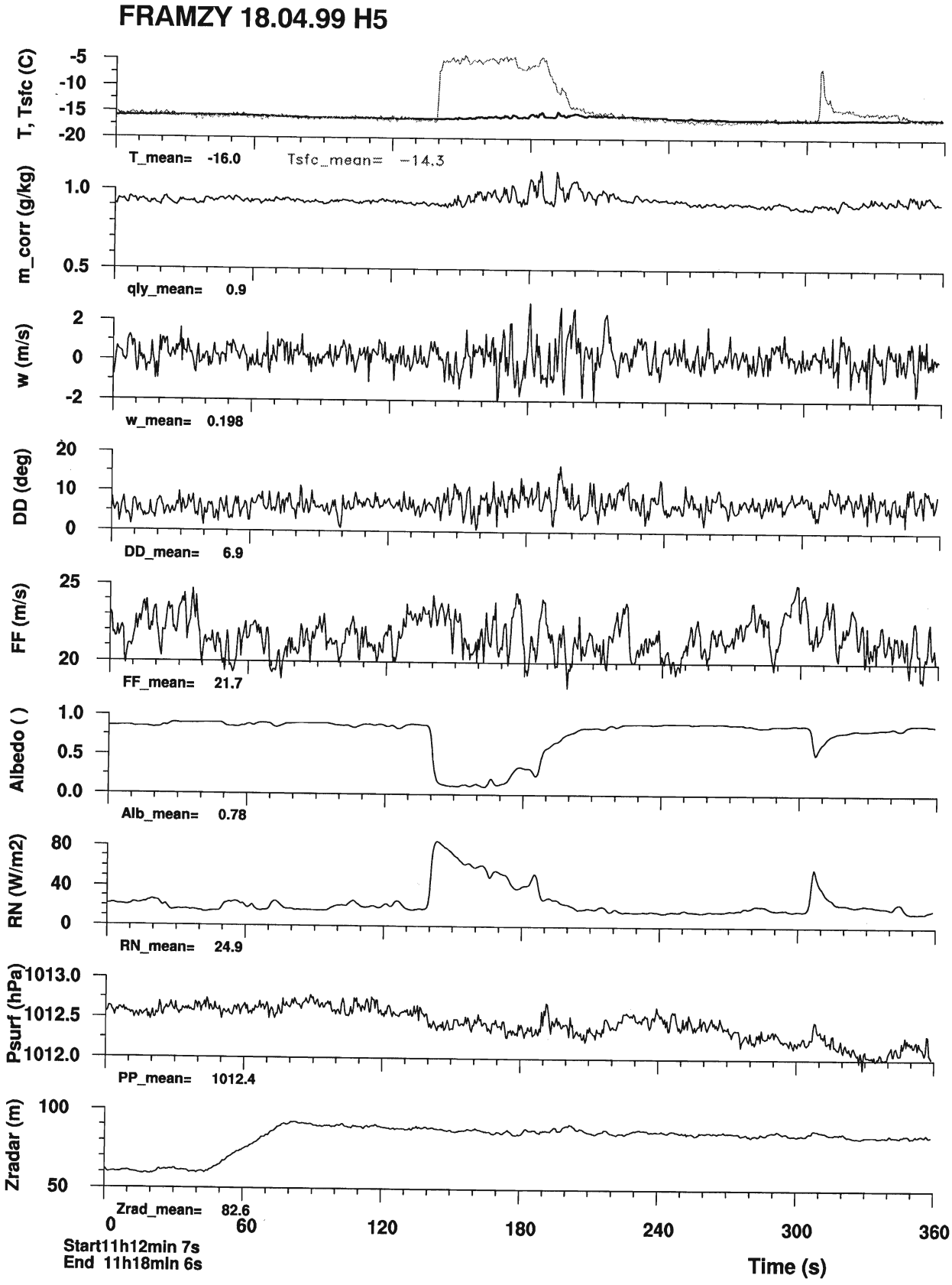

Figure 3.20: *As Figure 3.6, but for horizontal flight leg H5 on 18 April 1999.*

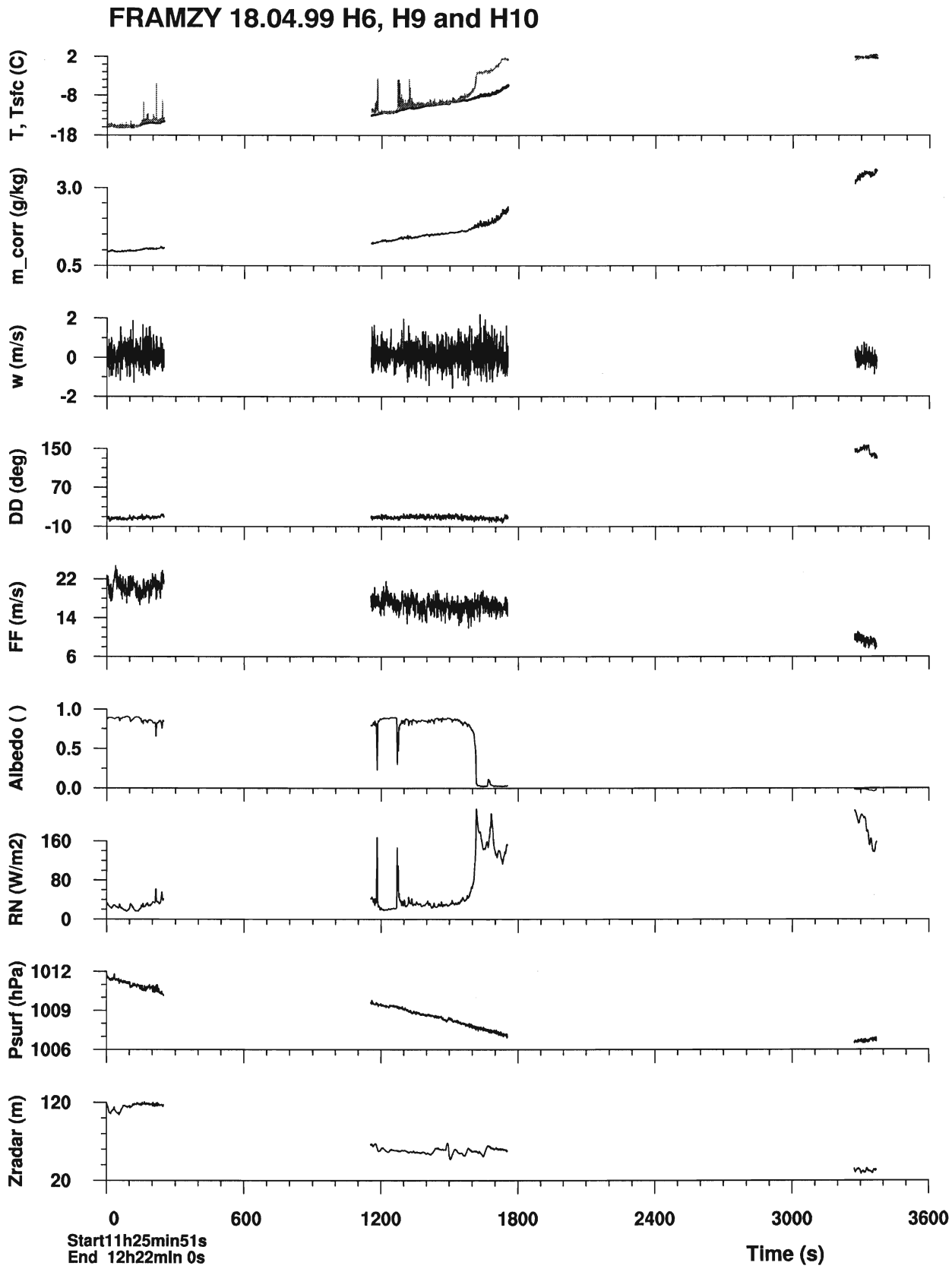

Figure 3.21: *As Figure 3.6, but for horizontal flight legs H6, H9, H10 on 18 April 1999.*

3.4.5 Aircraft cross section through a Fram Strait cyclone on 19 April 1999

On 19 April 1999, the Fram Strait cyclone crossed the ice border. The northern track of the flight pattern (Figure 3.22) is a continuous 35 min (approximately 210 km) low-level run crossing the northern sector of the cyclone. The southern track forms a cross-section which hits the center of the cyclone. The flight pattern includes low-level runs and profile soundings, but no stacks have been flown on this day. The entire pattern is located NE of the buoy array.

The wind information sampled during low-level runs (Figure 3.23) shows the gradual wind veering along the northern track from SE in the warm side to N in the cold side of the cyclone. The rotating flow around the cyclone center is clearly confirmed. The southern track shows a similar wind pattern, except the smallness of FF and the veering of DD over a very small flight distance in the western part of H4 identifying it to be located very close to the center of the low.

Figure 3.24 shows profiles giving an overview over the different air masses within the cyclone. P1 above open water at A is representative for the warm sector of the cyclone and indicates a low-level temperature of -1°C and exhibits no inversion. P2, located near B above closed ice and representative for the cyclone's cold rear side, indicates a flat, well-mixed boundary layer of 300 m depth and of -15°C temperature, overlaid by a strong inversion of 12 K. P4 and P5 are located in the vicinity of the cyclone's center. P4 shows similar characteristics as P2 (although z_i is smaller and boundary-layer is warmer) and belongs to the cold side of the cyclone, whereas P5, a descent profile, ends just inside the warm air. Above 500 m, temperature and mixing ratio are relatively similar in all profiles. Hence, the most important characteristic of a cyclone which is to contain different air masses is only seen in the lowest 500 m of the atmosphere.
The above-ice profiles (P2, P4) show wind velocities between 12 m/s and 14 m/s in the boundary layer and a sharp drop to 4 m/s within the capping inversion forming a zone of considerably strong wind shear. The profile representative for the warm sector (P1) exhibits only moderate velocities ranging from 4 m/s to 8 m/s.
The mixing ratio measured during ascent profiles P2 and P4 showed sharply marked super-saturation of 0.5 to 1 g/kg within a 80 m layer just above the capping inversion. This is an error in measurement and the incorrect parts of profiles P2 and P4 are left out in Figure 3.24. This error is very likely due to the sharp temperture gradient within the inversion layer which possibly let the instrument mist up.

The 35 min long low-level run H1 represents an E-W cross-section through the cyclone slightly N of its center (see Figure 3.22). Data from H1 are shown in Figure 3.25. H1 starts at A above open water not far away from the ice border. The ice border is reached after about 70 s or 7 km. This is seen in the abrupt increase in albedo and in the decrease in net radiation flux, but not in the time series of air and surface temperature. This is due to the fact that the temperatures of the sea surface and ice surface and air temperature are the same (around -2°C) within the warm sector of the cyclone. Leads and open water spots are reflected only in albedo and net radiation flux as long as the aircraft was inside the warm sector.
The warm sector with spatially uniform air temperature and mixing ratio ends after about 1200 s (120 km). This point marks the axis of the cyclone where the surface pressure reaches its minimum. Further westward, the cold sector starts with continuous decrease in air temperature and mixing ratio, increase in wind velocity, and veering in wind direction from SE to N. To the north

of the cyclone's center the transition from the warm to the cold side is smooth rather than a sharply marked front. Within the cold sector, the pressure gradient is about 3 hPa/100 km. The cold sector is marked by increased turbulence (see fluctuations in vertical velocity). Except for open water ponds, air and surface temperatures are in the same range and the stratification inside the boundary layer is slightly stable.
The time series of albedo indicates that the percentage of open water is larger in the cold sector than in the warm sector. This may be an effect of the different wind conditions: on-ice flow leading to ice convergence in the warm sector versus off-ice flow leading to ice divergence in the cold sector.

Figure 3.26 shows vertical fluxes of sensible heat H, latent heat E, momentum t_x, t_y parallel and perpendicular, respectively, to the mean low level wind direction of 83°and evaluated from 10 second intervals of horizontal flight leg H1. It is obvious that the usual method to evaluate vertical fluxes from aircraft data by calculating covariances with respect mean values averaged over the entire time series (after de-trending the data, if required) can only be applied for horizontal homogeneous turbulent conditions as usually found, for example, within a convective boundary layer above open water. This method can not be applied when leads and ponds of open water causing strong heating from below alternate irregularly with closed ice which may be even colder than the overlaying air. In order to calculate fluxes for inhomogeneous above-ice conditions, mean covariances have been calculated for independent 10 s intervals where the second interval starts 0.5 s later than the first interval and so on. Hence, Figure 3.26 shows time series of 10 s interval fluxes. Averages of these 10 s interval fluxes are indicated in the Figure.

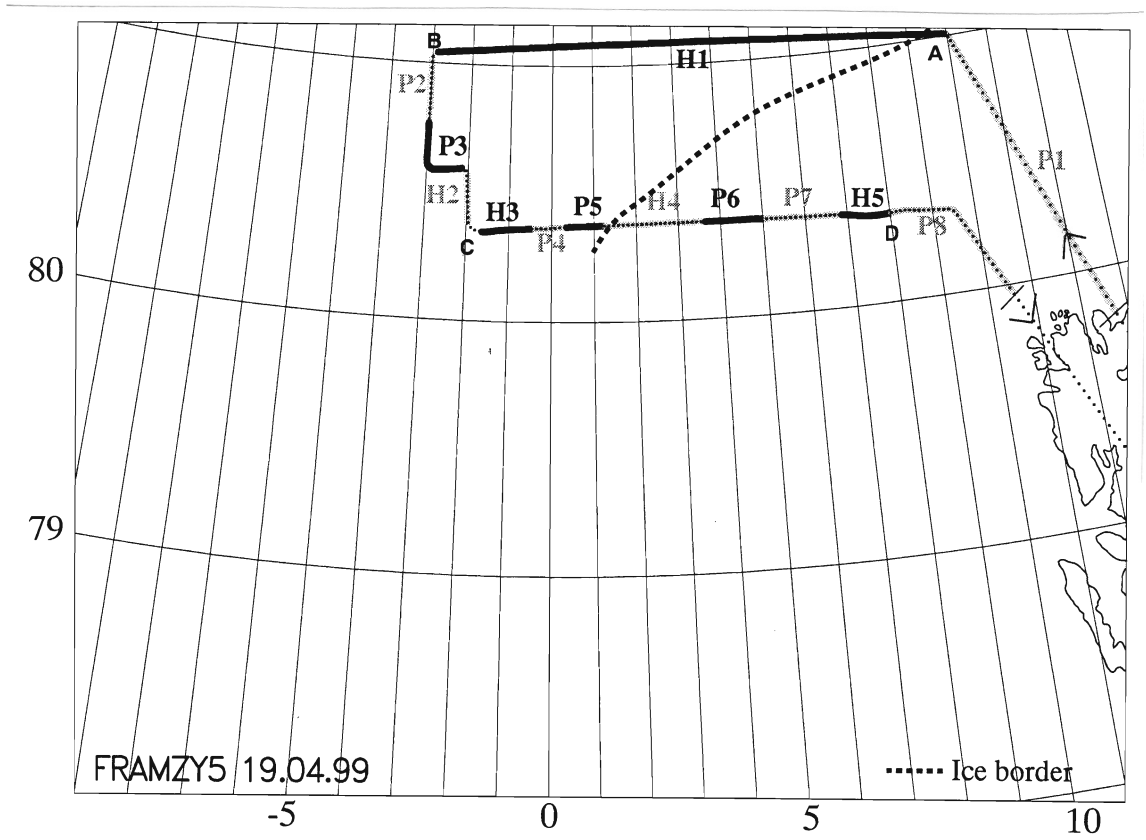

Figure 3.22: *As Figure 3.3, but for 19 April 1999.*

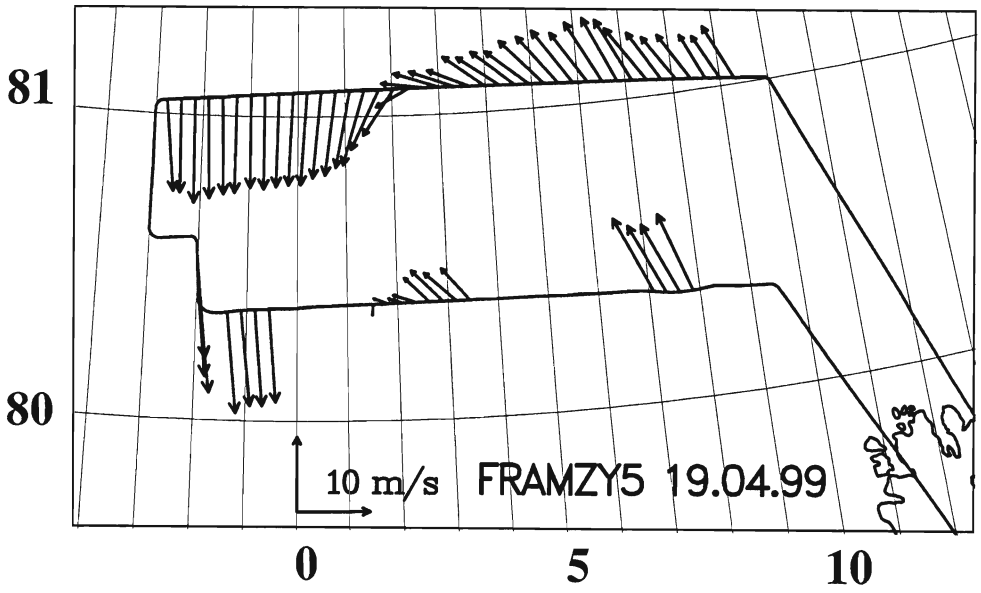

Figure 3.23: *As Figure 3.4, but for 19 April 1999.*

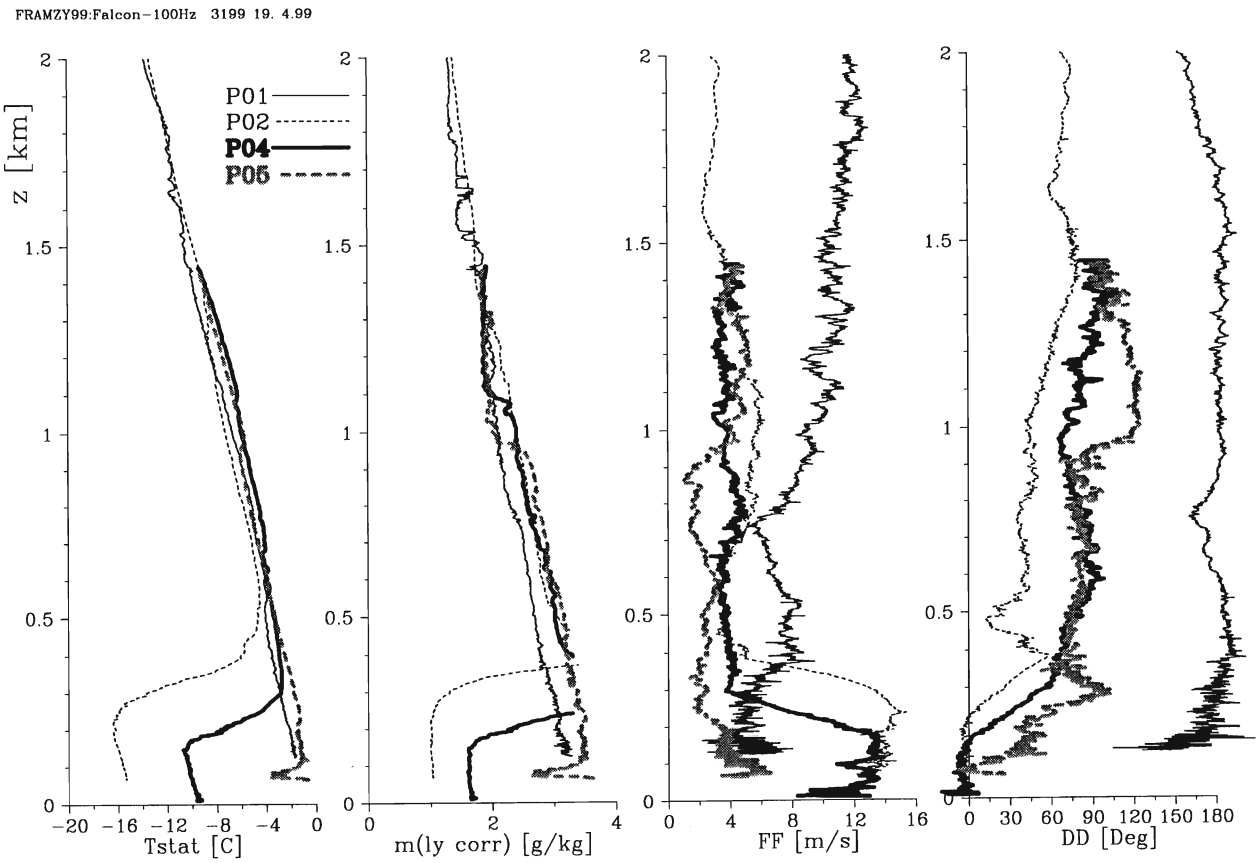

Figure 3.24: *As Figure 3.6, but for 19 April 1999.*

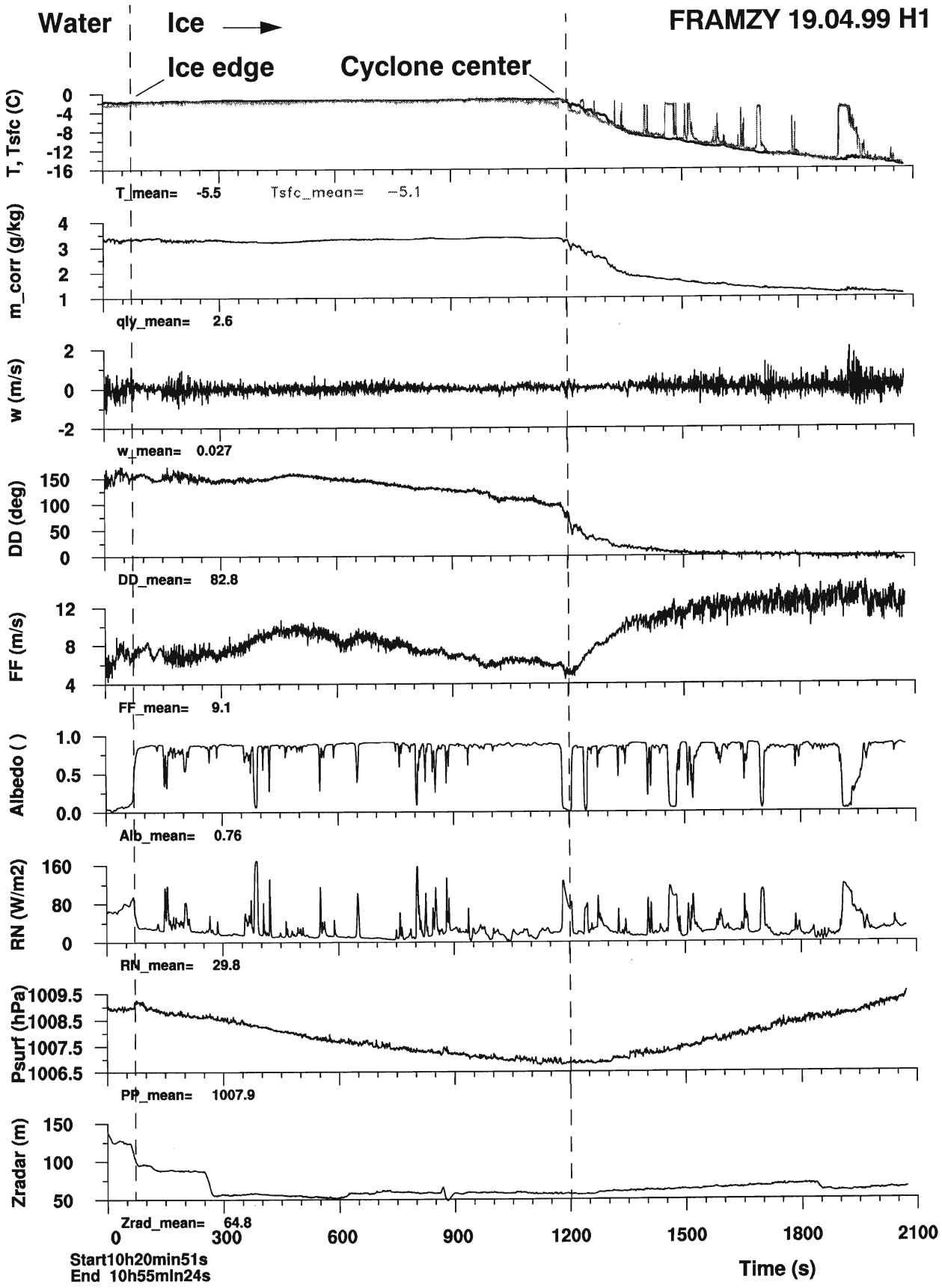

Figure 3.25: *As Figure 3.6, but for H1 on 19 April 1999.*

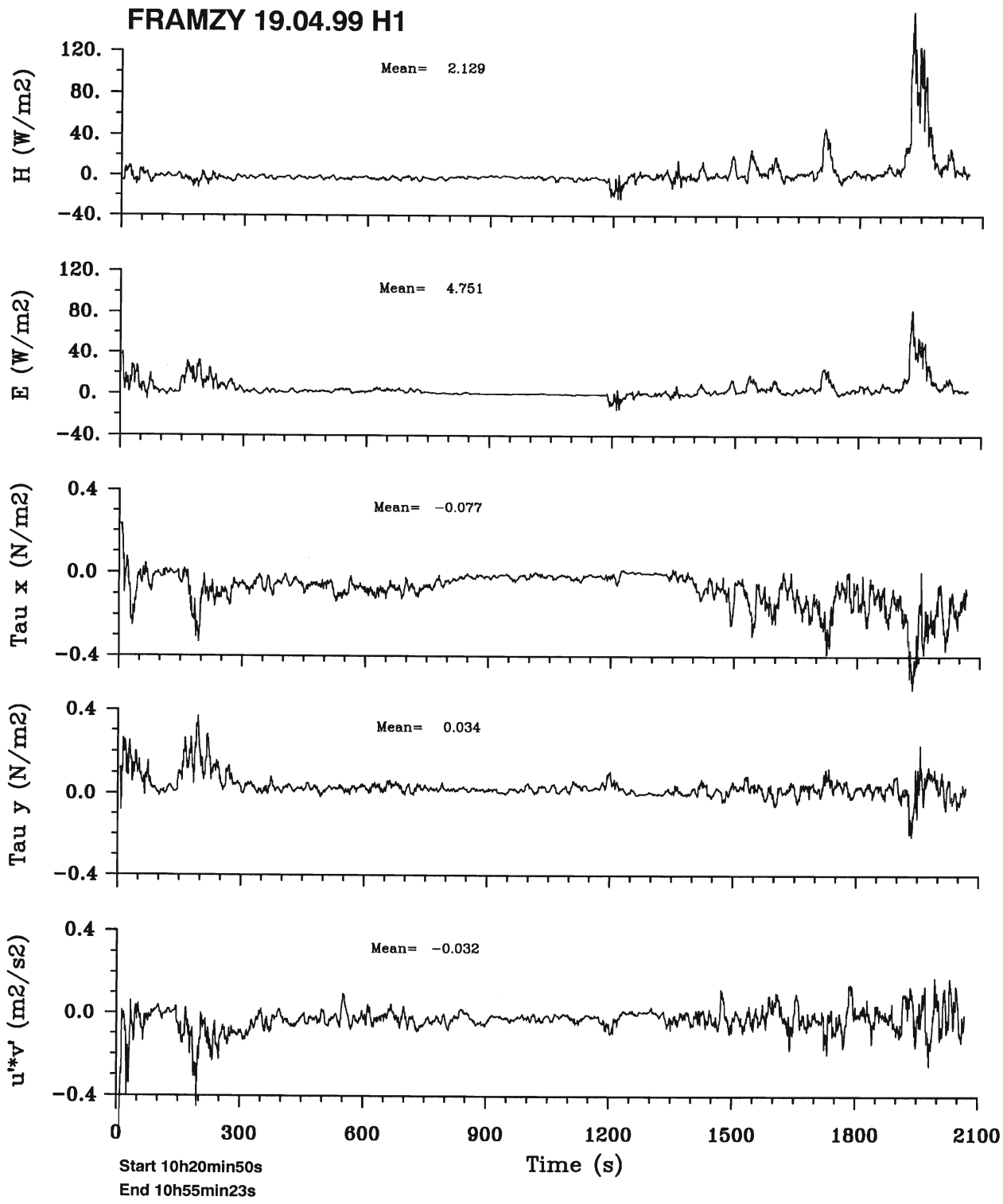

Figure 3.26: *Time series of vertical fluxes of sensible heat H, latent heat E, momentum t_x, t_y parallel and perpendicular, respectively, to the mean low level wind direction of 82° and evaluated from 10 s intervals of horizontal flight leg H1 flown by the Falcon-20 on 19 April 1999. Averages of these 10 s fluxes are indicated. The time scale in the abscissa can be converted to a length scale applying the mean Falcon flight speed of approximately 100 m/s.*

3.4.6 Cloud micropysical measurements on 18 April 1999

(A. Reuter, N. Buschmann, U. Maixner, GKSS-Research Center Geesthacht)

For the measurement of cloud microphysical properties, the FALCON was equipped with four standard PMS (Particle Measuring Systems Inc., Boulder, CO., USA) probes. GKSS Research Center (Geesthacht, Germany) hold responsible for the calibration and operation of this equipment. Table 3.3 summarizes the probes that had been utilized during the FRAMZY field phase. For the determination of cloud particle properties, the entire size range from 2 to 6400 µm had been covered by different PMS probes. A Nevzorov LWC/TWC probe had been used for integrally measuring the liquid water content (LWC) and total water content (TWC). With this instrument, the ice water content (IWC) can be derived by subtracting the LWC from the TWC.

Table 3.3: Different probes, operated by GKSS during the FRAMZY field experiment on board the FALCON; "n.a." stands for "not applicable".

Instrument	Purpose	size range / µm
PMS FSSP-100	cloud particle properties	2 - 47
PMS OAP-2D2-C	cloud particle properties	25 - 800
PMS OAP-2D2-P	precipitation particle properties	200 - 6400
Nevzorov LWC/TWC probe	LWC / IWC measurements	n.a.

The FSSP-100 is a scattering probe while the OAPs are optical imaging probes. A description of these PMS probes can be found in Brümmer (1993) or Hartmann et al. (1997). The applied calibration procedures are reported in Hartmann et al. (1997).

The Nevzorov LWC/TWC probe (IVO-2a), manufactured by SkyTech Research INC. (Toronto, CN), is a constant temperature hot wire probe, designed for aircraft use. The probe consists of two separate sensors for measuring the LWC and TWC (liquid plus ice water content) of clouds and fog in the range between 0.003 gm^{-3} and 3 gm^{-3}. Both sensors, mounted on a common sensor head, are aligned parallel to the air flow. Within an air speed envelope between 10 m/s and 180 m/s, the errors of the probe are within 10%. This has been proven by extensive tests in a high speed wind tunnel (Korolev et al., 1998).

The principle of operation is based on the determination of the heat loss of the sensors by evaporation of cloud water and by convective heat losses. Each sensor consists of a collector and a reference winding. The reference winding is shielded from impacts of cloud particles and therefore allows the direct calculation of the convective heat loss. This is an improvement compared to other constant temperature hot wire instruments like the King LWC probe where data analysis requires assumptions on the convective heat loss of the sensors. The LWC and TWC sensors consist of close single-layer windings of enamel-covered nickel wires. For the TWC sensor, the collector winding is cemented to the hollow cone of a textolite cylinder while the reference sensor is wound within a shallow groove cut into the same cylinder. For the LWC sensor, both windings are wound on solid copper rods and cemented to opposite edges of a flat textolite plate. Because of this design, the LWC collector sensor is only responding to water drops since ice crystals are reflected. Due to its conical shape, the TWC collector sensor responds to

water drops and ice crystals. Both sensors are operated separately by control boxes inside the fuselage, maintaining a fixed temperature for the collector windings and determining the power that is necessary to keep the temperature constant at the defined level. The sensors produce an analog signal between 0 and 10 V. For FRAMZY, a configuration of the Nevzorov probe was applied that allows the operation of the probe in one of the PMS canisters.

The GKSS data analysis strategy directs attention on providing calibrated microphysical parameters as liquid water content, ice water content, particle concentration, average diameter, effective radius and particle size spectra. This task can only be accomplished by use of state-of-the-art data processing schemes as e.g. described in Reuter and Bakan (1998).

Due to the function principle and limitations of the PMS probes, data processing has to account for speed dependent effects, digitization errors, and optical effects. To quantitatively assess these impacts, a series of laboratory measurements were carried out at GKSS during the past years with spinning glass disks containing opaque spots simulating cloud droplets at realistic air speeds up to 100 m/s. These simulations had been used to develop data processing schemes with known accuracy. The use of PMS probes together with the Nevzorov probes allows cross-checks of microphysical parameters, finally ensuring consistency of the dataset.

Regarding the EMI (electro-magnetic interference) situation on board the FALCON, some major improvements (filter-box, wiring) were realized before the start of the FRAMZY field phase. As a result, no noticeable EMI related performance degradation of the PMS probes was noticed during the missions.

In the following, microphysical properties of the cloud fields on April 18, 1999 are illustrated. On this day, the synoptic situation was characterized by a low pressure system in the Fram Strait, centered around 0°E and 76°N. Due to this cyclone, highly inhomogeneous cloud fields had been present in the experimental area which was located ahead of the northward moving cyclone in the marginal ice zone.

Figure 3.27 shows temperature, wind speed and relative humidity encountered during profile P7 above ice near the southwest corner point of the flight pattern. The 300 m boundary layer is overlaid by a capping inversion of about 11 K located between 300 m and 750 m. The relative humidity is close to 100% within the inversion, but indicates clearly sub-saturated conditions within the boundary layer. Since fog reaching down to the surface has been observed during the above-ice part of the mission (also during P7), it is very likely that the pronounced low-level jet of 25 m/s caused turbulent downward transport of small fog droplets formed inside the inversion into the sub-saturated boundary-layer air.

A complex cloud morphology was encountered on April 18. A large fraction of the area was covered by mid-level and high clouds. On 8 profiles, it could be observed that precipitation, originating from these higher clouds, was falling through the lower cloud-layers and also down to the surface. Figure 3.28 gives an example of large snow crystals measured by the PMS OAP-2D2-P probe at 20 m height. It can be seen that the size of the snow particles is in the order of several millimeters.

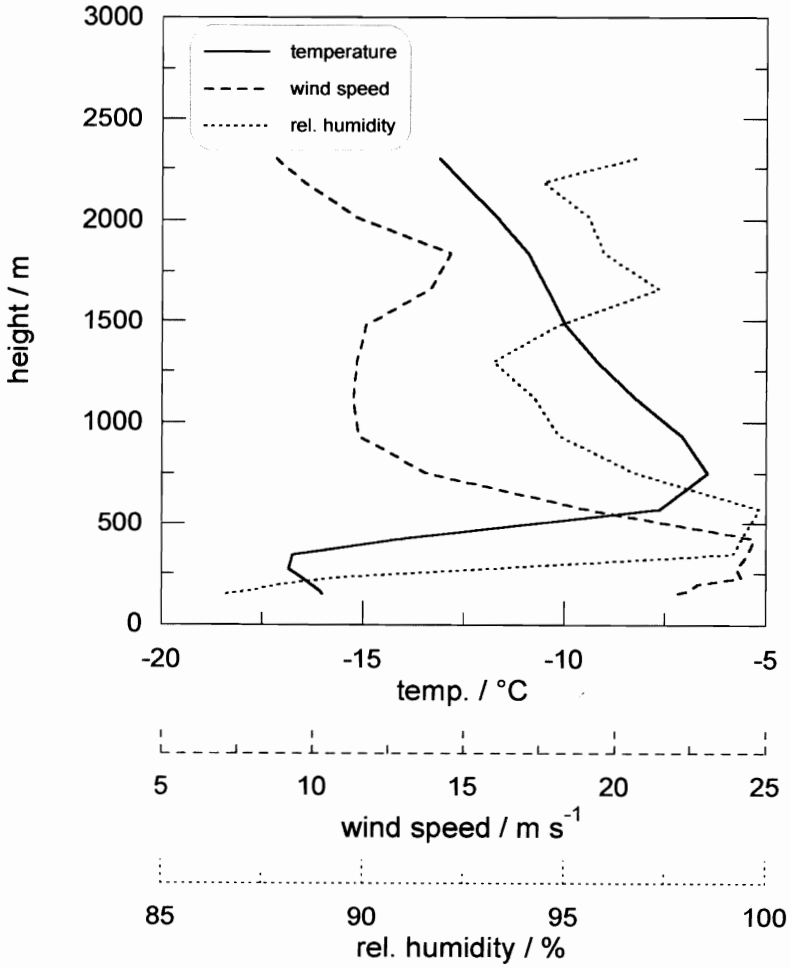

Figure 3.27: *Profiles of temperature, wind speed and relative humidity for profile P7 on 18 April 1999.*

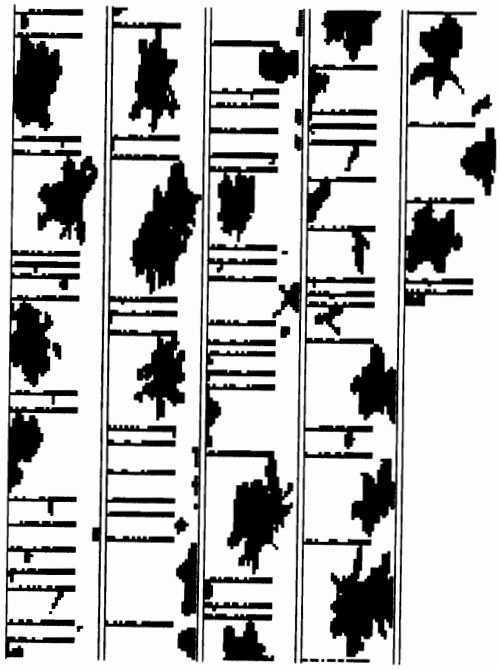

Figure 3.28: *Examples of large snow crystals, measured by the PMS OAP-2D2-P probe at 20 m height on 18 April 1999. The width of one column is 6.4 mm.*

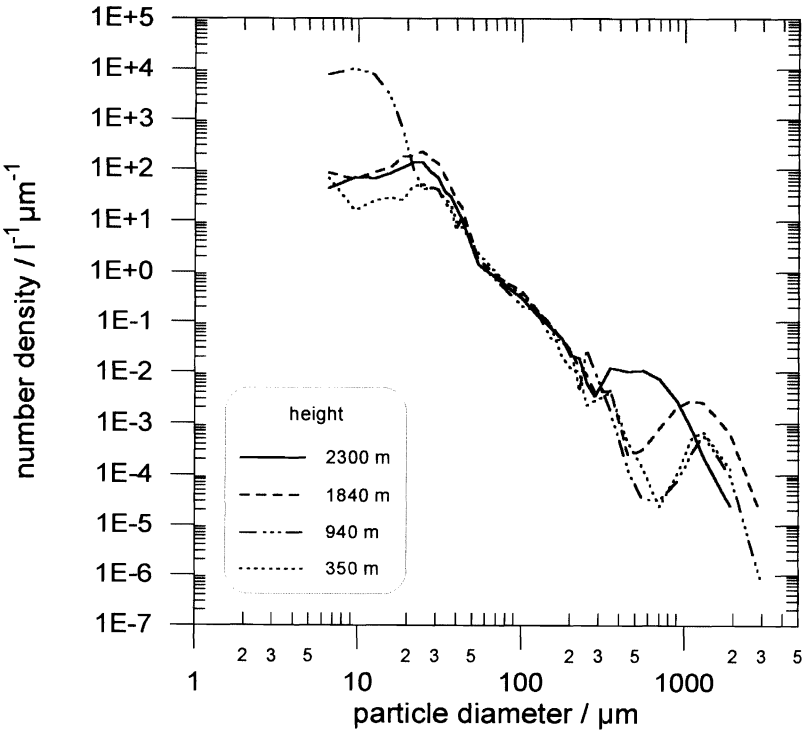

Figure 3.29: *Particle size spectra for profile P7 on 18 April 1999 at different altitudes.*

Figure 3.29 shows particle size spectra, combined on the basis of all three PMS probes and thus covering the size range from 5 µm to 6.4 mm. It can be seen that the precipitation particles (larger than 200 µm) present at 2300 m are growing while falling down to about 900 m. Below, no additional growth is observed. Caused by the comparatively low values for the relative humidity between about 1500 m and 1000 m (see Fig. 3.27), some of the precipitation particles are sublimating. This is reasonable since the fall velocity of those irregular formed particles is in the order 1.0 m/s (Pruppacher and Klett, 1997). Therefore, these particles need about 9 min to pass through this dry layer. Little variation in the size spectra can be noted in the embryonic drizzle particle size range between 50 µm and 200 µm. Here, a constant exponential decrease of the number density with particle diameter has been measured. The noticeable variation in the cloud particle size range below 50 µm is mainly determined by what a human observer usually labels a "cloud" since the high number densities of these small particles inside clouds (e.g. at 940 m) cause the extinction of the solar radiation and therefore an observable "cloud".

The definition of cloud boundaries on the basis of microphysical data is non-trivial when precipitation particles are present. As mentioned above, precipitation particles (per definition) settle from the height of their origin down to the surface. This leads to non-zero values for the total water content TWC (liquid water content plus ice water content) even in layers where no cloud particles are present. Hobbs and Ragno (1998) introduced different microphysical definitions of a cloud depending on the concentrations of cloud particles (smaller than 50 µm) and precipitation particles (larger than 100 µm in their publication). Figure 3.30 gives the total particle concentration for profile P7. When applying the most liberal cloud definition of Hobbs and Ragno (1998), the

entire layer between the surface and the top of P7 is one continuous cloud since the concentration of precipitation particles alone meets the definition. More frequently, however, the presence of cloud particles is required to define a cloud. Applying the corresponding criterion results in three cloud layers for P7, stretching from the surface to 300 m, from 600 m to 1300 m and from 1500 m to the top of P7.

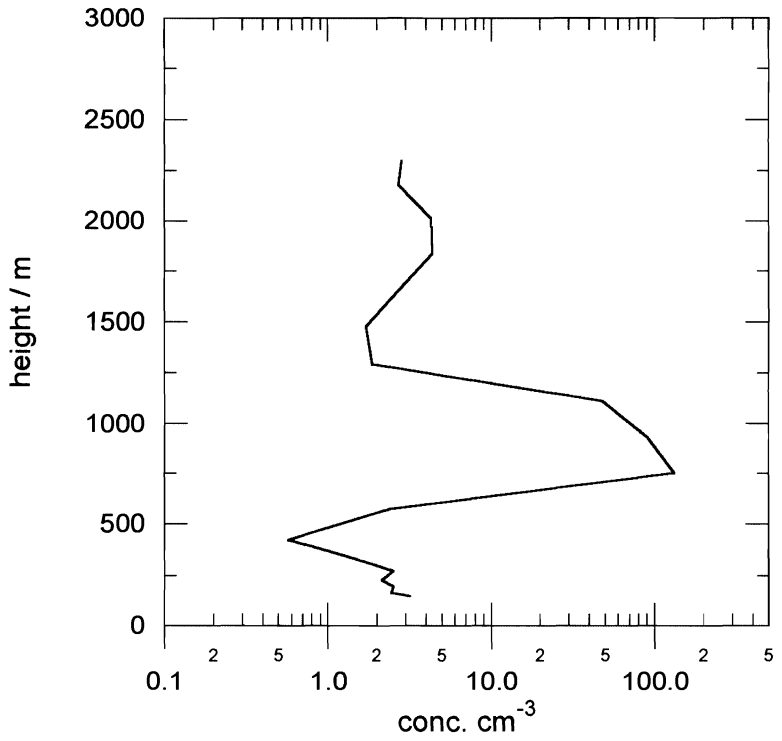

Figure 3.30: *Vertical profile of the total particle concentration for profile P7 18 on April 1999.*

Due to the occurrence of precipitation particles, the effective diameter D_{eff} (third moment of the size distribution divided by the second moment) reaches comparatively high values up to 960 µm (Fig. 3.31). It shows that in regions where significant concentrations of cloud particles are present (e.g. 600 m to 1000 m), these small particles cause an immense decrease of the effective diameter (down to 60 µm). Values for the average diameter D_{av} (first moment of the size distribution divided by the zero moment) are between 10 µm and 25 µm.

The derived TWC values also strongly reflect the presence of precipitation particles since they provide between 55% and 95% of the TWC on P7 as shown in Fig 3.32. To enable the identification of other microphysical processes in the data, additional TWC sub-ranges had been defined. Beside the total TWC (suffix "total") which denotes the integration of the TWC over the complete particle spectrum, a cloud TWC (suffix "cloud") for particles smaller than 50 µm and a precipitation TWC (suffix "precip.") for particles larger than 500 µm had been defined. For $TWC_{precip.}$ in Fig. 3.32, the sublimation of particles between 1000 m and 1500 m can be seen while the trend of TWC_{cloud} corresponds to the cloud definitions mentioned above. In the two cloud layers with bases at 600 m and 1500 m, TWC_{cloud} exhibits an increase with height in the lower two third of the cloud and a decrease near cloud top.

In this section it has been shown that the probe configuration applied during the FRAMZY flights was suited to characterize the microphysical properties of the cloud fields associated with cyclones in the Fram Strait during wintertime. The pronounced spatial and temporal variability of these systems, however, makes it difficult to assess the representativeness of the measured vertical profiles. Table 3.4 summarizes the properties of profile P7 as an example.

Table 3.4: Summary of microphysical properties of the 3-layer cloud system on 18 April 1999 as encountered on profile P7.

height / m	conc / cm^{-3}	D_{av} / μm	D_{eff} / μm	TWC_{tot} / $g\ m^{-3}$	$TWC_{prec.}$ / $g\ m^{-3}$	TWC_{cloud} / $g\ m^{-3}$
<150 - 300	2 - 3	23 - 25	354 - 446	0.28 - 0.45	0.21 - 0.36	0.02 - 0.02
600 - 1300	2 - 130	9 - 17	57 - 886	0.26 - 0.40	0.15 - 0.38	0.01 - 0.09
1500 - >2300	3 - 4	22 - 26	443 - 978	0.56 - 1.96	0.42 - 1.86	0.02 - 0.04

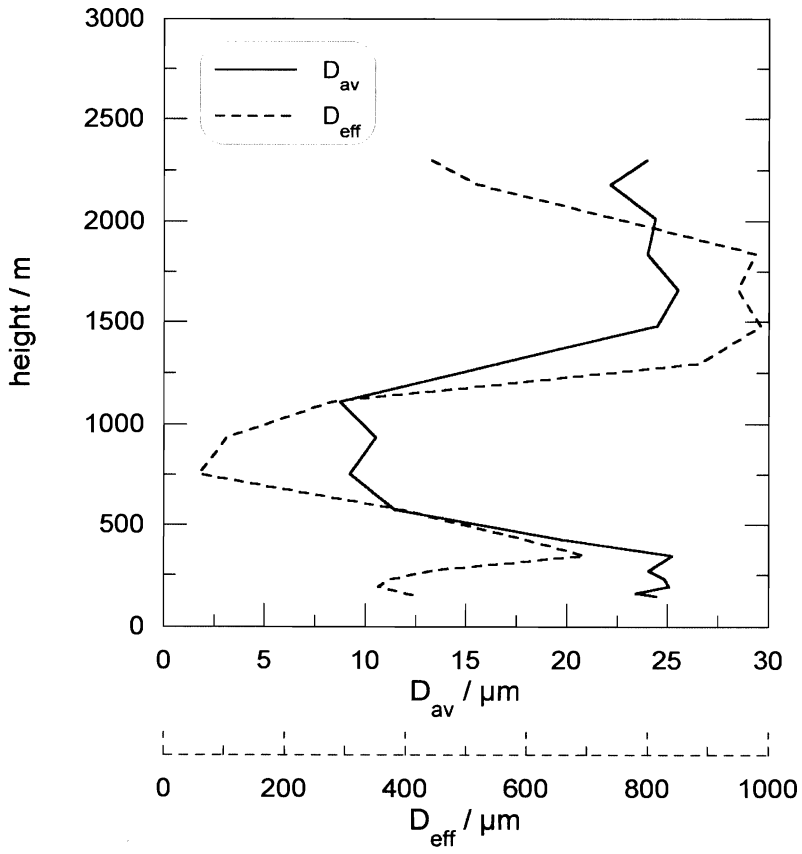

Figure 3.31: *Vertical profile of the average diameter D_{av} and the effective diameter D_{eff} for profile P7 on 18 April 1999.*

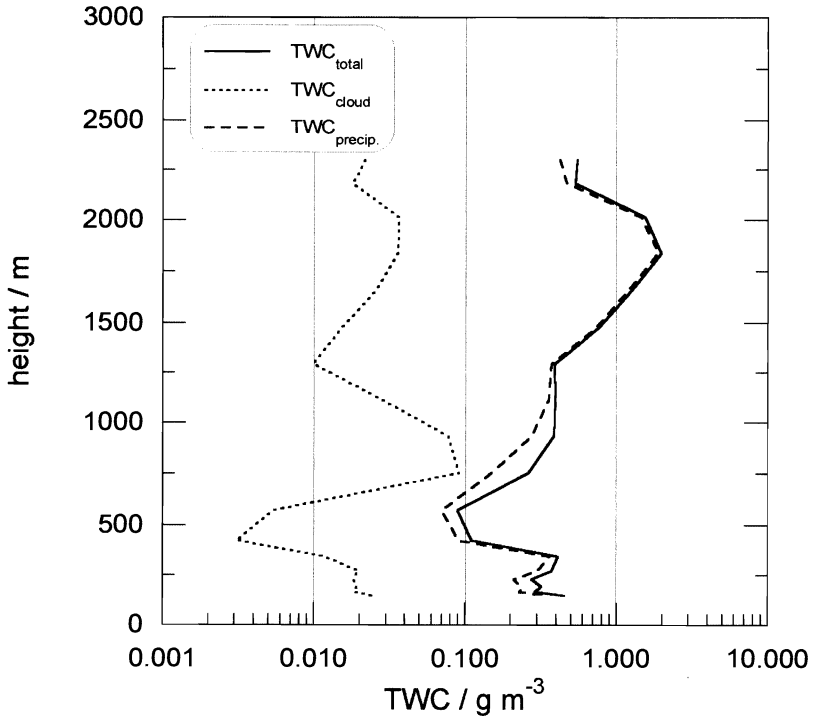

Figure 3.32: *Vertical profiles of different TWC ranges for profile P7 on 18 April 1999.*

References

Brümmer, B. (ed.), 1993: ARKTIS 1993: Report of the Field Phase with Examples of Measurements. *Berichte aus dem Zentrum für Meeres- und Klimaforschung, Reihe A: Metorologie, Universität Hamburg,* **11**, 186 pp.

Hartmann J., A. Bochert, D. Freese, C. Kottmeier, D. Nagel and A. Reuter, 1997: Radiation and Eddy Flux Experiment 1995 (REFLEX III). *Berichte zur Polarforschung*, **218**, 74 pp.

Hobbs, P.V. and A.L. Ragno, 1998: Microstructures of low and middle-level clouds over the Beaufort Sea. *Quart. J. R. Met. Soc.*, **124**, 2035-2072.

Korolev, A.V., J.W. Strapp and G.A. Isaac, 1998: The Nevzorov airborne hot wire LWC/TWC probe: Principle of operation and performance characteristics, *J. Atmos. Oceanic Technol.*, in press.

Pruppacher, H.R. and J.D. Klett, 1997: Microphysics of clouds and precipitation, *Kluwer Academic Publishers, Dodrecht, Netherlands.* 954 pp.

Reuter, A. and S. Bakan, 1998: Improvements of cloud particle sizing with a 2D-Grey Probe, *J. Atmos. Oceanic Technol.*, **15**, 1197-1204.

4. Ice buoy array

(Heinrich Hoeber, Meteorological Institute, University of Hamburg)

4.1 Instrumentation, intercomparison and data flow

According to the scientific objectives, the task of the ice drifter array was essentially twofold: (a) to measure the ice drift velocity and its horizontal derivatives on scales between 50 and 200 km, and (b) to measure the surface air pressure and its gradient. The platform chosen for this purpose was the CALIB ice beacon of METOCEAN Data Systems, Ltd, Dartmouth, Canada.

The CALIB ice beacon is housed in a plastic cylinder of 12 cm diameter and 92 cm height, and weighs 8.2 kilograms. Its main parts are the Argos transmitter including the transmitter's antenna, the power supply (batteries), a so-called ice temperature sensor, an optional barometric pressure sensor and a parachute allowing the beacon to be launched from an aircraft. 15 beacons were purchased, six of which were equipped with pressure sensors. Alkaline batteries were chosen which have an estimated lifetime of at least three months.

The **pressure sensor** was a Setra 276 barometric pressure sensor which is advertised with a system accuracy of ±1 hPa and a sensor accuracy of ±0.3 hPa. An intercomparison period of three and a half days - from 30 March to 3 April 1999 - at the airport of Longyearbyen, Svalbard, was scheduled prior to the deployment. Air pressure differences against the - arbitrarily chosen - station 5265 show that mean differences of between 0.1 to 1.8 hPa occurred between any two beacons of the set of six. An independent pressure instrument - a portable Vaisala sensor - was run simultaneously which was calibrated in the home institute in Hamburg against a mercury barometer before and after the field phase. Station 5265 indicated an average offset against the Vaisala sensor of +0.09 ± 0.26 hPa which was added to the differences between the sensors of the beacons. Table 4.1 shows the summed differences and their standard deviations within the intercomparison period.

Assuming that the mean differences remain constant during the following three weeks of the Framzy experiment, they can be (and will be) accounted for in the time series, and only the deviations from the mean remain as the error of the observations. The standard deviations of the mean range from ±0.13 to ±0.19 hPa for the six beacons and during the three and a half day period; this is within the limits of the assumed sensor accuracy given by the manufacturer.

Table 4.1: Pressure differences during the intercomparison period against Vaisala pressure sensor, which is calibrated against a mercury barometer in Met. Inst. Hamburg

Argos ID	5264	5265	5272	5273	5274	5286
Deployed as	# 3	# 1	# 5	# 4	# 2	# 6
Failure			X			X
Δp	0,7	0,09	0,64	0,45	1,12	1,94
$\sigma_{\Delta p}$	±0.13	--	±0.16	±0.15	±0.19	±0.17
N	91	--	81	82	96	90

The **position** is measured by the Argos system which applies a Doppler shift method using the frequency shift of the data transmitter frequency as observed by the overpassing satellite. Position was monitored during the intercomparison period when all beacons were assembled stationary at one point on Longyearbyen airport. The overall standard deviation of the latitude and longitude data are given in Table 4.2. The error is relatively large when all data of the intercomparison period are lumped together, but is about halved when class 3 data are considered separately, i.e. the data with the optimum signal conditions, as decided by the Argos system. The data will be processed by interpolation of the raw position data onto every full hour and taking overlapping two-hour increments, divided by time, as drift velocity of the ice. Since this procedure involves a certain smoothing, the error after interpolation as given in the last two lines of the Table is reduced by a factor of about 0.7 compared to the first two lines.

Table 4.2: Error (standard deviation of the mean) of location determination

	Degree	**Metres**
Latitude, all Argos classes	±0.0033	±366
Longitude, all Argos classes	±0.0193	±445
Latitude, class 3 only	±0.0016	±178
Longitude, class 3 only	±0.0102	±235
Latitude, after interpolation, all classes	±0.0022	±245
Longitude, after interpolation, all classes	±0.0147	±340

In view of the interpolation procedure of the position data, it is crucial that sufficiently dense location determinations, i. e., satellite overpasses with good signal quality, are available. The statistics are shown in Table 4.3. Omitting two stations which developed technical problems, it turned out that, with two satellites available, the average number of locations per day was about 22, ranging from 20 to 25. With an average of 0.9 per hour, the procedure of interpolating onto every hour appears to be justified. The transmission of data occurs more often than the location (since the signal quality for data transmission can be less than optimum) implying that hourly interpolation of the pressure data is also well supported by the sampling frequency.

Table 4.3: Statistics of location determination of ice beacons from 3 to 30 April 1999. Class 1 to 3 are summed. Stations 2 and 4 are omitted.

Number of stations	12	
Total number of locations	6715	
Station-Days	307	
Average Number of Locations per Day	219	
Average Number of Locations per Hour	9	
Number of Locations per Day: Winner	253	Station 6
Number of Locations per Day: Looser	203	S tation 8

4.2 Deployment of buoys

To launch the beacons, a DO228 was chartered from Lufttransport A/S, Svalbard. The launch of all beacons was due on one mission. Prior to the mission, the normal passenger door of the aircraft was replaced by a sliding door facilitating the drops. The mission was flown on Saturday, 3 April 1999, from 12 to 17.30 local time. Responsible engineer was Rudolf Kapp of the Meteorological Institute, U. of Hamburg.

The array of the 15 beacons was designed as a regular pentagon with air pressure stations at each corner and at the centre point; the rest of the beacons was to fill the gaps between the pressure stations, covering scales down to 50 km. The basic size of the array, i.e., the distance from the centre to each corner was chosen to be 110 km. In view of the ice conditions in the Fram Strait and the position of the ice margin towards the east, in particular, the centre point was fixed at 81 N/ 4 W, but allowance was made for a 50 km displacement from direction 20 deg during the 3 days between deployment and the start of the experiment; i.e., the respective upstream displacement of all stations was computed to give the nominal drop positions.

This planning was made possible only through the information on the ice situation which is provided in the Internet, in particular: www.natice.noaa.gov (the National Ice Centre of NOAA) and www.dcrs.dtu.dk/DCRS/latest-ice.html (the Danish Centre for Remote Sensing). Their efforts are gratefully acknowledged.

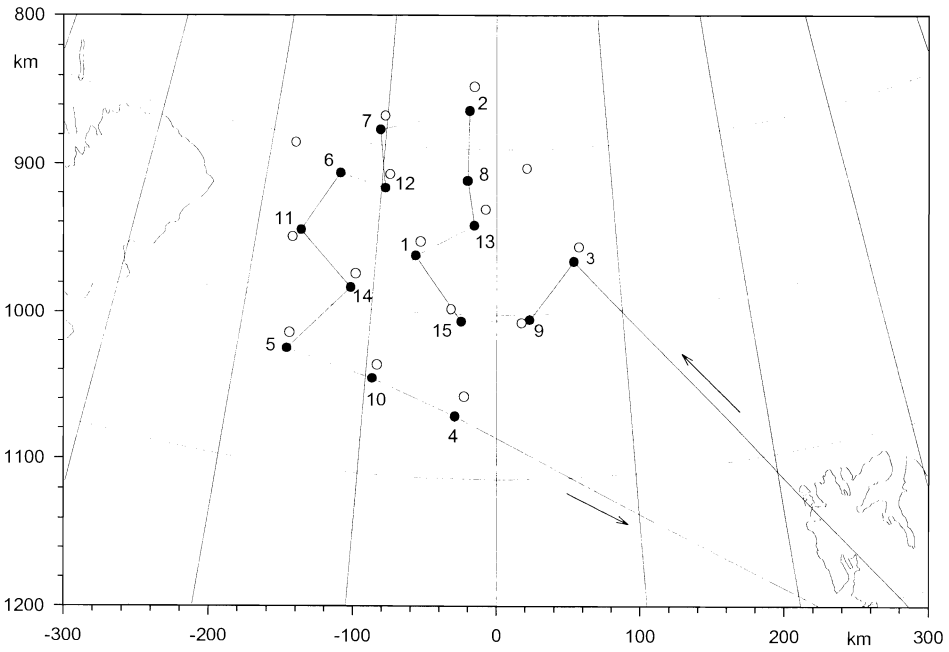

Fig. 4.1: *Track of DO228 deploying ice beacons on 3 April 1999. Open circles are nominal positions of the 15 beacons, full circles are actual launch positions.*

Fig. 4.1 shows the flight pattern during deployment. The open circles were the scheduled positions, i.e. the regular pentagon with a regular smaller square within. The planned flight track from

Longyearbyen would have had a total length of 833 nm, i.e. well within the range of a DO228. The full circles denote the actual drop positions. Station 8 was erroneously dropped on a westerly instead of an easterly longitude. The scheduled station 6 could not be reached due to a fog bank in the west. The actual total flight distance was a little less than the scheduled.

In view of the difficult flight conditions (strong northerly winds), the air drops can altogether be called successful. However, after deployment, station 5 for unknown reasons failed to report altogether, and station 6 failed to report air pressure data, providing only its position. Thus, unfortunately, the two westernmost pressure stations are missing, and the determination of pressure gradients must rely on stations 1 to 4 plus the nearby coastal station of Greenland.

In Table 4.4, the performance of all stations in the month of April 1999 is summarized.

Table 4.4: Station Performance in April 1999.

Station	Argos ID	Launch	Launch Position	Loss	Loss Position	Remarks
1	5265	3 April	81.343N/ 3.345W			w. pressure sensor
2	5274	3 April	82.235N/ 1.233W			w. pressure sensor
3	5264	3 April	81.310N/ 3.182E	16 April	79.262N/ 3.330W	w. pressure sensor
4	5273	3 April	80.372N/ 1.550W	18 April	76.007N/ 8.508W	w. pressure sensor
5	5272	3 April	- -	3 April	- -	failure
6	5286	3 April	81.800N/ 6.822W			pressure failure
7	5335	3 April	82.090N/ 5.263W			
8	5334	3 April	81.807N/ 1.260W			
9	5287	3 April	80.968N/ 1.303E	12 April	78.678N/ 3.873W	
10	8252	3 April	80.578N/ 4.737W			
11	8250	3 April	81.423N/ 8.183W			
12	5336	3 April	81.735N/ 4.823W			
13	5333	3 April	81.533N/ 0.940W			
14	8251	3 April	81.122N/ 5.897W			
15	5332	3 April	80.8957N/1.397W			

4.3 Buoy trajectories and ice drift

Preliminary evaluation of the position and hence the drift data reveals some of the general features of ice drift in the Fram Strait. Fig. 4.2 provides the drift of the station network from 4 to 21 April in four day intervals. The general drift direction is towards the south and south-southwest, i.e., it is governed by the East Greenland Current (EGC), but modulated by the wind forcing. Speed is between 0.2 and 0.4 m/s; highest values are around 0.5 m/s in the case of stronger wind forcing

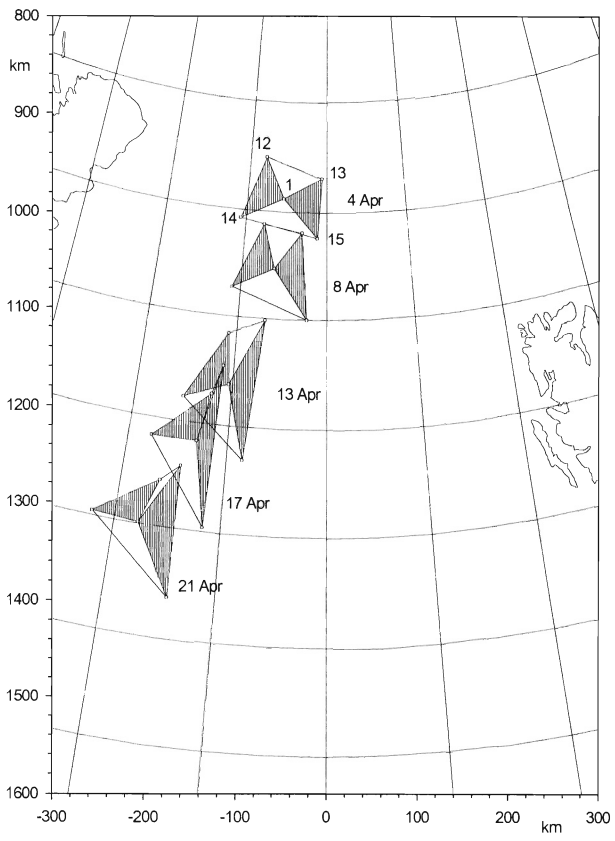

Fig. 4.2a: *Drift of small quadrilateral 12-13-14-15 with station 1 in the centre; from 4 to 21 April 1999.*

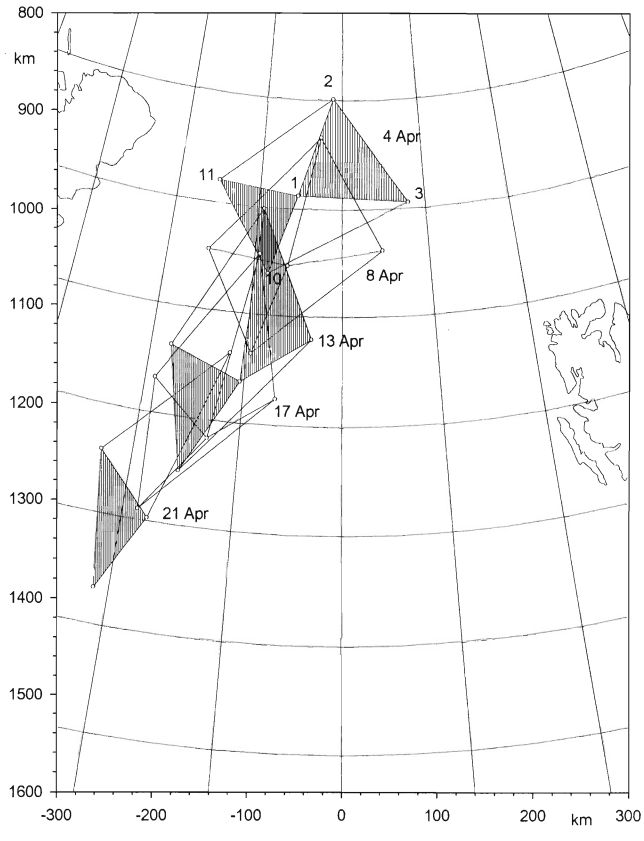

Fig. 4.2b: *Drift of large quadrilateral 2-3-10-11 with station 1 in the centre; from 4 to 21 April 1999. Station 3 is missing on 21 April. To avoid overlap, only every second figure is shaded.*

on 17/18 April.

Inspection of Fig. 4.2 (a) and (b) shows that divergence of the drift velocity is not significant on the large scale (100 km), but significant on the small scale (50 km), where convergence and divergence are observed in close proximity. Deformation as well as rotation occurs on both the large and the small scale. The opening and closing pattern of open water areas must, therefore, have been highly inhomogeneous in the area.

The most conspicuous signal in the drift velocity fields is the 12.4 hours period, most likely generated by oceanic forcing, i.e., the tidal oscillation (Fig. 4.3). It occurs at stations close to the ice margin as well as in the centre of the EGC and towards the Greenland coast. When the mean speed is small, the tidal ellipse even forces a northward motion, e.g., on 20 April. The oscillation appears as a horizontally homogeneous pattern within the scale of the array, since it cannot be detected in time series of distances between any two stations: The array oscillates as one homogeneous block. Surprisingly, this result is different from what was observed in an earlier campaign in 1991 north of Franz-Josef-Land.

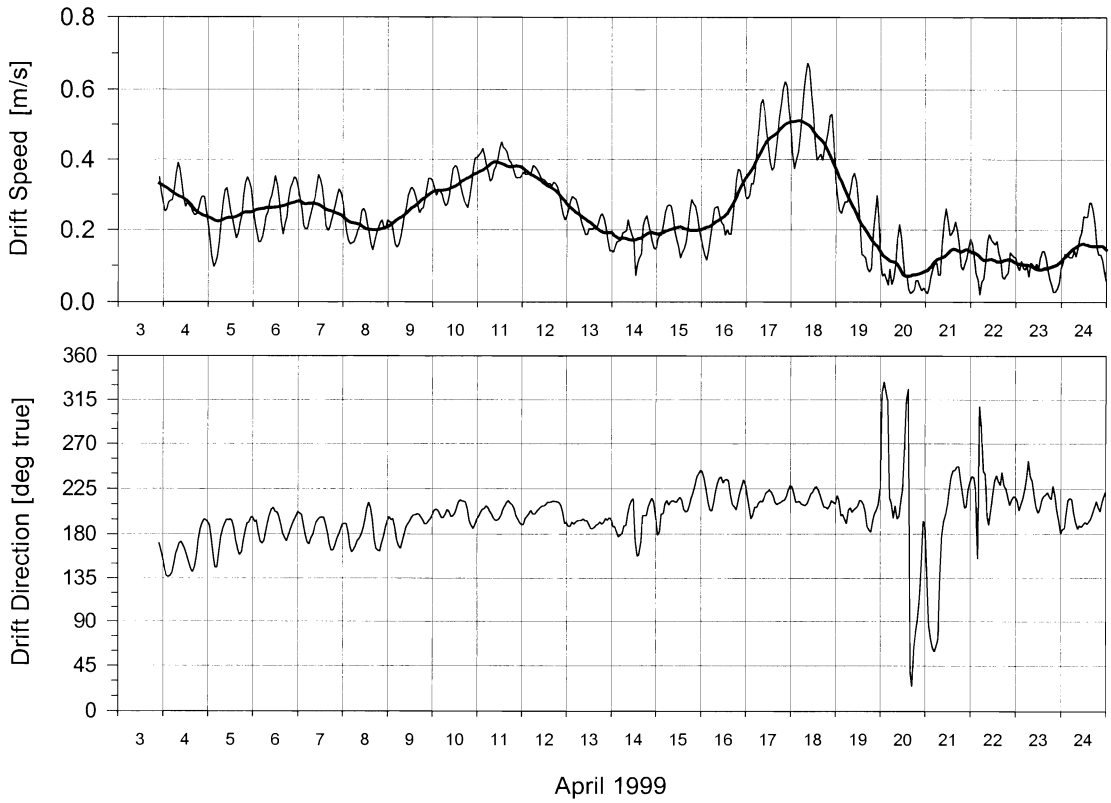

Fig. 4.3: *Example of ice drift speed (above) and direction (below) from 3 to 24 April 1999 in the Fram Strait around 80° North, measured by ice beacon No. 1. Bold line in the upper panel shows 24 hours running average. Note oscillation of lunar (semidiurnal) tidal period.*

Three of the beacons - No. 3, 9, and 4 - where installed at the eastern ice margin as close as safely possible. (In fact, these stations where among the first to be lost in the course of the campaign.) They were to support the determination of the lateral gradient of drift speed in this area. Fig. 4.4 shows the day-to-day variation of two latitudinal profiles of drift speed (see Fig. 4.1 to locate the indicated beacon numbers). At the margin, close to beacons No. 15 and No. 9, large gradients are observed (upper panel of Fig. 4.4), whereas in the central region the gradients are almost zero.The speed at the margin shows both an occasional deceleration of the drift (e.g., on 5 and 6 April) and an acceleration (e.g., on 8 and 9 April). However, this is not observed in the case of the more northerly profile including station No. 3 at the margin; here, the west-east profile of drift speed is more or less homogeneous (lower panel of Fig. 4.4). It appears that the outer fringe of the ice stream in the vicinity of station 9 is flowing under almost free drift conditions, thus reacting more readily to variations of the atmospheric forcing, whereas the central and the more northerly regions show much less variability, probably glued to the oceanic drift and consequently developing larger internal ice stress.

4.4 Time series of surface pressure

As noted in Table 4.4, surface pressure observations are available from four beacons starting

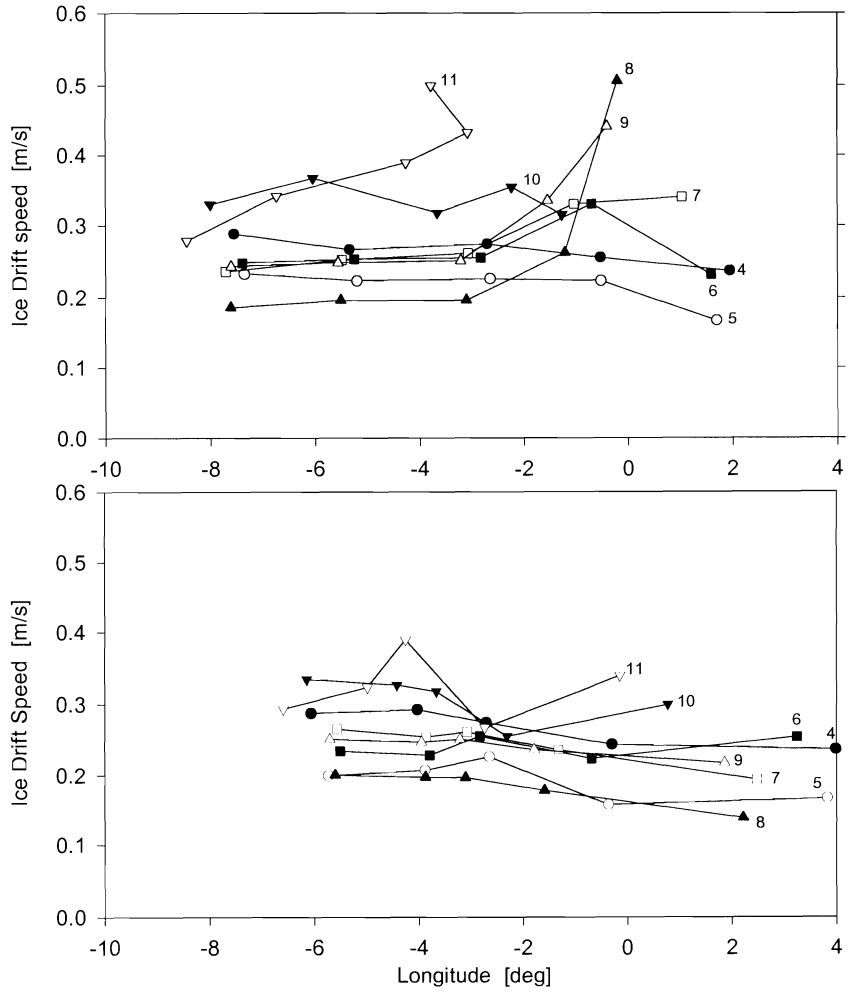

Fig. 4.4: *Daily latitudinal profiles of mean ice drift speed across the beacon array from 4 to 11 April 1999. Stations are from west to east: Nos. 11 - 14 - 1 - 15 - 9 (upper panel) and 6 - 12 - 1 - 13 - 3 (lower panel). Small numbers to the right of each profile indicate the date in April 1999.*

immediately after deployment around noon of 3 April. Loss of the first station - beacon No. 3 - occured in the night of 16/17 April; the second station - beacon No. 4 - was lost at noon of 18 April. Beacon No. 2 developed an unidentified problem; its pressure series shows gaps up to 24 hours starting on 16 April.

As illustrated in Fig. 4.5, the pressure variations during the campaign were moderate; the surface pressure varied from a maximum of 1038 hPa on 16 April to a minimum of 1003 hPa on 21 April. During most days of the period, the highest pressure is observed at the northern station No. 2, indicating a prevailing easterly component of the geostrophic wind. The most rapid pressure change occurred on 16/17 April in connection with the approach of a low pressure system which passed the array during the early hours of 18 April. With respect to the scientific objectives of the experiment, this low is considered to be the most interesting feature: see also sections 2 and 3. However, with a minimum pressure of 1006 hPa, the system is not particularly intense; the minimum pressure is higher than both the minima of 10 April and of 21 April. The lowest pressure occured at beacon 4 - the southernmost station -, and the north-south presssure gradient between

beacons 1 and 4 corresponds to a geostrophic wind component from the east of 8.0 m/s.

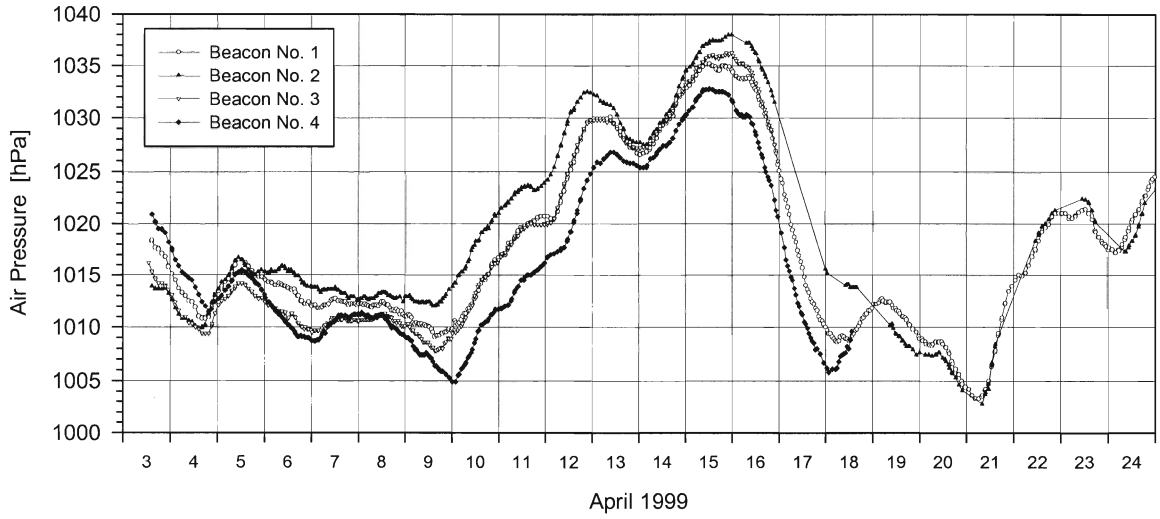

Fig. 4.5: *Time series of surface air pressure of the four ice beacons No. 1 to 4 (see Fig. 4.1 for station idenfication). Data are corrected using intercalibration results provided in Table 4.1.*

5. Research vessel Valdivia

(Gottfried Kruspe, Max-Planck-Institute for Meteorology, Hamburg)

5.1 Strategy and cruise

The cruise V178 of RV Valdivia from 8 April, 20.30 UT (leaving the port of Thorshavn, Faroer Islands) until 26 April, 15 UT (reaching port of Reykjavik, Iceland) was undertaken jointly by the Meteorologisches Institut (MI) of the University of Hamburg and the Institut für Meereskunde (IfM) under the guidance Dr. J. Backhaus (IfM). The meteorological research program on board was an integral part of the FRAMZY 1999 experiment, whose main field activities were centered more than 500 km north of from RV Valdivia's cruise. RV Valdivia represented the only marine platform for aerological soundings within the Greenland Sea during that time. The meteorological measurements encompassed upper air soundings, standard shipborne measurements (continuously recorded standard surface layer parameters), radiation measurements, cloud base measurements up to 7.5 km and measurements of the equivalent blackbody radiation temperature of the sea surface in combination with a two components ships inclination measuring set-up (see Table 5.1). A rain-radar was also installed on board, but the absence of measurable rain amounts impeded its application.

The IfM as the leading part of the interdisciplinary cruise was investigating oceanic convection and near surface water mass properties including phytoplankton. Continuous measurements of CO_2-concentrations in the surface layers of atmosphere and ocean were performed on board by the National Laboratory in Risø, Denmark.

The actual course of the cruise and thus the location of the aerological soundings between 61.5°N, 12°W and 75.4°N, 3°E (see Figure 5.1) pursued an already elaborated plan of IfM to recover formerly deployed moorings, to deploy new moorings and to cover 57 CTD- stations, several combined with calibration samples taken from CTD rosette sampler and biological stations. Afterall, the execution of the intended work was hampered at times by bad weather conditions (strong winds, heavy sea, frozen ship's deck), particulary the aerological schedule, which comprised four soundings per day (00, 06, 12, 18 UT), but eight per day (00, 03, 06, 09, 12, 15, 18, 21 UT) in cases when cyclone activity dominated in the region of the Fram Strait. Time series of position, heading, speed and apparent wind vector (Fig 5.3 line 1-4) exemplify at best the active nautical maneuvers during the cruise, also periods of steaming and of being on station. The actual widespread cruise is far appart from an optimal meteorological measuring strategy,- namely inspecting passing synoptic systems from a nearly fixed position, here proposed at 75°N, 5°W.

Dominant weather with respect to RV Valdivia's track:

8 April -12 April: RV Valdivia operated outside the polar circle, confronted with cyclone activity from successively eastwards moving lows and their fronts.

On 12 April, RV Valdivia reached first time a position in the polar circle between 67°-69°N and 8°-12°W and entered into a strong northeasterly large-scale flow, which was maintained in

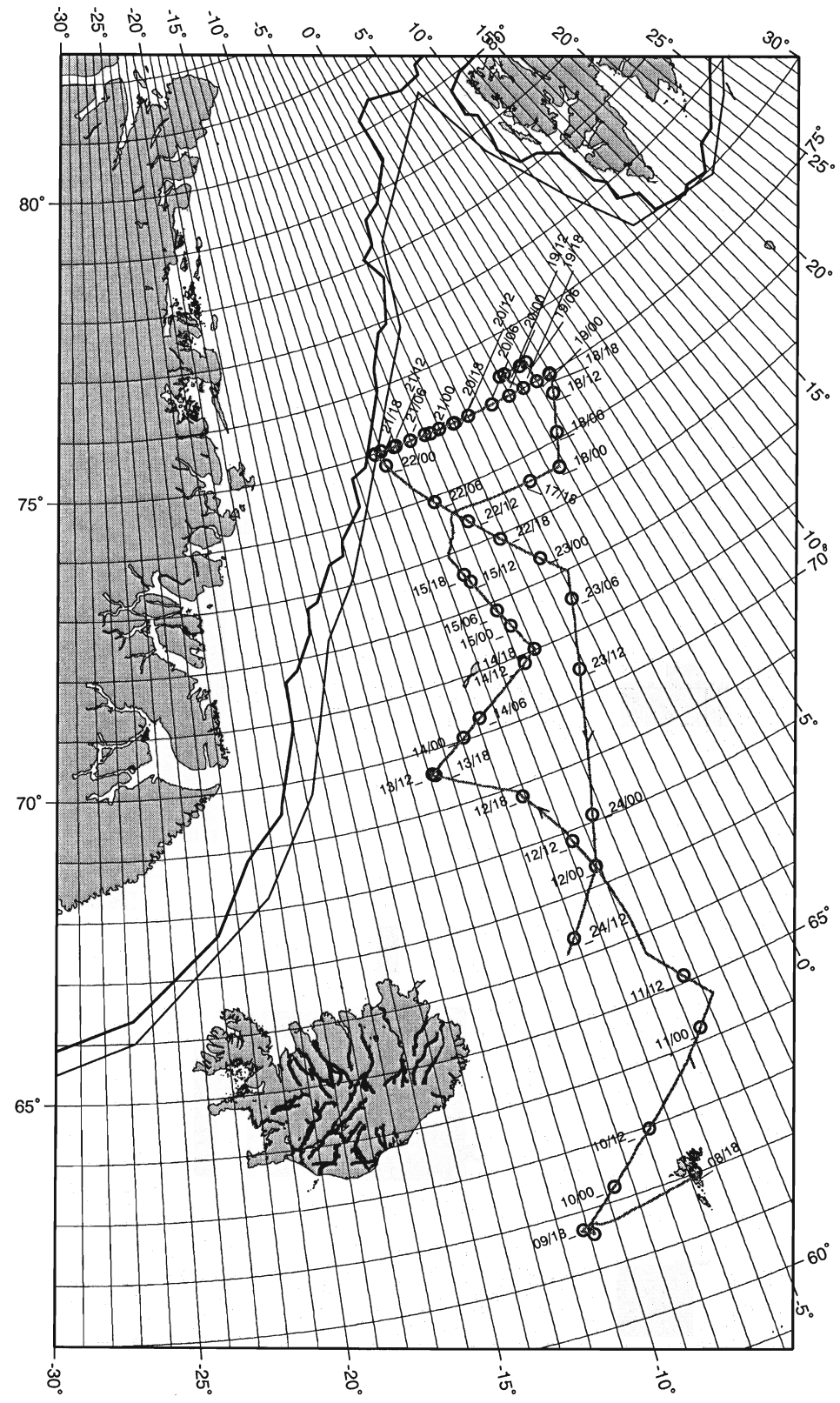

Figure 5.1: *Cruise of RV Valdivia during FRAMZY 1999 (#V178). Circles: position of aerological profiles. Soundings on 00, 06, 12, 18 UT were labelled by day/hour along the ship track. Ice boundaries for 22 April 1999 (from DNMI) for > 80 % coverage (thick curve) and between 10 and 30 % coverage (thin curve).*

the south by two distinct lows with cores over the middle North sea (po ~ 985 hPa) and central Russia (po ~ 980 hPa) and by a high pressure system between middle Greenland and the East Siberian Sea (po ~1015 hPa).

On 13 April, RV Valdivia operated stationary near 69.5°N and 12°W within the cold air flow on the rear side of the low with core over Scandinavia. A high-pressure ridge expanded from East Greenland into the Greenland Sea.

On 14 April, RV Valdivia was exposed to a pronounced cold air flow at positions between 70°N, 10°W and 72°N, 5°W, originating from a low with core over the Skagerak (po ~ 990 hPa).

15 April: RV Valdivia, heading further northwards (71.5°N - 73°N, 6°-7°W), operated within the northerly margin of a northeasterly cyclonic flow, which was maintained by a large cyclonic system south of the line Iceland-North Cape including low pressure centers over South Sweden (po ~ 990 hPa), the Norwegian Sea (po ~ 990 hPa) and south of Iceland (po ~ 1010 hPa) and an anticyclonic system north of the line Denmark Strait - Svalbård.

16 April: RV Valdivia kept position at 73°N , 4°W, undergoing the direct influence of a low, whose core was situated west of the Lofotes Islands (po ~ 990 hPa).

On 17 April, at the mean position of 74°N, 5°W, RV Valdivia was influenced synoptically by the rearside air of the occluded and spilling (5 hPa) low with its core, now southwest of Spitsbergen, heading into the Fram Strait.

18 April: The route of RV Valdivia between 73.5°N , 1°E to 75°N, 3°E led close to the center of the Fram Strait cyclone from the day before, which weakened to about 1005 hPa in its core.

19 April: RV Valdivia reached her northernmost position (75.4°N) and steamed from east to west within a transient zone between high pressure system with its core northeast of Iceland (po ~ 1010h Pa) and a cyclonic system of the same surface pressure with its core southeast of Spitsbergen, experiencing thus cold westerly off- ice winds.

20 April: RV Valdivia continued her westward course along 75°N and operated synoptically in the middle of the line between a low (po~1000hPa) north of Spitsbergen and a high (po~ 1020hPa) east of Jan Mayen.

21 April: Further westward course of RV Valdivia under similar synoptic conditions, i.e. weak horizontal pressure gradients.

22 April: RV Valdivia was cruising southeastwards, experiencing weak cyclonic weather conditions with weak winds from west.

23 April: RV Valdivia's southward track (72.5° - 68°N) along 3° - 5°W was synoptically escorted by a weak high pressure ridge, extending from Middle Greenland into the Greenland Sea.

24.April: RV Valdivia left the polar circle on this day at noon, under synoptic conditions of weak cyclonic influence, accompanied with advection of warm North Atlantic air masses.

General remarks:

As pointed out in Backhaus (1999, Report of Valdivia Cruise 178), "the conditions in the Greenland Sea during V178 were unusual, in that no drifting pancake ice was met. The intermediate trend of increasing temperature and salinity within the uppermost layers of the ocean continued."

The scientific crew involved in the meteorological research program consisted of 4 members, namely Stephan Henne (cand. rer. nat), Volker Jost (postgraduate), Dr. G. Kruspe (heading the FRAMZY-crew on board), and Michael Offermann (technician). They went on board in Tornshavn (Faroer Islands) on 8 April, ten hours before leaving, to activate the instruments, which were mounted weeks earlier in Hamburg. The ship's crew kept highly motivated all time regardless of the often very rough sea conditions. The routine programs were supported by the professional help of Captain Klaaßen and his excellent crew and, if necessary, encouraged by J. Backhaus (cruise leader in charge) and his friendly and cooperative team.

5.2 Surface measurements

5.2.1 Instrumentation

Details of the relevant instrumentation on board are summarized in Table 5.1. The most important meteorological *standard data*, namely static air pressure (P), air temperature (Ta), relative humidity (RH), apparent wind speed (ffr) and wind direction (ddr) were gained on the foredeck mast with aid of the Vaisala MILOS system of the Deutscher Wetterdienst (DWD). The temperature and humidity sensors were forced ventilated by the apparent wind. MILOS data were controlled daily with a handheld, electrically ventilated aspiration psychrometer and an anemometer. MILOS data and radiation data were displayed on-line with the aid of a modified MINERVA software of the Fa. Oesau. Near surface *water temperatures* (SST:Tw1, Tw2) were measured continuously on a stem at the ship's bow 2 m below the sea surface and midship in a special hydrographic shaft 6 m below the water surface using a thermosalinograph of the Bundesanstalt für Seeschiffahrt at Hamburg (BSH) measuring as well conductivity for salinity (SSS) calculation. The data of water temperature are crucial for later bulk calculations of surface fluxes.

The *three sensors for radiation measurements* (global shortwave radiation, longwave sky radiation, filtered black-body radiation from the sea surface) were disposed on the compass platform about 12 m above sea level. The Eppley pyranometer was shielded from the interfering radiation of the warm ships chimney by adequately mounted plates. Various ship superstructures caused shadows on the global radiation sensor Kipp & Zonen during sun elevations less then 15°, especially if the sunshine came from port side, ship's southwest direction.

The KT19-radiation thermometer, equipped with a 10-12 µ bandpass filter, was mounted on the railing of the compass platform on the port side, looking at the surface at a nadir angle of 50°. Measurements of ship's inclination for eliminating inadequate viewing angles of the radiometer took place in the portside lab 3 m above the sea-level. The absent reference bath for regular calibration of the received radiometer signals makes their interpretation to a stiff affair.

The *ceilometer* was mounted on the bridge crane deck at 10 m height, looking vertically at a tilt angle of 0°.

Apart of episodes of minor data losses due to technical reasons and sensor maintenance (see Table 5.2.), data from all systems installed are available for the whole time of the cruise.

Table 5.1: FRAMZY 1999: relevant instrumentation on board the RV VALDIVIA

Parameter	Sensor/Instrument	Height	Averaging Time	Sampling Rate	Rms-Accuracy Resolution
Sfc-pressure	PTB-Aneroid (Vaisala-MILOS, owner DWD) reduced to NN	10 m	60 s	10 s	0.1 hPa
Apparent wind vector wind vector	Wind vane, cup anemometer calculated one-line using GPS-positions	15 m	60 s	10 s	2°; 0.1 m/s 3°; 0.3 m/s
Air temperature	PT 100; forced ventilated	15 m	60 s	10 s	0.2 K
Relative humidity	Humicap (Fa. Rotronik) forced ventilated	15 m	60 s	10 s	3 %
Sfc-radiation temp.	Heimann-KT19	12 m	a) 60 s b) 6 s	1 s	not assignable
Gobal radiation from above	Kipp & Zonen	12 m	60 s	1 s	5 W/m²
Atmosph. terrestrial back radiation	Eppley pyrgeometer	12 m	60 s	1 s	5 W/m²
Water temperature Water temperature Conductivity	PT 100 thermosalinograph "	-2 m -6 m -6 m	60 s 60 s 60 s	10 s 6 s 6 s	0.05 °K 0.05 °K 0.05% salinity
Navigation parameter speed, heading speed	GPS-system: Anschütz-compass SAGEM-Log		60 s 60 s 60 s	10 s 10 s 10 s	0.3 m/s, 1 deg 1 deg 0.5 m/s
Pitch (X)- and Roll (Y)-movements of the ship	Clinometer Model MD900-T Applied Geomechanics Angular range ± 25 deg	3 m	1 s	1 s	0.03 deg

Upper air: pressure, temperature, relative humidity wind vector	DIGI-CORA (Vaisala) RS80-15G Radiosonde with GPS-module, carried by He-inflated 100 g ballons	Launch: 3 rsp.10 m	2 s	2 s 2 s	0.3, 0.2, 5% 1 m/s
Cloud base	Ceilometer CTK25 (Vaisala) λ = 905 nm	10	15 s	5.57 kHz	15 m
Rain radar	Type MRR1 Metek	5			

Table 5.2: Times of data loss caused by system breakdown or maintenance during 9-24 April.

SFC-data (Minerva)	Radiation sensors	KT19	Ceilometer
system errors: 10 April 14:12-14:20 UT 14:47-14:57 15:38-15:40 15:59-16:01 11 18:40-18:43 12 09:55-09:58 17 11:16-11:18 *GPS-failure, true wind read-out suspect:* 11 April 22:40 - 12 April 00:20 UT 13 April 14:55-15:05	*cleaning from salt:* 09 April 16:01-04 UT 12 09:06-10 13 09:07-10 14 08:19-21 20 07:20-30 *systems cleaned from snow:* 12 April 14:10-15 *ship navigates circles, to determine effects of shadowing by superstructures:* 21 April 16:25-16:40	*foil cleaned:* 09 April 16:03-05 UT 14 08:21-23 20 07:25-28 *tubus freed from snow:* 18 April 08:20-35 *calibration control:* 19 April 08:40-45 *diverse tests:change of foil, change of inclination* 21 April 18:49- 21:45	*pane cleaned:* 09 April 16:05-08 UT 12 16:05-08 13 09:07-10 14 08:20-23 18 08:30-34 20 07:20-23

5.2.2 Time series of recorded parameters

All quantities specified in Table 5.1 are plotted in Figures 5.2-5.6. The data reveal widely the raw data quality such as recorded during the campaign.

Figure 5.2 shows in the first line the geographical positions of RV Valdivia during the cruise. From 12 April, 21UT on, the ship operated within the polar circle, maintaining its northernmost position at about 75°N from 18 April 12 UT to 22 April 21 UT, to launch a series of CTD soundings from east (3°E) to west (10°W), stopping about 10 nm from the ice boundary, where frequently southward drifting growlers were observed. Changing positions between 62° and 75°N (south-north distance about 1500 km) and between 3°E and 10°W effected the interpretation of temporal and weather induced changes, particularly pronounced in the plots of water temperatures and consequently air temperatures.

The *surface pressure* (P; Fig 5.2., line 2) points at the described comprehensive synoptic variability along the track of the ship. During the period, when RV Valdivia operated within the polar circle, two different weather situations with respect to wind direction occurred: The first situation was linked with partly intense northerly flow, predominantly cyclonic flow and

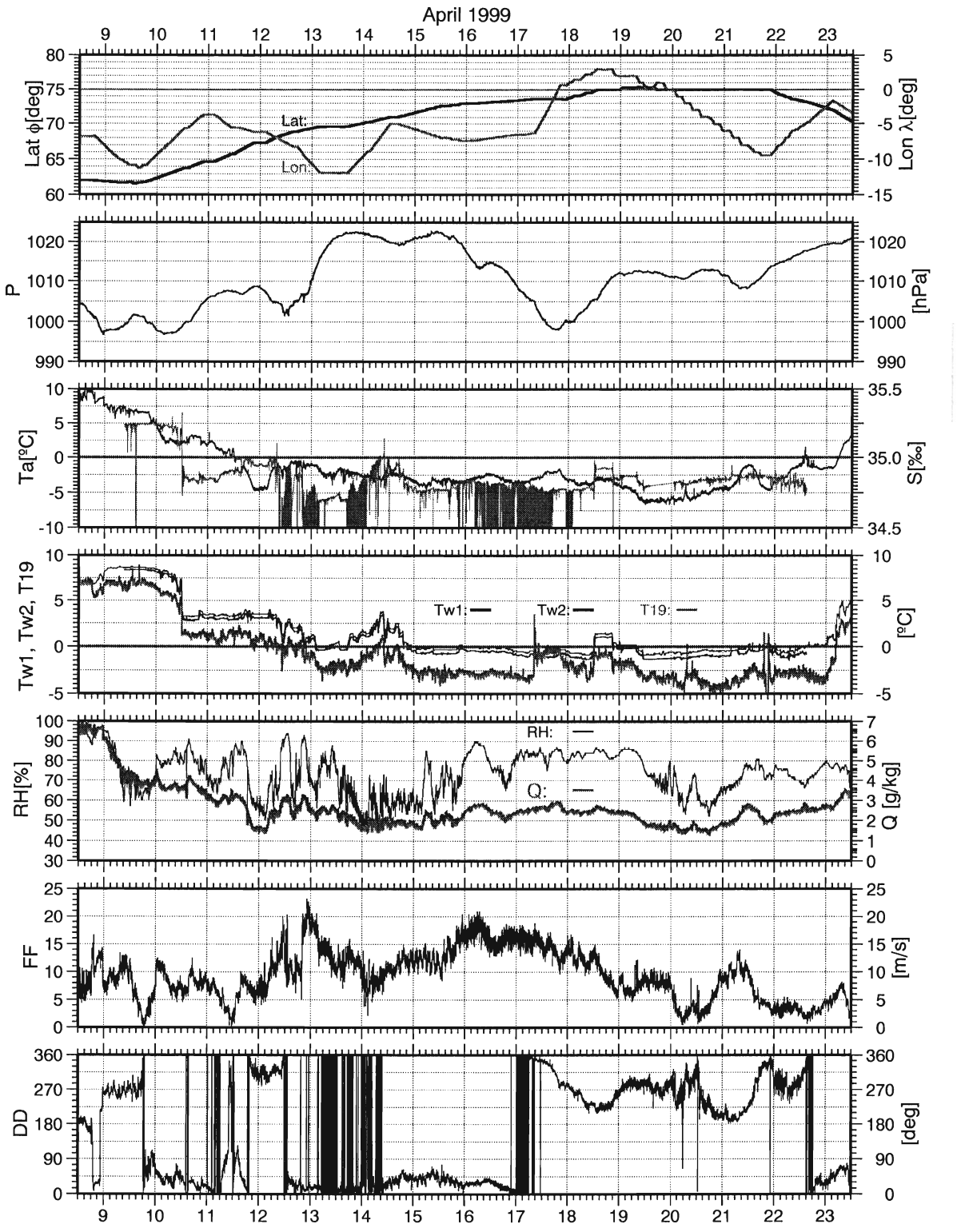

Figure 5.2: *Surface data measured at RV Valdivia: line 1: Lat, Lon: Latitude, Longitude of the cruise, line 2: P: pressure at NN, line 3: Ta: air temperature at 15 m height, S: salinity at 6 m depth, Line 4: Tw1, Tw2: water temperature at 2 m and 6 m depth, T19: temperature of KT19-radiation thermometer, line 5: RH: relative humidity from humicap at 15 m height; Q: specific humidity, calculated, line 6: FF: true wind speed at 15 m height, line 7: DD: true wind direction at 15 m height.*

changing surface pressure between 996 and 1022 hPa. Episodes of relative pressure minima were coupled with strong northerly to northeasterly winds (Fig 5.2, line 6,7). We particulary note the days of 12 April and 16, 17 April (the approach and passage of the Fram Strait cyclone (see Section 2)), when wind speeds of 15-20 m/s were registered in 15m height over longer time.

The *second situation* lasted from 18 April until mid-day of 22 April: It was characterized by rising pressure from 1000 to 1021 hPa with minor superimposed relative minima of 2-5 hPa at the surface (20 April 6UT; 21 April 9-14 UT). Moderate winds of less than 5m/s from SW to S prevailed during that time, except for the above mentioned passing cyclonic wave on 21 April, 0-12 UT, when the southerly wind increased to 10- 14 m/s.

The time series of the *water temperatures* along the track are shown in Fig 5.2, line 4. The plot contains three curves. Curve 'Tw1' represents the data from the sensor at 2m depth. This temperature is used below for estimating the vertical air-sea differences dT, dQ and the bulk fluxes in Fig 5.4, lines 1,2. 'Tw2' represents the data at 6 m depth, showing constantly 0.6 K smaller values, which probably is not based on natural stratification. It is argued,that the sensor at 2 m depth could be influenced by the warmer ship body, especially during times of working on station. Finally, the curve termed T19 represents one-minute averages of the radiation-thermometer KT19. The high-resolution output (one value per second) is plotted in Fig 5.3, line 7 together with the difference 'Tw1-Tkt19', which vary between 0.00 and 3.75K. The difference amounts quite constantly 2.5K from 14 April - 17 April and for some hours on 21-23 April. One notices times of vanishing differences (e.g. 17 April) and thereafter a gradual approach to the usual offset 2.5K, probably caused by snow in the tubus or a polluted and iced foil. The characteristic features of the Tw fine structure along the track were impressively reflected by the KT19- signals, for example the oceanic front, met on 10April, 11:51 - 11:54 UT at 63.67°N, and between 5.86 and 5.87°W, where the water temperature dropped from 4.6 to 1.6°C. The oceanic front was met again on 23 April as well. Furthermore, the episode of strong winds on 13 April and 15-17 April causing mixing of 2-3 K cooler water into the upper layers is clearly reflected from the radiometer data.

The plot of the *air temperature* (Fig 5.2, line 3) shows the decrease of temperature from 10°C to - 5°C along the track between Tornshåvn and the polar circle reached on 12 April 00 UT. The temperature minimum during this 'cyclonic' weather situtation was coupled with dry air (less than 60 % RH) and strong winds from NW. After 13 April 06 UT, temperature increased and varied only moderately around the -2.5°- value until 18 April. The coldest values along the track (-7.5°C) were reached on 19April during moderate (FF ~ 7 m/s) off-ice westerly flow. This occurred on the south side of the Fram Strait cyclone (see Section 2) which passed the latitude of RV Valdivia on 17 April at 18 UT. The passage of a small warm sector of a depression led on 21April to a temperature "wave" between -5 and -1°C. After that event, increasing temperature under anticyclonic conditions prevailed (0°C on 22 April 13 UT), reaching about +3°C on 23 April 12 UT at about 70°N, 4°W, the end of the meteorological programme during cruise V178.

The *humidity data* are shown in Fig 5.2, line 5 (relative humidity RH measured, specific humidity Q calculated). Q varied between 1.5 and 3.5g/kg along the track within the polar circle. The storm episodes were associated with humidities exceeding 85%. The observed

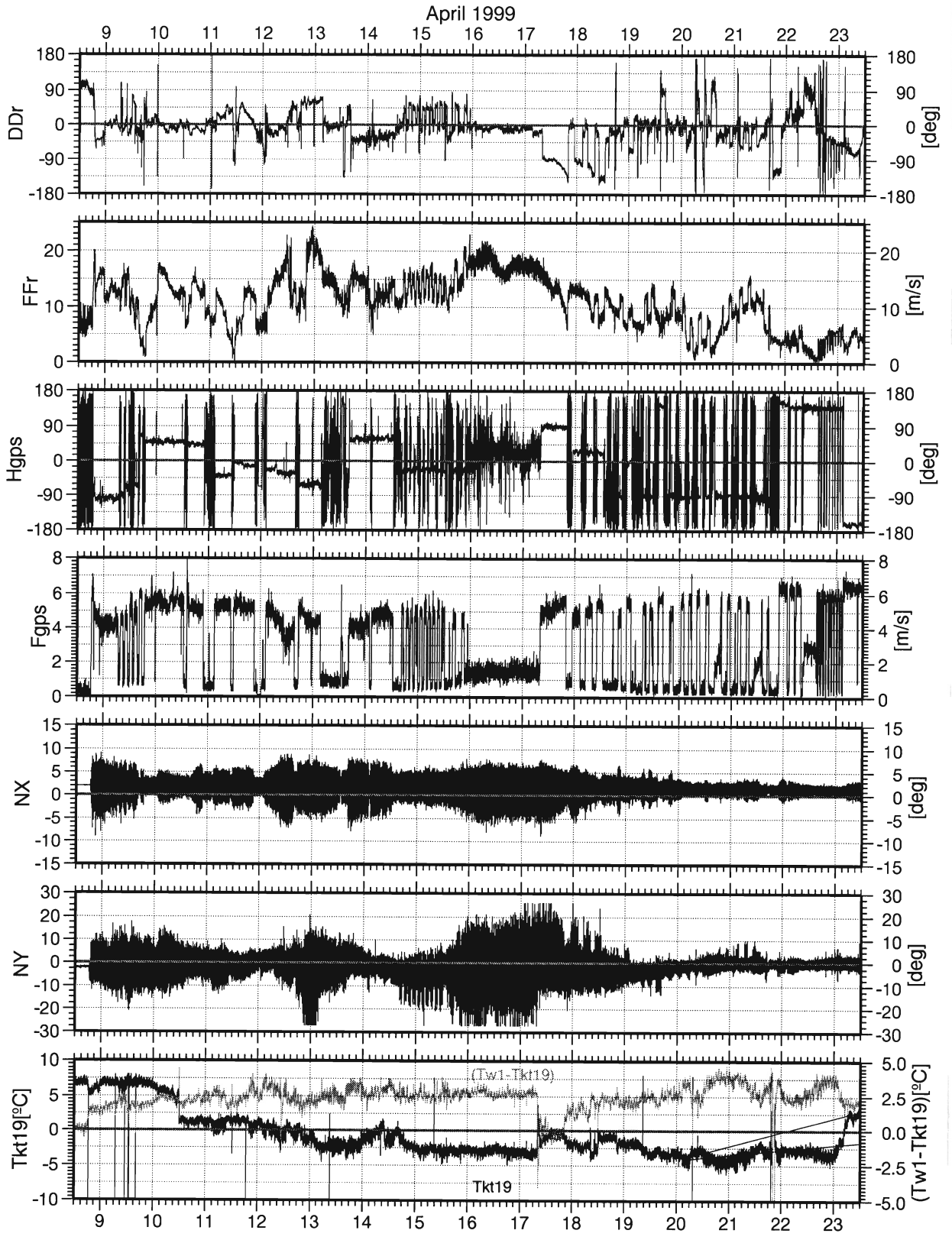

Figure 5.3: *Nautical and ship-related quantities: line 1: DDr: relative wind direction, > 0: indicates wind from starboard side, line 2: FFr: relative wind speed, line 3: Hgps: ship's heading from GPS navigation, line 4: Fgps: ship's speed from GPS navigation, line 5: NX: pitch angle, line 6: NY: roll angle, line 7: Tkt19 same as T19, but taken every 6 sec.*

weather 'ww' (Fig 5.5 line 6) indicated frequently snow fall.

Parameters, concerning *ship and cruise related data* are shown in Fig 5.3, line 1-6. The apparent wind in line 2, reveals maximal values of 25 m/s on 12 April. The curves of apparent wind direction (DDr) and speed (FFr) as well as ship's heading and speed (Hgps, Fgps) according to GPS navigation are useful informations for control of data which might be affected by the ship maneuvers, for example the ventilation of the water and air temperature and humidity sensors or ship induced waves affecting the surface skin temperature. During low ship speeds (Fgps < 1 m/s), GPS-navigation failed occasionally. Under these conditions, the 'true' windvector (FF, DD) was derived from the compass heading (Hcomp) and the apparent wind FFr according to FF=FFr and DD=Hcomp+DDr.

Ship's pitch (angle NX) and roll (angle NY) are shown in Fig 5.3 line 5,6. The storm episodes mentioned above are clearly reflected especially in the roll angle NY. Often pitch angle exceeded the instrumental limits of 25 deg. Unevenly distributed load, tractive forces during out-board oceanographic work might be responsible for the asymmetrical shape of the envelope of the inclination data recorded every second. The fine structure of the roll angle is furthermore closely related to ship speed and apparent wind direction. For future studies, inclination angles and radiation temperature were written on the same file.

Some derivated *quantities of the Prandtl-layer* are shown in Fig 5.4, lines 1-5, i.e. vertical differences of temperature and specific humidity referred to 10 m (dT_{10} = Ta (10 m) - Tw1; dQ_{10} = Q (10 m) - 0.98* Qs (Tw1)), bulk-fluxes of heat (line 2: sensible heat $H = c_p \rho c_H u_{10} dT_{10}$; latent heat $lE = -l \rho C_E u_{10} dQ_{10}$, l: heat of vaporization, E: evaporation) and momentum (line 3, $M = \rho c_D u_{10}^2$). The bulk formulas were applied with stability (z/L) - dependent transport coefficients (c_D, c_H,c_E) after Large and Pond (1981). Apart from 9 April, the air was always colder than the near surface water ; about -8 K on 12-13 April and 14 April and -6 K for a longer episode, namely on 10, 14 April and 19-20 April, were coupled with off-ice flow. The associated sensible heat fluxes were maximal 100-150 W/m^2. Concerning the latent heat fluxes, the Bowen-ratio (H/lE, line 4) is about "1" from 11 to 21April. The episodes of strongest wind and largest negative difference dT occurred not simultaneously, so that the total magnitude of the fluxes Qt = - (H + lE) became not exceptional.

The near surface *stability conditions* (line 5) were predominantly slightly unstable, except some longer periods on 10, 12, 20 April and 22April when free, windless convection occurred (z/L < -4).

Radiation measurements (downwelling global radiation Go and sky radiation Lo) are presented in Fig 5.4, line 6. Referring also to the plot of the *lower cloud base* (Cb, line 7), derived from the ceilometer set-up inherent software, we are able to discriminate different situations of cloudy boundary layers and the associated *global radiation*, which was maximal 600 W/m^2 during scattered cloud situations. The period 16-19 April, with global radiation less than 200 W/m^2 around noon was characterized by total coverage of stratiform clouds (CL = 6,7).

The *longwave sky radiation* (Lo) varies around 300 W/m^2, except for the cloudless periods on 20, 21 April, when Lo decreased to about 200 W/m^2.

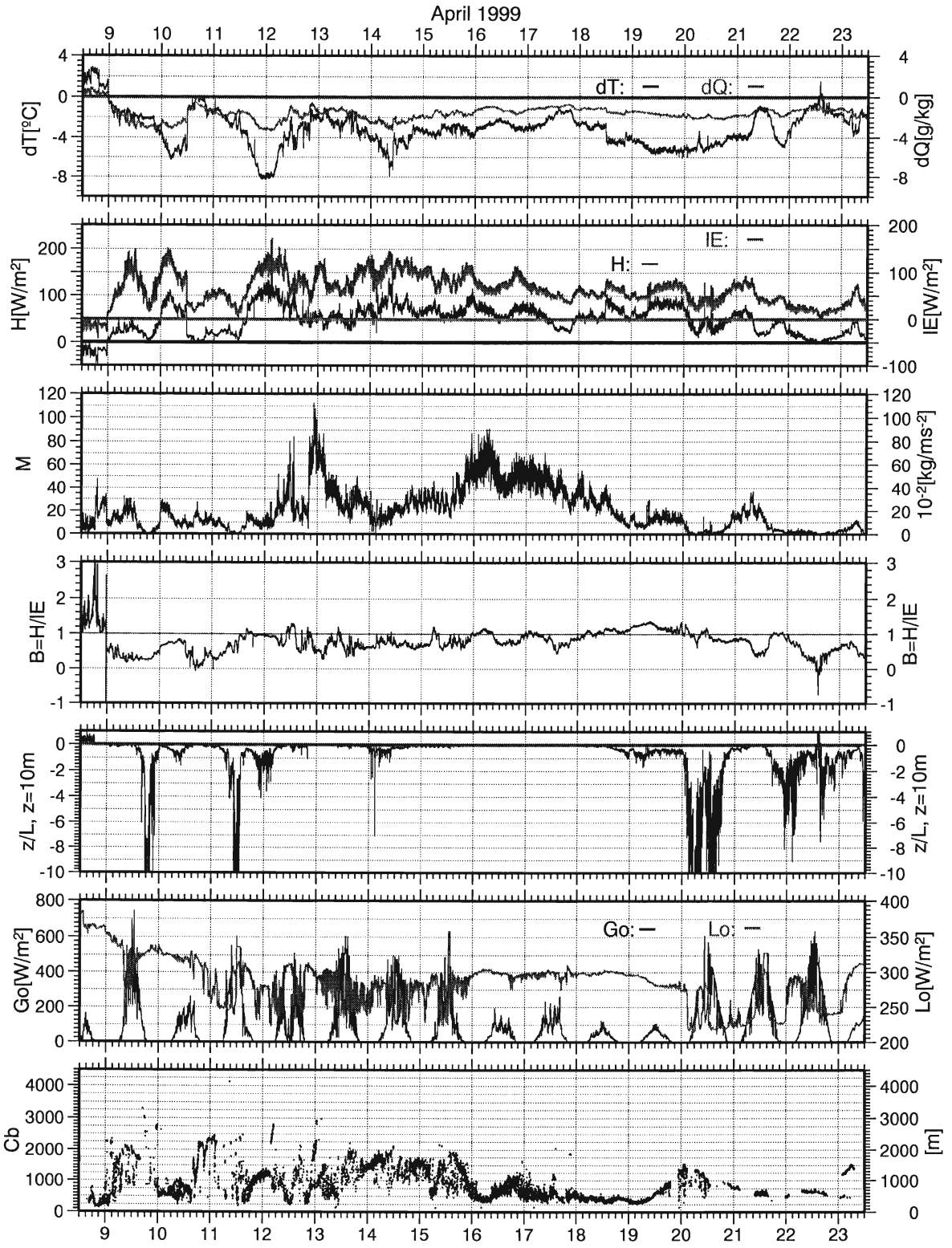

Figure 5.4: *Parameterized turbulence quantities, measured radiation and cloud base: line 1: dT, dQ: vertical differences of temperature, specific humidity between air- water with respect to 10 m, line 2: H: bulk heat flux (left ordinate); lE: bulk latent heat flux (right ordinate), line 3: M: momentum flux, line 4: B=H/lE: Bowen ratio, line 5: z/L: Monin Obuchov stability parameter, for z = 10 m, line 6: Go: downwelling global shortwave radiation, line 7: Lo: downwelling longwave radiation, line 8: Cb: lowest cloud base derived from Ceilometer.*

Time series of *energy balance* are given in Fig 5.5, lines 1-5. We define, that energy which reaches the sea-surface from above is counted positive. Thus the total turbulent heat fluxes H and lE enter with the reversed sign into the energy balance compared to the bulk formulas.

The net longwave radiation (Fig 5.5., line 1; $\Delta L = Lo - Lu$) and *net shortwave radiation* (line 2; $\Delta G = Go - Gu$) were calculated by assumptions about emissivity ($\varepsilon = 0.98$), albedo ($a = 0.06$) and a rate of reflected longwave sky radiation ($r = 0.02$) at the sea surface according to $Lu = \varepsilon \sigma Tw1^4 + r\ Lo$ (longwave radiation from the sea); $Gu = a\ Go$ (reflected shortwave radiation, Tw1 in °K).

The ocean always looses energy by *net longwave radiation* (Fig 5.5, line 1). Under situations of total low-clouds coverage (17-19 April; cloud base Cb 200-500 m; see Fig 5.4, line 7), the loss is of the order 10 W/m^2, but 100 W/m^2 if low clouds are absent. Scattered cloud situations are discernible by values which alter frequently between -10 and -100 W/m^2.

Time series of *net shortwave radiation* ($\Delta G = Go - Gu$, Fig 5.5, line 2) show the well-known daily cycle. Astronomically, the possible duration of the daylight (sun above horizon) amounts between 14 hours ($\phi = 65°N$) and 16 hours ($\phi = 75°N$).

Time series of net radiation ($Rn = \Delta G + \Delta L$; Fig 5.5, line 3) suggest radiative loss at the sea surface during night from 18 UT until 6 UT of maximal -50 W/m^2 (11-12 April, 20-21 April), depending on latitude and cloudiness. During day, the net shortwave radiation dominates the net radiation balance. Under clear-sky conditions at noon a gain of 500 W/m^2 was observed several times. Under conditions of low cloud coverage (stratiform clouds from 17-18 April) Rn is small over the whole day, except around noon, when temporary maximal 50 W/m^2 were observed.

The time series of *total heat flux* ($Qt = - (H + lE)$; Fig 5.5, line 4) indicates permanent energy loss of the ocean to the atmosphere. At the beginning and end of the cruise substantial trends were registered, on 9-12 April from 0 to -250 W/m^2 rsp. -100 to 0 W/m^2 from 20-22 April. Otherwise (12-20 April) Qt varies around -150W/m^2.

Finally, the *total energy balance* for the sea surface ($E0 = Rn + Qt$) is presented in Fig 5.5, line 5. Minimal values were reached during night (from 22 UT until 3 UT), varying according to cloudiness, wind and advected air mass typically between -400 and -100 W/m^2. During day, the pattern of the net shortwave radiation dominates the other components adding to the balance Eo. Values between > 400 W/m^2 and -100 W/m^2 were gathered along the track.

Hints of *precipitation* can be obtained from the phenomenological SYNOP weather data at station (ww, Fig 5.5 line 6). From 10 until 20 April, frequent hydrometeor events were observed, predominantly light snow (ww = 70). The most frequently reported low cloud types were CL = 6, CL = 7, also stratiform clouds (15-19 April). The hourly SYNOP observations of cloud coverage (N) and cloud type (CH, CM, CL), and weather (ww), coded according the WMO rules, are very helpful (see Fig 5.5 , line 7- line 10) for deeper analysis of the data.

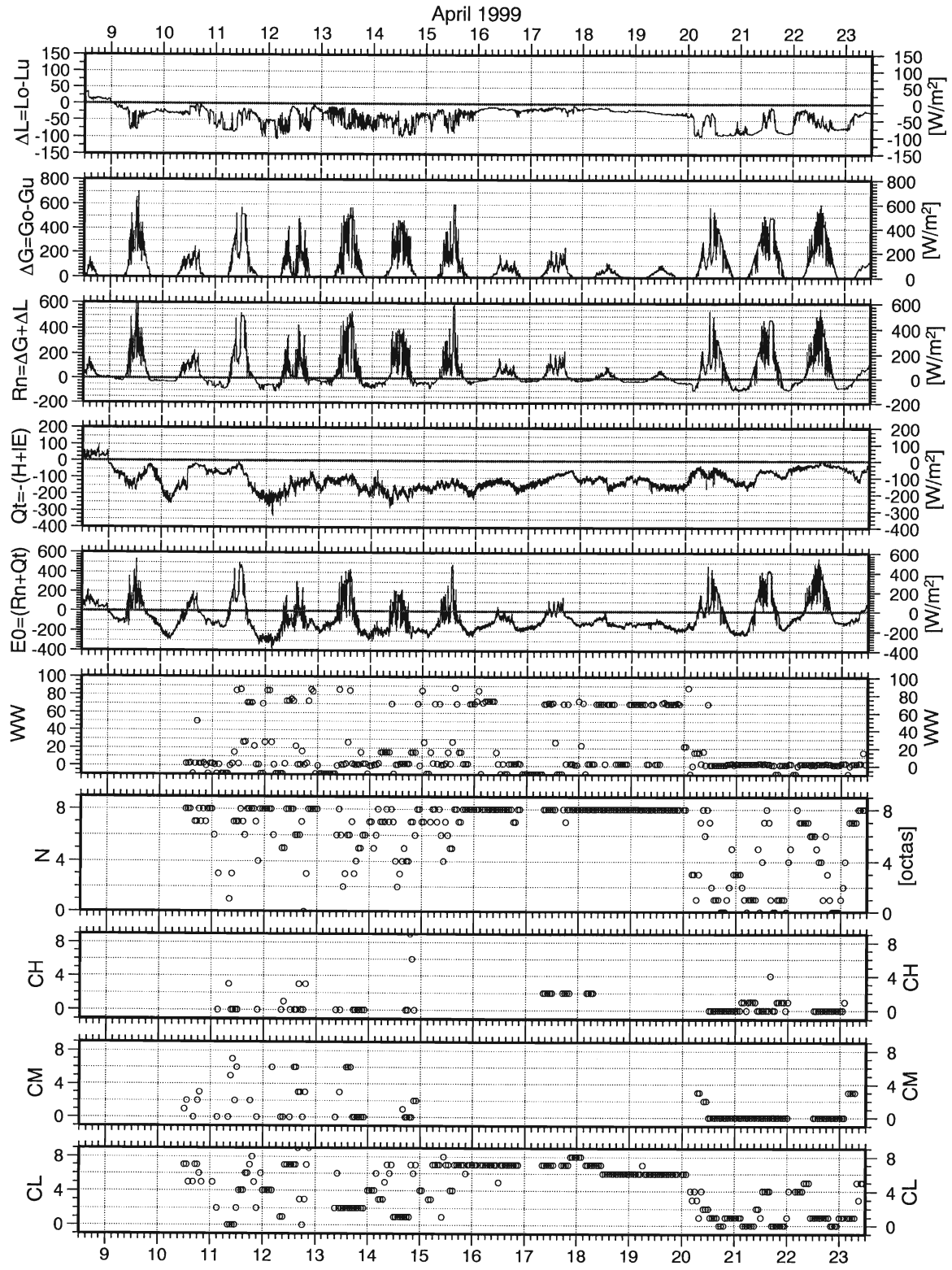

Figure 5.5: *Radiation and energy budget and phenomenological observations: line 1: ΔL: net longwave radiation, line 2: ΔG: net shortwave radiation, line 3: Rn: estimated net radiation, line 4: Qt: total heat flux, negative if ocean looses energy, line 5: E0: total energy budget at sea surface, line 6: WW: hourly WMO-coded weather type, line 7: N: hourly observed total cloudiness in octas (9 = sky obscured), line 8 - line10: type of hourly observed high (CH), middle (CM) and low clouds (CL) according to WMO classification.*

5.3 Radiosonde measurements

5.3.1 Instrumentation

The aerological system consisted of the Vaisala DigiCora system with GPS wind finding and Vaisala radiosondes of type RS80/15G. The 100 g balloons inflated with 0.6 m^3 helium provided ascent rates of 250-300 m/min and reached burst heights up to 22 km, exceeding thus the tropopause level between 7 and 12 km by 10 km and more. The radiosondes were monitored by the DigiCora's sounding mode "Research", which allows for flexible launching and flight conditions. The differential mode was used for wind finding, incorperating so the ship's motion in the wind calculation. Data were stored in original binary form every two seconds as well as in ASCII-code, separately for PTU and wind data, applying the Vaisala Metgraph software after the operator has deactivated the flight. The Teletype protocol of the flight was also written to a file. The reception of the radiosonde signals with aid of the directional UHF-antenna, which was mounted on the compass deck, was by far sufficient even in high wind conditions. At the beginning of the experiment, severe problems occurred with the local GPS antenna and therefore GPS winds were poor. Fortunately, a substitute antenna could be mounted after the improvement of the weather situation allowed outdoor working.

Beside the technical components, a sheltered place for inflating the balloons and launching the radiosondes are crucial for a successful aerology. These requirements were absent during the experiment. One has to note as an aggravating circumstance, that the special aerology container could not be placed on board, solely the main deck was reserved for a bulky hydrographic winch, extra posed for special oceanographic profiling. The Vaisala launcher belonging to the DigiCora system was inapplicable under heavy sea conditions and icy deck situations.

From 8 until 17 April, the aerological program was handicapped by high wind speeds and rough sea conditions, which led to considerable loss of radiosondes during launches as consequence of wind eddy formation behind the ship, pressing the still slow-rising balloons down into the water. Several terms of the schedule could not be served in time for reasons of incalculable bad risk if working on deck when formidable wave crushers overran it. From 18 April on the wind situation improved. Balloon inflating and launching could better be realized now from a small platform on the starboard side at 10 m height near the marine bridge by applying tentatively an simple method: The balloons (diameters about 1.3 m at the surface) were subdued by a person under a 1.5 x 1.5 m^2 tarpaulin cloth and filled from another person per eye with aid of a tubed and pressure reducing inflating pistol.

Table 5.3 gives a day by day overview of the performed soundings. Columns are arranged according to a 3-hourly sounding schedule. For each sounding the table contains launch time, position (latitude, longitude), covered height interval for p, T-data, and percentage of correct wind records compared to the maximum possible record number. Falsified data of relative humidity are also noted in the table, for example the sounding on 12 April 12 UT, which reveals instead of relative humidity the temperature characteristic of humicap, that became frosted by sublimation (see also Figure 5.12, line 1). A total of 57 radiosondes were successfully launched. Eight soundings per day were done, when RV Valdivia reached her northernmost position, exposed here to a quasi-stationary situation of stratiform clouds.

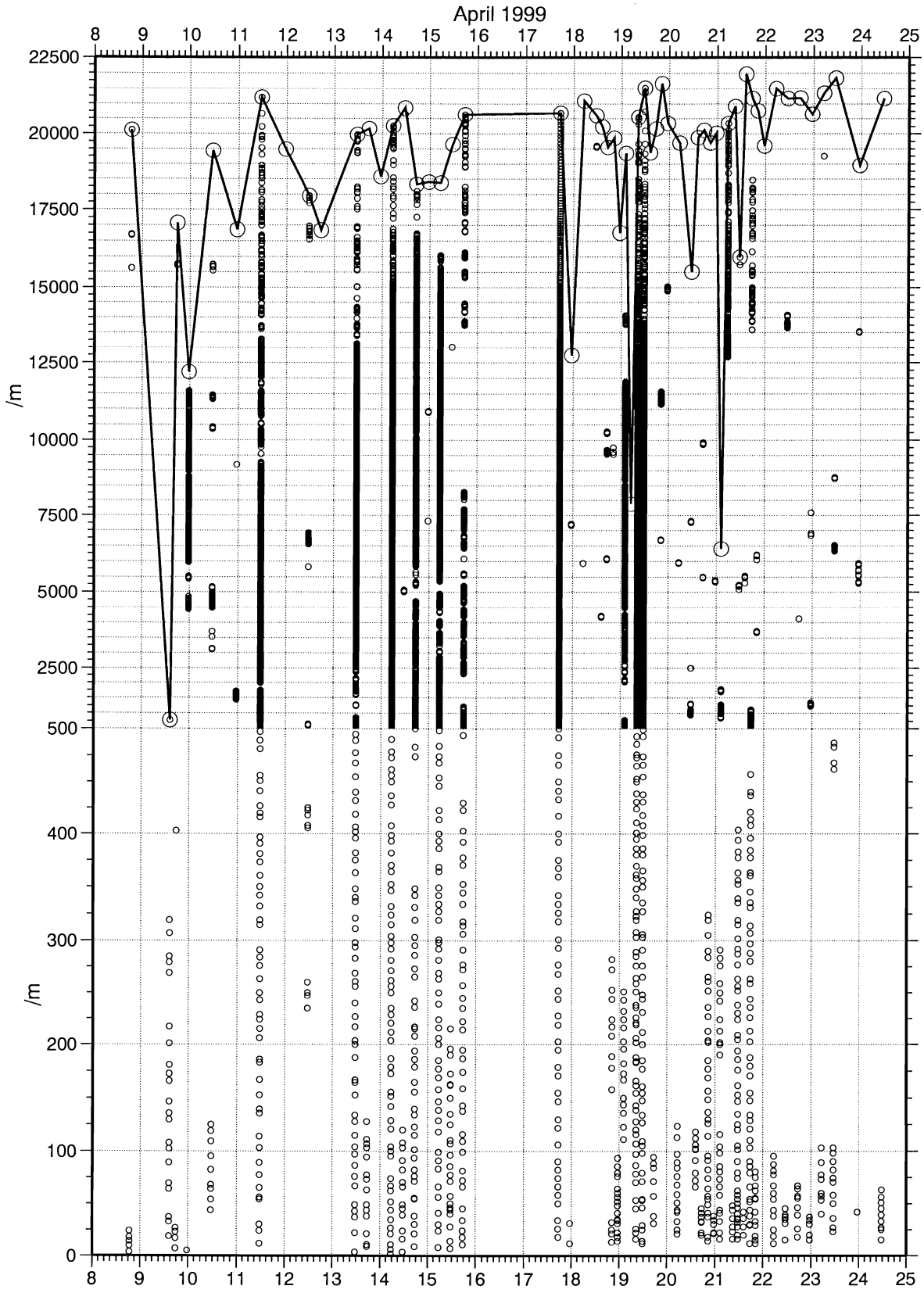

Figure 5.6: *Time plot of maximal achieved aerological sounding heights (large open circles) and marking of height intervals without reliable winds (small open circles). Note enlarged scale up to 500 m.*

According to this and other experience, GPS wind finding is up to now unable to provide constantly correct wind data during a longer period such as a field campaign, that is clearly demonstrated by Figure 5.6. This time-height chart shows the maximal sounding heights, mainly confined by natural burst of the balloons and the height intervals without correct wind data marked by small open circles. Nine out of 57 soundings were almost without wind (data loss > 75 %). Further three soundings have wind data gaps between 60 % and 75 %. Correct wind data within the lowest 150 m is ensured only in 67 % of the soundings. The frequent loss of wind data can be attributed to 'not or delayed' unwinding of the GPS antenna of the radiosonde after launch.

5.3.2 Aerological profiles

a. Time-height presentation of various quantities

The continuity of the aerological data set is interrupted by a gap of soundings from 15 April 18 UT until 17 April 18 UT, consequently it consists of the episodes before the passage of the Fram Strait cyclone at RV Valdivia's position and the time after it.

Both episodes differ not only with respect to data (wind) quality and sounding frequency, but also with respect to weather conditions.

Episode 10 April 0 UT - 15 April 18 UT:
The presentation of the *isolines of temperature* (Fig.5.7) indicates a frontal wave on 11-12 April, causing tropospheric cooling up to 8km height and one day later tropospheric warming up to 1.5 km. Thereafter, until 15 April rather uniform vertical stratification and steadily decreasing temperature prevailed. The gradually cooling enfolds the whole troposphere and is partly caused by the northward cruise of RV Valdivia. The higher troposphere and lower stratosphere exhibit a temperature pattern more rich in detailed structures than the lower troposphere. *Specific humidity* (Fig. 5.8) clearly reflects the different character of the advected air, e.g. passage of cold front on 11 April 13 UT and the warm front event on 12 April 16 UT as well. The observations from 14 April 00 UT to 15 April 12 UT (isolines of relative humidity are not presented) indicate moist (cloudy) layers (> 80 %) between 0.4 and 1.8 km height. Although wind data (Figs. 5.9, 5.10) are poor, the warm front event is clearly indicated by dense isotaches (Fig. 5.9) of the zonal wind component. Wind directions between northwest and northeast predominated during the considered episode up to 2.5 km, except the warm front passage, when south east winds up to 20 m/s strength near 1.5 km were gathered.

Episode 17 April 06 UT - 23 April 12 UT:
This episode is characterized by steady rising of the *pressure* height levels, about 150 m within the lower troposphere. The trend is overlayed by wavy variations, which indicate relative minima of pressure heights on 17 April 18 UT, 20 April 00 UT and, meterologically most effective, on 21 April 06 UT (Fig. 5.7, line 1). *Temperature* isolines suggest for the time 19 April 06 UT (passing of the cold front at the surface) to 21 April 00 UT (passing of the warm front) cold air up to the tropopause. Consequently, the cold section is enclosed from up to several kilometer higher situated isotherms. Most intensive heating by warm front passing

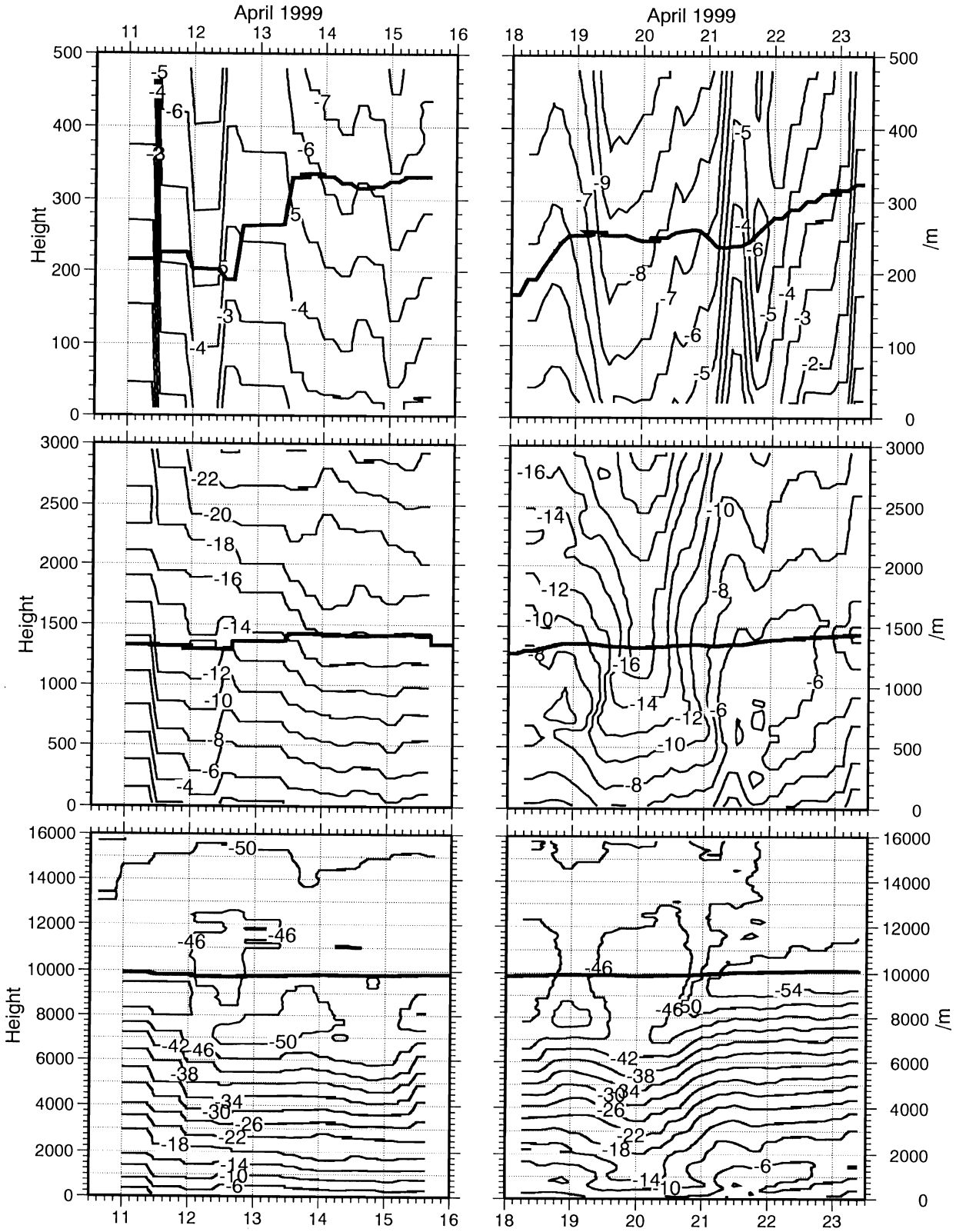

Figure 5.7: *Time height cross section of temperature [°C] and designated vertical isobares: line 1: Data gridded in steps of 10 m, bold curve: 980 hPa-isobar, line 2: Data gridded in steps of 25 m, bold curve: 850 hPa-isobar, line 1: Data gridded in steps of 100 m, bold curve: 250 hPa-isobar.*

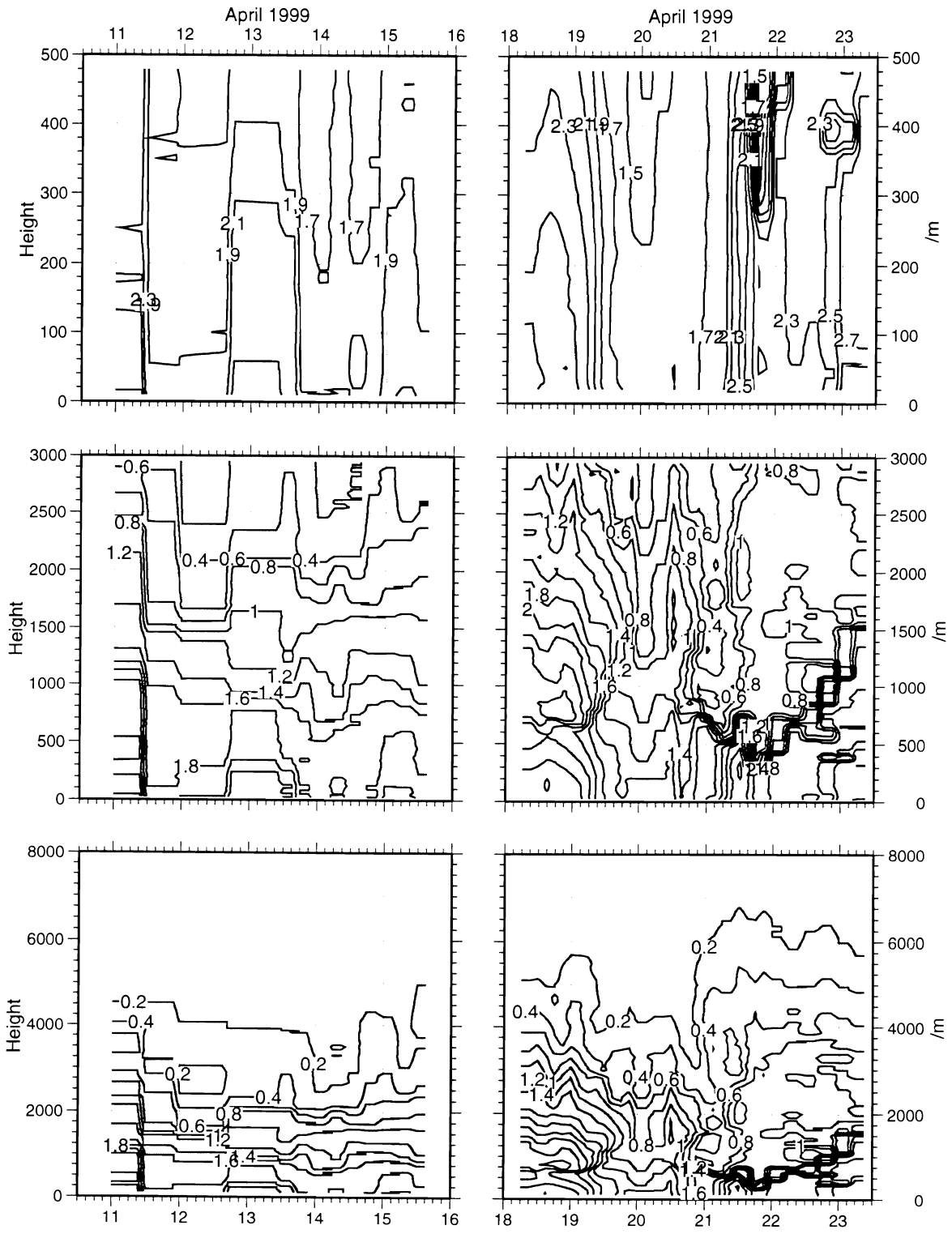

Fig.5.8. Time-height cross section of specific humidity [g/kg]

Figure 5.8: *Time height cross section of specific humidity [g/kg]. Data gridded in steps of 10, 25, 100 m rsp.*

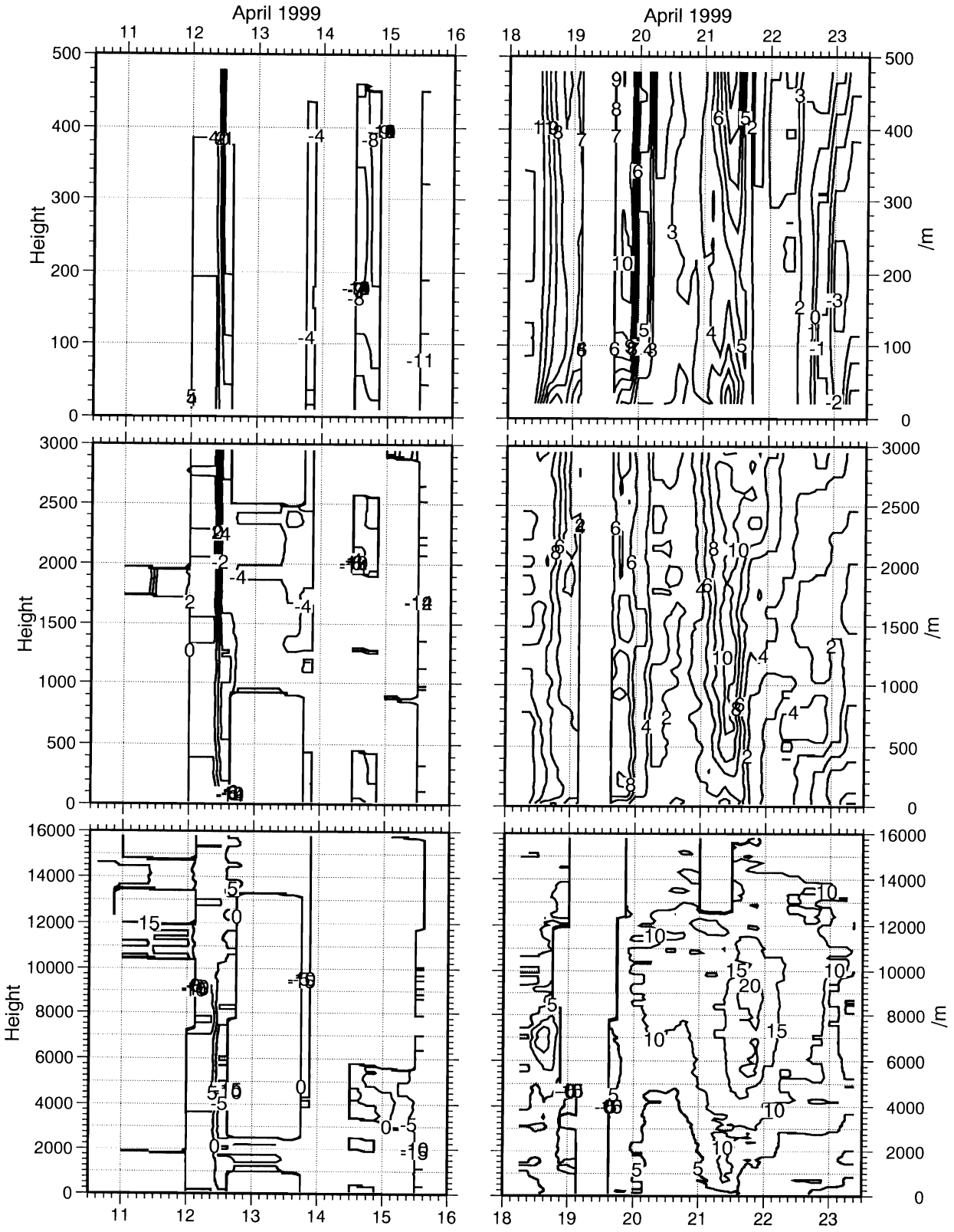

Figure 5.9: *Time height cross section of zonal wind speed [m/s]. Data gridded in steps of 10, 25, 100 m rsp.*

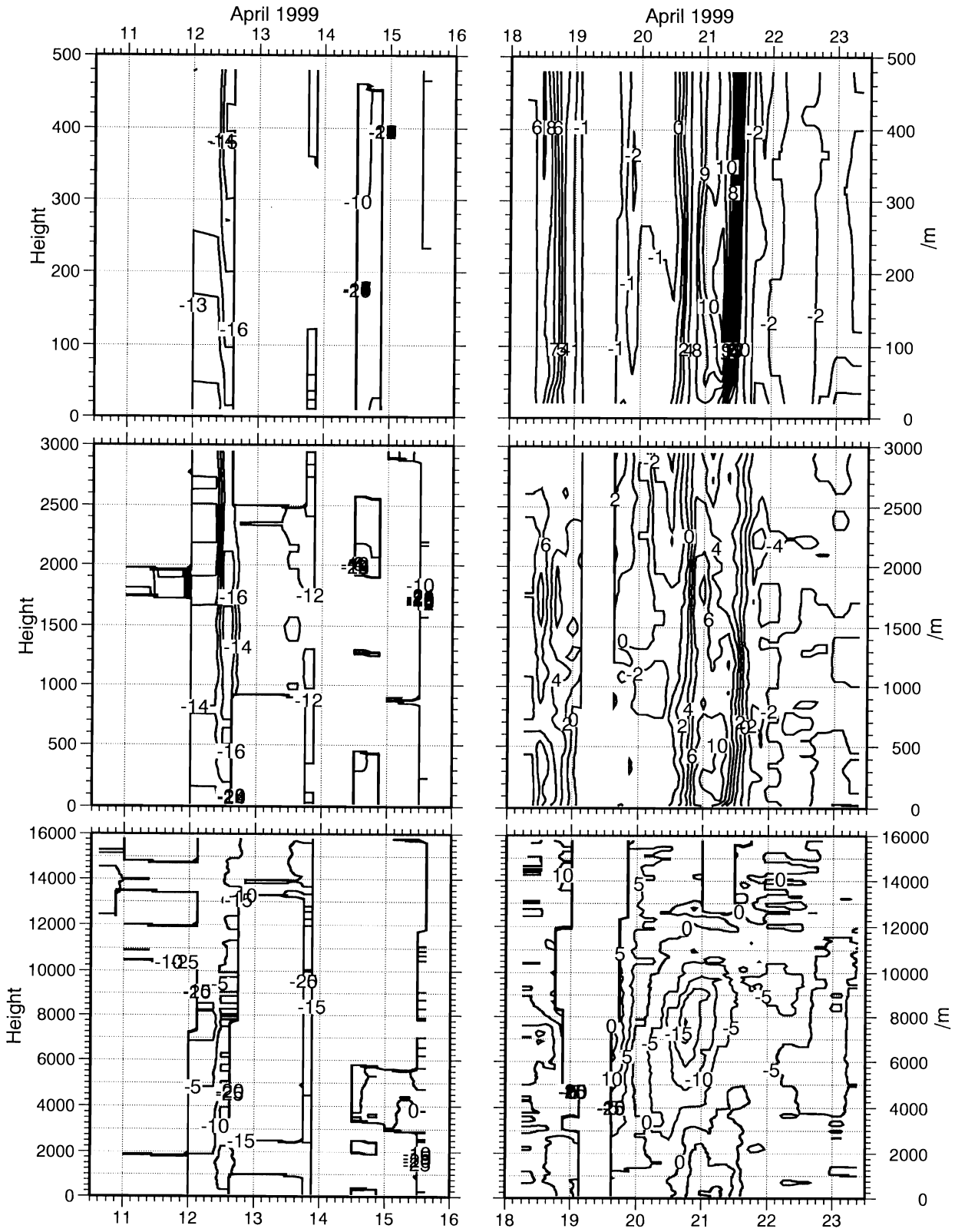

Figure 5.10: *Time height cross section of meridional wind speed [m/s]. Data gridded in steps of 10, 25, 100 m rsp.*

occurred on 21 April. Consecuting warming by anticyclonic sinking continued steadingly until the end of the campaign. The process was interrupted briefly on 21 April towards evening by a passing tropospheric wave, which effected cooling of the troposphere up to 5 km. The warm intervals of the considered episode are characterized by pronounced temperature inversion layers between 0.4 and 1.5 km (see Fig. 5.15). Considering *moisture* (Fig.5.7), the cold section is featured by low relative humidities up to the tropopause. High relative humidities (> 90 %) in various levels up to 6 km occured until 18 April at noon. On the other hand, very dry conditions occur from 22 April on up to 4 km, above the moist cloud layers located variably between 0.3 and 1.5 km (see Fig. 5.16).

Wind data are more complete for this episode (Figs. 5.9, 5.10). The low tropospheric (< 4 km) wind speeds are greater in the defined cold section (> 10 m/s) than those gained during the two adjacent warm phases (< 5 m/s). Beneath the tropopause, between 5 and 9 km, jet like structures of isotachs from 15 to 25 m/s indicate considerable baroclinicity and vicinity to the polar front, so e.g. on 18 April 18 UT (dominant zonal west component), 20 April 18 UT (dominant meridional north component) and 21 April 18 UT (dominant zonal west component).

b. Vertical profiles

The profiles of temperature T, relative humidity RH, wind speed FF and wind direction DD are given in Fig 5.11-5.18.

Explanations to the aerological profile series:
The ordinate signifies the height. The abscissa is a running scale; it is plotted in detail for the first profile in each line (e.g. -30°C for temperature). The running vertical strokes stand for a fixed value, which is defined by the first stroke of the line. The identifying information at the end of the profile above the strokes means 'day/hour' of the sounding. For position and exact launch time see Table 5.3. For clarity, the profiles were displayed as alternating thick and fine curves. The profiles are seperated from each other by a fixed spacing. All profiles are plotted twice: for the entire height range 0-22km (Figs. 5.11-5.14) and for the boundary layer height range 0-3 km (Figs. 5.15-5.18).

Charcteristic features of the data:
Information inherent in the various profiles cannot be discussd in detail. For the more general variation of the atmospheric structure, the varying synoptic conditions must be considered (see Section 2 and Appendix A).

Atmospheric boundary layer:
Boundary layer (BL) heights, modified by synoptic (subsidence) and mesoscale processes of vertical motion (entrainment process) and advection of different air masses over the sea surface (e.g. off-ice flow) undergo reasonable changes, as can be concluded from the plot of temperature profiles in Figs. 5.11, 5.15. The first (cyclonic) episode (08/18- 15/18) indicates generally well mixed temperature stratification and weak capping temperature inversions.

Pronounced boundary layer inversions are observed during the second (anticyclonic) episode

(17/18-24/12), especially during the cruise from east to west along 75°N: constant mixed layer (ML) situations with capping inversions of 5 K near 600 m prevailed from 18 April 00 to 19 April 06 UT, although the surface wind speed changed from 15 to 6 m/s and wind directions from NW to SW; continuous growing of the BL inversions from 600 to 1450 m is obvious on 19 April, when RV Valdivia cruised westward from 2°E to 0°W. Accompanied temperature decrease of 3 K and constant moderate (FF ~ 7 m/s) winds from west suggest air mass transformation and development of internal boundary layers downstream of the about 285 km apart ice edge. Contrary to it, rising inversion heights downstream of the ice edge indicate, that the horizontal and vertical temperature differences were inadequate to establish the anticipated BL phenomena. Continuous declining of the inversion heights from 1460 to 450 m occurred from 19 April 21 UT to 21 April 09 UT, when RV Valdivia cruised westward from 0° to 8°W, now located about 55 km apart the ice edge. The situation is characterized by instationary wind conditions: speed decreased first to near zero and increased over the day up to 8 m/s, on 21 April 09 UT up to 14 m/s. Wind direction changed on 20 April from NW to SSW, to continue until 21 April at noon. Temperature increased accordingly from -6°C to -1°C. Finally, the profiles 21/18 and 21/21 represent RV Valdivia's shortest distance from the ice boundary, about 7 km, where the inversion height amounted to about 900 m. The wind speed had decreased to 2 m/s, the temperature to -5°C and wind had changed to NW, parallel to the ice boundary. The lowest inversion height was measured at 22 April 00 (420 m), when RV Valdivia was already cruising southeastward. The inversions were coupled with stratiform low level clouds (SC, ST; cloud base see Fig. 5.4, line 7, cloud type see Fig. 5.5, line 10), which is documented indirectly by values > 90 % of the RH profiles in Figs. 5.12, 5.16. With respect to relative humidity, the profiles discussed reveal quite different structures, if comparing line1 and partly line 2 with line 3 of the figures in consideration. Above the lower inversions, advected air of arctic origin is very dry. Within the more and more stabilizing atmosphere above the mixed layer, double and more layered moisture structures emerge from local temperature inversions within the first 3 km.

Pronounced layers in the upper troposphere:
The mean height of the tropopause within the polar circle was 8.5 km. The adjacent layers above the tropopause (inversion or isothermal layer) revealed a mean thickness of 4 km, followed by a layer of vertically decreasing temperature (~ - 1 K/km) up to the burst height of the balloons. In two cases, no tropopause could be observed. Referring to all soundings, 62 % of them showed tropopauses between 6-8 km, in 14 % of the tropopause exeeded the 10 km level. Higher tropopauses (> 12 km) refer mainly to soundings outside the polar circle and/or anticyclonic synoptic weather conditions. Low tropopause levels coincide with frontal events.

Table 5.3: Aerological soundings during FRAMZY 1999 on board RV VALDIVIA: launchtime, position, height interval, %-age of wind-records[a]

April 1999	00 UT	03 UT	06 UT	09 UT	12 UT	15 UT	18 UT	21 UT
8							18:35 UT 62.01N, 6.77W h: 3-20117 m ff: 100 %	
9						14:21 UT 61.58N, 10.83W h: 3-780 m ff: 5 %	17:25 UT 61.69N, 11.17 W h: 3-231, 3231-17074 m ff, p-T-RH: 82 %	
10	23:20 UT 62.23N, 9.66W h: 3-12184 m ff: 56 %				11:23 UT 62.96N, 7.79W h: 3-19429 m ff: 95 %			
11	23:21 UT 64.22N, 4.65W h: 3-16853 m ff: 98 %				11:23 UT 65.11N, 4.47W h: 3-21199 m ff: 9 %			
12	23:30 UT 67.31N, 6.16W h: 3-19478 m ff: 100 %				11:26 UT 69.83N, 6.73W h: 3-17937 m ff: 96 %, RH: none		17:22 UT 68.81N, 8.14W h: 10-16847 m ff: 100 %	
13					11:23 UT 69.58N, 11.72W h: 3-19975 m ff: 19 %		17:21 UT 69.61N, 11.84W h: 3-20158 m ff: 99 %	
14	23:19 UT 70.04N, 9.88W h: 3-18574 m ff: 100 %		5:22 UT 70.27N, 8.82W h: 3-20262 m ff: 1 %		11:19 UT 70.86N, 5.73 W h: 3-20865 m ff: 99 %		17:21 UT 71.01N, 4.99W h: 3-18316 m ff: 15 %	
15	23:25 UT 71.52N, 5.66W h: 3-18391 m ff: 100 %		5:23 UT 71.84N, 6.03W h: 3-18359 m ff: 16 %		11:23 UT 72.45N, 6.79W h: 3-19653 m ff: 64 %		17:25 UT 72.60N, 6.98W h: 3-20640 m ff: 34 %	
16								
17							17.21 UT 73.60N, 1.28W h: 3-20545 m ff: 2 %	
18	23:17 UT 73.58N, 0.61E h: 10-12738m ff: 100 %		5:19 UT 74.10N, 1.50E h: 10-21082m ff: 100 %		11:20 UT 74.69N, 2.52E h: 10-20597m ff: 100 %	14:22 UT 75.00N, 2.95E h: 10-20230m ff: 100 %	17:13 UT 74.99N, 2.90E h: 10-19552m ff: 100 %	20:15 UT 74.98N, 2.93E h: 10-19851m ff: 100 %
19	23:16 UT 74.99N, 1.98E h: 10-16766m ff: 100 %	2:19 UT 75.35N, 1.99E h: 10-19359m ff: 38 %	5:17 UT 75.35N, 1.99E h: 10-7870m ff: 100 %	8:18 UT 75.35N, 1.51E h: 10-20548 m ff: 1 %	11:30 UT 75.35N, 0.32E h: 10-21513m ff: 1 %	14:15 UT 75.35N, 0.01W h: 10-19370m ff: 100 %	17:16 UT 75.00N, 1.00E h: 10-20171m ff: 100 %	20:14 UT 75.00N, 0.64E h: 10-21662m ff: 99 %
20	23:17 UT 75.00N, 0.05W h: 10-20336m ff: 100 %		5:51 UT 75.00N, 1.31W h: 10-19688m ff: 99 %		11:20 UT 75.00N, 2.97W h: 10-15507m ff: 98 %	14:25 UT 74.99N, 3.99W h: 10-19872m ff: 100 %	17:18 UT 74.99N, 4.04W h: 10-20111m ff: 99 %	20:22 UT 75.00N, 5.01W h: 10-19694m ff: 98 %

21	23:22 UT 74.99N, 5.62W h: 10-20012m ff: 100 %	2:22 UT 75.00N, 6.01W h: 10-6400m ff: 93 %	5:21 UT 75.00N, 7.01W h: 10-20341m ff: 90 %	8:42 UT 75.00N, 8.00W h: 10-20919m ff: 100 %	11:23 UT 75.00N, 8.15W h: 10-15986m ff: 97 %	14:20 UT 75.00N, 9.01W h: 10-21963m ff: 100 %	17:34 UT 74.99N, 9.46W h: 10-21167m ff: 90 %	20:17 UT 74.98N, 9.45W h: 10-20770m ff: 99 %
22	23:19 UT 74.75N, 9.02W h: 10-19594m ff: 100 %		5:20 UT 73.91N, 7.00W h: 10-21492m ff: 100 %		11:21 UT 73.41N, 5.60W h: 10-21175m ff: 99 %		17:19 UT 72.93N, 4.32W h: 10-21180m ff: 100 %	
23	23:16 UT 72.36N, 2.73W h: 10-20645m ff: 99 %		5:22 UT 71.53N, 2.14W h: 10-21355m ff: 100 %		11:18 UT 70.42N, 3.31W h: 10-21837m ff: 98 %			
24	23:20 UT 68.12N, 5.4W H: 10-18949m ff: 98 %				11:23 UT 66.33N, 8.10W h: 10-21171m ff: 99 %			

a. *Comments to the table cells:*
Row 1: Launchtime of the radiosonde, Row 2: Position of RV Valdivia during launch, Row 3: Height interval of usable p-T-RH (pressure, temperature, relative humidity) data, Row 4: Percentage of usable wind data within the total sounding interval: ff

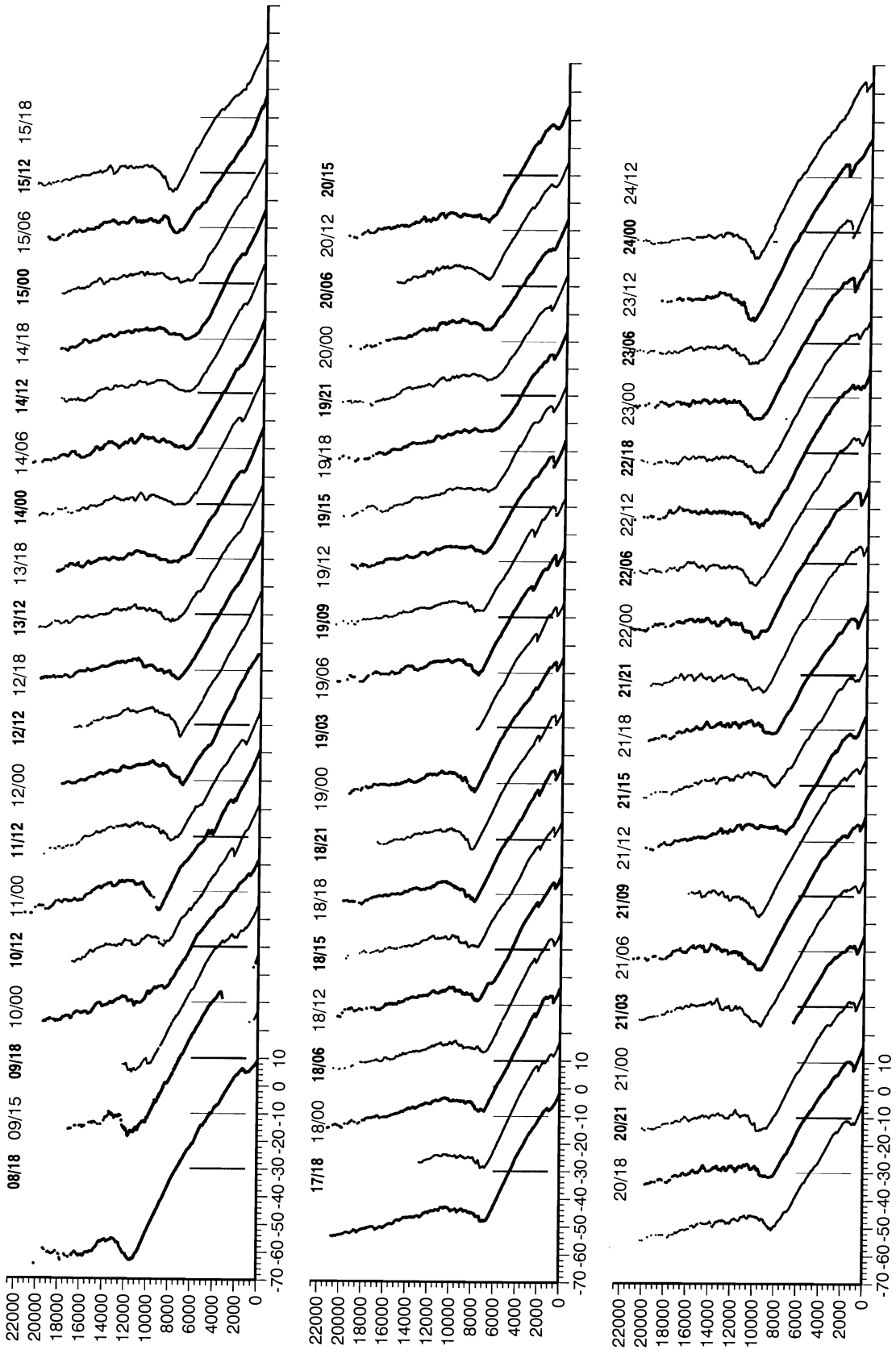

Figure 5.11: *Temperature pofiles up to 22 km: line 1: 8 April 18 UT - 15 April 15 UT, line 2: 17 April 18 UT - 20 April 15 UT, line 3: 20 April 18 UT - 24 April 12 UT. Vertical strokes represent the value T = -30°C for each sounding labelled above.*

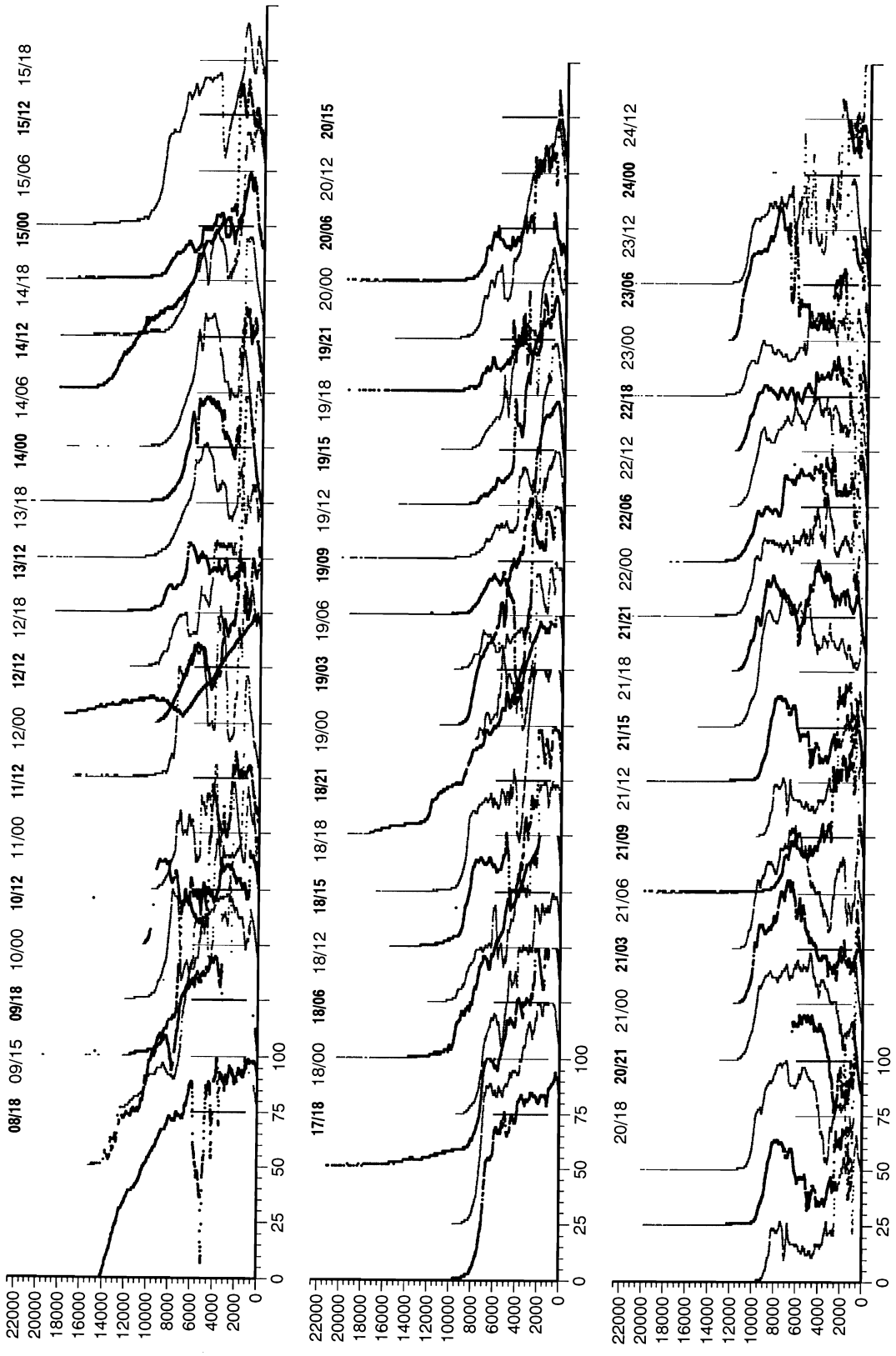

Figure 5.12: *Relative humidity profiles pofiles up to 22 km: line 1: 8 April 18 UT - 15 April 15 UT, line 2: 17 April 18 UT - 20 April 15 UT. Vertical strokes of line 1,2 represent the value RH = 75 % for each sounding labelled above, line 3: 20 April 18 UT- 24 April 12 UT. Vertical strokes represent the value RH = 25 % for each sounding labelled above.*

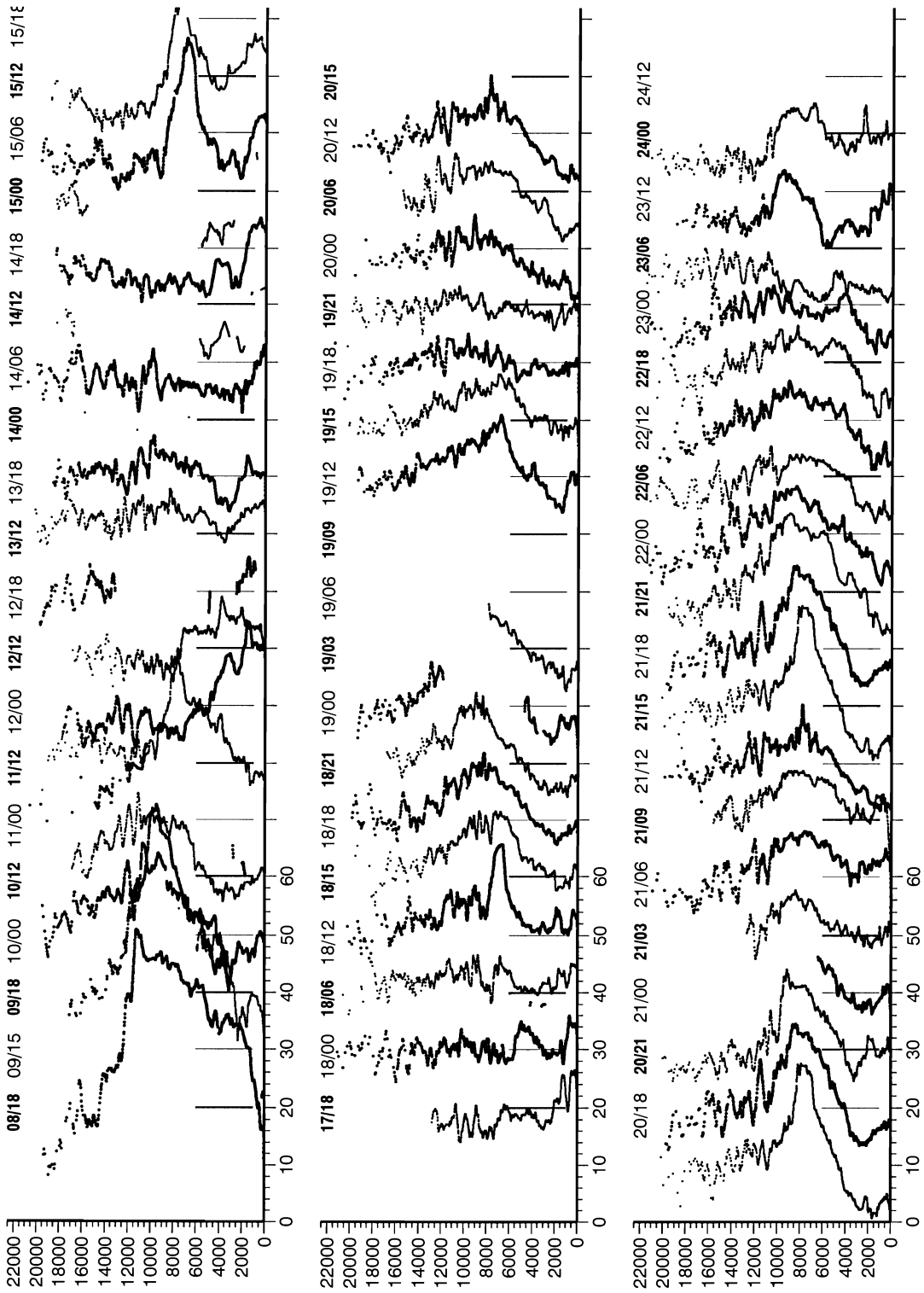

Figure 5.13: *Wind speed profiles up to 22 km: line 1: 8 April 18 UT - 15 April 15 UT, data availiability: 09/15: none; 09/18: > 3 km; 10/00: < 6 km; 11/12: > 2 km, sporadic; 13/12: > 1 km, sporadic; 14/06: none; 14/18: sporadic; 15/06: none; 15/18: sporadic, line 2: 17 April 18 UT - 20 April 15 UT, data availiability: 17/18: none; 18/00: < 13 km; 19/03: 5-12 km no data; 19/06: > 8 km none; 19/09: none; 19/12: none, line 3: 20 April 18 UT - 24 April 12 UT, data availiability: 21/03: > 6 km none, line 1 - line 3: Vertical strokes represent the value FF = 20 m/s for each sounding labelled above.*

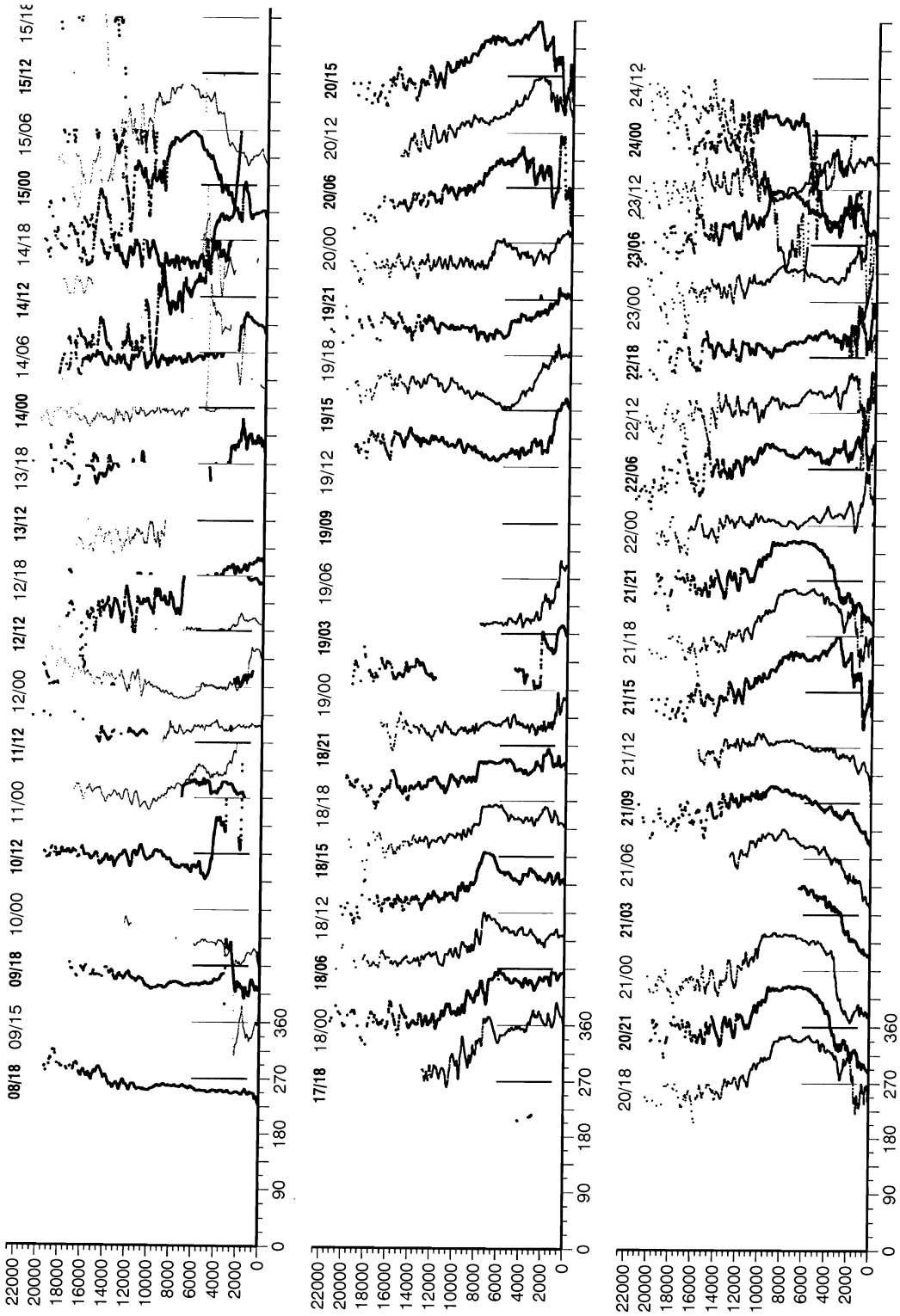

Figure 5.14: *Wind direction profiles up to 22 km: line 1: 8 April 18 UT - 15 April 15 UT, data availiability: 09/15: none; 09/18: > 3 km; 10/00: < 6 km; 11/12: > 2 km, sporadic; 13/12: > 1 km, sporadic; 14/06: none; 14/18: sporadic; 15/06: none; 15/18: sporadic, line 2: 17 April 18 UT - 20 April 15 UT, data availiability: 17/18: none; 18/00: < 13 km; 19/03: 5-12 km: no data; 19/06: > 8 km none; 19/09: none; 19/12: none, line 3: 20 April 18 UT - 24 April 12 UT, data availiability: 21/03: > 6 km none, line 1- line 3: Vertical strokes represent the value DD = 270° for each sounding labelled above.*

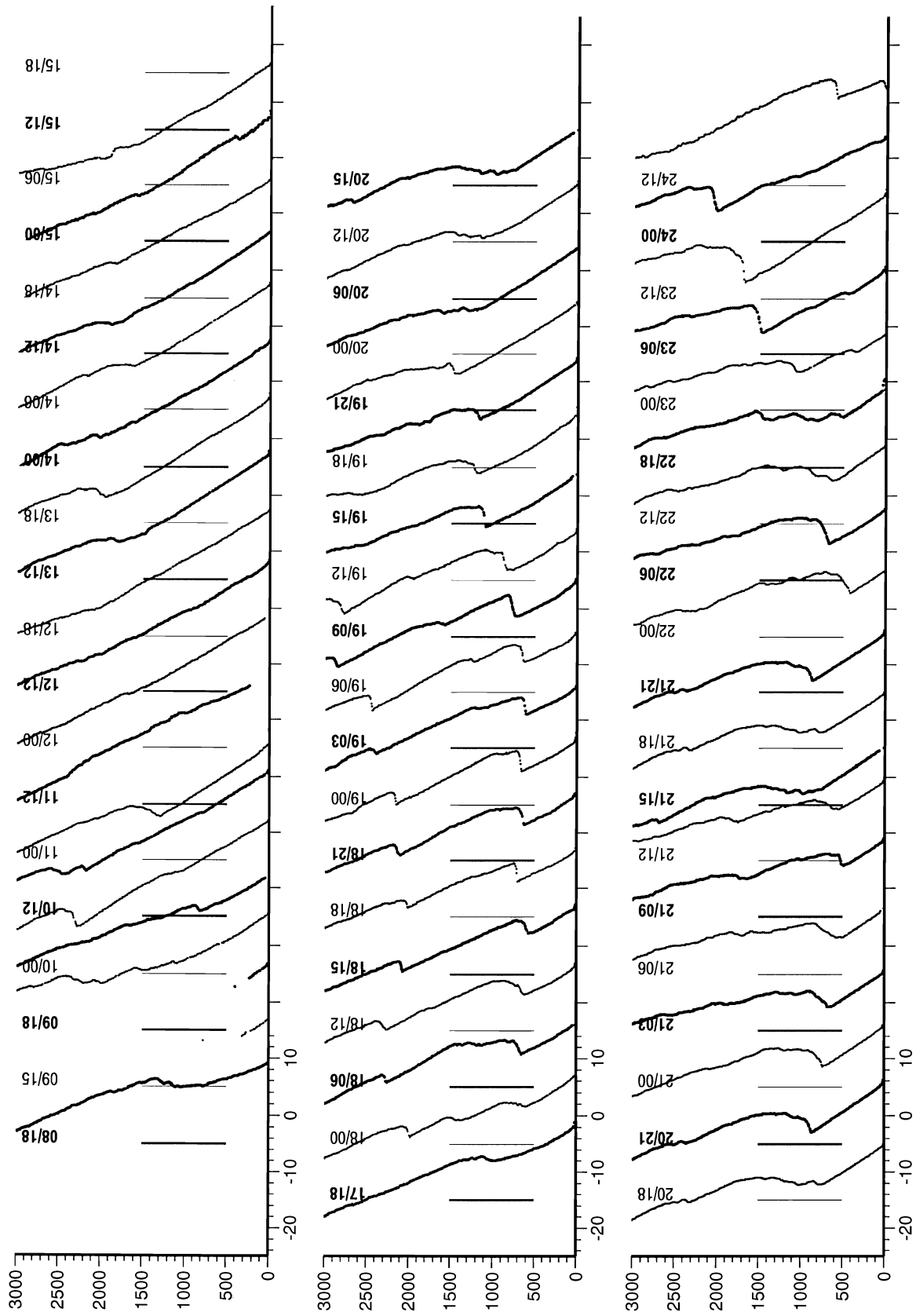

Figure 5.15: *Temperature pofiles up to 3 km: line 1: 8 April 18 UT - 15 April 15 UT, line 2: 17 April 18 UT - 20 April 15 UT, line 3: 20 April 18 UT - 24 April 12 UT. Vertical strokes represent the value T = -15°C for each sounding labelled above.*

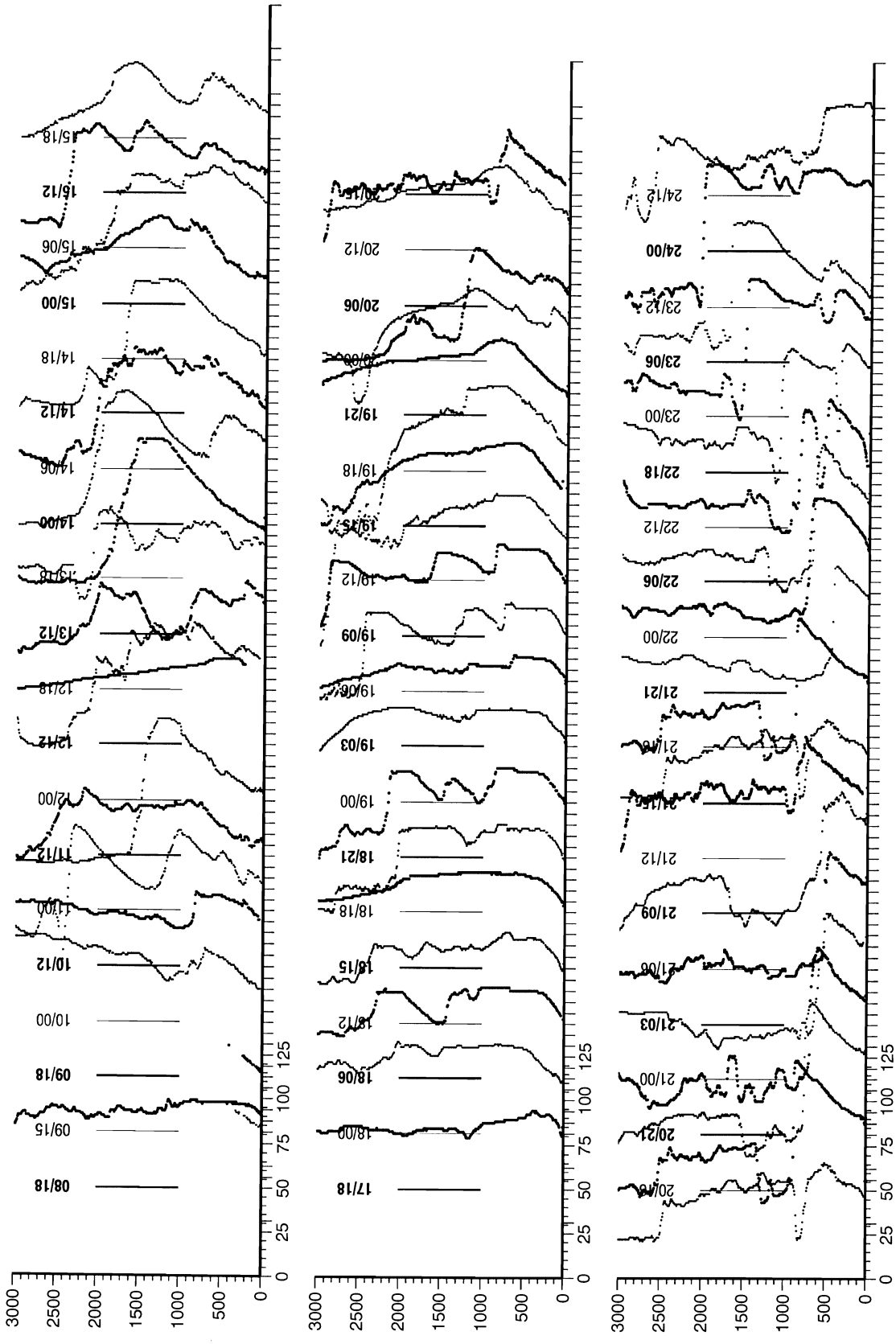

Figure 5.16: *Relative humidity profiles pofiles up to 3 km: line 1: 8 April 18 UT - 15 April 15 UT, line 2: 17 April 18 UT - 20 April 15 UT, line 3: 20 April 18 UT - 24 April 12 UT. Vertical strokes represent the value RH = 50 % for each sounding labelled above.*

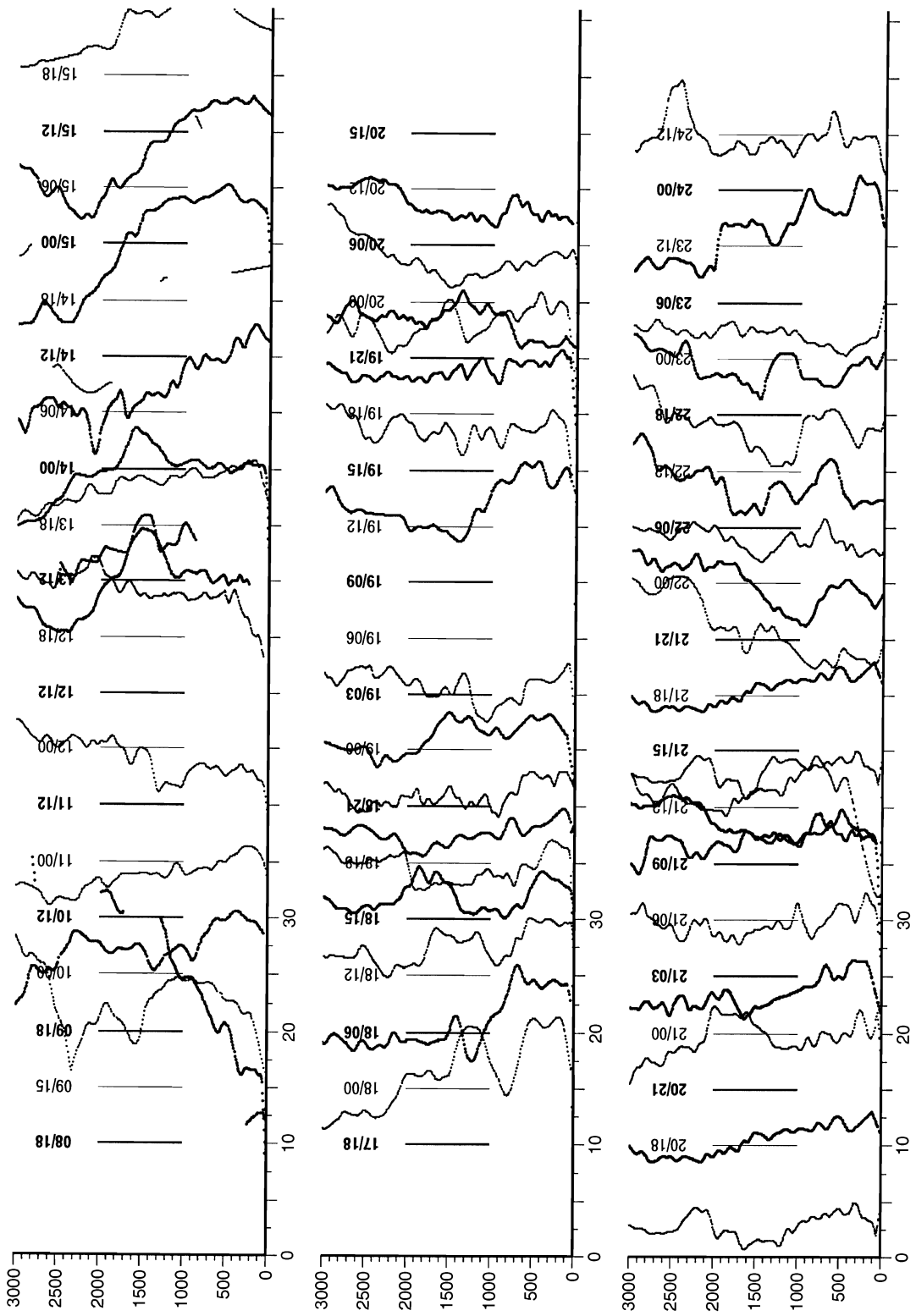

Figure 5.17: *Wind speed profiles up to 3 km: line 1: 8 April 18 UT - 15 April 15 UT, data availiability: 09/15: none; 11/12: none; 13/12: > 1 km, sporadic; 14/06: none; 14/18: sporadic; 15/06: none; 15/18: sporadic, line 2: 17 April 18 UT - 20 April 15 UT, data availiability: 17/18: none; 19/09: none; 19/12: none, line 3: 20 April 18 UT - 24 April 12 UT, data availiability: 21/03: > 6 km none. Vertical strokes represent the value FF = 10 m/s for each sounding labelled above.*

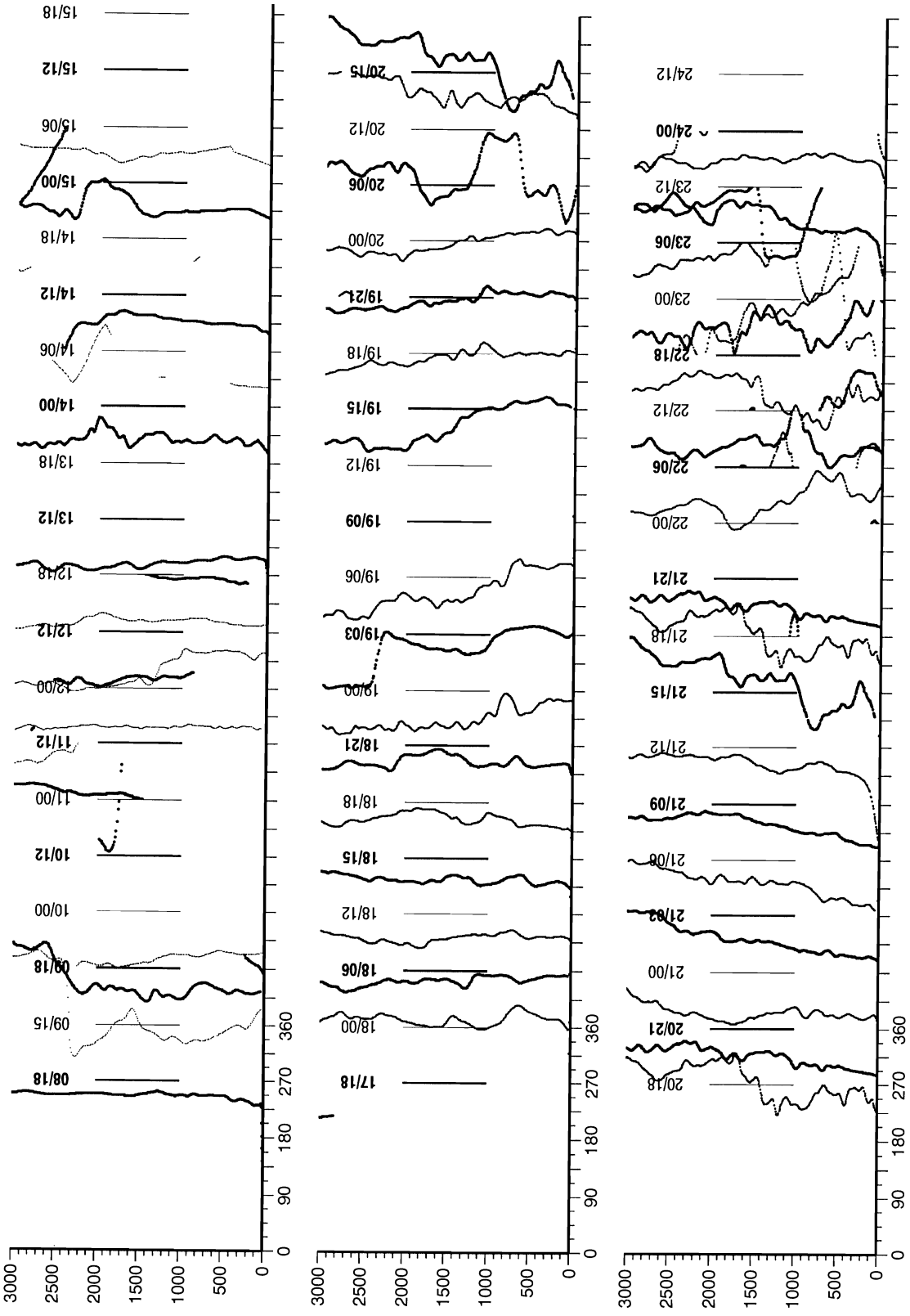

Figure 5.18: *Wind direction profiles up to 3 km: line 1: 8 April 18 UT - 15 April 15 UT, data availiability: 09/15: none; 11/12:none; 13/12: > 1 km, sporadic; 14/06: none; 14/18: sporadic; 15/06: none; 15/18: sporadic, line 2: 17 April 18 UT - 20 April 15 UT, data availiability: 17/18: none; 19/09: none; 19/12: none, line 3: 20 April 18 UT - 24 April 12 UT. Vertical strokes represent the value DD = 270° for each sounding labelled above.*

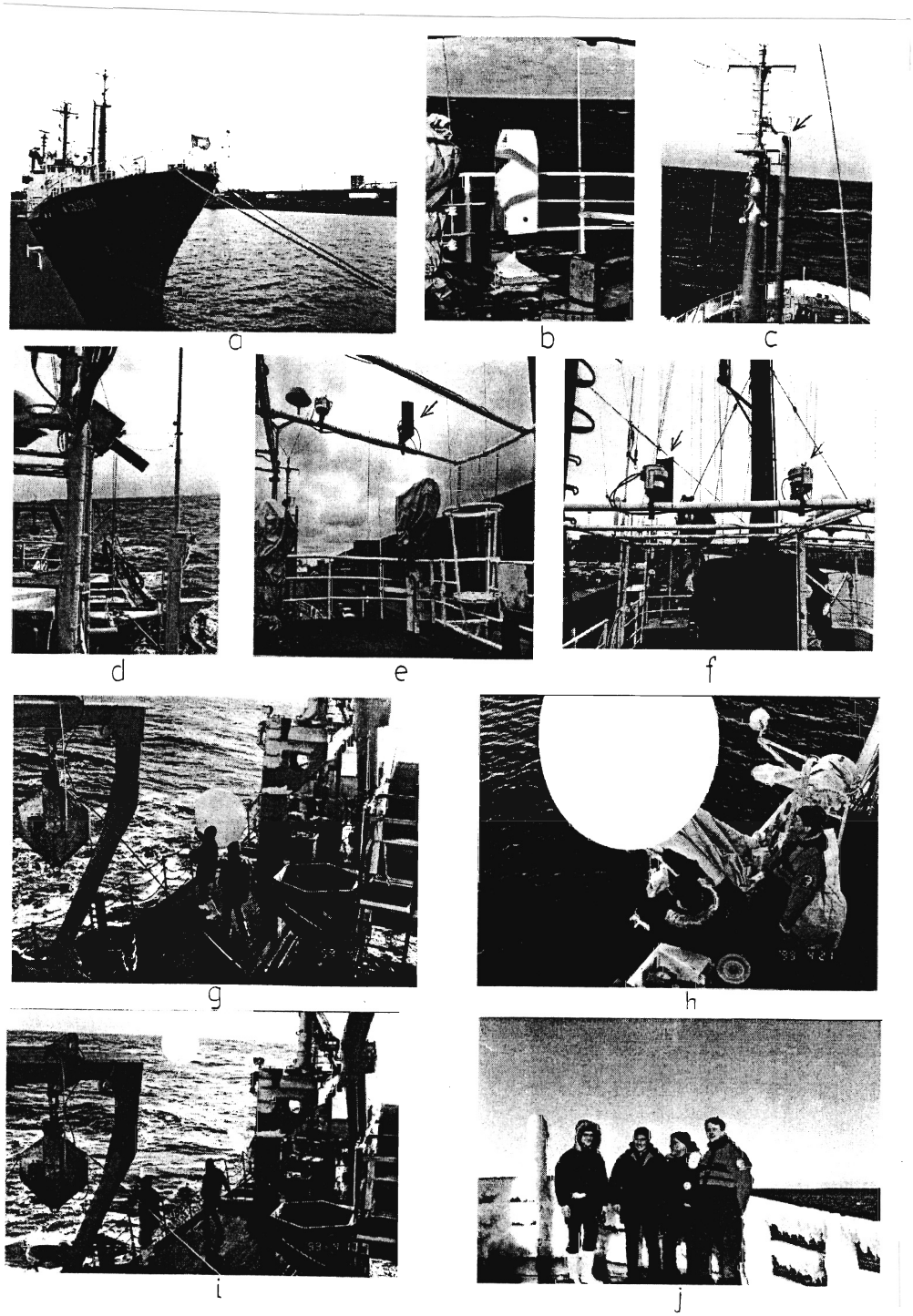

Figure 5.19 a-j: *Fotos of instrumentation on board RV Valdivia during FRAMZY 1999 (M.Offermann): (a) RV Valdivia in the harbor in Hamburg during loading before the cruise, (b) Ceilometer on the crane deck, (c) Fore mast of the ship with meteorological sensors for temperature, humidity and wind, (d) KT19 radiation thermometer on the compass deck viewing at the sea surface, (e), (f) Radiation sensors (Kipp & Zonen pyranometer, Eppley pyrgeometer) on the compass deck viewing upwards, (g) Launching the radiosonde from the main deck; at right side: VAISALA launcher for use on land, (h) Launching the radiosonde from the bridge deck at 10 m height, (i) The meteorological FRAMZY 1999 crew on the iced fore deck: from left to right: S. Henne, V.Jost, G.Kruspe, M. Offermann.*

6. Satellite data

(F. Papke, Meteorological Institute, University of Hamburg, S. Bakan, Max-Planck-Institute for Meterology, Hamburg)

6.1 General remarks

Essential information for the planning of research flight missions, like the general overview of the actual weather conditions, or the location of interesting phenomena like cyclones, and fronts can only be provided by satellite images not older than a few hours. Important for this campaign, satellite images would also be used for observations of ice boundary and ice drift.

The satellite data used for mission planning during this campaign stem mainly from the AVHRR radiometers on board the satellites NOAA 14 and 15. Due to the rather high resolution of about 1km in the sub-satellite point, the near polar orbit, and the AVHRR sensor characteristics, these data seemed to be most promising for the mission decisions and campaign documentation.

A major drawback for ice observation with AVHRR images is the masking by clouds. This may be avoided with the help of microwave images, which are either available from the passive SSM/I instrument on board the NOAA/DMSP satellite series or from the active SAR system on board the European ERS I/II satellites. Unfortunately, there are no microwave images of ground resolution similar to NOAA/AVHRR available (for details see below). And as information from these sources has only been partly available in near real time the mission planning relied mostly on AVHRR imagery.

Any requests for data or products mentioned in this Section should be directed to S. Bakan via email: bakan@dkrz.de

6.2 Satellite data acquisition

The used satellite images during the FRAMZY '99 field campaign came from two sources:

- High resolution satellite images from NOAA/AVHRR received, processed, and stored by Tromsø Satellite Station (TSS)
- Actually AVHRR images from Dundee Satellite Receiving Station with a low spatial resolution (Quicklooks)

6.2.1 Tromsø Satellite Station

High resolution images of channels 2 (central wavelength at ~ 0.9 μm) and 4 (~ 11μm) were ordered for the time period 1 - 30 April 1999. During the campaign period the images were extracted from TSS via File Transfer Protocol (FTP).

The acquired images contain 1024 lines with 1024 pixels each derived by re-sampling of the original AVHRR data to a polar stereographic projection with fixed corners and a centre point at 0E and 79N. Further, the radiometric pixel values are transformed from the original 10 to 8 bit/pixel after radiometric calibration and by ignoring 2% of the highest and lowest values. Therefore, the byte data contain the brightness temperatures in channel 4 with a resolution of 0,5% and the reflectivity in channel 2 at 0.4% resolution. Images of these two channels were available twice a day, one scene in the morning, and one scene at noon to printout and display for the daily main briefings.

A list of the available image files is given in Table 6.1. For illustration and reference one thermal image per day (around noon time) during the field period is given in Appendix B1.

Table 6.1: Available AVHRR images (Ch. 2+4) from TSS Tromsø (see Section 6.2.1)

Satellite	Date	Time	Code	Satellite	Date	Time	Code
NOAA-14	99/04/01	03:12:02	14784	NOAA-14	99/04/01	11:33:00	14800
NOAA-14	99/04/02	03:00:57	14820	NOAA-14	99/04/02	11:20:56	14835
NOAA-14	99/04/03	02:49:52	14861	NOAA-14	99/04/03	11:09:51	14876
NOAA-14	99/04/04	04:18:49	14903	NOAA-14	99/04/04	10:58:47	14918
NOAA-14	99/04/05	04:07:45	14944	NOAA-14	99/04/05	10:47:44	14959
NOAA-14	99/04/06	03:56:41	14988	NOAA-14	99/04/06	10:36:39	15003
NOAA-14	99/04/07	03:45:37	15030	NOAA-14	99/04/07	12:05:35	15051
NOAA-14	99/04/08	03:33:36	15074	NOAA-14	99/04/08	10:14:31 11:55:30	15088 15094
NOAA-14	99/04/09	03:22:29	15120	NOAA-14	99/04/09	11:42:26	15140
NOAA-14	99/04/10	03:11:24	15161	NOAA-14	99/04/10	11:31:24	15176
NOAA-14	99/04/11	03:00:20	15210	NOAA-14	99/04/11	11:20:19	15225
NOAA-14	99/04/12	04:29:18	15251	NOAA-14	99/04/12	11:09:16	15266
NOAA-14	99/04/13	02:37:13	15296	NOAA-14	99/04/13	10:58:12	15311
NOAA-14	99/04/14	04:07:11	15337	NOAA-14	99/04/14	10:47:08	15352
NOAA-14	99/04/15	03:56:08	15378	NOAA-14	99/04/15	10:35:04	15393
NOAA-14	99/04/16	03:44:04	15421	NOAA-14	99/04/16	10:23:59	15436
NOAA-14	99/04/17	03:33:00	15466	NOAA-14	99/04/17	11:52:58	15490
NOAA-14	99/04/18	03:21:55	15504	NOAA-14	99/04/18	11:41:53	15524
NOAA-14	99/04/19	03:10:49	15549	NOAA-14	99/04/19	11:30:51	15564
NOAA-14	99/04/20	03:02:47	15599	NOAA-14	99/04/20	11:19:46	15614
NOAA-14	99/04/21	02:47:43	15640	NOAA-14	99/04/21	11:07:43	15655
NOAA-14	99/04/22	02:36:40	15683	NOAA-14	99/04/22	10:56:38	15699
NOAA-14	99/04/23	02:24:36	15726	NOAA-14	99/04/23	10:45:35	15748
NOAA-14	99/04/24	03:54:32	15793	NOAA-14	99/04/24	10:34:32	15803
NOAA-14	99/04/25	03:43:27	15829	NOAA-14	99/04/25	10:23:25	15843
NOAA-14	99/04/26	03:32:25	15865	NOAA-14	99/04/26	11:52:21	15891
NOAA-14	99/04/27	03:20:19	15919	NOAA-14	99/04/27	11:40:18	15945
NOAA-14	99/04/28	03:09:17	15975	NOAA-14	99/04/28	11:29:16	15990
NOAA-14	99/04/29	02:58:11	16017	NOAA-14	99/04/29	11:18:10	16032
NOAA-14	99/04/30	02:46:06	16058	NOAA-14	99/04/30	11:07:06	16076

6.2.2 Quicklooks from Dundee

AVHRR quicklooks of all scenes in all channels are available in the internet from the Dundee Satellite Receiving Station. These images are re-sampled from the original data to a standard grid projection with a spatial resolution of 4 km. With 900 lines and 512 pixels per line, these quicklooks are very helpfully for an overview of the larger scale weather conditions. About eight of these quicklook images are available per day, providing good temporal coverage for the tracking of cyclones.

Each image contains a header for identification. Grid and coast lines are superimposed to the images. Four images per day in channels 2 and 4 were archived during the campaign on Exabyte tape and the image of channel 4 was printed out for reference. A list of the archived images is given in Table 6.2.

Table 6.2: Available quicklook images (Ch.2+4) from Dundee Satellite Receiving Station (see Section 6.2.2)

Satellite	Date	Time	Satellite	Date	Time
NOAA 14	99/04/01	06:39	NOAA 15	99/04/01	08:55
NOAA 14	99/04/01	13:13	NOAA 15	99/04/01	18:45
NOAA 14	99/04/02	06:28	NOAA 15	99/04/02	08:33
NOAA 14	99/04/02	13:02	NOAA 15	99/04/02	18:23
NOAA 14	99/04/03	06:17	NOAA 15	99/04/03	08:11
NOAA 14	99/04/03	12:51	NOAA 15	99/04/03	18:01
NOAA 14	99/04/04	06:06	NOAA 15	99/04/04	07:49
NOAA 14	99/04/04	12:40	NOAA 15	99/04/04	19:18
NOAA 14	99/04/05	05:55	NOAA 15	99/04/05	09:07
NOAA 14	99/04/05	12:29	NOAA 15	99/04/05	18:56
NOAA 14	99/04/06	05:44	NOAA 15	99/04/06	08:45
NOAA 14	99/04/06	12:18	NOAA 15	99/04/06	18:34
NOAA 14	99/04/07	05:33	NOAA 15	99/04/07	08:22
NOAA 14	99/04/07	12:07	NOAA 15	99/04/07	18:12
NOAA 14	99/04/08	05:21	NOAA 15	99/04/08	08:00
NOAA 14	99/04/08	11:56	NOAA 15	99/04/08	19:30
NOAA 14	99/04/09	05:10	NOAA 15	99/04/09	09:18
NOAA 14	99/04/09	13:24	NOAA 15	99/04/09	19:08
NOAA 14	99/04/10	06:39	NOAA 15	99/04/10	08:56
NOAA 14	99/04/10	13:13	NOAA 15	99/04/10	18:46
NOAA 14	99/04/11	06:28	NOAA 15	99/04/11	08:34
NOAA 14	99/04/11	13:02	NOAA 15	99/04/11	18:24
NOAA 14	99/04/12	06:17	NOAA 15	99/04/12	08:12
NOAA 14	99/04/12	12:51	NOAA 15	99/04/12	18:02
NOAA 14	99/04/13	06:06	NOAA 15	99/04/13	07:50
NOAA 14	99/04/13	12:39	NOAA 15	99/04/13	19:20
NOAA 14	99/04/14	05:54	NOAA 15	99/04/14	09:08
NOAA 14	99/04/14	12:28	NOAA 15	99/04/14	18:57

NOAA 14	99/04/15	05:43	NOAA 15	99/04/15	08:46
NOAA 14	99/04/15	12:17	NOAA 15	99/04/15	18:35
NOAA 14	99/04/16	05:32	NOAA 15	99/04/16	08:24
NOAA 14	99/04/16	12:06	NOAA 15	99/04/16	18:13
NOAA 14	99/04/17	05:21	NOAA 15	99/04/17	08:02
NOAA 14	99/04/17	11:55	NOAA 15	99/04/17	19:31
NOAA 14	99/04/18	05:10	NOAA 15	99/04/18	09:19
NOAA 14	99/04/18	13:24	NOAA 15	99/04/18	19:09
NOAA 14	99/04/19	06:38	NOAA 15	99/04/19	08:57
NOAA 14	99/04/19	13:12	NOAA 15	99/04/19	18:47
NOAA 14	99/04/20	06:27	NOAA 15	99/04/20	08:35
NOAA 14	99/04/20	13:01	NOAA 15	99/04/20	18:25
NOAA 14	99/04/21	06:16	NOAA 15	99/04/21	08:13
NOAA 14	99/04/21	12:50	NOAA 15	99/04/21	18:03
NOAA 14	99/04/22	06:05	NOAA 15	99/04/22	07:51
NOAA 14	99/04/22	12:39	NOAA 15	99/04/22	19:21
NOAA 14	99/04/23	05:54	NOAA 15	99/04/23	09:09
NOAA 14	99/04/23	12:28	NOAA 15	99/04/23	18:59
NOAA 14	99/04/24	05:43	NOAA 15	99/04/24	08:47
NOAA 14	99/04/24	12:17	NOAA 15	99/04/24	18:37
NOAA 14	99/04/25	05:32	NOAA 15	99/04/25	08:25
NOAA 14	99/04/25	12:06	NOAA 15	99/04/25	18:15
NOAA 14	99/04/26	05:21	NOAA 15	99/04/26	08:03
NOAA 14	99/04/26	11:55	NOAA 15	99/04/26	19:33
NOAA 14	99/04/27	05:09	NOAA 15	99/04/27	09:21
NOAA 14	99/04/27	13:23	NOAA 15	99/04/27	19:10
NOAA 14	99/04/28	06:38	NOAA 15	99/04/28	08:59
NOAA 14	99/04/28	13:12	NOAA 15	99/04/28	18:48
NOAA 14	99/04/29	06:27	NOAA 15	99/04/29	08:37
NOAA 14	99/04/29	13:01	NOAA 15	99/04/29	18:26
NOAA 14	99/04/30	06:16	NOAA 15	99/04/30	08:14
NOAA 14	99/04/30	12:50	NOAA 15	99/04/30	18:04

6.2.3 ERS2/SAR images

Near and mid infrared AVHRR images have the definite drawback that even thin clouds may cover surface details. Therefore, sea ice observations are better based on active radar or passive microwave data, that interfere hardly with clouds. On board the European ERS2 satellite the SAR (Synthetic Aperture Radar) instrument may be operated in a pure imaging mode, in which the backscattering intensity is recorded as the pixel information. This quantity is very different for sea water and for ice and exhibits also differences for different ice types and/or ages.

The group around W. Alpers, Institut für Meereskunde, Universität Hamburg, managed to get the reception of approximately 100 SAR images of the experimental region scheduled by

ESRIN. AMI (Active Microwave Instrument) radar measurements from the ERS2 satellite can provide more detailed information about structures inside the ice field than passive sensors. The problem with this high spatial resolution SAR mode (< 10 m) is, however, that the spatial coverage per image is down to about 100 x 100 km^2. Unfortunately, no processed images were available during the field phase.

6.2.4 Computer facilities at Longyearbyen

One PC was carried to Longyearbyen in order to receive, process, and store the satellite images. For the campaign an internet access was installed by a local internet provider at Longyearbyen who made available a Windows NT-Server, which was connected by ISDN to the internet. Our PC was connected to the server by a local area Ethernet connection. Thus, internet services like FTP, Telnet and WWW were available during the campaign.

Printed image outputs were produced on a HP Deskjet 1200 color printer and a photo quality Alden 9315 CTP (grey level) printer. A sketch of the hardware configuration is given in Fig. 6.1.

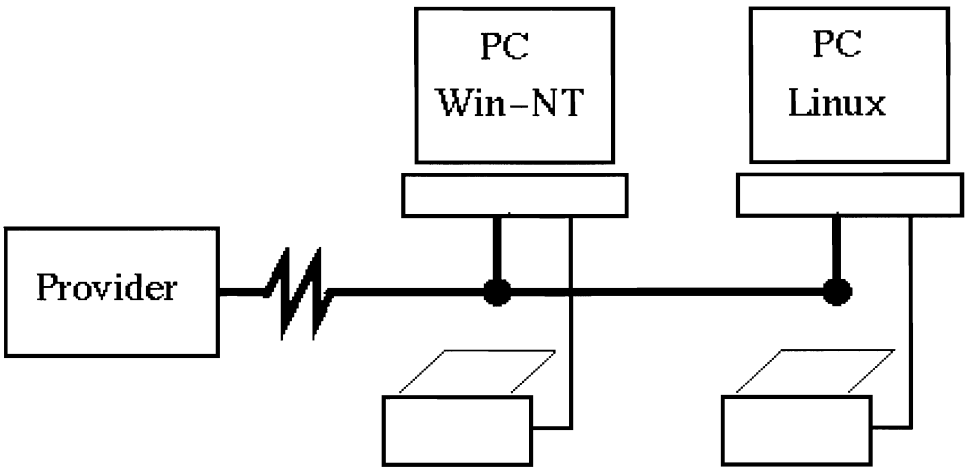

Figure 6.1: *Sketch of the hardware equipment and connections for satellite image processing at Longyearbyen*

6.3 Use of the AVHRR images during the field campaign

As the objective of the campaign was to take a closer look on mesoscale cyclones in the Fram Strait, their cause, structure, life cycle, and their effect on the sea ice, the available satellite images were used for the following purposes:

- to give an overview of the weather conditions for research flight planning
- to determine and track the location of cyclones

– to orient the experimenters about cloud coverage before and during the flights.

The satellite images proved very useful for the intended purposes.

After the campaign the satellite images were archived on Exabyte tape and as paper prints for future reference.

6.4 Ice drift and concentration

One of the major issues of the FRAMZY '99 campaign was to get a better understanding of atmospheric influences on the sea ice drift and concentration in the Fram Strait.

6.4.1 Ice motion video loop

A sequence of daily high resolution AVHRR images was used to display the ice drift through the Fram Strait during April 1999 in a video loop. For better visualisation of each scene the near infrared channel 2 was copied to the red and green and the inverse of the mid-infrared channel 4 was copied to the blue channel of a colour image. This composite created a RGB full colour image, in which ice and clouds appear approximately white and the warm water in deep blue. The scenes in the loop are almost identical to those displayed for the thermal channel only in Appendix B1.

Although the loop contains only one scene per day the general southward ice drift through the Fram Strait becomes clearly visible. Interesting local features like cracks developing in the ice field Northeast of Greenland in mid April or the wind dependent circulation in the Northeast polynia are nicely visible on closer inspection of the loop.

The observation of the ice drift is disturbed by clouds in the atmosphere that cover ice and/or adjacent ocean areas frequently. And as only one scene per day is applied, atmospheric cloudiness appears to behave rather erratic, indicating the fast development of atmospheric phenomenon compared to sea ice motions. Often convective cloud streets due to cold air flow from the ice are visible over the ocean. Also thin cirrus can frequently be detected. Occasionally the whole scene is covered by clouds due to cyclone activity in or near the target area. The most prominent of these cases is the cyclone passing the Fram Strait region on 17-20 April 1999.

6.4.2 SSM/I derived ice properties

If cloud-free sea ice observation is required, microwave satellite data are the appropriate choice. Due to the large wavelength of a few mm this spectral range is virtually insensitive to cloud particles, except for very large precipitation particles. Therefore, data from the SSM/I (Special Sensor Microwave/Imager) radiometer on board the US-Air-Force DMSP (Defence Meteorological Satellite Project) satellite is widely used to derive ice classification, concentration and drift.

The group of W. Emery, National Snow and Ice Data Center (NSIDC) at the CCAR (Colorado Center for Astrodynamics Research) provided us with SSM/I-derived ice concentration and ice drift images of the Greenland Sea during April 1999. The originals can be found on the Web at the adress: *http://polarbear.colorado.edu/rt_ssmi/Fram.html*

In Fig. 6.2, examples of SSM/I-derived ice concentrations (left) and ice drift vectors (right) for the 17 and 20 April are given. These show the immense drift velocities (up to 100 cm/s) due to the cyclone passing the area on 17 April and the resulting retreat of the ice edge to the northwest of Svalbard in the scene from 20 April (which restored to the location before the cyclone by 25 April).

The complete set of drift images throughout the campaign can be found in Appendix B2. The location of the ice edge varied little during April 1999 while ice drift varies considerably, depending on wind conditions and location.

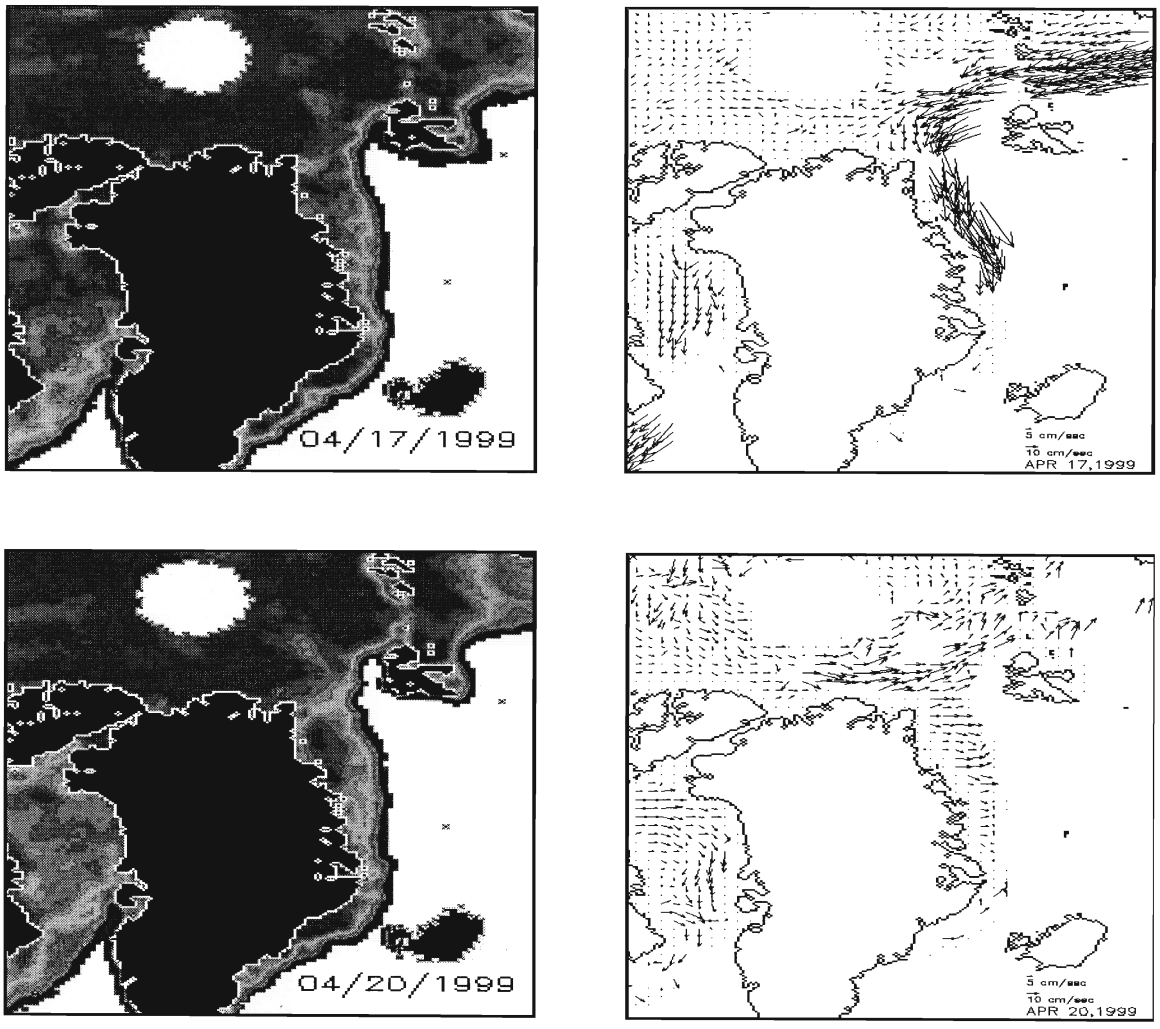

Figure 6.2: *Ice concentration (left) and drift (right) for 17 and 20 April 1999*

7. Regional modeling

(K.H. Schlünzen and S. Dierer, Meteorological Institute, University of Hamburg; D. Jacob and T. Semmler, Max-Planck-Institute for Meteorology, Hamburg)

Two models (REMO and METRAS) of different scale, resolution, physics and numerics are applied to study the influence of large-scale parameters (general circulation) and mesoscale parameters (sea ice distribution, sea ice temperature and water temperature) on the genesis and development of Fram Strait cyclones. The numerical simulations will also lead to a more general understanding of the data measured during the FRAMZY'99 experiment. Additionally, the models were applied for pre-simulations of the experimental set-up of the buoy array.

For the numerical experiments on the mesoscale-α the regional climate model REMO (Jacob and Podzun, 1997; Section 7.1.1) is used with a prescribed time-dependent sea ice distribution and is forced at the lateral boundaries with ECMWF analyses. The mesoscale-β model METRAS (Schlünzen, 1990; Schlünzen et al., 1996; Section 7.1.2) is applied with an interactive sea ice model (Birnbaum, 1998). METRAS is nested into REMO.

7.1 Applied models and data sets

The simulation domain of the REMO-model for the simulation of the FRAMZY'99 peroid is given in Fig. 7.1. The REMO model simulation domain covers the North Pole, Iceland, Spitsbergen and the east of Greenland. REMO is used with a horizontal resolution of 1/6° and extends up to 10 hPa using 20 vertical layers unequally stretched. Simulating the ARKTIS 1993 period (see Section 7.3), the METRAS model area is situated in the Fram Strait between Greenland and Spitsbergen with its centre at 80° N and at 0° E. The horizontal extension of the model area is about 400 km in North-South and East-West direction, respectively, with a horizontal resolution of 7 km. In vertical direction the METRAS model extends up to an altitude of 10 km with absorbing layers in the upper 6 km. The lowest grid level is placed 10 m above ground. The thickness of the model layers is increasing with height, reaching a value of 1000 m within the absorbing layers.

The REMO model (Section 7.1.1) is initialised and driven at the lateral boundaries with analysed data (ECMWF) and is run continuously for the central period of FRAMZY'99 (3 to 24 April 1999). The REMO results will be used to force the METRAS model (one-way nesting). For a pre-simulation of the expected buoy drift in the FRAMZY'99 experimental area, idealised forcing data were used in METRAS (Section 7.1.2). With these the influence of different initial and boundary values on the ice drift has been studied.

7.1.1 REMO model description

The regional model REMO is based on the dynamical concept of the Europamodell, the operational weather forecast model used by the German Weather Service (Majewski, 1991). It can be alternatively used with two physical parameterisation packages, namely the one applied in the "Europamodell" of the German Weather Service and the one used in the global climate model ECHAM (Roeckner et al., 1996). With the latter package, long term simulations are

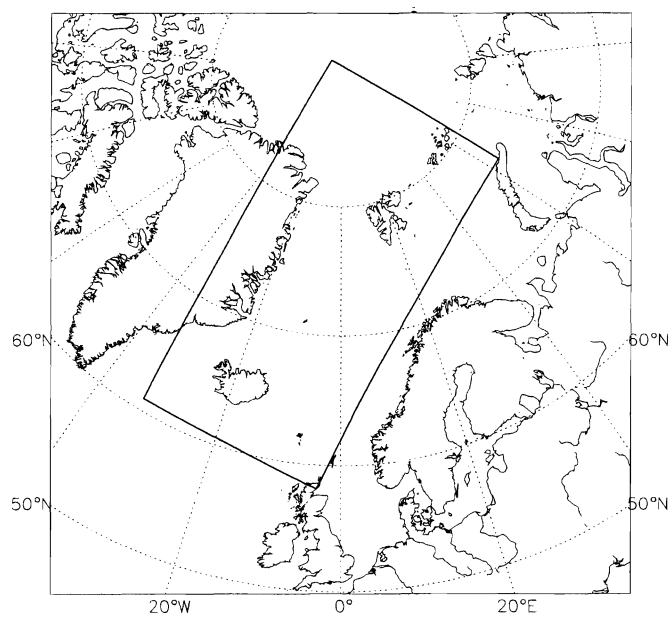

Figure 7.1: *Model areas of REMO and METRAS.*

possible with the prognostic, hydrostatic three-dimensional model, which simulates atmospheric phenomena on the meso-α-scale on different time scales. In order to hindcast special weather situations perfect boundaries, here analyses from the ECMWF, are used for initialisation and as lateral boundaries.

To study the FRAMZY'99 period REMO has been used with the ECHAM4 physics on a horizontal resolution of 1/6° driven every 6 hours by ECMWF analyses data available on 0.5° resolution. The orography, the variance of the orography and the orography induced surface roughness length is derived from the GTOPO30 data set (U.S. Geological Survey's EROS Data Centre, Sioux Falls, South Dakota). The other lower boundary conditions like surface background albedo, the soil type data set, forest ratio, leaf area index, vegetation ratio and field capacity of soil are maintained from the global data set of land surface parameters (Claussen et al., 1994).

For sea ice cover in REMO the surface temperature from the ECMWF analysis is used. If the surface temperature in a grid cell is below -1,79°C, the cell will be totally covered with sea ice, otherwise no ice will be within the cell. In a further experiment it is planed to use in each grid cell a partial sea ice cover derived from satellite data.

7.1.2 METRAS model description and set-up

The prognostic, three-dimensional, non-hydrostatic model METRAS is applicable to simulate phenomena of the mesoscale-β and mesoscale-γ. The characteristic horizontal extension of the simulated phenomena lies between some kilometres and up to 600 kilometres with a characteristic time scale of some hours to some days. Wind, temperature, humidity, cloud and

rain water content are calculated from prognostic equations. Pressure and density are derived from diagnostic equations. To consider a time dependent lateral forcing a nudging technique is applied (Lenz et al., 2000; Majewski et al., 1995). The nudging coefficients chosen for this study influence the model results up to a distance of 70 km from the lateral boundaries.

Sea ice model

The sea ice distribution and surface temperature can either be prescribed in space and time or be calculated interactively by application of a sea ice model (Birnbaum, 1998). In the sea ice model four ice thickness categories are distinguished (less than 10 cm, 10 to 40 cm, 40 cm to 1 m, more than 1 m). The sea ice model simulates dynamic effects like convergence and divergence of sea ice due to i.e. advection and internal ice stress (ribs) as well as thermodynamic effects like freezing and melting of sea ice. The dynamic and thermodynamic parts of the sea ice model can be used alternatively or simultaneously. In case of using the thermodynamic part, the sea ice is resolved by several vertical layers.

In the present studies the dynamic mode of the sea ice model is used. Surface temperatures are kept constant at the prescribed value for ice (-40°C) and water (-1.8°C) separately. A different percentage of ice coverage within a grid box is considered by application of the blending height concept (von Salzen et al., 1996). The subgrid-scale ice coverage might change with time due to the ice drift. This changes the surface temperature of a single grid box with time. At the time of initialisation the northern and western part of the METRAS simulation area are covered by ice of 1.5 m thickness. The ice coverage is 100 percent. The south-easterly part of the simulation area is open water, there is no orography included in the simulation area.

The atmospheric forcing of the sea ice model is taken from METRAS winds and stabilities. The ocean forcing is prescribed on the basis of measured ocean flows in the area of the Fram Strait (K. Hatten, 1998; pers. communication) in an idealised way: in the western part of the area the flow is in a southerly direction, in the eastern part the flow is in a northerly direction. The flow velocity is 15 cm/s at the western and eastern boundary. In between it is prescribed according to a sine function.

Forcing at lateral boundaries

For the pre-simulations of FRAMZY'99 the forcing data used to nudge METRAS at the open boundaries are prescribed consistent to a mesoscale cyclone that was observed during the field experiment ARKTIS 1993 (Brümmer and Hoeber, 1999). For the sensitivity studies a good control of all initial and boundary parameters of the model run is essential. Therefore the METRAS simulations are nudged with wind fields of an idealised cyclone. The observed cyclone during ARKTIS 1993 moved straight to the North. For the idealised cyclone the same track was used, but sensitivity studies concerning the influence of the cyclone track on the sea ice drift have been performed (Section 7.3.2).

Initialisation

The initialisation profiles are derived from the soundings taken at RV Polarstern at 00 UTC on 13 March 1993. The ship was located in the experiment area, surrounded by pack ice, while the cyclone passed through the area (see Fig. 7.1). The model run started at 00 UTC on 13 March 1993 and ended at 06 UTC on 14 March. For comparison and evaluation of the model results, cyclone pressure as well as the position of Polarstern are used.

The results of the coupled METRAS/sea ice model are evaluated with respect to the simulated ice drift and surface pressure (Section 7.3). After checking the results for plausibility, the simulated drift trajectory and pressure values are compared to those measured at Polarstern. Despite the idealised forcing data used, a qualitative agreement between the simulation and the measurements can be expected.

7.2 REMO simulations of atmospheric fields for the FRAMZY'99 period

REMO was initialised for 3. April 1999 at 00 UTC and continuously run until the 24. April 1999. The meteorological parameters sea level pressure, 850 hPa temperature, 500 hPa geopotential height, 10 m wind, 2 m temperature, precipitation, sensible heat flux and latent heat flux have been evaluated from the 17. to the 20. April 1999 to validate the model and to examine the capability of the model to simulate the observed FRAMZY cyclone.

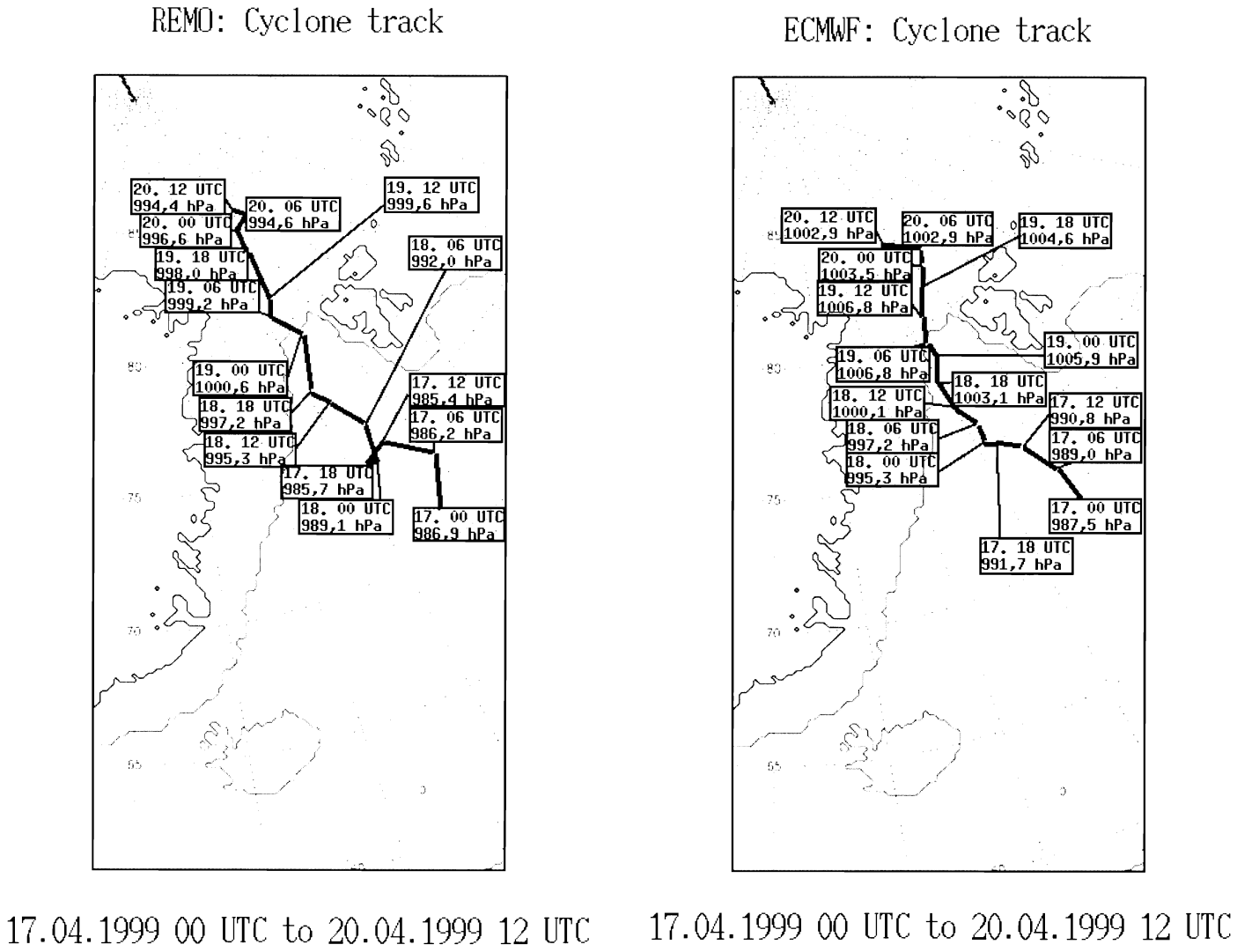

Figure 7.2: *Cyclone track in REMO and ECMWF.*

7.2.1 Model results for the observed cyclone

In the REMO simulation a cyclone moved northward from 71° N at the 17. April 00 UTC to 84,5° N at the 20. April 12 UTC. It remained quasi-stationary southwest of Spitsbergen from 17. April 1999, 18 UTC, until 18.April 1999, 06 UTC. The minimum pressure (ca. 985 hPa) occurred on 17. April 1999, 12 UTC (see Fig. 7.2). The cyclone was observed by ship, air craft and ice buoys. The model results are quite similar to the ECMWF analyses (see Section 7.2) and the weather charts of the German weather service (Appendix A), although there are some differences in the position and in the intensity of the cyclone. In REMO the cyclone is throughout the whole period up to 6 hPa deeper than the one in the analyses. Furtheron in REMO the cyclone is about 1 degree too far northerly positioned on 19. April 1999 at 12 UTC (see Fig. 7.2). The development of the sea level pressure in REMO from 18. to 19. April 1999 is shown in Fig. 7.3.

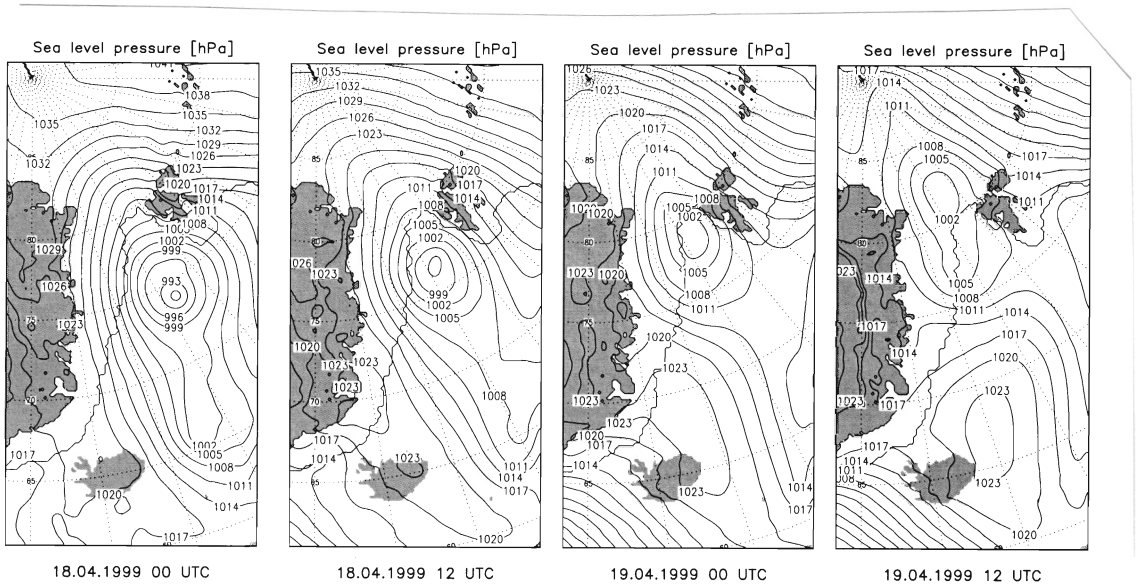

Figure 7.3: *Simulated sea level pressure from 18. to 19. April 1999.*

At 19. April 1999, 12 UTC, a cold air flow from ice to water can be observed (Fig. 7.3). This induces an unstable stratification and rising air because of the relatively warm water and the cold air in the 850 hPa level (Fig. 7.4). The result is an ice-water-circulation which works very similar to the well known land-sea-circulation and induces low pressure over the water due to the expansion of the warmer air. A second cyclone at the ice edge south of the original one can be seen at 19.4.1999, 18 UTC (Fig. 7.13 left).

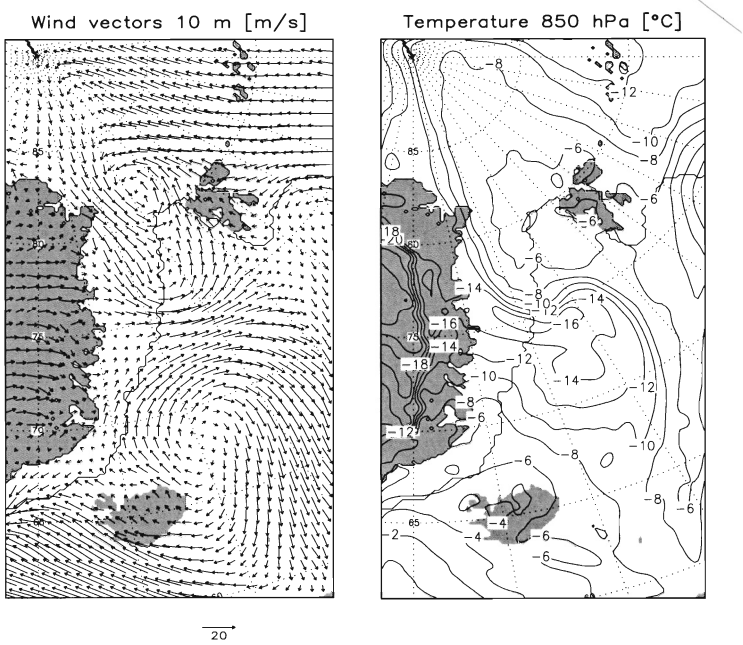

Figure 7.4: *Simulated wind vectors (left) and 850 hPa temperature (right) at 19. April 1999, 12 UTC.*

The negative (upward) sensible and latent heat fluxes resulting from the off-ice air flow are further indications for the unstable stratification (see Fig. 7.5). Furtheron there is much precipitation in the zone of convergence over the ice east of Greenland.

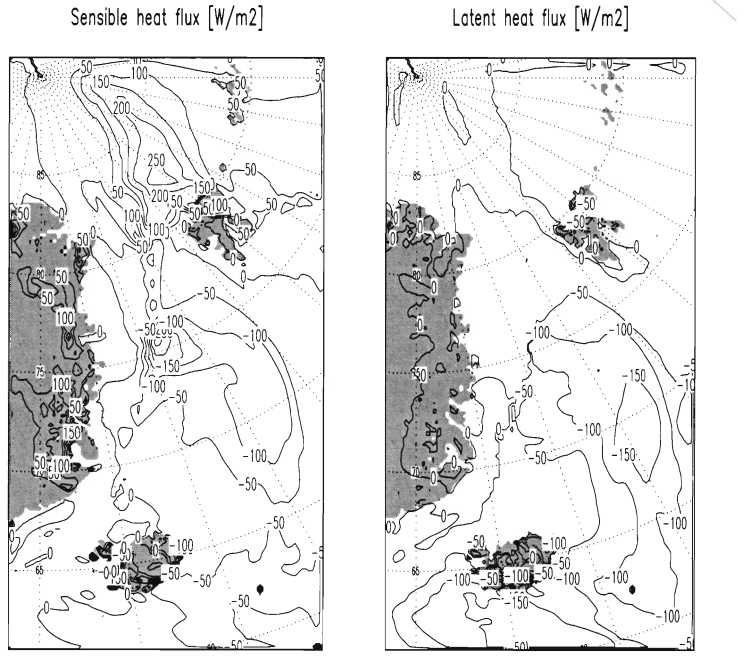

Figure 7.5: *Simulated mean sensible (left) and latent (right) heat fluxes at 19. April 1999 from 11 to 12 UTC.*

The second cyclone can also be seen in the 500 hPa geopotential height. Already on 18. April 1999 at 12 UTC a second trough begins to develop south of the first one (Fig. 7.6). This second trough deepens below the first one on 19. April 1999 at 00 UTC and moves north-eastward. Because of the lack of moisture over the ice the first trough vanishes later.

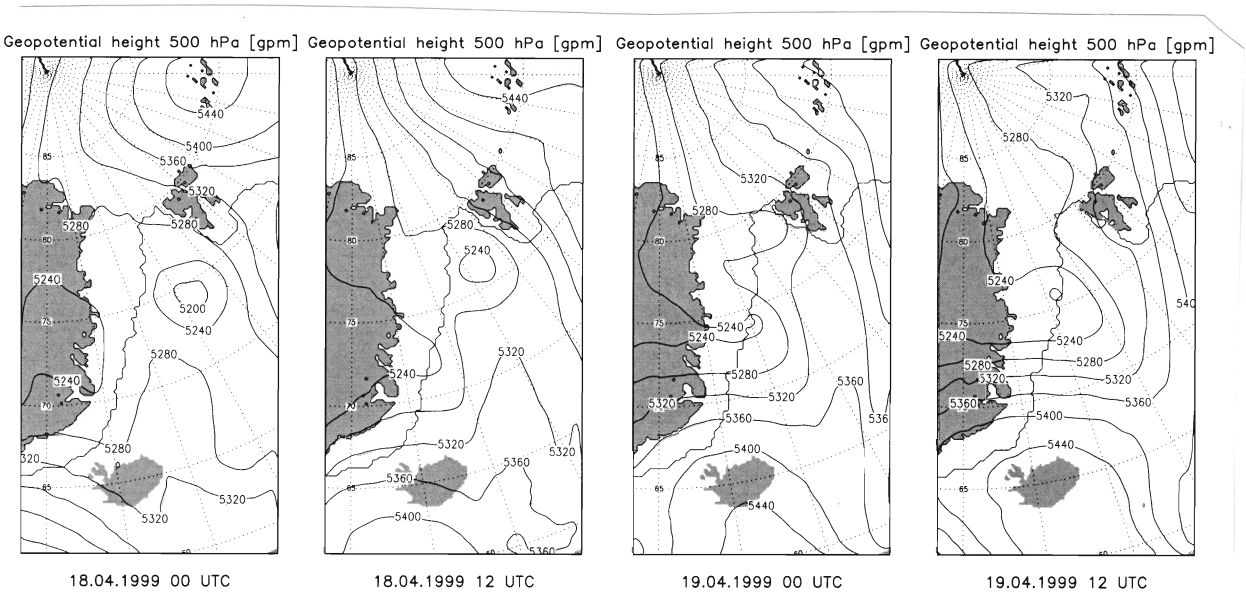

Figure 7.6: *Simulated 500 hPa geopotential height from 18. to 19. April 1999.*

In the 850 hPa temperature the northward moving cyclone can be recognized from the northward displacement of warm air (see Fig. 7.7). This induces a stable stratification over the cold ice and weakens the precipitation corresponding to the cyclone.

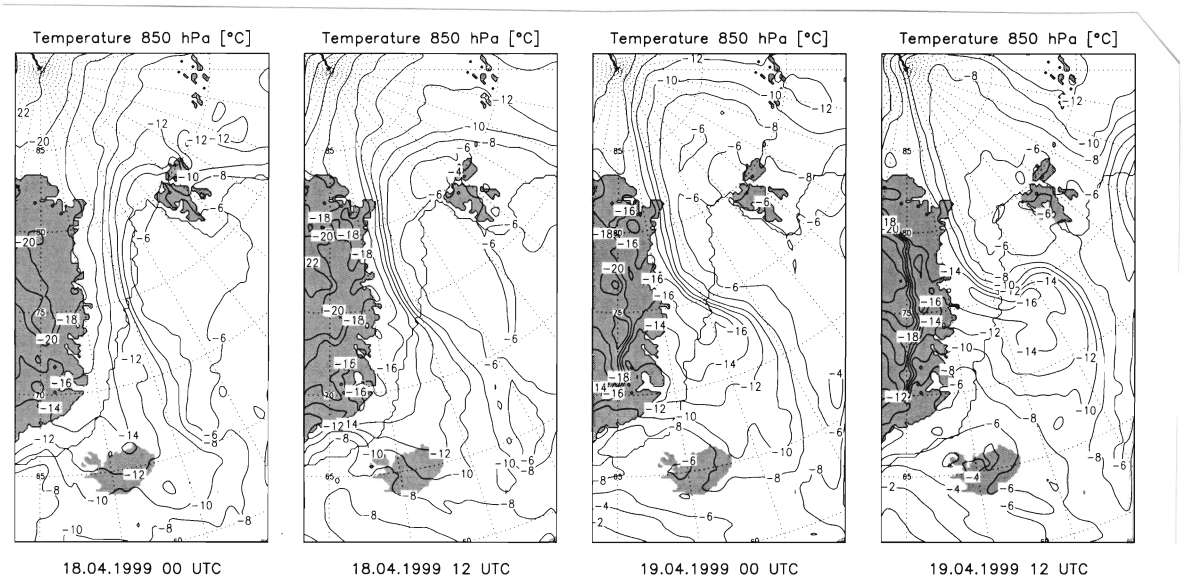

Figure 7.7: *Simulated 850 hPa temperature from 18. to 19. April 1999.*

7.2.2 Assessment of the results

A comparison between the REMO results on the one hand and the ECMWF analyses (see Section 2) and the weather charts of the German Weather Service (see Appendix A) on the other hand reveals similar large scale structures.

However, there are some differences in the fine structures. In REMO the original low pressure system is more intensive, which can be seen both in the sea level pressure and in the 500 hPa geopotential height. There are also strengthened gradients in the 850 hPa temperatures in the REMO results. Neither in the analyses nor in the weather charts a second low develops. As an example the sea level pressure and the 850 hPa temperature from the ECMWF analyses and from REMO are shown in Fig. 7.8.

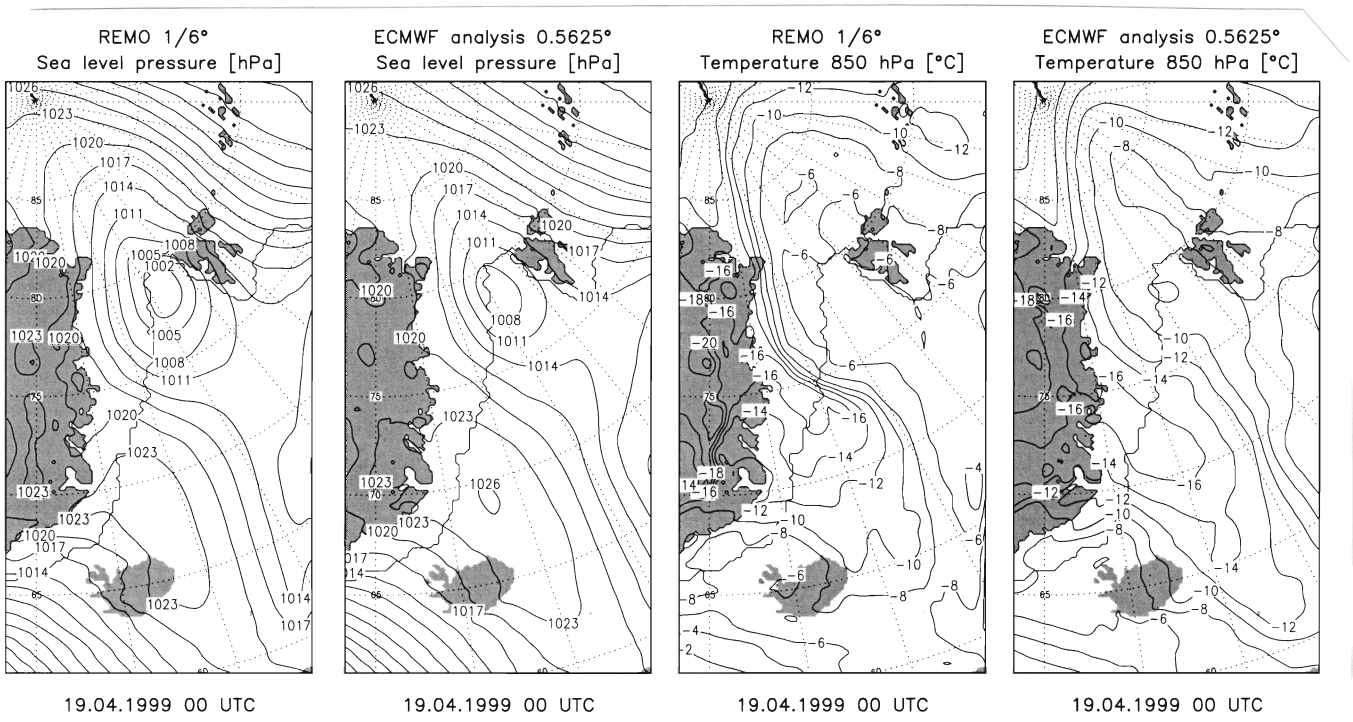

Figure 7.8: *Comparison of REMO results with ECMWF analyses at 19. April 1999, 00 UTC.*

All differences could be due to the coarser resolution of the ECMWF model and the sparse observational density in this region. The question if the additional details of the REMO results are not only plausible but realistic shall be answered by comparing the REMO results with the observations of the FRAMZY field experiment (ice buoys, ship and air plane measurements).

The simulated ice edge in REMO has been compared with ice charts of the Norwegian meteorological institute in Tromsoe. The observed ice edge and the one determined by REMO are in rough agreement with each other, although there seems to be a systematic difference: The ice edge in REMO is shifted to the south up to 50 km near Spitsbergen compared with the area of open drift ice (ice coverage of 40 to 70 %) from the Norwegian meteorological institute (see Appendix C).

An easy solution to correct for the ice edge differences will be to prepare the SSMI derived ice coverage as input for REMO. Furthermore REMO should consider a partial sea ice cover, i. e. a percentile coverage of sea ice is admitted in each grid cell, instead of having only totally ice free and totally ice covered grid cells. Then a transition between sea ice and open water is possible as in the ice charts instead of the unrealistic sharp ice edge.

7.2.3 Sensitivity studies on ice edge influence

To study the influence of the ice edge on the cyclone development three sensitivity experiments with different ice edges have been performed. They were initialised for 3. April 1999 at 00 UTC as was the reference run. The ice edges were prescribed north of the Fram Strait, south of the Fram Strait and north of Iceland (Fig. 7.9). The initial temperature field and lateral forcing data were kept. Only the water surface temperatures were increased to -1.79°C, if there was ice in the reference run and water in the sensitivity run, respectively. In the same way the ice surface temperatures were reduced to -1.79°C, if there was water in the reference run and ice in the sensitivity run.

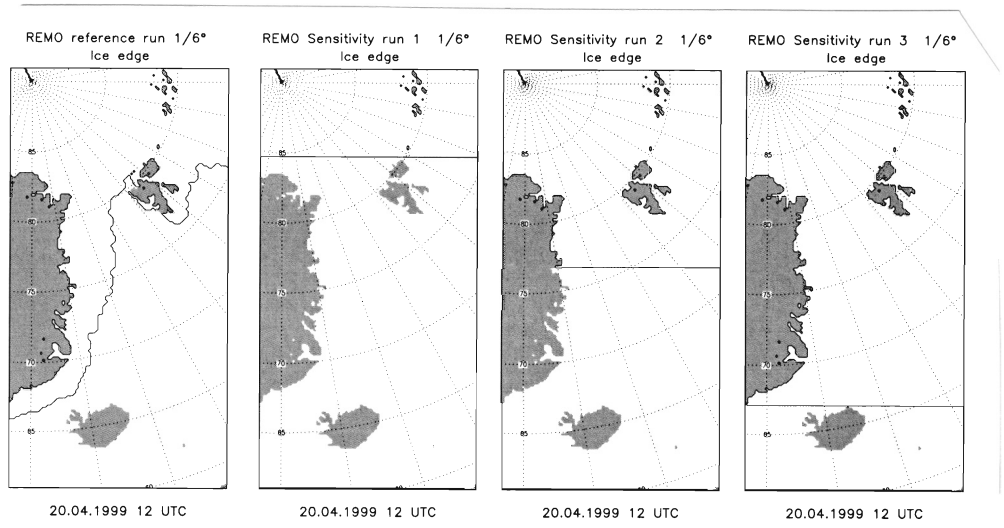

Figure 7.9: *Ice edges in REMO reference and sensitivity runs.*

In spite of the large displacements of the ice edge there are few differences between the cyclone results on 17. April 1999. Obviously the phenomena are mainly determined by the large-scale circulation pattern. The cyclone is situated close to the boundary of the simulation area. Therefore the influence of the lateral boundary conditions on the development of the cyclone is quite large at this time. On the following days (at 18. to 20. April) noticeable differences reveal. On 18. April cold air can be seen at the 850 hPa level for sensitivity run 3 (far southerly positioned ice edge). Similar to the reference run, but much more southerly positioned and 36 hours earlier, there are a strong off-ice air flow, a strong temperature difference between water and ice (Fig. 7.10) and intense sensible and latent heat fluxes (Fig. 7.11). Since the atmospheric temperatures at initialisation is the same for run 3 as for the basic run, intense sensible heat fluxes occur at the former ice edge. Even in the 500 hPa geopotential height the effect of the ice-water-circulation can be seen near the southerly positioned ice edge with the geopotential height lowest in the third sensitivity run (Fig. 7.12).

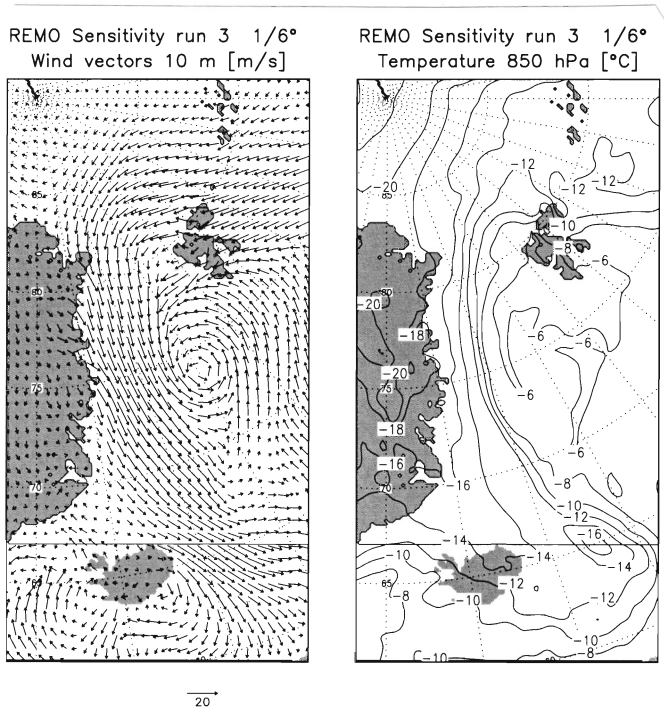

Figure 7.10: *10 m wind vectors (left) and 850 hPa temperature (right) in sensitivity run 3 at 18. April 1999, 00 UTC.*

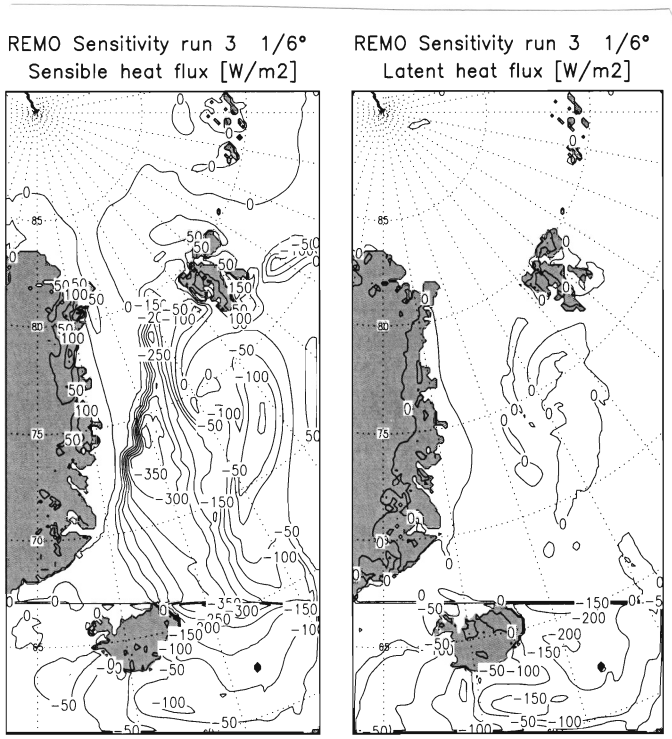

Figure 7.11: *Mean sensible (left) and latent (right) heat fluxes in sensitivity run 3 from 17. April 1999, 23 UTC to 18. April 1999, 00 UTC.*

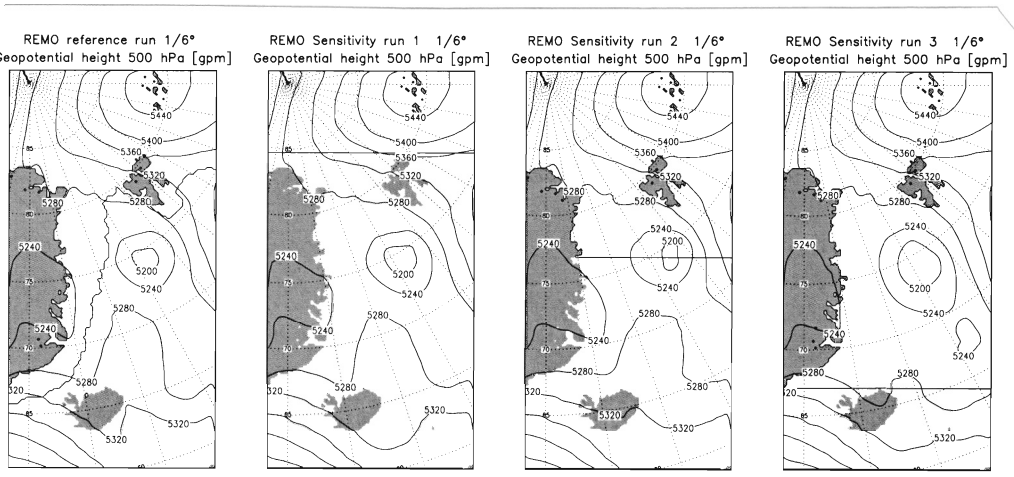

Figure 7.12: *500 hPa geopotential height in the reference and sensitivity runs at 18. April 1999, 00 UTC.*

In sensitivity run 3 the cyclone is weaker than in the other runs due to weak heat and moisture fluxes over the ice. At the 19. April 1999, 18 UTC remarkable differences arise in the pressure pattern: The secondary cyclone developing at the ice edge in the reference run south of the primary large scale dependent cyclone cannot be found or is at least weakened in sensitivity runs 1 and 3 (Fig. 7.13). There is generally more precipitation in sensitivity run 1 than in the other ones due to the higher supply of moisture.

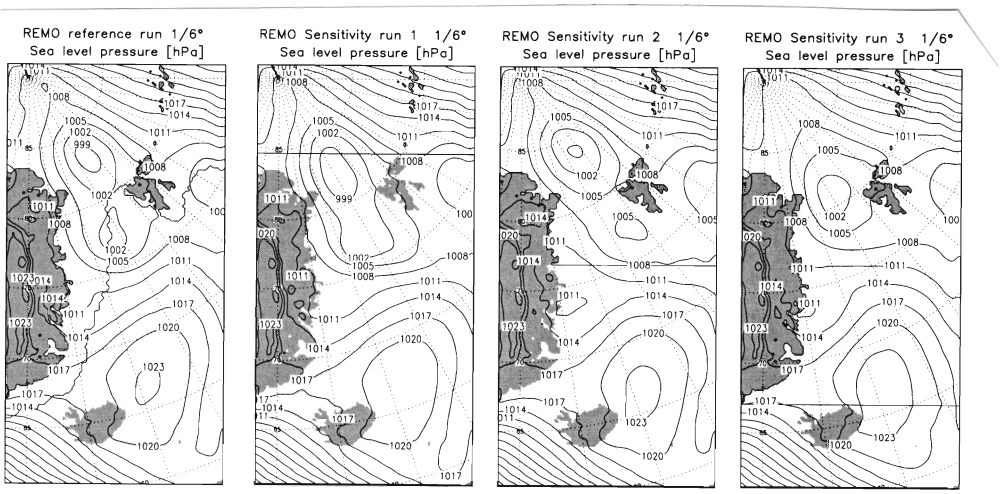

Figure 7.13: *Sea level pressure in the reference and sensitivity runs at 19. April 1999 18 UTC*

The further development shows a weakening of the temperature gradients in 850 hPa as well as the pressure gradients. As a result of this and cyclone movement over the ice the precipitation connected with these cyclones weakens in all runs. But there is still the largest precipitation in sensitivity run 1 due to the most northerly ice edge (not shown).

7.2.4 Conclusions

REMO is able to simulate the large-scale meteorological structures in the Arctic region and gives additional and at least plausible information about the mesoscale phenomena. It is necessary to see from the measurements performed in the FRAMZY experiment, if the additional information is not only plausible but realistic. The most remarkable information is the one of a second cyclone developing at the ice edge in the reference run. Phenomena like the ice-water-circulation and the weakening of the cyclone over ice due to the reduced energy input can be seen in the reference run as well as in the sensitivity runs considering modified ice edges. Also the dependence of the wind direction on the amount of precipitation can be recognized: The largest amounts of precipitation occur, if the wind is directed from ice to water connected with intense heat exchanges. So, all REMO runs clearly show the dependence of the development of cyclones on the ice edge.

7.3 Influence of mesoscale parameters on the sea ice drift (simulations with METRAS)

Sensitivity studies have been performed to study the dependence of the ice drift on different initial and boundary values (ice coverage, ice thickness, sea ice temperature, cyclone track, ocean current). The simulation results were also investigated with respect to the possible movement of the ice drift buoys to be expected at different sites within the FRAMZY'99 area.

7.3.1 Results of basic model run

The input data for the basic model run are given in Section 7.1.2. A comparison of the simulated wind fields at a height of 10 m and the simulated ice drift shows a strong influence of the atmospheric forcing on the ice drift (Fig. 7.14). The ice edge is marked by isolines of 1% and 90% ice coverage. The simulated cyclone moves northward through the simulation area and shows its fingerprint in the simulated ice drift. The ice drift vector is directed to the right of the wind vector in accordance with observations (e.g. Nansen, 1902).

Besides the atmospheric forcing, the ice drift is influenced by the ocean current, which results in an intensified southerly component at the western boundary and an additional northerly component at the eastern boundary of the simulation area. The simulated wind velocities at 10 m height are about 7 to 9 m/s while the measured wind is varying between 5m/s and 6m/s in the warm-sector of the cyclone and about 22 m/s in the cold front (Brümmer and Hoeber, 1999). Altogether the simulated wind is weaker than the measured one because the forcing wind field that was prescribed is too weak. The mean simulated ice drift velocities are about 17 cm/s to 19 cm/s. The ice drift velocity measured during the ARKTIS'93 experiment varied between 0.1 m/s and 1m/s with a mean drift velocity of 0.2 m/s in the North and 0.6 m/s in the East Greenland current (Brümmer and Hoeber, 1999). Therefore, the simulated ice drift is in the range of the measured values. The mean ratio between ice drift velocity and wind velocity at 10 m height is about 3 percent, which is a reasonable value (Nansen, 1902) and lies at the lower boundary of the measured mean ratio that varies between (5% ± 3%) and (9% ± 3%).

Due to the ice movement the ice edge is displaced towards north and east (Fig. 7.15). The

displacement that takes place at the western ice edge is much stronger (~30 km) than at the northern ice edge (~7 km). This is a consequence of the atmospheric forcing: at the western ice edge the wind is most of the time directed towards open water and sea ice can freely move while the northern ice edge is mainly moved towards the pack ice.

Based on the simulated ice drift, trajectories are derived from 10 minute mean values of the ice drift velocity calculated at every grid cell. For the ice in energy grid all the displacement in x- and y-direction is calculated every 10 minute interval resulting in the new position. For position of the RV Polarstern the calculated drift (Fig. 7.16, top) and the drift of the ship (Fig. 7.16, bottom) are quite similar. The trajectories differ in detail: the horizontal extension of the simulated drift (3 km x 1.5 km) is smaller than the drift experienced by RV Polarstern (8 km x 5,5 km). Reasons are different initial position with respect to the track of the polar low, the weaker wind velocity in the model simulation compared to the measurements, the track of the polar low itself and differences in surface parameters (ocean current, ice thickness, ice coverage, surface temperatures). The influence of these parameters on the simulated drift trajectories are investigated in Section 7.3.2.

In addition to the position, the surface pressure simulated at the positions along the simulated drift trajectory is compared with the data measured at the RV Polarstern (Fig. 7.17). The simulated surface pressure is taken from 10 minute-mean values and is in the order of the measured one. The decrease of the simulated pressure is about 6 hPa and therefore remarkably underestimating the measured one (~20 hPa). The reason is again the lower wind speed in the simulation. The pressure minimum in the measurements is reached at 18 UTC and in the simulation at about 12 UTC. The time lag is a consequence of the different starting positions of the trajectories resulting from differences on the track of the idealised low used in the model.

In summary, the simulation results are plausible, agree qualitatively with the measurements but differ quantitatively. This is acceptable, keeping in mind the idealisations used for this run. Especially the weak wind velocity in the forcing data effects the ice drift and the pressure decrease. The intensity of the lateral forcing also remarkably influences the model results and should be weakened.

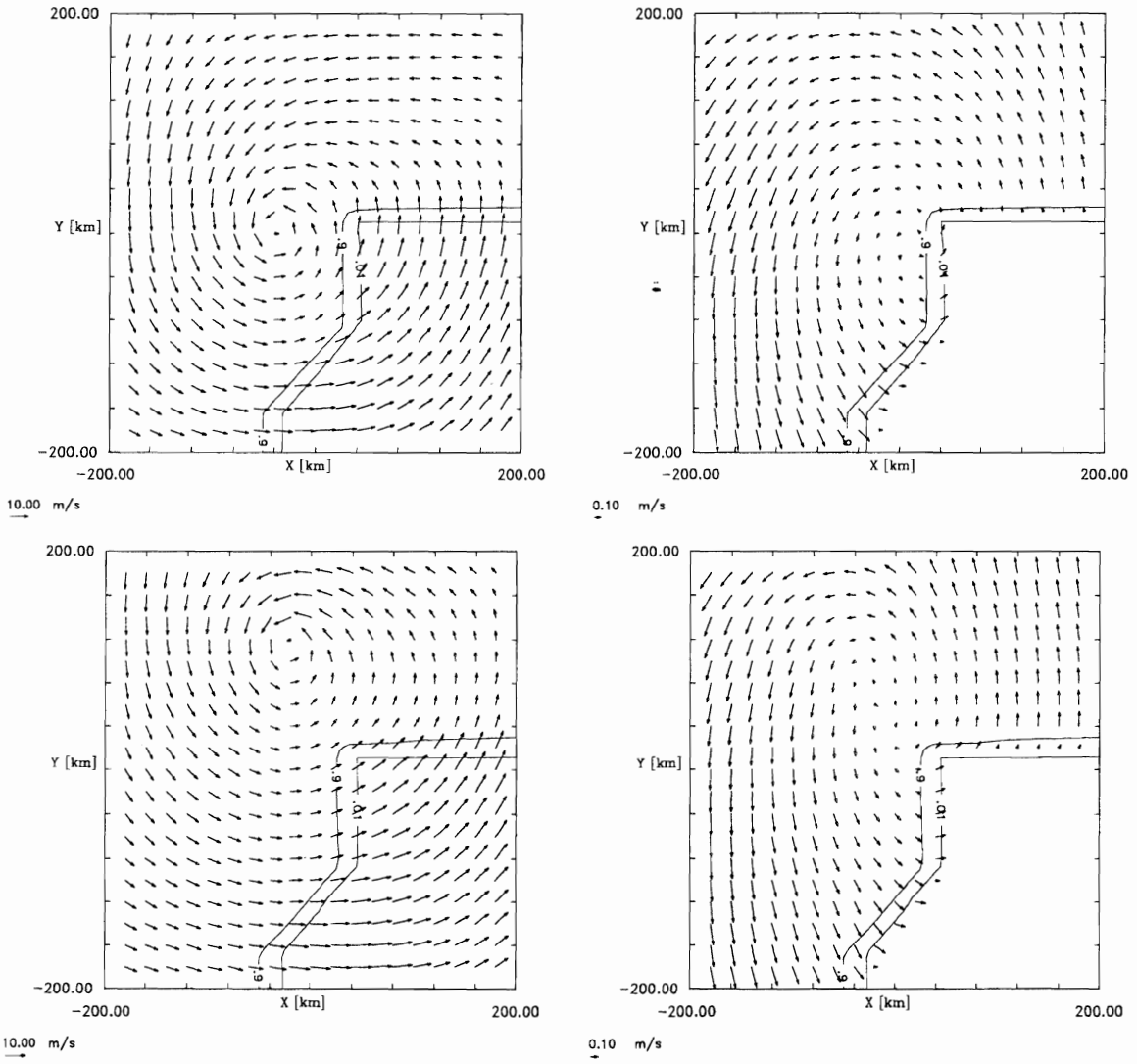

Figure 7.14: *Wind field at 10 m height (left) and ice drift field (right) in the METRAS results at 12 UTC (top) and 18 UTC (bottom). The ice edge is marked by isolines of 1% and 90% ice coverage.*

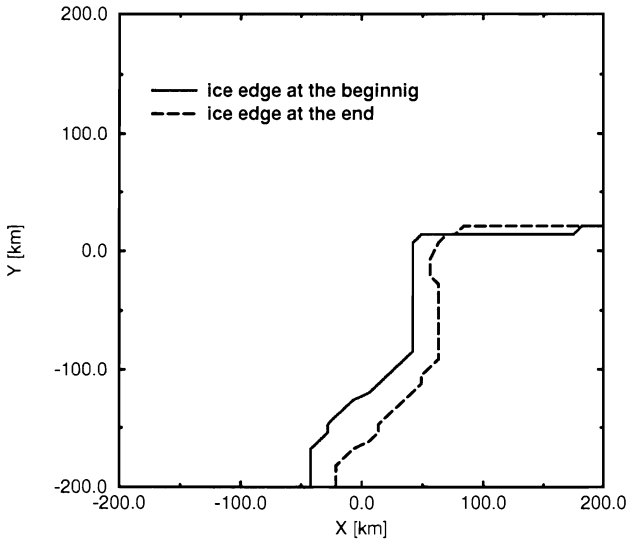

Figure 7.15: *Position of the ice edge at the beginning, 00 UTC on 13 March (----) and at the end of the simulation, 06 UTC on 14 March (- - -).*

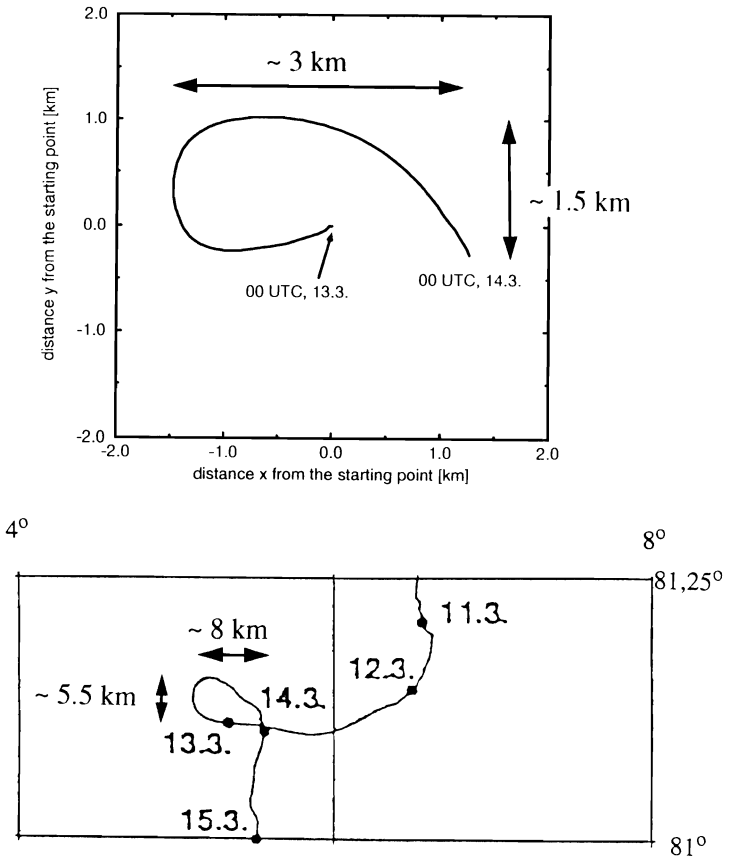

Figure 7.16: *Simulated (top) and measured drift (bottom) for the position of RV Polarstern.*

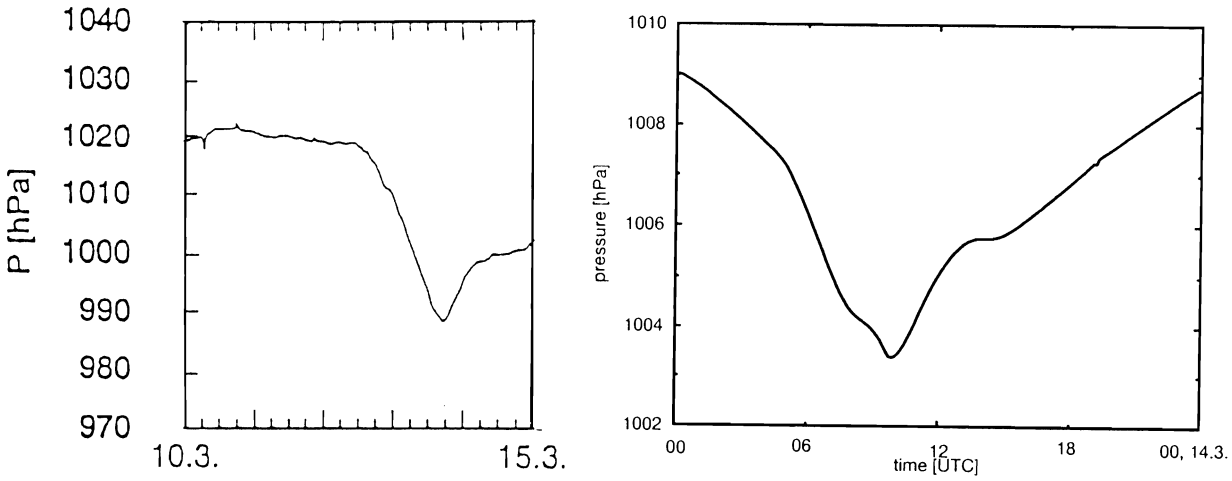

Figure 7.17: *Surface pressure simulated (right) and measured (left) for the positions of Fig. 7.16.*

7.3.2 Sensitivity of ice drift on mesoscale parameters

Sensitivity studies have been performed to investigate the dependence of the sea ice drift on ice thickness, ice coverage, ocean current, cyclone track and surface temperature field. The model simulations differ in one parameter only (Table 7.1) and are else based on the basic model run (Section 7.3.1). The sensitivity simulations are compared with the basic model run regarding differences in the sea ice drift and ice coverage.

Table 7.1: Varied parameters in the METRAS sensitivity studies

Changed Parameter	Basic Simulation	Sensitivity Simulation
ice thickness	1.5 m	4.0 m
ice coverage	100 %	95 %
ocean current	with (see Section 7.1.2.)	without
cyclone track	moving northerly, approximately in the middle of the model domain (Fig. 7.14)	crossing the model domain from the south-west to the north-east
ice surface temperature	homogenous (-40°C)	inhomogeneous (Fig. 7.18)

a. Ice thickness

Due to the fact that it is not possible to get detailed information about the ice properties, parameters like ice thickness remain within a range of uncertainty. The ice thickness is increased to 4 m (Table 7.1) in order to investigate its effect on the ice drift. The comparison with the basic run shows large differences in the ice drift velocity (~12 cm/s bias; Table 7.2). The deviations have a maximum at 12 UTC (~14 cm/s). This difference might be a consequence of the longer time period that is needed to accelerate ice of higher thickness from the starting value

of 0 cm/s. However, movement of thicker ice floes is less dependent on the atmospheric forcing. Therefore differences in the ice drift velocities are quite reasonable. Additionally, the average ice drift direction differs, reaching a bias of 40 degrees at 00 UTC, 14.3. The different ice drift effects the displacement of the ice edge (Fig. 7.18). There are only slight differences at the northern ice edge, where the displacement is small in general, but the western ice edge is moved about 10 km less than in the basic run.

Table 7.2: Bias of ice drift velocity (sensitivity run - basic run) at 12 UTC, 18 UTC, 00 UTC 2nd day, 06 UTC 2nd day. Values are in cm/s.

Sensitivity simulation	12 UTC	18 UTC	00 UTC 2nd day	06 UTC 2nd day
ice thickness	-14	-12	-12	-9
ice coverage	0	1	1	-0
ocean forcing	-7	-7	-6	-5
cyclone track	7	7	7	3
surface temperature field	-1	0	1	-0

b. Ice coverage

To study the sensitivity of ice drift on the ice coverage this is reduced to 95% (Table 7.1). The variation of 5% is in the range of uncertainty that is realistic for the estimation of ice coverage (Lüpkes, 1999, personal communication). The bias of the ice drift velocity is low (~1 cm/s) but with deviations in the ice drift direction (bias ~10 degrees). The displacement of the ice edge is similar to the basic case. Small deviations occur at the western ice edge. The northern ice edge's displacement is not effected by the ice coverage. However, despite the small changes in the average values of the drift, the form and the extension of the drift trajectory for RV Polarstern is changed. In the basic run, the extension of the simulated drift trajectory is 1.5 km x 3.5 km while in the simulation with lower average ice coverage the trajectory reaches an extension of 2.5 km x 4 km. Therefore, the average ice coverage may be one of the reasons for the underestimated extension of the drift trajectory.

c. Ocean forcing

To investigate the influence of the ocean current on the ice drift, a sensitivity study with an ocean flow of 0 cm/s is performed. The lack of ocean forcing results in a remarkably lower mean ice drift velocity with a bias between 5 cm/s and 7 cm/s which is about 25 % of the mean drift velocity in the basic model run (~20 cm/s). The highest differences occur at the eastern and western boundary of the model domain where the ocean current has its maximum values. Most of the simulation time the atmospheric and ocean forcing have the same direction. The missing ocean forcing therefore causes a reduction of the ice drift velocity. Differences in the ice drift direction are between ~10 and 20 degrees. The deviations in the ice drift direction increase at the end of the simulation period when the directions of the oceanic and the atmospheric forcing become quite different. At this time the cyclone is in the northern part of the model area, the model domain is mainly influenced by north westerly winds while the ocean forcing of the basic run is still in North-South direction.

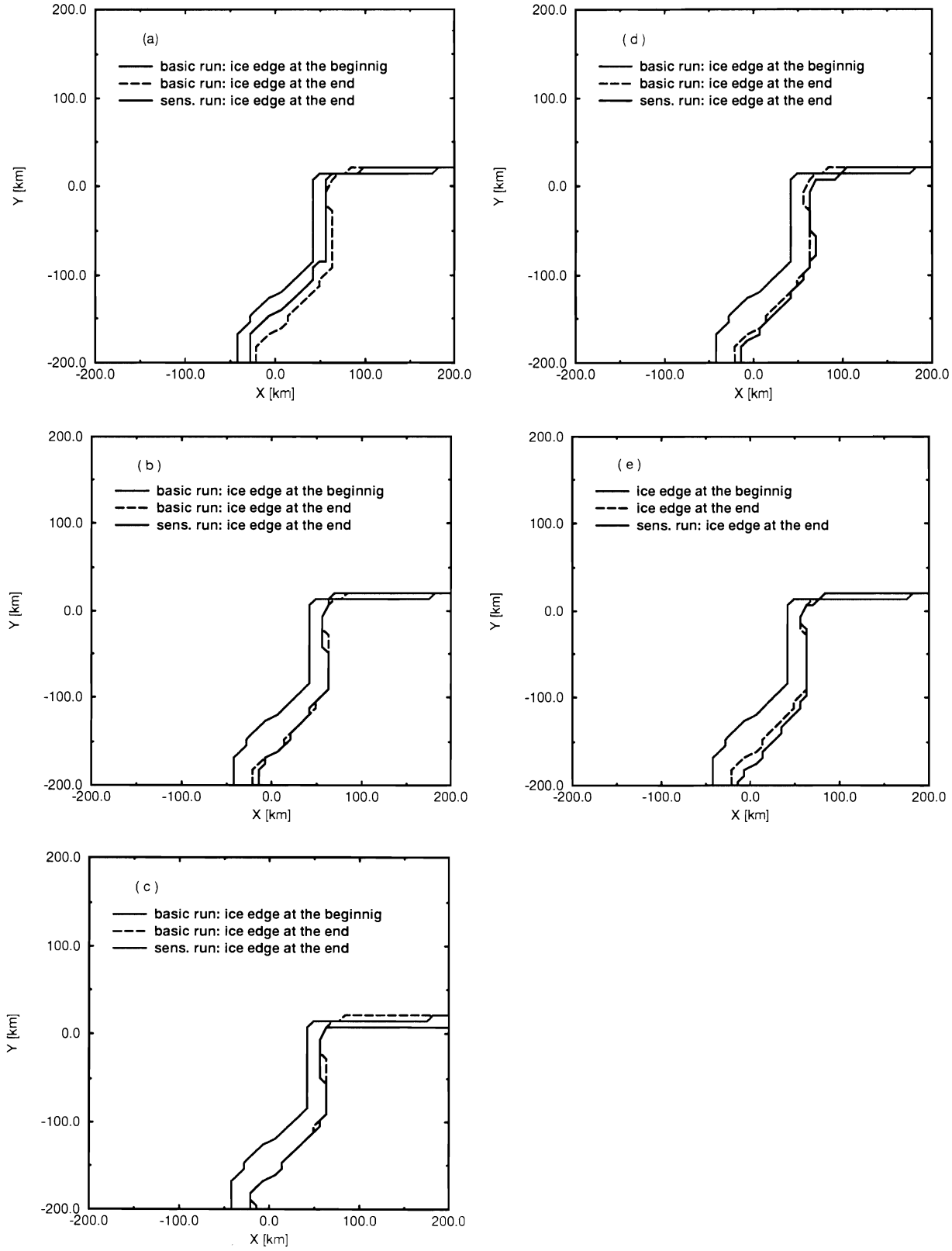

Figure 7.18: *Ice edge at the beginning (.....) and at the end of the simulation in the basic model run (- - -) and in the sensitivity simulations (----) (a) ice thickness, (b) ice coverage,(c) ocean current, (d) cyclone track, (e) surface temperature field.*

By changing the ice drift, the ocean flow also influences the displacement of the ice edge. In the results of the basic model run, the ice edge extending in east-west-direction is moved northerly by ~7 km. Neglecting the ocean current it is moved southerly by ~7 km. The reason is the southward component of the atmospheric forcing at the end of the simulation. It results in a stronger southward movement of the ice compared to the northward motion at the beginning of the simulation because the wind flow is directed to the open water. In the basic run, the displacement in southerly direction forced by the atmosphere is counteracted by the ocean forcing. The differences at the ice edge extending in North-South direction are only small due to the fact, that at its position in the middle of the model area the ocean flow velocity in the basic run is very small.

d. Cyclone track

In the basic model run the cyclone passes approximately in northerly direction. In the sensitivity run the cyclone track is varied: the cyclone moves north-easterly, starting from the south-western part of the model area. Significant changes in the ice drift velocity as well as in the ice drift direction occur. The mean drift velocity in the sensitivity simulation is ~7 cm/s higher than in the basic run. Due to the different atmospheric forcing, the ice drift direction changes (bias ~20 degrees). There are only slight changes in the displacement of the ice edge, probably because the atmospheric forcing does not differ significantly at the ice edges (Fig. 7.18). Finally, changing the atmospheric forcing does not only change the ice drift but also the ice coverage which may affect the heat transfer between ocean and atmosphere.

e. Surface temperature

A more detailed prescription of the ice surface temperature (Fig. 7.19) results in remarkable deviations between the surface temperature fields at the ice edge. The bias of ice drift velocities is small (0 cm/s to 1 cm/s). However, deviations occur especially at the ice edge extending in North-South direction. This is the region where the differences in the surface temperature field are strong. In this area the bias of ice drift velocity is about 3 cm/s during the whole simulation. This is the reason why the displacement of the westerly ice edge is different in both model simulations (Fig. 7.18). If a more detailed ice surface temperature field is prescribed, the ice edge is further displaced to the east (~ 7km), caused by differences in the flow field at the ice edge. Concluding, the prescription of a more detailed surface temperature field does not change the mean values of the ice drift, but may cause remarkable local deviations.

7.3.3 Pre-simulation of buoy movements

During the FRAMZY experiment an array of ice drift buoys was placed in the experimental domain in order to receive information about the ice drift. This information includes pressure measurements used to derive the atmospheric forcing and to estimate the internal ice stress. The pre-simulation of buoy movement is performed to investigate how an buoy array with a starting configuration similar to the one used during the FRAMZY'99 experiment is affected by a cyclone moving through it. A buoy array with its centre at 80.5 N and 2.5 W and a horizontal resolution of 40 km is assumed in the model domain (Fig. 7.20, left). The results of the ARKTIS'93 simulation (Section 7.3.1) are used to calculate the movement of the buoys. Additionally, variations in the results due to changed parameters (Section 7.3.2) are investigated.

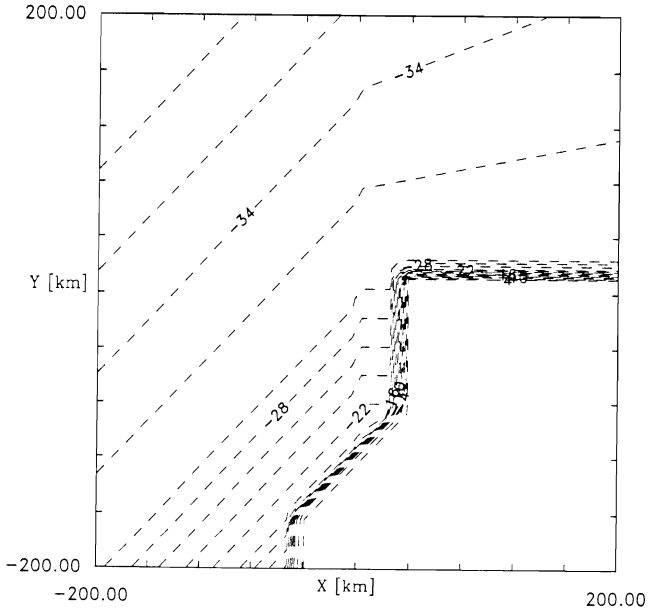

Figure 7.19: *Ice surface temperature field prescribed in the sensitivity run (from -2° C to -40°C, increment 2K).*

The whole buoy array has an extension of 160 km x 160 km. Therefore a cyclone crossing this area effects different parts of the array differently. Looking at the results of the basic simulation (Fig. 7.20, left), the western part of the array is strongly influenced by the ocean flow adding a southerly velocity component to the ice drift. In the eastern part the pattern of the trajectories indicates that the centre of the cyclone passes near this area. The trajectories in the northern part of the buoy array are especially influenced by easterly winds in the northern part of the cyclone. The southern part of the array is mainly effected by westerly winds in the southern part of the cyclone. Due to these different influences, the relative positions of the buoys in the array change (Fig. 7.20, right). Comparing the buoy array at the beginning and at the end of the simulation, the initial configuration is changed by shearing and a slight rotation.

In case of varied ice thickness, ice coverage and ice surface temperature field, the extension of the drift trajectories vary but the buoy array behaves similar to the basic run. In the simulation without the ocean flow, the extension of the trajectories decreases as well as the shearing of the array. The rotation of the array dominates in this case. In case of a different cyclone track the ice drift is faster, therefore the buoys are further displaced and the deformation of the array is different to the one in the basic run. The buoys are displaced further south (Fig. 7.20). The array is still rotated but the deformation of the field is different to the one in the basic run (Fig. 7.20). Concluding, the configuration of the buoys seems to be suitable to study the ice drift and the internal ice stress. The simulations point out that variations of ocean and atmosphere flows mainly influence the ice drift and therefore result in different deformations of the buoy array.

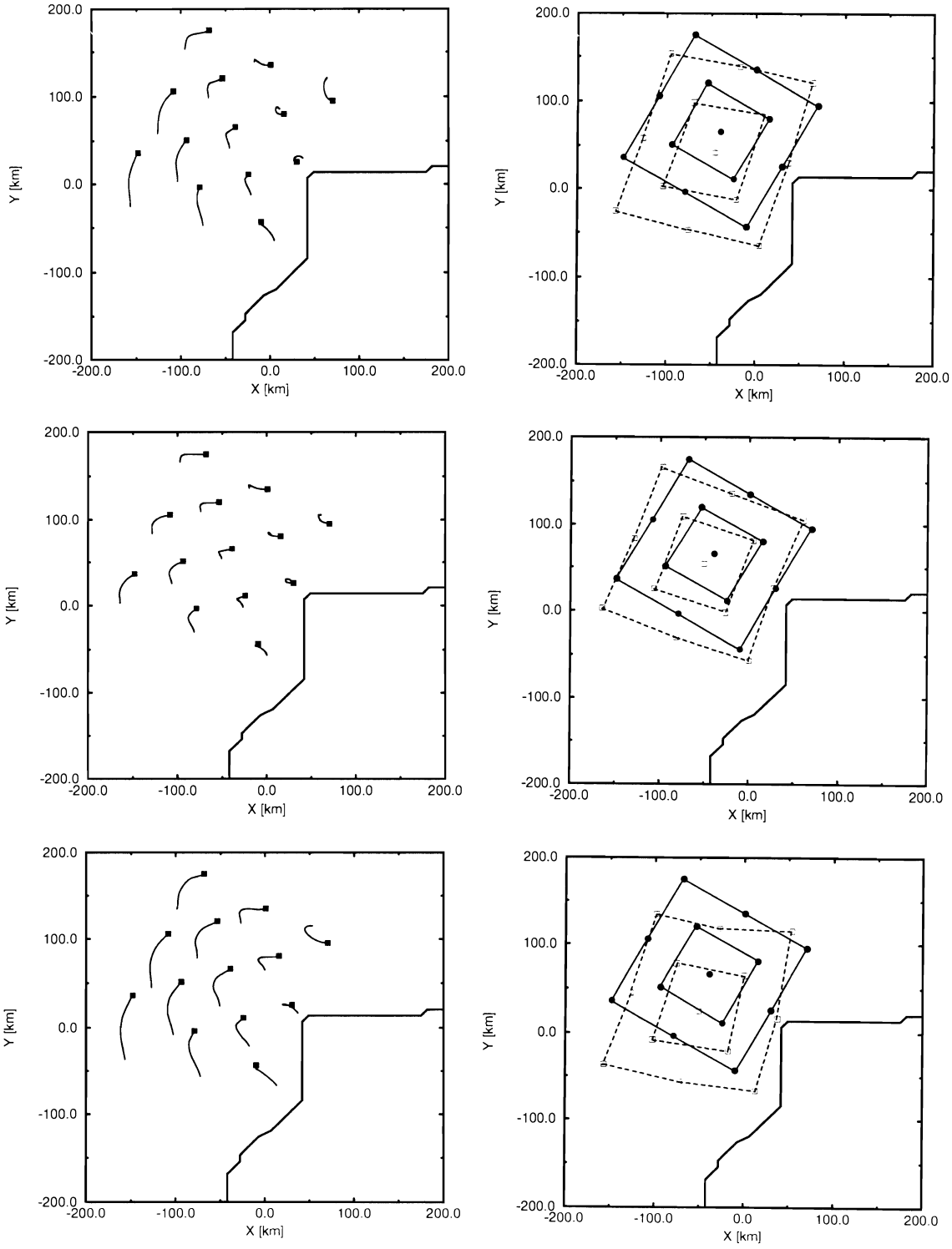

Figure 7.20: *Left side: Ice drift trajectories of the buoys. The trajectories are increased to three times their extension so that they are easily recognizable. The starting point is marked by a filled square. Right side: Configuration of the buoy array at the beginning (filled circles) and at the end of the simulation (open squares). Top: Basic simluation, middle: simulation with varied ocean flow, bottom: simulation with varied atmospheric forcing. The ice edge at the beginning of the simulations is marked by (---).*

7.3.4 Conclusions

A situation during the ARKTIS'93 experiment is simulated with the model METRAS coupled with a sea ice model. The results of the simulation are plausible and show a qualitative agreement with the measurements. The quantitative comparison shows some differences: the ice drift as well as the pressure decrease are underestimated in the simulation. The underestimation results mainly from the prescribed lateral forcing data. The wind prescribed is weaker than in the measurements. Repeating the simulation with higher mean wind velocity (~16 m/s) results in a more extended drift trajectory (7,5km x 13km). The pressure decrease of ~20 hPa along the simulated trajectory agrees well with the pressure measured at RV Polarstern. Keeping in mind the idealized forcing, the good agreement with the measurements shows that the model system of METRAS coupled with a sea ice model is suitable for investigating the influence of a cyclone on the ice drift.

Sensitivity studies concerning different initial and boundary conditions are performed. Concluding, the variations of ice thickness, ocean and atmospheric forcing result in remarkable changes of the ice drift, changing the mean values of ice drift velocity and direction. Influence of the ice coverage and surface temperature field are less relevant for the average ice drift but change the drift locally as well as the heat fluxes to the atmosphere. Therefore, in order to realistically simulate the influence of a cyclone on the ice drift and its response to the atmosphere, it is necessary to prescribe or calculate ice thickness, ice coverage, ocean current, cyclone track and surface temperature as realistic as possible. The sensitivity studies also indicate the necessity of a model pre-run: this one is performed to calculate a stationary ice drift field and surface temperature field before starting the main simulation. This is inevitable because dependent on ice thickness and ice coverage the duration for receiving stationary drift velocities is quite different. Last but not least, the nudging should be reduced in the model simulations to enlarge the boundary value independent simulation area of the model.

The simulation of an ice drift buoy array with a starting configuration similar to the FRAMZY experiment shows that this configuration is suitable to investigate the ice drift and the internal stress of the ice. Furthermore, especially the variation of the atmospheric and ocean forcing strongly effects the displacement of the array.

7.4 Further studies

The whole experimental phase of FRAMZY'99 has been simulated with REMO (1/6°), forced by ECMWF analysed data. The simulated large-scale meteorological structures are in good agreement with the analysed data from ECMWF and the weather maps of the Deutscher Wetterdienst. The regional model REMO provides additional information like the development of a second cyclone at the ice edge, which does not take place, if the ice edge is modified. A further task is to examine if the additional information of the REMO results is not only plausible but realistic. Therefore the results will be compared with the experimental results and available analysed data. With METRAS the main period of the FRAMZY cyclone on 18/19 April 1999 will be investigated by applying the full model hierarchy (METRAS nested in REMO) and using the interactive METRAS sea ice model. METRAS results shall be compared with measured data from the FRAMZY experiment. Verified METRAS results will be used for validation of REMO

results.

References

Arpe, K., Bengtsson, L., Christoph, M., Claussen, M., Dümenil, L., Esch, M., Giorgetta, M., Schlese, U., Schulweida, U., Roeckner, E. et al. (1996): The atmospheric general circulation model ECHAM-4: Model description and simulation of present-day climate. Max-Planck-Institut für Meteorologie, Hamburg, Germany, Report No. 218.

Birnbaum, G. (1998): Numerische Modellierungen der Wechselwirkung zwischen Atmosphäre und Meereis in der arktischen Eisrandzone. Berichte zur Polarforschung, Alfred-Wegener-Institut für Polar- und Meeresforschung, Bremerhaven, 268, pp 160.

Brümmer, B. and H. Hoeber (1999): A mesoscale cyclone over the Fram Strait and its effect on the sea ice. J. Geophys. Res.

Claussen, M., U. Lohmann, E. Roeckner and U. Schulzweida (1994): A global dataset of land surface parameters. Max-Planck-Institute for Meteorology, Hamburg, Report 135

Jacob, D. and R. Podzun (1997): Sensitivity studies with the regional climate model REMO Meteorology and Atmospheric Physics, Vienna, Austria, 63 (1-2), 119-129.

Lenz, C.-J., K. Bigalke, D. Majewski, K.H. Schlünzen, M. Schatzmann (2000): Calculation of meteorological data with atmospheric models of different horizontal resolution. In preparation.

Majeweski, D., W. Edelmann, U. Schättler, P. Prohl, E. Heise, G. Doms, B. Ritter, A. Link, M. Gertz, T. Hanisch (1995): Dokumentation des EM/DM Systems. Verlag Deutscher Wetterdienst, Offenbach am Main, Germany, pp 191.

Majewski, D. (1991): The Europa-Modell of the Deutscher Wetterdienst. Seminar Proceedings ECMWF, 2, 147-191.

Nansen, F. (1902): The oceanography of the North Polar Basin. The Norwegian North Polar Expedition 1893-1896, scientific results, Vol. 3, pp 427.

Schlünzen, K.H. (1990): Numerical studies on the inland penetration of sea breeze fronts at a coastline with tidally flooded mudflats. Beitr. Phys. Atmosph., 63, 243 - 256.

Schlünzen, K.H., K. Bigalke, C. Lüpkes, U. Niemeier und K. von Salzen (1996): Concept and realization of the mesoscale transport- and fluid-model 'METRAS'. Meteorologisches Institut, ZMK, Universität Hamburg, METRAS Techn. Rep., 5, pp 156.

von Salzen, K., M. Claussen und K.H. Schlünzen (1996): Application of the concept of blending height to the calculation of surface fluxes in a mesoscale model. Meteorol. Zeitschrift, N.F. 5, 60 - 66.

8. Concluding remarks

(B. Brümmer, Meteorological Institute, University of Hamburg)

8.1 Assessment of logistical and technical success

A comprehensive network of measuring systems including of ice buoys, aircraft, ship, and satellite was employed during the field experiment FRAMZY 1999. For the first time, such a network was installed to measure the ice drift in the Fram Strait and its forcing caused by various weather systems, particularly cyclones.

An array of 15 Argos ice buoys - measuring position and 6 of them air pressure in addition - was deployed in the northern part of the Fram Strait by dropping them on parachutes from an aircraft. In spite of the not ideal weather conditions during deployment (strong winds of more than 25 m/s at low levels), 14 of 15 ice buoys functioned well a the beginning. Unfortunately, it was a "pressure" buoy which failed, and it was again a "pressure" buoy which stopped pressure measurements after some time. The pressure part of the buoys appears to be relatively sensitive. In order to ensure a good coverage of the pressure field within an ice buoy array more "pressure" buoys should be used although they are nearly twice as expensive as the simple drift buoys.

For the first time, an meteorologically equipped aircraft, the German research aircraft Falcon, was flying through a Fram Strait cyclone and over the field of drifting ice buoys. It could be demonstrated that aircraft measurements were feasible logistically and technically in such conditions. In order to perform successful flight operations, a longer range aircraft was necessary and weather conditions had to be tolerable not only in the experimental field but also at Longyearbyen airport both during start and estimated time of arrival because airport alternates are not available on Spitsbergen. In that respect the experimentators were lucky. In addition, all equipment on board the aircraft worked well and on-line steering of flight missions by the latest informations from the Argos ice buoys, the NOAA satellites (via Tromsø Satellite Station), and the DWD weather forecasts functioned well, too.

Measurements on board the research vessel Valdivia were successful in spite of the partly adverse circumstances. An aerology container for filling and preparing the radiosonde ballons could unfortunately not be installed on board the ship because of competitive equipment installation requests by the oceanographic research programme. Nevertheless, the aerological programme could be performed as planned, except for a one and a half day long period when the FRAMZY cyclone passed on its way from south to north the Valdivia. Storm and freezing sea water on deck prevented any radiosonde launches for safety reasons of the scientific crew.

8.2 Assessment of scientific success

Beside the fulfilment of the logistical and technical preconditions, the scientific success of a meteorological experiment depends largely on the weather encountered compared to the weather envisaged. In this respect the experimentators were lucky. A cyclone moved between 17 and 19 April 1999 over the experimental area and could be documented by all scientific equipment: ice buoys, aircraft, ship, and satellites. For the first time, a Fram Strait cyclone could be interested by an research aircraft. In this way detailed measurements of the horizontal and vertical structure

of the cyclone and of the atmospheric forcing of the ice drift were sampled. On days without a cyclone, the ice drift was measured continuously by the buoys and, in addition, the atmospheric forcing was measured by aircraft in four cases. Furthermore, the aircraft documented the baroclinic conditions at the ice edge, as a potential for cyclone generation, in these cases. The measurements during FRAMZY 1999 represent a unique data set of the ice drift in the Fram Strait and its forcing under different atmospheric conditions to be used for comparisons and validations of the various uncoupled or coupled research and routine models and of remote sensing methodologies for ice drift and ice extent.

Preliminary comparisons of the measurements with weather analyses (e.g. ECMWF analyses) show that the proper position of the ice edge is a problem in the model. In the ECMWF analyses, the ice edge is about 100 km too far south and east in the Fram Strait. Simulations by the regional models REMO and METRAS will have to account for this in order to allow meaningful comparisons with observations of the other atmospheric and surface parameters.

One further (see Section 7.2), although very detailed cyclone observation appears to be not enough to reach all the objectives listed in section 7.3 with sufficient significance. Further measurements are needed. A future experiment should be performed at a somewhat earlier time in the year (e.g. March), because the ice volume export through Fram Strait is largest at that time and cyclone frequency in the Fram Strait is higher in winter than in summer.

Acknowledgement:
Many thanks are due to Mrs. Sabine Bartols for typing the manuscript.

Die *Berichte aus dem Zentrum für Meeres- und Klimaforschung* erscheinen in 6 Reihen mit folgendem Inhalt:

Reihe A:	Meteorologie
Reihe B:	Ozeanographie
Reihe C:	Geophysik
Reihe D:	Biogeochemie und Meereschemie
Reihe E:	Hydrobiologie und Fischereiwissenschaft
Reihe Z:	Interdisziplinäre Zentrumsberichte

Alle Beiträge sind unredigiert und geben allein die Meinung des Verfassers wieder. Sie sollen in erster Linie dem sich mit dem jeweiligen Thema befassenden Personenkreis als Arbeitsunterlagen dienen und sind oft gleichzeitig Berichte für die Institutionen, die die betreffenden Arbeiten gefördert haben.

Exemplare dieser Arbeit können bezogen werden über:

Meteorologisches Institut
Bundesstr. 55
D-20146 Hamburg

E-mail: bruemmer@dkrz.de
http://www.mi.uni-hamburg.de

ISSN 0947-7128
Zentrum für Meeres- und Klimaforschung der Universität Hamburg
Bundesstr. 55 - 20146 Hamburg

Berichte aus dem Zentrum für Meeres- und Klimaforschung - Reihe A

Meteorologisches Institut
Bundesstr. 55, 20146 Hamburg **http://www.mi.uni-hamburg.de**

1. Schlüssel, P. ; Taurat, D. (1992): The benefits from a synergy of passive satellite measurements with active LIDAR soundings.

2. Brinkop, S. (1992): Parameterisierung von Grenzschichtwolken für Zirkulationsmodelle.

3. Brümmer, B. [Hrsg.] (1992): ARKTIS 1991- Report on the field phase with examples of measurements.

4. Schulz, J. (1993): Fernerkundung des latenten Wärmeflusses an der Meeresoberfläche.

5. Nodorp, D. (1993): Ein Zirkulationsmodell mit transientem Antrieb.

6. Marotzke, K. (1993): Physikalische Modellierung der Ausbreitung störfallartig freigesetzter schwerer Gase zur Abschätzung von Gefahrenbereichen im bebauten Gelände.

7. Martin, T. (1993): Multispektrale Meereisklassifikation mit passiven Satellitenradiometern.

8. Lunkeit, F. (1993): Simulation der interannualen Variabilität mit einem globalen gekoppelten Atmosphäre-Ozean Modell.

9. Kollewe, M. (1993): Fernerkundung von Wolken mit der Sauerstoff Absorptionsbande im nahen Infrarot.

10. Standfuss, C.; Hollweg, H.-D.; Graßl, H. (1993): The impact of a Radiation Budget Scanner aboard Meteosat second generation on the accuracy of regional budget parameters.

11. Brümmer, B. [Hrsg.] (1993): ARKTIS 1993- Report on the field phase with examples of measurements.

12. Richter, M.C. (1994): Niederschlagsmessung mit dem vertikal ausgerichteten FM-CW-Doppler-radar-RASS-System - Validierung und Anwendung.

13. Festschrift zum 70. Geburtstag von Prof. Dr. G. Fischer (1994).

14. Khvorostyanov, V.I. (1994): Mesoscale processes of cloud formation, cloud radiation interaction, and their modelling with explicit cloud microphysics.

15. Wyputta, U. (1994): Untersuchungen zum Stofftransport in die Antarktis anhand von Messungen an der Georg-von-Neumayer-Station.

16. Müller, G. (1995): Mesoskalige Zellularkonvektion in Abhängigkeit von unterschiedlichen physikalischen Prozessen und synoptischen Randbedingungen - Numerische Simulationen.

17. Hollweg, H.-D. et al (1995): Interaction at mm and optical frequencies. Part I: Current problems in radiative transfer simulations.

18. Hollweg, H.-D. et al (1995): Interactions at mm and optical frequencies. Part II: Specific atmospheric absorption and emission features: Investigation and modelling.

19. Grötzner, A. (1995): Subskalige partielle Meereisbedeckung in einem globalen atmosphärischen Zirkulationsmodell.

20. Schlüssel, P. (1995): Passive Fernerkundung der unteren Atmosphäre und der Meeresoberfläche aus dem Weltraum.

21. Bartsch, B. (1996): Fernerkundung des Wasserdampfgehalts der Atmosphäre über Land aus rückgestreuter Sonnenstrahlung.

22. Taurat, D. (1996): Windfelder über See unter Verwendung von Satellitendaten und Druckanalysen.

23. Schlünzen, K.H. (1996): Validierung hochauflösender Regionalmodelle.

24. Donat, J. (1996): Windkanalexperimente zur Ausbreitung von Schwergasstrahlen.

25. Roth, B. (1996): Bildung von H_2SO_4-H_2O-Aerosol in einem vertikalen laminaren Strömungsreaktor.

26. Thiemann, S. (1996): Die vertikale Struktur der konvektiven Grenzschicht während arktischer Kaltluftausbrüche über See.

27. Standfuss, C. et al (1996): Earth Radiation Budget - General Purpose Data Base.

28. Niemeier, U. (1997): Chemische Umsetzungen in einem hochauflösenden mesoskaligen Modell.

29. Schneider, W. (1997): Die Nordostwasser Polynja: Entstehung und Hydrographie.

30. v. Salzen, K. (1997): Entwicklung und Anwendung eines Modells für die Dynamik und Zusammensetzung sekundären und marinen Aerosols.

31. Klugmann, D. (1998): Messung von Niederschlag und Vertikalwind in der unteren Atmosphäre mit Millimeterwellen-Doppler-RADAR-Profilern.

32. Brümmer, B. and S. Thiemann (1999): Field Campaign ACSYS 1998: Aircraft measurements in Arctic on-ice air flows.

33. Brümmer, B. (2000): Field experiment FRAMZY 1999 - Cyclones over the Fram Strait and their impact on sea ice. Field report with examples of measurements.